Dynamical Evolution of Young Embedded Stellar Clusters: Environmental Effects on the Formation of Planetary Systems

by

Eva-Marie Proszkow

A dissertation submitted in partial fulfillment
of the requirements for the degree of
Doctor of Philosophy
(Physics)
in The University of Michigan
2009

Doctoral Committee:

Professor Fred C. Adams, Chair
Professor Nuria P. Calvet
Professor August Evrard
Professor Timothy A. McKay
Professor Mark E. Newman

To my parents

ACKNOWLEDGEMENTS

Over the past nine years, I have had the good fortune of being surrounded by gifted physics educators and researchers. For that I'm very grateful to the faculty at both the University of Michigan and Xavier University. I'm especially grateful to Fred Adams who, as my thesis adviser, has fostered in me a sense of scientific curiosity while providing the guidance, expertise, and critique necessary to help me accomplish my education and research goals. Another scientist who has been particularly influential in my education is Marco Fatuzzo who was first my undergraduate research adviser, later my teacher, and finally my collaborator (Chapter II, Adams et al. 2006). I thank him for his lessons and encouragement.

Many other talented collaborators have been instrumental in the research that is presented in this thesis. In particular, I spent more than a year as a visiting student at the Smithsonian Astrophysical Observatory's Center for Astrophysics, working with a group of scientists involved in the *Spitzer* Young Stellar Cluster Survey and the c2d Legacy Program. Throughout that time, Lori Allen and Phil Myers were gracious hosts. Phil became a surrogate adviser and mentor during those visits, and I benefited from his years of experience in the field. It was with his encouragement that I applied the tools I had developed to study the internal dynamics of stellar clusters to the larger problem of cluster formation (Chapter V, Proszkow & Myers 2008). I am also thankful to Lee Hartman and John Tobin with whom we worked closely during our study of kinematics of the Orion Nebula Cluster (Chapter IV, Proszkow et al. 2009). Their observational insight and perspective challenged

me to think beyond the purely theoretical realm to develop measurements that could be more directly compared with astronomical observations.

Being a graduate student requires significant support from outside of academia as well, and I thank my friends and family, near and far, who have helped me in so many ways during this journey. I am incredibly grateful to my parents for all the years of love and support, and for always believing in me no matter how big I dreamed. I also want to thank my brother Peter for his companionship, endless comic relief, and free 24-hour IT support. Finally, and most sincerely, I want to thank my husband Nick for his constant friendship, love, and strength. For the last three years he has sacrificed much and complained little, and for that I am truly blessed.

TABLE OF CONTENTS

LIST OF TABLES

Table

LIST OF FIGURES

Figure

LIST OF APPENDICES

Appendices

CHAPTER I

Introduction

In typical spiral galaxies, such as our Milky Way, the vast majority of star formation occurs embedded deep within giant molecular clouds (GMCs). These stellar nurseries are primarily composed of cold dense molecular hydrogen mixed with small amounts of dust and other heavy elements. The volume averaged density of GMCs is roughly $\sim 10^3$ cm^{-3}, but they are highly non-uniform, and in the densest regions young stars are born.

Infrared observations of GMCs over the last 30 years have provided strong evidence that clustered star formation is a dominant mode of star formation. It is estimated that more than 90% of all stars form within clusters of more than ~ 100 members. At the earliest ages, these young stellar clusters are deeply embedded in their parent molecular clouds and, veiled by dust and dense gas, are unobservable at visible wavelengths. Stars form out of the material in the cloud, and thus the process of star formation is by nature destructive to embedding clouds. More importantly, young stellar objects are associated with powerful winds and outflows and the most massive stars emit substantial amounts of UV radiation throughout their short lifetimes. These strong winds and radiation fields disperse much of the remaining embedding material and sculpt cavities into the surrounding clouds. A combination of these processes transforms embedded clusters into exposed visible clusters over a relatively short period of time. In fact, clusters with ages greater than ~ 5 Myr are rarely associated with molecular gas (Leisawitz et al. 1989; Lada & Lada 2003; Allen et al.

2007). On average, 10% to 30% of the dense molecular cloud material is converted into stars before gas dispersal halts star formation in the cluster.

As the smallest (non-trivial) scale on which star formation occurs, and because isolated star formation comprises a small fraction of all star formation, young embedded clusters represent fundamental units of star formation. Thus an understanding of their creation and evolution provides deeper insight into many astrophysical processes. On the largest scales, stellar evolution is responsible for recycling galactic material and so accurate descriptions of star formation and evolution are necessary components of galactic evolution theories. On the scale of individual stars, conservation of angular momentum requires that star formation be accompanied by circumstellar disk formation. These disks are the progenitors of planetary systems. Therefore, star and planet formation are intrinsically linked and the star formation environment may have significant consequences for solar system formation, stability, and habitability. Star formation theories should also provide insight into general properties of the galactic stellar population, such as the apparent universality of the stellar initial mass function (IMF), the distribution of binary companions, and the frequencies and structure of planetary systems. The clustered environment in which most star formation occurs places limits on the star formation efficiency, the size of planet-forming disks and the timescale on which planet formation can occur. In addition to dispersing the embedding molecular gas and thus limiting star formation efficiency, strong radiation fields produced by young stellar objects can photoevaporate disks surrounding young stars and restrict their planet-forming potential. Stellar clusters also provide dense environments in which gravitational interactions between cluster members can affect circumstellar disks, limiting planet formation and disrupting young solar systems.

In this thesis we study the dynamics of embedded stellar clusters from the protocluster stage, through the embedded star-forming stages, and out to ages of ~ 10 Myr when the

embedding material has been removed from the cluster. Although stellar clusters continue to evolve on longer timescales, this research focuses on the young cluster environment in which planet formation is likely to occur. In Chapters II and III we present a study in which the relevant dynamical properties of young stellar clusters are explored over a host of possible star formation environments. We discuss the implications for planet formation and solar system survivability within these clusters. In Chapter IV we present an observable kinematic signature which may be used as a tracer of initial cluster dynamics. We discuss this signature in light of recent observations of the nearby massive star-forming region the Orion Nebula Cluster. In Chapter V we discuss the effect of large scale tidal interactions on dense protocluster cores within GMCs and examine the implications these interactions have for stellar cluster formation. A table summarizing all the simulations completed as a part of this thesis work is included in Appendix A.

1.1 Observations of Young Embedded Clusters

Embedded clusters are distinguished from other types of stellar clusters by their association with significant amounts of molecular gas and dust. This interstellar material is optically thick at visible wavelengths, with extinctions as high as $\mathcal{A}_V \sim 100$ magnitudes (Vrba et al. 1975; Strom et al. 1976; Chini et al. 1977; Wilking & Lada 1983). In contrast, the extinction is much less severe in near-infrared bands J, H, and K ($1.2, 1.6$, and 2.2μm, respectively): $\mathcal{A}_K \sim \mathcal{A}_V/10$, allowing infrared observations to penetrate the embedding gas and reveal very young stellar objects (Zinnecker et al. 1993, and references therein). Observations in the near-infrared have the additional advantage that stars are significantly brighter during their pre-main sequence phase in these bands than they are throughout the remainder of their main sequence life cycles. This property allows for easier detection of young stellar objects in embedded clusters over a wide range of masses through the use of infrared photometry.

To date, most embedded clusters have been identified through the use of two main observational techniques: [1] systematic infrared surveys of molecular clouds (Lada et al. 1991; Carpenter et al. 2000), including the recent *Spitzer Space Telescope* c2d Survey of Large, Nearby, Interstellar Clouds (see Evans et al. 2003, and associated papers), and [2] infrared surveys of regions containing signposts of recent star formation such as outflows, bright IRAS sources, Herbig AeBe stars, and bright rimmed clouds (Hodapp 1994; Carpenter et al. 1993; Minier et al. 2005; Testi et al. 1998; Sugitani et al. 1995). Regions of interest are targeted by these techniques and clusters are then identified by an enhanced surface density of stars relative to the background. These methods of cluster identification result in some inherent ambiguity in the spatial sizes of clusters, i.e., the measured cluster radii. In nearby clusters, the radius is often identified with that of a circle center on and encompassing all cluster members in the field. For more distant clusters, the half-light radius is sometime quoted as the cluster radius. Therefore, the term cluster radius is not always well defined observationally, and the measured cluster radii may vary from the true value by a factor of ~ 2.

Identifying individual stars as cluster members is more difficult and requires additional information such as proper motions, multi-band photometry, and/or observations of spectral features indicative of stellar youth such as infrared excess or Hα emission. In early cluster studies total cluster membership was often determined on a statistical basis only, by comparing the cluster population to the expected number of background contamination sources. More recently multi-fiber spectrometers, space-based infrared telescopes such as the *Spitzer Space Telescope*, and advances in our understanding of the photometric colors of young stars have allowed for cluster membership to be established on an individual basis for stars within the vicinity of a young embedded cluster. Allen et al. (2007) provides a more complete review of recent developments in the techniques used to identify young

stellar objects.

The kinematics of young embedded clusters may be investigated by employing appropriate Doppler shift techniques as well as conducting proper motion studies of individual cluster members. The bulk line-of-sight motions of moderately low density interstellar gas is most often measured using the spectral lines produced by the (1-0) transition of ^{13}CO or the (1-0) transition of C^{18}O (Bally et al. 1987; Wilson et al. 2005; Kirk et al. 2007). These lines trace gas at column densities of roughly $N_H \sim 1.1 \times 10^{26}$ cm^{-2} and $N_H \sim 8.5 \times 10^{26}$ cm^{-2}, respectively (Binney & Merrifield 1998). Higher density molecular cloud cores are also observed in young embedded clusters. The mass distributions of these cores is similar to (though not identical to) the initial mass function of field stars (Motte et al. 1998; Johnstone et al. 2000; Walsh et al. 2007; Alves et al. 2007). This similarity, combined with the frequent association of these cores with the youngest stellar objects (class 0 sources), is a relatively strong indication that the starless dense cores may represent the earliest stages of star formation. The motions of these dense cores are most commonly probed using Doppler shift of the (1-0) emission line in N_2H^+ which traces gas at densities up to $n_H \sim 10^6$ cm^{-3} (Tafalla et al. 2002; Walsh et al. 2004; 2007; Kirk et al. 2007).

Another way to investigate the internal kinematics of young clusters is through proper motion surveys of clusters or individual pre-main sequence stars (Jones & Walker 1988; Ducourant et al. 2005). While these surveys provide two-dimensional information regarding the motion of the stars in the plane of the sky, they require detailed astrometry and long baselines. Doppler techniques such as those used to study the motions of dense gas may also be applied to individual stellar spectra. The advent of multi-fiber spectrometers such as MIKE and Hectoschelle (Szentgyorgyi et al. 1998; Walker et al. 2007) has made radial velocity studies of large samples of stars much easier to complete. Cluster members are first

identified by color-magnitude selection, Hα emission, or other signposts of stellar youth. Then spectra are taken near the Hα line ($\lambda \sim 6560$ Å) and velocities are determined by fitting the stellar spectra with models that include Doppler shift effects (Fűrész et al. 2006; 2008; Tobin et al. 2009). This technique, however, does require that the stars be observable at visible wavelengths as so is most applicable in partially or fully exposed clusters where the extinction in the visible bands is relatively low.

1.2 Properties of Young Embedded Clusters

Giant molecular clouds located in the arms of spiral galaxies serve as the primary site of star formation within most late-type galaxies. Inside these large ($d \sim 10 - 50$ pc), cold ($T \sim 10$ K), dense ($n \gtrsim 10^3$ cm^{-3}) clouds, the majority of star formation is concentrated in relatively small, high density regions approximately a parsec (1 pc $= 3 \times 10^{18}$ cm) in extent and containing on the order of a few hundred solar masses of gas and stars. Some of the earliest studies of star formation within molecular clouds indicated that almost all of the youngest stellar objects were actually associated with dense young clusters rather than distributed throughout the cloud. The survey of the Orion Molecular Cloud completed by Lada et al. (1991) suggested that as much as $\sim 96\%$ of all star formation within the cloud was occurring within 4 young clusters. Recent observations continue to indicate that clustered star formation is a dominant mode within molecular cloud complexes, though some distributed star formation is still observed. Surveys of molecular cloud complexes recently completed with the *Spitzer Space Telescope* have produced estimates of the total fraction of star formation occurring in clustered environments that range from $\sim 70 - 90\%$ (Megeath et al. 2005; Padgett et al. 2008). Outside of our own galaxy, Whitney et al. (2008) found that young stellar objects in the Large Magellanic Cloud are highly clustered on the smallest scales resolvable with the *Spitzer Space Telescope* (~ 3 pc).

Nearby embedded cluster catalogs which are complete down to the smallest clusters ($\sim$

30 members) have been presented by Lada & Lada (2003) and Porras et al. (2003). (Groups of stars with $N \lesssim 35$ have relaxation times that are comparable to or less than their crossing times and thus are not usually considered to be "clusters," but rather loose associations of stars.) A more recent survey of many of the nearest clusters contained in these catalogs has been completed as a part of the *Spitzer* Young Cluster Survey. Preliminary results of this cluster survey have been presented by Megeath et al. (2004) and Allen et al. (2007), and additional results are in preparation. In light of these published catalogs, we discuss the general characteristics of embedded clusters in the solar neighborhood.

Embedded clusters within the nearest 2 kpc of the Sun have (total stellar) masses ranging over almost 3 orders of magnitude from ~ 20 $M_\odot$ to more than 1000 $M_\odot$. The embedded cluster mass distribution function is roughly flat over the range from $50 - 1000$ $M_\odot$ (Lada & Lada 2003), which implies that the total mass of cluster members is equally distributed over logarithmically spaced mass bins. Additionally $\sim 90\%$ of clustered star formation in the solar neighborhood occurs in embedded clusters with more than ~ 100 members.

Defining a *typical* cluster size is a difficult task which is further complicated by the nonspherical geometry of many clusters (Gutermuth et al. 2005; Schmeja & Klessen 2006), and the threshold limits inherent to cluster identification via surface density enhancements (Allen et al. 2007). However, in general, embedded clusters have radii R_c ranging from a tenth of a parsec to a few parsecs, and roughly constant surface densities. Figure 1.1 presents the cluster radii R_c and memberships N for clusters contained in the Carpenter (2000) (triangles) and Lada & Lada (2003) catalogs (diamonds). There is considerable scatter in the embedded cluster membership-size relation but it may be roughly fit by the function:

$$R_c = R_{sc}\sqrt{\frac{N}{300}} \tag{1.1}$$

where N is the cluster membership and R_{sc} is a scaling radius in parsecs. Values of R_{sc} may range from ~ 1 to 3 pc.

In starburst galaxies where star formation rates are much higher and star formation occurs in much larger clusters ($N \sim 10^5 - 10^6$), the cluster membership-size relation may be somewhat different from that observed in the solar neighborhood. Mengel et al. (2008) present masses (both photometric and dynamical) and half-light radii for 12 massive clusters in the interacting Antennae galaxies. The masses of these clusters range from 0.2×10^6 $M_\odot$ to 3×10^6 $M_\odot$ and the cluster radii range from $1 - 8$ pc. Figure 1.1 also displays the data from this study of the Antennae galaxies, indicated by the pluses and x's. The solid line indicates the $R_c \sim N^{1/2}$ relationship found in nearby embedded clusters (Carpenter 2000; Lada & Lada 2003). This cluster membership-size relation (equation [1.1]) deviates from the observations at the largest cluster sizes. The dotted line denotes a cluster membership-radius relation with a power law index of 1/4 which more nearly approaches the values observed in extremely massive star-forming clusters in interacting galaxies.

Young embedded clusters display two general morphologies: [1] centrally concentrated and [2] hierarchical. Clusters such as the ONC (Hillenbrand & Hartmann 1998), IC 348 (Muench et al. 2003), and NGC 7129 (Muzerolle et al. 2004; Allen et al. 2007) are just a few examples of centrally concentrated clusters which are often accompanied by a lower density halo of young stellar objects surrounding the high density peak. On the other hand, clusters such as NGC 1333 (Lada et al. 1996), and NGC 2264 (Lada et al. 1993) exhibit multiple high density peaks and structure over a large range of spatial scales, and are thus classified as hierarchical (Lada & Lada 2003).

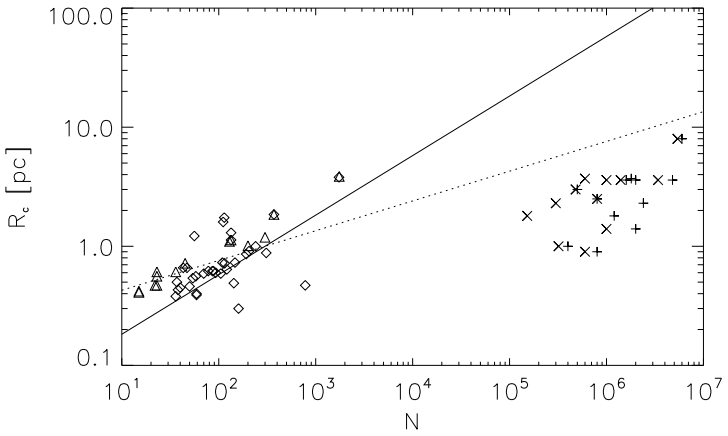

Figure 1.1: Observed cluster radii R_c in the solar neighborhood and in the interacting Antennae galaxies displayed as a function of cluster membership N. Diamonds correspond to clusters included in the Lada & Lada (2003) catalog, and triangles represent data from the Carpenter (2000) catalog of young clusters in the solar neighborhood. The solid line corresponds to the cluster membership-size relation with power law index equal to 1/2 as found in nearby embedded clusters. The pluses and x's in this plot are taken from the Antennae galaxy survey of Mengel et al. (2008), where the masses have been converted to stellar memberships N by assuming an average stellar mass of 0.5 $M_\odot$. Pluses indicate the membership derived from the dynamical masses of the clusters whereas x's indicate memberships derived from the photometric masses. The dashed line indicates a cluster membership-size relation with power law index equal to 1/4 and more nearly approaches the values observed in the extremely massive star-forming clusters observed in these interacting galaxies.

Average aspect ratios for clusters range between 1 and 4 (Hillenbrand & Hartmann 1998; Carpenter et al. 1997; Gutermuth et al. 2005, Gutermuth et al. 2009, in preparation). In cases where elongation is apparent, the cluster is often aligned with the larger scale geometry of the molecular cloud in which it is embedded. These observations suggest that forming clusters maintain an imprint of the molecular cloud environment in which they are born. In addition, in a number of embedded clusters, the youngest stars (class 0/I sources) appear to trace the densest gas, whereas the slightly more evolved stars (class II sources) are more dispersed throughout the cluster. Examples of young clusters with distinctly different distributions of class 0/I sources and class II sources include the Serpens region (Winston et al. 2007; Gutermuth et al. 2008a), the ONC (Lada et al. 2000), and NGC 2264 (Teixeira et al. 2006).

Although the most massive stars are preferentially found near the center of open clusters, varying amounts of mass segregation are observed in young embedded clusters. The

Trapezium is a well known example of a cluster that has significant mass segregation but is possibly too young for the segregation to be the result of dynamics (Hillenbrand & Hartmann 1998; Bonnell & Davies 1998). NGC 2071 and NGC 2024 (Lada et al. 1991) also exhibit evidence of mass segregation, with the most massive stars residing near the clusters' centers. However, this is not always the case. Many young embedded clusters, including Mon R2, display no strong evidence of mass segregation or any variation of the mass distribution over different regions of the cluster (Carpenter et al. 1997).

Giant molecular clouds are highly non-uniform, and the densest portions of GMCs are the sites of embedded cluster formation (Ballesteros-Paredes et al. 2007). These high density regions are $1-10$ pc in size and contain $\sim 10^2-10^5$ $M_\odot$ of stars and gas (Kramer et al. 1998; Heyer & Terebey 1998). Observations of deeply embedded clusters indicate that the gas density profiles are often centrally concentrated and may be reasonably approximated by the density profile $\rho \sim r^{-1}$ (Larson 1985; Myers & Fuller 1993; Jijina et al. 1999). In some less embedded clusters, regions of triggered star formation, or regions containing young massive stars whose radiation is sculpting the surrounding cloud, the embedding gas often displays more structure, and may appear to be flattened, layered, or filamentary (Deharveng et al. 2005; Churchwell et al. 2006). Orion B is an example of a cluster-forming cloud which is believed to have been compressed by the nearby OB1 association (Wilson et al. 2005), as is the DR 21 ridge near the Cyg OB2 association (Schneider et al. 2006; Kumar et al. 2007).

The onset of massive star formation within an embedded cluster often marks the beginning of the end of star formation within that cluster. Ionizing radiation produced by massive O stars and non-ionizing far-ultraviolet (FUV) radiation produced by B stars heat the surrounding embedding material, increasing the pressure and resulting in rapid expansion of the gas. This mechanism may remove embedding gas from the cluster on timescales

as short at $\sim 10^4$ years (Whitworth 1979) and is observed to be occurring in many nearby star-forming regions including Mon R2, NGC 7129, IC 5146, and IC 348 (Beckwith et al. 1976; Hillenbrand 1995; Luhman et al. 2003; Herbig & Dahm 2002). In smaller clusters which lack massive star formation, winds from low mass stars are likely responsible for dispersing the interstellar material, albeit on longer timescales (Matzner & McKee 2000). Examples of regions where stellar winds appear to be removing the embedding material include IRAS 20050 (Chen et al. 1997) and NGC 1333 (Quillen et al. 2005).

In addition to setting the final star formation efficiency (SFE) of a cluster, the mechanisms and timescale of interstellar gas dispersal are major factors in determining whether or not a young embedded cluster is destined to evolve into a bound open cluster. As gas is removed from the cluster, the higher velocity stars become gravitationally unbound. If the SFE of the cluster is sufficiently low and the gas removal timescale relatively short, the entire cluster may become unbound as gas is expelled from the cluster. This phenomenon of embedded cluster 'infant mortality' provides one explanation for the discrepancy between the embedded cluster formation rate and the bound open cluster formation rate, which is an order of magnitude lower (Lada & Lada 2003, and references therein).

Recent kinematic observations of the protostellar cores (N_2H^+ cores) in embedded clusters reveal that the velocities of these objects are significantly lower than would be expected in virial equilibrium. Typical embedded clusters with $R_c = 1$ pc and $N = 300$ stars require core-to-core velocity dispersions of roughly 1 km s^{-1} to remain supported against global gravitational collapse. However, in embedded regions such as NGC 1333, ρ Oph, and clusters within the Perseus Molecular Cloud, the velocity dispersions are much lower: ~ 0.45 km s^{-1}, 0.64 km s^{-1}, and $0.09 - 0.55$ km s^{-1}, respectively (Walsh et al. 2004; André 2002; Kirk et al. 2006). In NGC 2264, the expected velocity dispersion for virial equilibrium is $\sim 3-4$ km s^{-1}; however, Peretto et al. (2006) find that the cores are moving

with dispersions roughly $2-3$ times smaller than this virial velocity. If these cores are indeed the earliest stage of star formation, this finding implies that stars in clusters are born with substantially subvirial velocities.

The initial configuration (spatial and kinematic) of young embedded clusters has significant consequences for the later evolution of the clusters and the formation of planetary systems around stars in those clusters. This thesis focuses on the dynamics of young embedded clusters and studies how the initial embedded cluster environment affects cluster evolution and subsequent planet formation. Cluster evolution from the earliest embedded phases, though the gas removal phase, out to ages of 10 Myr is studied using N-body simulation techniques and employing initial conditions appropriate for young embedded clusters. These initial conditions are motivated by the wealth of observational data that has become available over the last 30 years (and especially in the last 5 years with the *Spitzer Space Telescope*) regarding the young embedded clusters in our solar neighborhood.

This work focuses on the evolution of intermediate-sized clusters which have initial conditions that are subvirial and somewhat less concentrated than those considered in previous theoretical studies. Many previous studies of cluster dynamics have focused on either small groups with $N \leq 100$ stars (Lada et al. 1984) or on large stellar clusters with $N > 10,000$ members (Portegies Zwart et al. 1998; Boily & Kroupa 2003b). Some studies have concentrated on intermediate-sized clusters with $N \sim 100-1000$ stars (Kroupa 1995a) but consider densities as high as 10^5 cm^{-3} and focus on the long term evolution of the clusters $\sim$ 100 Myr -1 Gyr. In contrast, our simulations remain targeted on the short term evolution ($t \lesssim 10$ Myr) of clusters with maximum average densities on the order of $n \sim 10^3$ pc^{-3}. These conditions reflect the environments in which most stars form. This research centers on one particular aspect of the star formation process, namely circumstellar disk and solar system disruption. Specifically, we consider how radiation

fields and close encounters in a clustered environment can limit or disrupt the formation of planetary systems. Because the planetary formation processes occur relatively early in a star's lifetime ($\sim$ 10 Myr), our simulations target the early evolution of young stellar clusters.

This research is also distinctive in that it is statistical in nature. Our initial cluster survey indicates that $\sim$ 100 realizations (simulations) of each set of cluster parameters are required in order to produce a robust statistical description of the output measures describing the evolution of a cluster (see Chapters II and III, and also Adams et al. 2006). Specifically, the results of multiple realizations are combined to produce distributions of stellar positions within the cluster and distributions of close encounters between cluster members. In addition, we determine the distribution of parameters that describe the temporal evolution of the cluster, i.e., the bound fraction, virial ratio, velocity isotropy parameter, etc. With these statistical descriptions of cluster evolution in hand, we discuss the implications of specific cluster initial conditions on the observed kinematics of cluster members and the formation of planetary systems within young stellar clusters. As shown in subsequent chapters, we find that the cluster environment has a *moderate* influence on forming solar systems. In other words, the effects are large enough that they must be included to provide a working understanding of star and planet formation, but not so large as to dominate the process. In keeping with this intermediate level of efficacy, the effects of clusters must be described in terms of probability distributions. These results, including the relevant probability distributions, are presented in this thesis.

CHAPTER II

Early Evolution of Stellar Groups and Clusters: Environmental Effects on Forming Planetary Systems

2.1 Introduction

Current data indicate that a significant fraction of the stellar population is born in groups and clusters embedded within the densest regions of giant molecular clouds (GMCs). Advances in infrared astronomy during the past two decades have afforded astronomers with an unprecedented view of these stellar nurseries. These clouds form relatively rapidly ($1 - 10$ Myr) out of intergalactic gas and dust as a result of the complex interplay of spiral density waves, supernova explosions, phase transitions, and instabilities (e.g., Elmegreen 1991; Heitsch et al. 2006, and references therein). Once formed, GMCs obtain a highly clumpy structure, possibly due to collisions in supersonic turbulent flows (e.g., Klessen et al. 2000). This highly nonuniform structure contains numerous cores with masses ranging from a few to a few thousand solar masses. These dense cores (which have been mapped in NH_3; see the compilation of Jijina et al. 1999) are the sites of star formation. Specifically, fragmentation within the more massive cores ($M > 50$ $M_\odot$), possibly resulting from Jeans instability, decoupling of fluid and MHD waves (Myers 1998), and/or from the decay of turbulence (Klessen & Burkert 2001; 2000), form gravitationally unstable substructures whose subsequent collapse leads to the formation of protostars (e.g., Shu 1977; Fatuzzo et al. 2004). At the end of this complex process, young embedded groups/clusters appear

to be basic units of star formation, accounting for a significant fraction (perhaps as high as 90%) of the stars that populate our Galactic disk. The evolution of these young clusters and their resulting effects on stellar and planetary formation represents a fundamental set of astrophysical problems.

The *typical* size of star formation aggregates remains poorly defined. Lada & Lada (2003) and Porras et al. (2003) presented catalogs of nearby embedded clusters, the former including systems with $N \geq 30$ out to 2 kpc, and the latter including systems with $N \geq 10$ out to 1 kpc. The cumulative distributions for the number of stars born in units of size N, as a function of N, are presented in Figure 2.1 for both catalogs. The squares represent the 2 kpc sample, and the triangles represent the 1 kpc sample; the dashed curve shows the 1 kpc sample subjected to the same criteria as the 2 kpc sample ($N \geq 30$). The two samples provide a consistent estimate for the probability distribution of group/cluster sizes. One should keep in mind that these samples are not complete. Some of the distant groups/clusters in the sample may have larger stellar membership (than reported) because the faint (low-mass) end of the stellar initial mass function (IMF) is not fully observed. On the other hand, small groups with $N \sim 30 - 100$ may well exist and not be included in the samples at all. As a result, the true distribution of cluster sizes N could be skewed toward either higher or lower N than shown in Figure 2.1. For the sake of definiteness, however, in this chapter we take this sample to be representative.

Large clusters such as the Trapezium in Orion (with $N > 1000$) are known to be disruptive to the star formation process (e.g., Störzer & Hollenbach 1999). In contrast, small groups with $N \leq 100$ often have relatively little impact (e.g., Adams & Myers 2001). As shown in Figure 2.1, however, the majority of stars observed in embedded clusters are found in systems that contain between 100 and 1000 members (at least for these observational samples). The evolution of these intermediate-sized systems and their effects

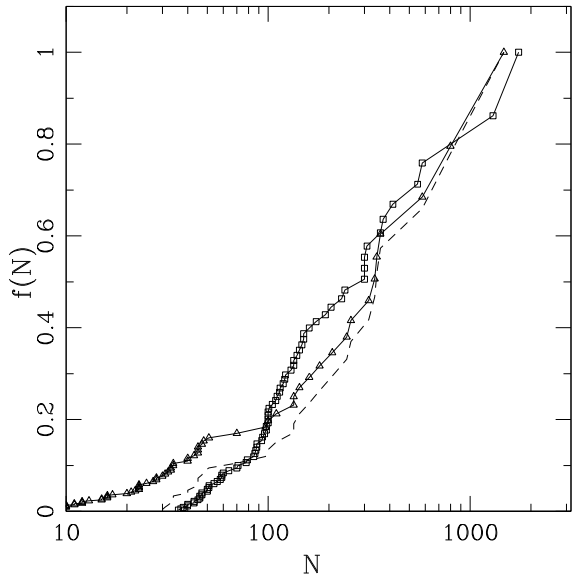

Figure 2.1: Cumulative distribution of group/cluster sizes as a function of system size N. The quantity $f(N)$ is the fraction of the total number of stars in the sample that live in groups/clusters of system size N or smaller. The curve marked by squares corresponds to the 2 kpc sample, which is complete down to $N = 30$ (Lada & Lada 2003); the curve marked by triangles is the 1 kpc sample, which is complete down to $N = 10$ (Porras et al. 2003). The dashed curve shows the 1 kpc sample subjected to the same selection criteria as the 2 kpc sample.

on star and planetary formation are thus of fundamental importance. These systems can influence star and planet formation through dynamical interactions among kernels, competitive accretion, scattering interactions among star-disk systems and/or or early planetary systems, and by disruptive radiation from other stars (especially the larger ones that live near cluster centers).

This chapter considers the dynamics of intermediate-sized stellar systems with $N = 100 - 1000$. In the two data sets described above (Lada & Lada 2003; Porras et al. 2003), the fraction of stars that are found in systems with $N < 100$ is 19% and 20%, respectively, whereas the fraction of stars found in systems with $N > 1000$ is 24% and 20%. The majority of stars (about 60%) are found in systems within our range of study. A large body of previous work on the dynamical evolution of N-body systems exists. The evolution of

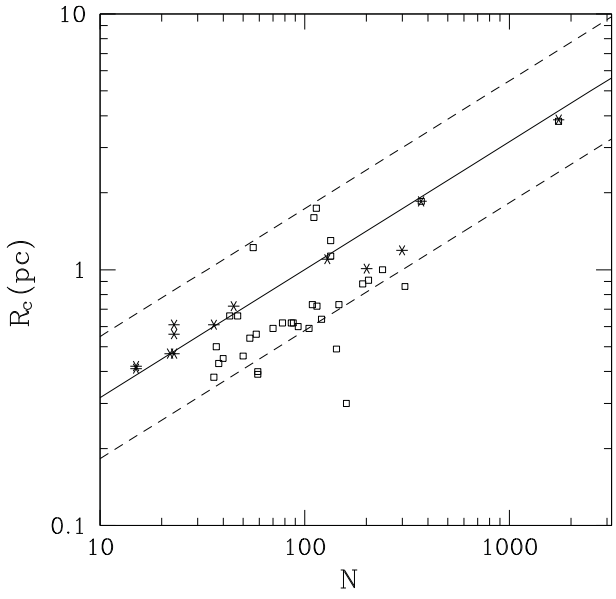

Figure 2.2: Observed group/cluster radii R_c as a function of system size N. The squares represent data taken from the compilation of Lada & Lada (2003); the stars represent data from the work of Carpenter (2000). The solid curve is a rough fit to the data with the form $R_c = R_{sc}(N/300)^{1/2}$ with $R_{sc} = \sqrt{3}$ pc; the two dashed curves have the same functional dependence with the length scale R_{sc} larger or smaller by a factor of $\sqrt{3}$. For most of this work we use the lower curve, with $R_c = 1$ pc $(N/300)^{1/2}$ in order to determine the greatest possible effects of the cluster environment.

stellar clusters has been investigated for both small $N \leq 100$ (Lada et al. 1984) and large $N > 10,000$ (e.g., Portegies Zwart et al. 1998; Boily & Kroupa 2003b). The dynamical effects of binaries has also been explored both in the context of globular clusters (Hut & Bahcall 1983) and young clusters (Kroupa et al. 1999; Kroupa & Bouvier 2003). Some work on intermediate-sized systems has been performed (see Kroupa 1995a, and references therein). On a smaller system scale, planetary disruption has been explored by numerous authors (e.g., de La Fuente Marcos & de La Fuente Marcos 1997; 1999; Adams & Laughlin 2001; Smith & Bonnell 2001; Hurley & Shara 2002; David et al. 2003; Fregeau et al. 2006), and the few-body problem has been investigated by Sterzik & Durisen (1998). Although these works have greatly advanced our understanding of the dynamics of many-body systems, a great deal of work remains to be done. This chapter concentrates on the range of parameter space populated by most young stellar clusters, N in the range $100 \leq N \leq 1000$,

and seeks to determine the effect of the cluster environment on forming stars and planetary systems.

In addition to its focus on intermediate-sized clusters, this work differs from previous studies in the starting conditions. Most previous N-body simulations of stellar groups have invoked virial arguments to set the initial velocities of the system members. A distinguishing aspect of this study is the adoption of subvirial starting conditions. This initial condition is motivated by clump dispersion measurements obtained from recent observations of four systems in which the stars are (apparently) born with speeds substantially lower than virial (assuming that observed clumps are progenitors of individual protostars or stars). Specifically, in the NGC 1333 cluster, the observed clump-to-clump rms velocity is only ~ 0.45 km s^{-1}, somewhat less than that expected if the clumps were in virialized orbits ($v \sim 1$ km s^{-1}); furthermore, the clump-to-clump rms velocity is much lower for subgroups within the larger complex (Walsh et al. 2004). Similarly, the velocity dispersion for 45 clumps (condensations) in ρ Oph was estimated to be ~ 0.64 km s^{-1}, with similar results obtained for 25 clumps in the NGC 2068 protocluster (see André 2002, and references therein). As another example, the clump to clump velocities in the NGC 2264 region are estimated to be about 3 times smaller than that expected in virial equilibrium (Peretto et al. 2006).

This chapter undertakes a statistically comprehensive study of the dynamical evolution of young stellar clusters with populations in the range $100 \leq N \leq 1000$ and uses N-body simulations to follow these systems from their nascent, embedded stages out to ages of 10 Myr. One goal of this study is to explore how early evolution depends on the number N of system members. The systems begin with a gaseous component that is subsequently removed (e.g., at time 5 Myr). Multiple realizations of equivalent initial conditions are performed in order to build up robust distributions of the output measures. We find that

100 realizations (simulations) of each set of initial conditions are required to provide good statistics for the output measures. These measures include closest approaches of cluster members, their radial locations and mass profiles (which largely determine the radiation exposure), as well as the time evolution of the bound cluster fraction, the virial ratio, the velocity isotropy parameter, and the half-mass radius. Because of the large number of simulations required for each set of initial conditions, we limit this preliminary study to six cluster types: $N = 100, 300$, and 1000, with both subvirial and virial initial conditions.

The output measures are used to determine the impact of the cluster environment on star and planet formation. Toward that end, we determine the distribution of FUV luminosities for groups and clusters as a function of system size N. This ultraviolet radiation acts to destroy circumstellar disks and to inhibit planet formation. This work provides a measure of its efficacy as a function of group/cluster size N (Section 2.3). We also calculate the cross sections for newborn planetary systems to be disrupted by passing stars (binaries). These cross sections (Section 2.4) are used in conjunction with the distributions of closest approaches from the N-body simulations to provide a measure of solar system disruption as a function of system size N. Armed with a robust statistical description of the evolution of young clusters, we undertake a detailed analysis of the particular system NGC 1333 (Section 2.5). Recent observations of this young cluster (Walsh et al. 2007) provide position and velocity information on the $N = 93$ N_2H^+ clumps found within the system. Since the observations specify only three of the six components of phase-space, we must reconstruct the cluster conditions through multiple realizations, thereby producing an ensemble of calculations that can then be compared with the results of our theoretical study. Our results and conclusions are summarized in Section 2.6.

2.2 Numerical Simulations of Young Embedded Clusters

For the first part of this study we perform a suite of N-body simulations for intermediate-sized clusters as they evolve from their embedded stage out to ages of ~ 10 Myr. Cluster evolution depends on the cluster size N, the initial stellar profile, the initial gas profile, the star formation history, the stellar IMF, and the gas disruption history. Given the large number of parameters needed to adequately describe young clusters (see also below), this initial study does not consider every combination of parameters that these systems could attain. Instead, we identify a baseline set of parameters that represent a typical cluster and perform many realizations of this benchmark model. We find that for every set of cluster parameters, one must perform many realizations of the initial conditions in order to fully sample the output measures. This study explores the variation of the cluster size N and the effects of subvirial versus virial starting conditions. A wider exploration of parameter space is presented in Chapter III. For each set of input parameters, we perform 100 equivalent realizations in order to build up a statistical representation of the output measures. The input parameters and output measures are described below.

The N-body integrations are performed using NBODY2 (Aarseth 1999; 2001). This version of the integration package is relatively fast and allows for many realizations of each set of initial conditions to be run, as required to obtain good statistics. In this initial study, however, we do not include the binarity of the stellar systems. In sufficiently dense and long-lived clusters, binaries can absorb and store enough energy to affect the evolution of the cluster system. This chapter focuses on the dynamics of systems with $N = 100 - 1000$, where we expect interactions to be sufficiently rare and sufficiently distant that binarity has only a small effect on overall energy budget of the cluster (see also Kroupa 1995b; Kroupa et al. 2003). This approximation is checked for consistency in two ways. First, we perform a set of test simulations including binaries (using NBODY6; Aarseth 1999) and

find that the results are the same. As a second check, we use the distributions of closest approaches found from our ensemble of simulations and find that binary interactions are not energetically important in these systems (see below).

2.2.1 Parameter Space

Cluster membership, N. Figure 2.1 indicates that most stars form in clusters with stellar membership N in the range $100 \leq N \leq 1000$, with roughly half of stars belonging to clusters with size $N < 300$ (and half with $N > 300$). We thus consider the value $N = 300$ as the center of our parameter space, and explore the evolution of clusters with $N = 100, 300$, and 1000.

Initial cluster radius, R_c. Young clusters are found to have radii R_c within the range $0.1 - 2$ pc. An observationally determined relation between R_c and N is shown in Figure 2.2, where squares represent data taken from the compilation of Lada & Lada (2003) and stars represent data from Carpenter (2000). A correlation between R_c and N is clearly evident, although significant scatter exists. The data can be fit by the relation of the form

$$R_c = R_{sc}\sqrt{\frac{N}{300}}, \tag{2.1}$$

where $R_{sc} \approx 1 - 2$ pc. This relation corresponds to a nearly constant surface density of stars $N/R^2 \approx$ *constant*. The solid curve shown in Figure 2.2 uses $R_{sc} = 1.7$ pc; the dashed curves have the same functional dependence but are scaled (up or down) by a factor of $\sqrt{3}$ and quantify the spread in this correlation. For this study we adopt this functional dependence to specify the initial radius of the stellar component and use $R_{sc} = 1.0$ pc. This value is near the lower end of the observed range and thus maximizes the density, which in turn leads to dynamical interactions near the upper end of the range expected in these cluster systems.

Initial stellar profile. Embedded clusters display structure that can be characterized as centrally condensed or hierarchical (Lada & Lada 2003). In a complete treatment, one

should explore both spherical and nonspherical stellar distributions. In this initial study, however, we focus on the spherical case, where stars are randomly placed within a sphere of radius R_c. For the sake of definiteness, the initial density of stars is taken to have the form $\rho_* \sim r^{-1}$ so that the initial stellar mass component is distributed according to $M_*(r) \sim r^2$ (out to the boundary at R_c). This form is consistent with the expected density profiles for gas in cluster-forming cores (see below).

Although there is evidence for a nearly universal initial mass function (IMF) for stars in young clusters, it remains unclear how stellar mass correlates with the initial position within a cluster. Massive stars are preferentially found near the centers of open clusters (e.g., Elmegreen et al. 2000), but the same trend need not be universally true for embedded clusters. Some clusters show evidence for mass segregation (Testi et al. 1998; Hillenbrand & Hartmann 1998; Jiang et al. 2002) and theoretical considerations suggest that mass segregation has a primordial origin in some systems (Bonnell & Davies 1998; Hillenbrand & Hartmann 1998; Carpenter et al. 1997). However, the relative importance of dynamical versus primordial mass segregation in clusters with $100 < N < 1000$ remains uncertain. Given the evidence for some primordial mass segregation, we adopt a simple algorithm consistent with observed groups: for a given system, we sample the stellar masses from a standard IMF and then relocate the most massive member to the cluster center. The remaining stars are then placed randomly so that the initial stellar component has density $\rho_* \sim r^{-1}$ within the radial range $0 \leq r \leq R_c$. This approach thus provides a minimal treatment of primordial mass segregation. A more detailed treatment should be considered in follow-up studies. The issue of mass segregation is important because massive stars can produce powerful winds, outflows, and radiation fields that, if centralized, can more readily disrupt the gaseous component of a cluster (as well as planet-forming disks around other stars).

Initial speeds. As discussed above, stars often appear to be born in young embedded clusters with initial speeds substantially less than the virial values (André 2002; Walsh et al. 2004; Peretto et al. 2006). To set the initial stellar velocities, we sample from an isotropic distribution that is characterized by a given expectation value for the virial ratio $Q \equiv |K/W|$ (Aarseth 2003), i.e., the ratio of kinetic to potential energy, where $Q = 0.5$ for virialized systems. One goal of this study is to explore the effects of subvirial starting conditions. For the sake of definiteness, we adopt a baseline value of $Q_i = 0.04$ for our subvirial simulations (i.e., starting speeds about 30% of the value needed for virial equilibrium). For comparison, we also study the virialized initial condition $Q_i = 0.5$ for (otherwise) the same starting conditions.

Spread in star formation times. A system of stars evolving from such an initially subvirial state would collapse into a dense core within a crossing time if all of the stars formed (and hence began falling toward the center) at exactly the same time. The resulting traffic jam at the cluster center would be unphysical, however, because the stars must have a spread in formation time. In this study, we assume that forming stars are tied to their kernels (the collapsing pockets of gas), which are moving subsonically, until the collapse phase of an individual star formation event is completed. After their collapse phase, newly formed stars are free to fall through the gravitational potential of the group/cluster system. Here we assume that the star formation epoch lasts for a given span of time $\Delta t = 1$ Myr, which is comparable to the crossing time. For comparison, the expected collapse time for an individual protostar is much smaller, only about 0.1 Myr (see Shu 1977; Adams & Fatuzzo 1996; Myers & Fuller 1993).

Initial gas potential. Observations of young embedded clusters indicate that the gas density profiles may have (roughly) the form $\rho \sim r^{-1}$ (Larson 1985; Myers & Fuller 1993; Jijina et al. 1999, see also the discussion of McKee & Tan 2003) on the radial scale of the

cluster ($\sim$ 1 pc). For these simulations we need to include the gravitational potential of the gaseous component and eventually let it disappear with time. In order to smoothly extend the initial gas potential out to large radii, we adopt a Hernquist profile so that the initial gas distribution is characterized by the potential, density, and mass profiles of the forms

$$\Psi = \frac{2\pi G \rho_0 r_s^2}{1+\xi}, \qquad \rho = \frac{\rho_0}{\xi(1+\xi)^3}, \qquad \text{and} \qquad M = \frac{M_\infty \, \xi^2}{(1+\xi)^2}, \tag{2.2}$$

where $\xi \equiv r/r_s$ and r_s is a scale length (Hernquist 1990). Note that $M_\infty = 2\pi r_s^3 \rho_0$. In practice we identify the scale r_s with the cluster size (Figure 2.2), so that $r_s = R_c$. The density profile within the cluster itself thus has the form $\rho \sim r^{-1}$; the steeper density dependence $\rho \sim r^{-4}$ occurs only at large radii (effectively outside the cluster) and allows the potential to smoothly join onto a force-free background. The mass enclosed within $\xi = 1$, denoted here as M_{gas}, is the effective gas mass within the cluster region itself (note that the density and mass profiles extend out to spatial infinity and that the asymptotic mass $M_\infty = 4M_{gas}$). The star formation efficiency (SFE) within the cluster is thus given by $\varepsilon_{SF} = M_{T*}/(M_{T*} + M_{gas})$, where M_{T*} is the total stellar mass in the cluster. Although observational determinations of SFE are subject to both uncertainties and system-to-system variations, typical values for a sample of nearby embedded clusters lie in the range $\varepsilon_{SF} = 0.1 - 0.3$ (Lada & Lada 2003). This study adopts a baseline value $M_{gas} = 2M_{T*}$ (so that $\varepsilon_{SF} = 0.33$). Thus, the mass that will end up in stars over the time interval $\Delta t = 1$ Myr is predetermined. Over the time Δt, the stellar masses become dynamically active and begin to fall through the potential (thus, the total mass of the cluster is kept constant over the time Δt when stars are being formed).

Gas removal history. Stellar aggregates are initially deeply embedded in dense gas, but they quickly disrupt the gaseous component through the action of stellar winds and outflows, radiative processes, and supernovae (e.g., Whitworth 1979; Matzner & McKee

2000; Gutermuth et al. 2004). Although the details of the gas removal processes are not fully understood, observations indicate that clusters older than about 5 Myr are rarely associated with molecular gas, so that gas removal must occur in these systems on a comparable timescale (Lada & Lada 2003). The fraction of stars that remain gravitationally bound after gas removal has been explored both analytically (e.g., Adams 2000; Boily & Kroupa 2003a) and numerically (e.g., Lada et al. 1984; Geyer & Burkert 2001; Boily & Kroupa 2003b). Gas affects the dynamical evolution through its contribution to the gravitational potential. As gas leaves the system, the gravitational well grows less deep and the stellar system adjusts its structure. Stars filling the high-velocity part of the distribution will thus leave the system, but a fraction of stars can remain bound after the gas has been removed. The value of this fraction depends on the SFE, the geometries of the gaseous and stellar components, the gas dispersal history, and the stellar distribution function. This chapter uses a simple model for gas removal: the gas is removed instantaneously at a given time $t = 5$ Myr (e.g., Leisawitz et al. 1989) after the star formation process begins (recall that stars are randomly introduced over a time interval Δt, the beginning of which defines the time $t = 0$). This choice of parameters allows the gas to remain in the system as long as possible (according to the currently available observations; see Lada & Lada 2003). These simulations thus represent an upper limit on the level of interactions expected in astronomical clusters. Note also that the gas potential is considered fixed while gas remains within the cluster. For clusters with subvirial starting conditions, the stars fall toward the cluster center and the gas could become more concentrated as well. This effect is small in the present case because gas dominates the potential, but could be considered in further work.

Binary test. In order to test the validity of our approximation of ignoring binarity, we performed a test simulation using both NBODY6 (which includes binaries; Aarseth

1999) and NBODY2 (where the masses of the two binary companions are combined to make a single star). The comparison runs are made for a cluster with $N = 300$ and radius $R_c = 1$ pc, which defines the center of our parameter space (see above). We also use a subvirial start, an initial $Q_i = 0.04$, because the subvirial runs should have more interactions and hence be more affected by binaries. In the test runs, gas is included as a Plummer sphere (with scale radius $r_s = 1$ pc) since the original N-body codes are written with the Plummer potential. The Plummer potential and density profiles are given by

$$\Phi_P = -\frac{GM}{\sqrt{r^2 + r_s^2}} \qquad \text{and} \qquad \rho_P = \left(\frac{3M}{4\pi r_s^3}\right)\left(1 + \frac{r^2}{r_s^2}\right)^{-5/2}, \tag{2.3}$$

respectively. The gas mass is equal to the total stellar mass. Over a timescale of 10 Myr, we find that the evolution of the fraction f_b of bound stars, the virial parameter Q, and the half-mass radius $R_{1/2}$ are virtually identical for the two cases.

2.2.2 Output Measures

One goal of this work is to provide a statistical description of the systems under study. Two systems with identical sets of cluster parameters (N, R_c, ...) will have stars located at different starting locations and can evolve in different ways (for example, the history of close encounters will change). To provide a more complete description of the evolution of young clusters, we perform an ensemble of "effectively equivalent" simulations through multiple realizations of the system, i.e., we use the same set of cluster parameters but different choices for the random variables. In this manner, we can build up full distributions for the output measures of the systems (see also Goodman et al. 1993; Giersz & Heggie 1994; Baumgardt et al. 2002, and references therein).

2.2.2.1 Time Evolution

To characterize the time evolution, a variety of output measures are computed for each simulation, including the cluster's bound fraction, virial ratio, half-mass radius, and

velocity isotropy parameter. These measures are calculated every 0.25 Myr throughout each 10 Myr simulation. For each system studied, the output measures of all the realizations (effectively equivalent simulations) are combined and averaged. We can then investigate the temporal evolution of each measure as well as use the measures to compare the different systems studied.

One important quantity is the fraction f_b of stars that remain gravitationally bound as a function of time. For example, we would like to know how $f_b(t)$ depends on the cluster size N and the starting conditions (virial vs. subvirial). The bound fraction f_b of the cluster is defined by $f_b \equiv N_{bound}/N$, where N is the initial number of stars in the cluster and N_{bound} is the number of stars that have negative total energy at a given time. The bound fraction functions $f_b(t)$ are shown in Figure 2.3 for the six types of clusters considered here. Gas is removed at time $t = 5$ Myr, so the fraction of bound stars decreases after that epoch. Figure 2.3 shows that the subvirial clusters retain more of their stars for longer times.

In addition to f_b, we track the evolution of three other cluster diagnostics. The half-mass radius $R_{1/2}$ is defined to be the radius that encloses half of the stellar mass that is still gravitationally bound to the system. Over the long term, the half-mass radius $R_{1/2}$ is an increasing function of time, although it can decrease during the initial evolution of subvirial clusters. Within groups/clusters, young stars are often born with speeds much smaller than that required for virial equilibrium, but attain larger (virial) speeds as the system evolves. We can monitor this approach to equilibrium by tracking the evolution of the virial ratio Q (the ratio of kinetic to potential energy for the stellar population). We also track the evolution of the isotropy parameter $\beta \equiv 1 - v_\theta^2/v_r^2$, where v_θ and v_r are the (averaged) $\hat{\theta}$ and $\hat{r}$ components of the velocity. The isotropy parameter provides a measure of the degree to which the cluster members have radial orbits. An isotropy parameter of $\beta = 0$ corresponds to an isotropic velocity distribution, whereas $\beta = 1$ corresponds to a

cluster where the members are moving primarily in the radial direction.

The time evolution of the aforementioned cluster diagnostics are shown in Figure 2.3 for cluster sizes $N = 100, 300$, and 1000, and for both subvirial and virial starting conditions. As shown, the bound fraction is a slowly decreasing function of time, with a substantial (unphysical looking) jump at $t = 5$ Myr when the gas is removed. The half-mass radius $R_{1/2}$ remains nearly constant until gas removal at $t = 5$ Myr, when it becomes an increasing function of time. The isotropy parameter β is substantially radial ($0 < \beta < 1$) over the entire evolution time for clusters with subvirial starting conditions but shows a slight downward tendency at late times, indicating some evolution toward isotropy. For virial clusters, the parameter β is close to zero (isotropic) for the first 5 Myr of evolution but develops a definite radial characteristic ($\beta \sim 0.5$) for the second half of the time interval after the gas is removed. These same general trends are evident in the ensemble of results summarized in Table 2.1. For each cluster size ($N = 100, 300$, and 1000) and each starting condition (virial or subvirial) we have found the average values of the fraction f_b of stars that remain bound after 10 Myr. Similarly, we have found averages of the viral parameter Q, the half-mass radius $R_{1/2}$, and the isotropy parameter β for the first 5 Myr (while the clusters retain gas) and the second 5 Myr of evolution (when the clusters are gas-free). The final line of the table gives the output parameters for our simulations of NGC 1333 (see Section 2.5).

2.2.2.2 Radial Distributions

As a group/cluster system evolves, interactions between members result in a distribution of stellar positions and velocities. As the gas is removed from the system, high-velocity stars are more likely to become gravitationally unbound and leave the system, whereas low-velocity stars tend to condense into a central bound core. Complicating this process, dynamical mass segregation also takes place, albeit on somewhat longer timescales. As one

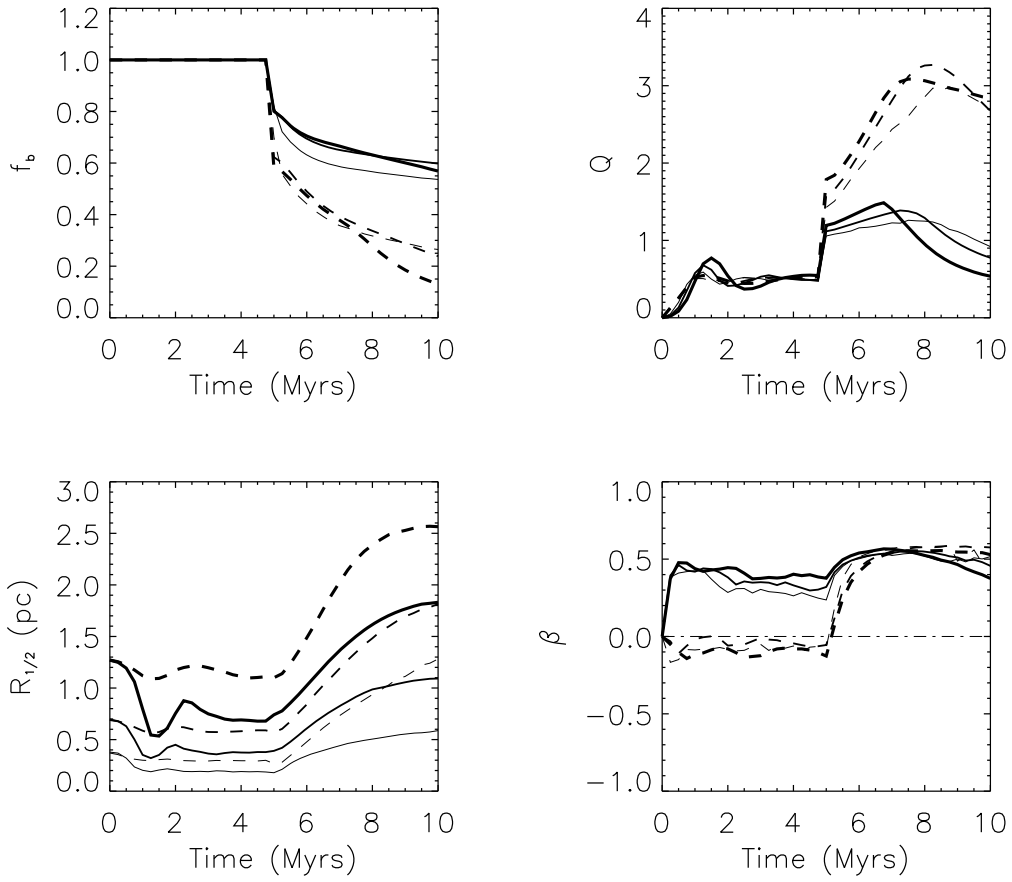

Figure 2.3: Time evolution for output measures f_b, Q, $R_{1/2}$, and β for cluster simulations with $N = 100, 300$, and 1000. In each panel, the solid curves show the time evolution functions for subvirial initial conditions and the dashed curves show the time evolution for virial starting conditions. The boldness of the curves denotes the cluster size, with the darkest curves for $N = 1000$ and the lightest curves for $N = 100$. The top left panel shows the fraction of stars that are bound as a function of time f_b, the top right panel shows the time evolution of the virial parameter Q, the bottom left panel shows the time evolution of the half-mass radius $R_{1/2}$, and the bottom right panel shows the velocity isotropy parameter β. In all of these simulations, the gas is removed at time $t = 5$ Myr, which leads to structure in all of the time evolution functions as shown here.

Table 2.1: Cluster Evolution Parameters

Cluster Type	f_b 10 Myr	Q 0-5 Myr	Q 5-10 Myr	$R_{1/2}$ [pc] 0-5 Myr	$R_{1/2}$ [pc] 5-10 Myr	β 0-5 Myr	β 5-10 Myr
100 Subvirial	0.536	0.489	1.15	0.211	0.457	0.320	0.502
100 Virial	0.265	0.511	2.48	0.301	0.832	-0.0849	0.515
300 Subvirial	0.598	0.491	1.15	0.413	0.861	0.368	0.511
300 Virial	0.239	0.517	2.72	0.596	1.31	-0.0404	0.513
1000 Subvirial	0.569	0.497	1.04	0.780	1.44	0.410	0.500
1000 Virial	0.130	0.527	2.74	1.15	2.09	-0.0993	0.485
NGC 1333	0.689	0.525	0.690	0.117	0.238	0.230	0.339

way to characterize the evolution of these systems, we produce mass profiles $M(r)$ averaged over the 10 Myr time interval of interest. Specifically, the radial position of every star is recorded at intervals of 0.25 Myr throughout each simulation. The resulting data set is used to create a mass profile $M(r)/M_{T*}$ at each time, where M_{T*} is the total mass in stars that remain bound. The profiles are then averaged over all time steps and averaged over the 100 equivalent realizations of the system to produce the average radial mass profile associated with each type of group/cluster. The integrated mass distribution $M(r)$ can be fit with a simple function of the form

$$\frac{M(\xi)}{M_{T*}} = \left(\frac{\xi^a}{1+\xi^a} \right)^p , \tag{2.4}$$

where $\xi = r/r_0$, and the scale length r_0 and the index p are free parameters that are fit to the output of the simulations. The index a can also be varied: we find that the subvirial clusters can be fit with $a = 2$, whereas the virial clusters require $a = 3$. The best-fit parameters for the various simulations are given in Table 2.2. The table also shows the fitting parameters for the mass profiles averaged over the first 5 Myr (before gas removal) and over the second 5 Myr (after gas has left the system). The final line of the table gives the fitting parameters for the simulations of NGC 1333 (see Section 2.5). Figure 2.4 shows the radial mass profiles from both the simulations and the fitting functions. The simulation profiles are time-averaged over the first 10 Myr of evolution (and over 100 realizations of each starting condition).

We can also find profiles $N(r)$ for the number of stars enclosed within the radius r. These profiles are essentially the probability distributions for the radial positions of the stellar members. These profiles $N(\xi)/N$ can be fit with the same form as equation [2.4]. Although not shown here, the fitting parameters are nearly the same as those of the mass profiles and are used (in Section 2.3) when we need to calculate the probability of finding a star at radius r. The similarity between the integrated mass distributions $M(r)/M_{T*}$ and

Table 2.2: Output Parameters for Mass Distributions

	$0-10$ Myr		$0-5$ Myr		$5-10$ Myr		
Cluster Type	p	r_0 [pc]	p	r_0 [pc]	p	r_0 (pc)	a
100 Subvirial	0.686	0.394	0.680	0.264	1.02	0.453	2
100 Virial	0.436	0.698	0.406	0.486	0.776	0.793	3
300 Subvirial	0.785	0.635	0.747	0.484	1.01	0.781	2
300 Virial	0.493	1.19	0.489	0.846	0.605	1.56	3
1000 Subvirial	0.820	1.11	0.769	0.899	0.970	1.34	2
1000 Virial	0.586	1.96	0.590	1.53	0.689	2.45	3
NGC 1333	0.552	0.300	0.436	0.241	0.924	0.299	2

the cumulative radial probability distributions $N(r)/N$ further suggests that dynamical mass segregation is not occurring in the clusters on this short (10 Myr) of a timescale.

One goal of this study is to characterize this class of groups and clusters. Toward this end, recent observational studies have determined the central densities for clusters (e.g., Gutermuth et al. 2005). However, the mass profiles found here imply that the central density of these clusters suffers from an ambiguity: if a mass profile has the form given by equation [2.4], the density profile takes the form $\rho \propto ap\xi^{ap-3}(1+\xi^a)^{-(p+1)}$, which diverges in the limit $\xi \rightarrow 0$. As a result, the central density for these mass profiles – and this class of systems – is not well defined. In contrast, the total depth of the gravitational potential is well-defined and can be written in the form

$$\Psi_* = \frac{GM_{T*}}{r_0}\psi_0, \qquad \text{where} \qquad \psi_0 \equiv \int_0^\infty \Big(\frac{1}{1+u^a}\Big)^p du, \tag{2.5}$$

where we assume that the mass profile has the form of equation [2.4], which defines the indices a and p, as well as the scale length r_0. The total mass of stars in the cluster is M_{T*}, so that Ψ_* represents the total depth of the stellar contribution to the potential. For embedded clusters, the gas contribution to the potential (equation [2.2]) should be added to obtain the total potential. Note that in the limit $ap \rightarrow 1$, the integral in the definition of ψ_0 diverges and the central potential is no longer defined. However, all of the clusters considered here display well-defined central potentials. For the indices listed in Table 2.2,

the value of the dimensionless potential ψ_0 lies in the range $\psi_0 = 1.5 - 5.4$. The resulting stellar potential can be written in terms of a velocity scale $\sqrt{\Psi_*}$, which falls in the range $\sqrt{\Psi_*} = 0.64 - 2.4$ km s^{-1} for the clusters considered here.

2.2.2.3 Distribution of Closest Approaches

The cluster environment facilitates close stellar encounters that can disrupt solar systems. Within the ensemble of N-body simulations described above, we can find the distributions of close encounters. These distributions, in conjunction with the cross sections for disruptions of planetary systems (see Section 2.4; Adams & Laughlin 2001), binary-disk systems (Ostriker 1994; Heller 1993; 1995; Kobayashi & Ida 2001), and binary-star interactions (Heggie et al. 1996; McMillan & Hut 1996; Rasio et al. 1995), can then be used to estimate the probability of physically important interactions as a function of system size N (and other initial conditions).

Specifically, the close encounters for each star are tracked throughout each cluster simulation; the resulting data are labeled with both stellar mass and cluster age. The total distribution of closest approaches for each simulation is calculated, and these distributions are then averaged over the 100 equivalent realizations of the system. The result is an integrated distribution of closest approaches for each type of cluster. The results are presented in terms of an interaction rate, i.e., the number of close encounters with $r \leq b$ that the *typical star* experiences per million years (1 Myr is a convenient unit of time and is approximately the cluster crossing time). This interaction rate is a function of closest approach distance b and can be fit with an expression of the form

$$\Gamma = \Gamma_0 \left(\frac{b}{1000 \text{ AU}} \right)^{\gamma} . \tag{2.6}$$

The rate Γ is thus the number of close encounters with $r \leq b$ per star per million years. For each type of group/cluster, the parameters Γ_0 and γ were varied to find the best fits using the Levenberg-Marquardt procedure. The resulting parameter values are given in Table

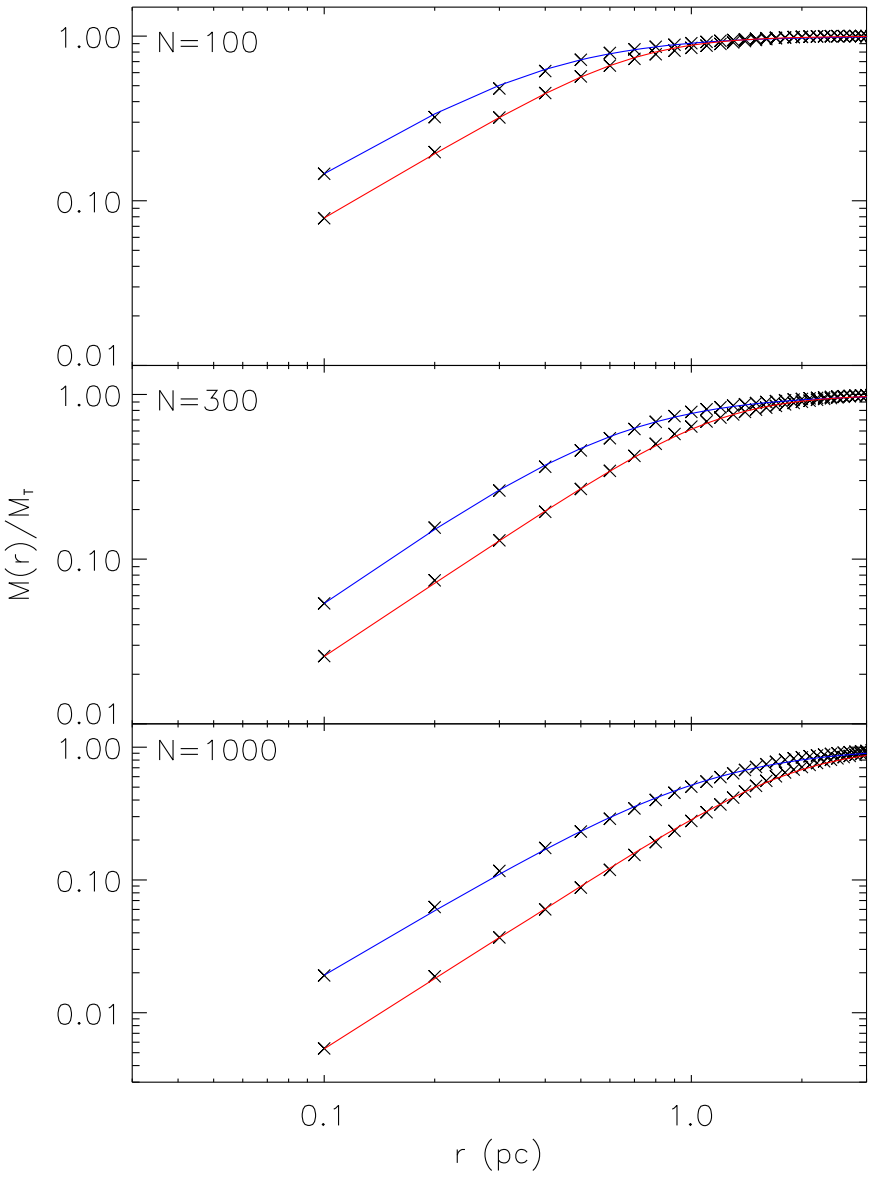

Figure 2.4: Time-averaged mass profiles $M(r)/M_{T*}$ for the six classes of starting conditions. The averages are taken over the first 10 Myr and include only the stars that remain bound to the cluster (at each time). The top panel shows the stellar mass distribution $M(r)$ as a function of radius r for clusters with $N = 100$ and both virial (*bottom curve*) and subvirial (*top curve*) starting conditions. Each mass profile is compiled from the results of 100 simulations with different realizations of the same starting conditions. Similarly, the middle panel shows the mass distributions for clusters with $N = 300$ and the bottom panel shows the distributions for $N = 1000$.

2.3 for the six classes of systems studied here (and best fit lines are indicated in Figure 2.5). The table also lists the fitting parameters for the closest approach distributions taken over the first 5 Myr of the simulations (when gas is still present) and the second 5 Myr time interval (after gas removal). These results are consistent with those obtained previously (e.g., Scally & Clarke 2001 found similar interaction rates for the Orion Nebula Cluster, which is somewhat larger with $N = 4000$ stars). Note that the interaction rates are higher for the first 5 Myr interval than the second 5 Myr, by a factor of ~ 5, consistent with the spreading out of the cluster with time, especially after gas is removed at the 5 Myr mark. Note also that the total interaction rate over 10 Myr is the average of the values over the two separate time intervals. The interaction rates are higher for the clusters with subvirial starting conditions. In these systems, the orbits are more radial than in the case of virial initial conditions (where the velocity distributions are more isotropic; see Table 2.1), and more of the stars pass near the cluster center where the density is higher.

The fitting functions (given by equation [2.6] and Table 2.3) provide a good working description of the distribution of closest approaches for each ensemble of simulations with given starting conditions. In order to interpret the meaning of these results, it is useful to compare with analytic estimates (Binney & Tremaine 1987, hereafter BT87). For a cluster of size N and radius R_c, the surface density of stars is roughly $N/(\pi {R_c}^2)$. For each crossing time τ_c of the cluster, a given star will thus experience close encounters at the rate

$$\delta\Gamma \approx \frac{N}{\pi {R_c}^2} 2\pi b \delta b \tau_c^{-1}, \tag{2.7}$$

with impact parameter (the closest approach distance in this approximation) between b and $b + \delta b$ (BT87), where the time unit is the crossing time. The total rate Γ_b of close approaches (at distance $\leq b$) per crossing time is thus approximately given by

$$\Gamma_b \approx \frac{N b^2}{{R_c}^2} \tau_c^{-1} \approx 0.007 \left(\frac{b}{1000 \text{ AU}} \right)^2 \tau_c^{-1}, \tag{2.8}$$

where we have used the observed scaling of cluster radius with N (Figure 2.2 and equation [2.1]) to obtain the second approximate equality. Since the cluster crossing times τ_c are of order 1 Myr, this calculation produces an interaction rate with the same form as the fitting formula with $\Gamma_0 \approx 0.007$ and $\gamma = 2$. As shown in Table 2.3, the fitting parameters for close approaches are in rough agreement with these estimated values, at the crudest level of comparison. The detailed forms are somewhat different – the numerically determined interaction rates are less steep (as a function of b) and somewhat larger than the analytic estimate.

The differences between the numerical interaction rates and the analytic estimate arise for several reasons. The crossing time is somewhat shorter than 1 Myr, so the rate increases accordingly. In addition, clusters have enhanced density in their centers and support more interactions there. Suppose that a cluster has a core, a long-lived central region of enhanced stellar density. If the core contains $N/10$ stars at a given time and has radius $R_c/10$, the effective surface density, and hence the interaction rate per crossing time, would be 10 times higher than the estimate given above. Note that the local crossing time would be smaller by a factor of ~ 10, but that stars would (on average) spend only 10% of their time in the core, so these latter two effects tend to cancel. The shallower slope of the distribution ($\gamma < 2$) is expected for sufficiently close encounters where the interaction energy $2Gm/b$ is comparable to the typical velocity $\langle v \rangle$ of a cluster star. In this case, the stars no longer travel on straight-line trajectories during the encounter (as implicitly assumed above) so that the impact parameter is larger than the distance of closest approach (BT87). Since $\langle v \rangle \sim 1$ km s^{-1}, this effect comes into play when $b \sim 2Gm/\langle v \rangle^2 \sim 900$ AU, i.e., just inside the regime of interest. In the extreme limit of small b, the interaction rate becomes linear $\Gamma_b \propto b(2Gm/\langle v \rangle^2)$ so that $\gamma \rightarrow 1$. Note that the slopes found from the numerical simulations lie in the range $1 \leq \gamma \leq 2$.

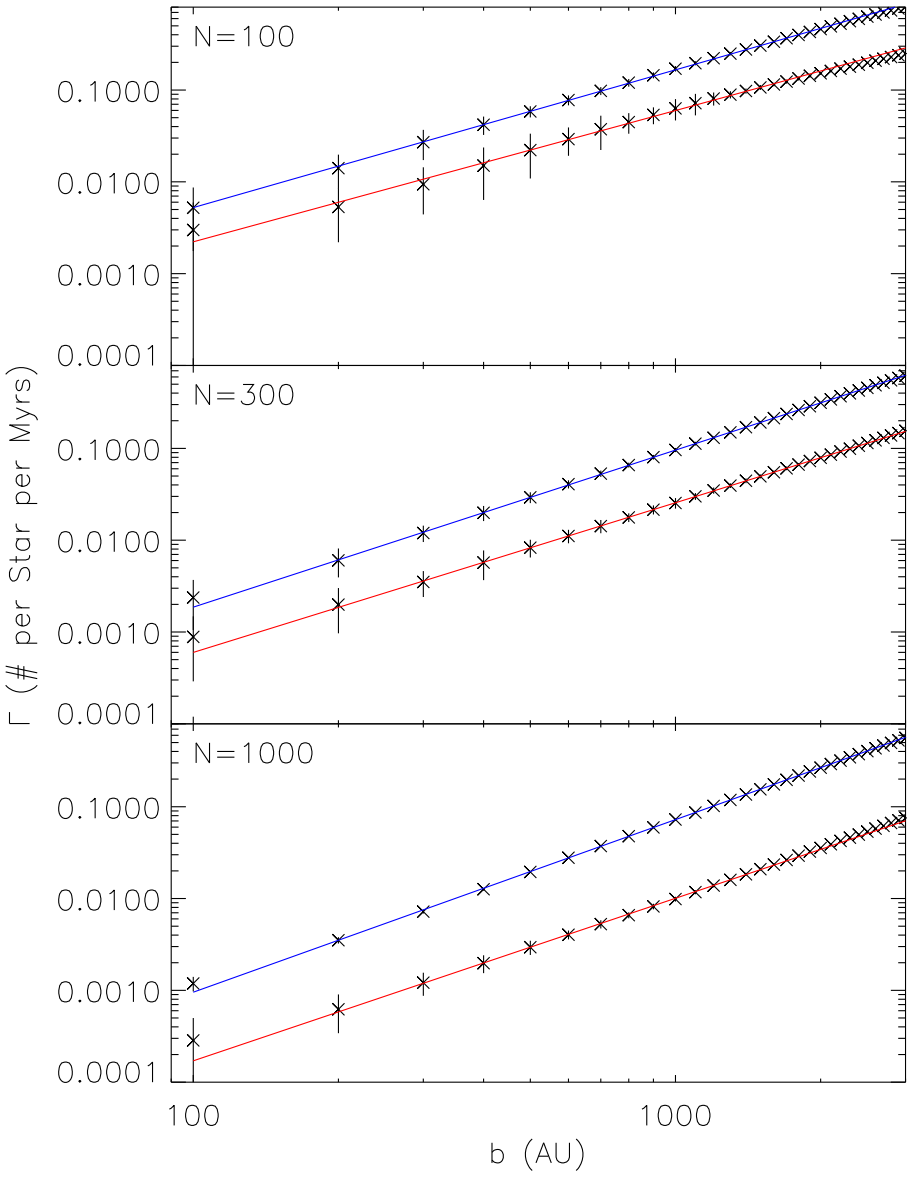

Figure 2.5: Distribution of closest approaches for the six classes of starting conditions. The top panel shows the distributions of closest approaches, plotted as a function of impact parameter, for clusters with $N = 100$ and both virial (*bottom curve*) and subvirial (*top curve*) starting conditions. Each distribution is compiled from the results of 100 simulations, i.e., 100 realizations of the same starting conditions. Similarly, the middle panel shows the distributions of closest approaches for clusters with $N = 300$ and the bottom panel shows the distributions for $N = 1000$. The error bars shown represent the standard deviation over the compilations.

Table 2.3: Output Parameters for Distributions of Closest Approach

	$0-10$ Myr		$0-5$ Myr		$5-10$ Myr		
Cluster Type	Γ_0	γ	Γ_0	γ	Γ_0	γ	b_C [AU]
100 Subvirial	0.166	1.50	0.266	1.54	0.0672	1.42	713
100 Virial	0.0598	1.43	0.0870	1.46	0.0333	1.37	1430
300 Subvirial	0.0957	1.71	0.168	1.73	0.0240	1.59	1030
300 Virial	0.0256	1.63	0.0440	1.64	0.00700	1.53	2310
1000 Subvirial	0.0724	1.88	0.133	1.89	0.0112	1.83	1190
1000 Virial	0.0101	1.77	0.0181	1.79	0.00210	1.74	3650
NGC 1333	0.941	1.56	1.39	1.62	0.490	1.42	238

These simulations were performed using an N-body code that does not consider the binarity of the interacting units (NBODY2; Aarseth 1999). Given the distribution of closest approaches calculated here, we can check this approximation for self-consistency. For an interaction rate of the form of equation [2.6], and for a 10 Myr time span, the typical star will experience (on average) one encounter with the characteristic impact parameter b_C given by

$$b_C \equiv 1000 \text{ AU} \Big(10 \Gamma_0 \Big)^{-1/\gamma}. \tag{2.9}$$

For the six classes of clusters considered here, the characteristic impact parameter lies in the range $b_C = 700 - 4000$ AU (as listed in Table 2.3). For comparison, the peak of the binary period distribution is at $P \approx 10^5$ days (Duquennoy & Mayor 1991), which corresponds to a separation of ~ 42 AU $\ll b_C$. These results indicate that for the majority of binary systems, the separation is much less than the typically expected close approach b_C (over the 10 Myr time span considered here). Furthermore, the orbital energy at the typical flyby radius of a couple thousand astronomical units corresponds to a velocity scale of ~ 0.5 km s^{-1}, i.e., a typical star is expected to receive only a single velocity perturbation of this magnitude. Although this velocity kick is comparable to the mean velocity scale of the cluster given by $v_m \sim \sqrt{GN\langle m \rangle / R}$, most of the interactions take place near the center of the cluster potential where $v \sim \sqrt{\Psi_0} \sim 3.5 v_m$, so the expected velocity perturbations are

not devastating (one $\sim 15\%$ kick in velocity, a $\sim 2\%$ kick in energy) . These results, taken together, imply that our approximation of ignoring binarity is justified. For completeness we note that some binary systems can be produced via three-body interactions during the evolution of a cluster. Care must be taken to identify these systems once formed, and to exclude the binary orbits from the determination of the closest approach distribution.

2.2.2.4 Comparison of Virial and Subvirial Initial Conditions

One issue of interest is the differences between the clusters with initial conditions where members are in virial equilibrium, $Q_i = 0.5$ (virial clusters), and those where the members are started with subvirial velocities, $Q_i = 0.04$ (subvirial clusters). The initial conditions lead to some important differences, as illustrated in Table 2.4, which lists the ratios of the parameters for the subvirial simulations to those from the virial simulations. The subvirial clusters have higher bound fractions, with $50\% - 60\%$ of their members remaining bound at $t = 10$ Myr. For comparison, the virial clusters have only $13\% - 27\%$ of the initial cluster membership bound at $t = 10$ Myr. In the subvirial clusters, stars fall toward the center after they form and thus spend more of their time inside the cluster gas (which is assumed to be static, i.e., not in a state of collapse). The removal of gas thus has less effect on the subvirial clusters, and more stars remain bound. For both virial and subvirial clusters, the initial velocity distribution of the cluster members is isotropic. Since stars in the subvirial clusters are started with small velocities, however, they tend to fall toward the cluster center and rapidly develop relatively larger radial velocities. As a result, the isotropy parameter β for subvirial clusters is larger (more radial with $\beta \approx 0.3 - 0.4$) than that of the virial clusters, which have $\beta \approx 0$ (and slightly negative) for the first 5 Myr of evolution. After the gas is removed, both the virial and subvirial clusters have larger isotropy parameters, indicating increased radial motion as the cluster expands in the absence of the gas potential.

Table 2.4: Ratio of Parameters for Subvirial and Virial Initial Conditions

N ($t = 0$)	f_b $0 - 10$ Myr	Q $5 - 10$ Myr	$R_{1/2}$ $0 - 5$ Myr	$R_{1/2}$ $5 - 10$ Myr	Γ_0 $0 - 10$ Myr
100 Stars	2.02	0.464	0.701	0.549	2.78
300 Stars	2.50	0.423	0.693	0.657	3.74
1000 Stars	4.38	0.380	0.678	0.689	7.17

The mass distributions (Figure 2.4) and distributions of closest approaches (Figure 2.5) also depend on the starting conditions. The subvirial clusters have more centrally condensed radial profiles throughout the 10 Myr evolution time. Before gas expulsion, the half-mass radii for the subvirial clusters are about 70% of the half-mass radii of the virial clusters. This result can be understood if the subvirial clusters act as if they have zero temperature starting states, so they collapse to a radial scale roughly $\sqrt{2}$ times smaller than their initial size. In comparison, virial clusters tend to retain their starting radial size (before gas removal). After gas expulsion, the subvirial clusters continue to have half-mass radii about 70% of those of the virial clusters, although the subvirial clusters with $N = 100$ are somewhat more concentrated. The mass distributions show that the scale radii of the subvirial clusters are $55\% - 65\%$ of those of the virial clusters, and the central potentials are deeper by a factor of $1.2 - 2$. The distributions of closest approach for clusters with virial and subvirial starting conditions are similar and can be fit with a single power-law form over the radial range of interest ($100 - 1000$ AU). The power-law indices are roughly the same, but the subvirial clusters show a higher interaction rate by a factor of $3 - 7$.

2.3 Effects of Cluster Radiation on Forming Solar Systems

Given the characterization of cluster dynamics found in the previous section, we now estimate the effects of ultraviolet radiation from the background cluster on nascent solar systems. The radiation from the parent star can drive mass loss from its planet-forming disk and thereby affect planet formation (Shu et al. 1993), but this effect is often dominated

by radiation from the background star cluster (Johnstone et al. 1998; Adams & Myers 2001). In this chapter we focus on the effects of FUV radiation (Adams et al. 2004), which tends to dominate the effects of EUV radiation (Armitage 2000). We first calculate the distributions of FUV luminosity (Section 2.3.1) and then determine the extent to which the radiation compromises planet formation (Section 2.3.2). Throughout this section, we present results as a function of cluster size N. In this context, we consider the cluster to have a stellar membership of N primaries, and we ignore binarity. Although some fraction of the cluster members will have binary companions, the vast majority of the companions will have low mass and will not contribute appreciably to the FUV luminosity. Note that in the early stages of cluster evolution, the system will contain a substantial amount of gas and dust, and this dust can attenuate the FUV radiation. The gas (and dust) is removed from the cluster relatively early so that the FUV radiation eventually has a clear line-of-sight to affect forming planetary systems. Nonetheless, since we do not model the dust attenuation, the results of this section represent an upper limit to the effects of radiation.

2.3.1 Probability Distributions for FUV Luminosity

In this subsection, we calculate probability distributions for the FUV radiation emitted by stellar aggregates with varying size N (the number of cluster members). The total FUV luminosity from a cluster or group of stars is given by the sum

$$L_{FUV}(N) = \sum_{j=1}^{N} L_{FUVj}, \tag{2.10}$$

where L_{FUVj} is the FUV luminosity from the jth member. In this approximation, we assume that the FUV luminosity for a given star is determined solely by the stellar mass. We further assume that the stellar mass is drawn from a known probability distribution, i.e., a known stellar IMF.

In this problem, low-mass stars have a negligible contribution to the total UV flux. To a good approximation, we can ignore the contribution of all stars smaller than 1 $M_{\odot}$. To

specify the IMF, we are thus not concerned with the detailed shape at low stellar masses; we only need to correctly account for the fraction of stars with $M_* > 1$ $M_\odot$ and the slope at high stellar masses. For the sake of definiteness, we assume that the stellar IMF has a power-law form for mass $M_* > 1$ $M_\odot$ with index Γ, i.e.,

$$\frac{dN}{dm} = Am^{-\Gamma} = \mathcal{F}_1(\Gamma - 1)m^{-\Gamma}, \tag{2.11}$$

where m is the mass in units of solar masses and the slope $\Gamma = 2.35$ for the classic form first suggested by Salpeter (1955); this slope remains valid today for a wide variety of regions (Massey 2003, and references therein). In the second equality, we have normalized the distribution according to the convention

$$\int_1^\infty \frac{dN}{dm} dm = \mathcal{F}_1, \tag{2.12}$$

where $\mathcal{F}_1$ is the fraction of the stellar population with mass larger than 1 $M_\odot$. For a typical stellar mass function (such as that advocated by Adams & Fatuzzo 1996), the fraction $\mathcal{F}_1 \approx 0.12$. For completeness, note that in practice we cut off the IMF at $m = 100$ (see below); taking the integral out to ∞ here results in an inaccuracy of $\sim 0.2\%$ (which is much smaller than the accuracy to which we know $\mathcal{F}_1$).

To specify the FUV luminosity as a function of stellar mass, $L_{FUV}(m)$, we use the models of Maeder and collaborators (Maeder & Meynet 1987; Schaller et al. 1992). Specifically, these papers provide a grid of stellar models as a function of both mass and age. We use the zero-age models to specify the stellar luminosity and effective temperature. The FUV radiation is dominated by the largest stars, which reach the main sequence rapidly. Since the model grids do not extend to arbitrarily high masses, we enforce a cutoff of 100 $M_\odot$. Using a blackbody form for the atmosphere, we then calculate the fraction of the luminosity that is emitted in the FUV regime (6 eV $< h\nu <$ 13.6 eV). The result is shown in Figure 2.6.

The expectation value $\langle L_{FUV} \rangle_*$ of the FUV luminosity is thus given by the integral

$$\langle L_{FUV} \rangle_* = \int_1^\infty L_{FUV}(m) \frac{dN}{dm} dm \approx 8.20 \times 10^{35} \, \mathrm{erg/s} \, . \tag{2.13}$$

This expectation value is normalized so that it is the expected FUV luminosity *per star*. Due to the wide range of possible stellar masses and the sensitive dependence of FUV emission on stellar mass, this expectation value is much larger than the FUV radiation emitted by the majority of stars. We thus only expect the FUV radiation from a given cluster to converge to that implied by the expectation value in the limit of larger numbers N of stellar members, where large N is determined below. Small clusters will often experience large departures from the expectation value.

We want to calculate both the expectation value and its variance for the FUV luminosities of the entire cluster. The sum given by equation [2.10] is thus the sum of random variables, where the variables (individual contributions to the FUV power) are drawn from a known distribution (determined by the stellar IMF and the luminosity-mass relation). In the limit of large N, the expectation value of the FUV power is thus given by

$$L_{FUV}(N) = N \langle L_{FUV} \rangle_* \, . \tag{2.14}$$

Furthermore, the distribution of possible values for $L_{FUV}(N)$ must approach a Gaussian form as $N \to \infty$ because of the central limit theorem (e.g., Richtmyer 1978), although convergence is slow. This Gaussian form is (as usual) independent of the form of the initial distributions, i.e., it is independent of the stellar IMF and the mass-luminosity relation. The width of the distribution also converges to a known value and is given by

$$\langle \sigma \rangle_{\mathrm{FUV}}^2 = \frac{1}{N} \sum_{j=1}^{N} \sigma_j^2 \quad \Rightarrow \quad \langle \sigma \rangle_{\mathrm{FUV}} = \sqrt{N} \sigma_0 \, , \tag{2.15}$$

where σ_0 is the width of the individual distribution, i.e.,

$$\sigma_0^2 \equiv \langle L_{FUV}^2 \rangle - \langle L_{FUV} \rangle_*^2 \, . \tag{2.16}$$

For our usual choice of stellar properties, the dimensionless width $\widetilde{\sigma}_0 = \sigma_0/\langle L_{FUV}\rangle_* \approx 26.4$, i.e., the variation in the possible values for the FUV luminosity is much greater than the expectation value. The effective signal-to-noise ratio (S/N) for variations in FUV luminosity is thus given by

$$S/N \equiv \frac{\langle\sigma\rangle_{\rm FUV}}{L_{FUV}(N)} = \frac{\sigma_0}{\sqrt{N}\langle L_{FUV}\rangle_*} \approx \frac{26.4}{\sqrt{N}}\,. \tag{2.17}$$

This definition thus defines a critical value of cluster members N_C, i.e., the number required for the variations in FUV luminosity to become sufficiently well defined so that the variations are smaller than the expectation value. This critical value of $N_C \equiv \widetilde{\sigma}^2 \sim 700$. For $N < N_C$, the FUV radiation experienced by a solar system living in the cluster is essentially determined by the largest star in the aggregate; this largest member is, in turn, drawn from the probability distribution implied by the stellar IMF. For clusters with $N > N_C$, it makes sense to consider expectation values for the FUV radiation provided by the aggregate. However, the boundary is not sharp. Even for $N > N_C$, the total FUV luminosity $L_{FUV}(N)$ will be subject to substantial fluctuations from system to system.

We have performed a set of numerical sampling experiments to show that the mean and variance of the distribution agree with the analytic predictions derived above. The results are in good agreement. The mean and variance are shown as a function of cluster size N in Figure 2.6. These numerical experiments show that the convergence to a purely Gaussian distribution is rather slow. The central value and variance of the actual distribution approach the values predicted by the central limit theorem much faster than the distribution itself approaches a normal form. As a result, the median of the distribution can be significantly different from the mean or expectation value, especially for cluster with small stellar membership N. Figure 2.6 also shows the median expected FUV flux as a function of cluster size N. The median is only about 8% of the mean for small clusters with $N \approx 100$ and approaches 80% of the mean for larger systems ($N = 1000 - 2000$). We

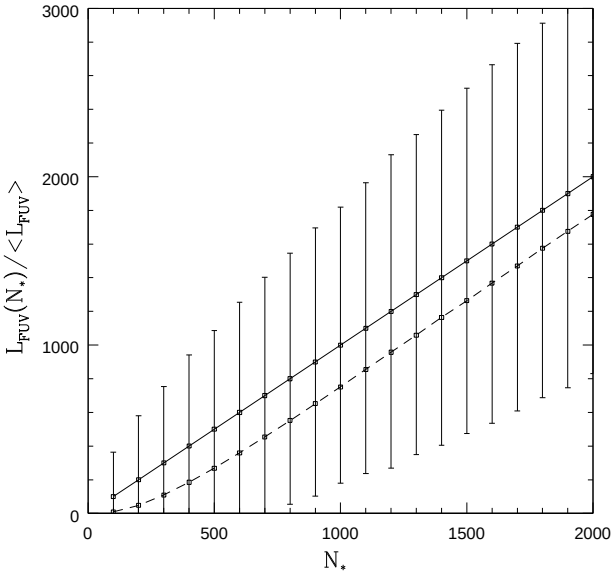

Figure 2.6: Mean, variance, and median of the distribution of total FUV luminosity for clusters of size N as a function of N. The squares connected by the solid line depict the mean FUV luminosity averaged over many realizations of a cluster of size N. The error bars represent the variance about the mean. As shown in the text, the mean $\langle L_{FUV} \rangle \propto N$ and the variance $\sigma \propto N^{1/2}$. The median is shown by the dashed curve and is much smaller than the mean for small clusters and slowly converges to the mean as $N \to \infty$.

note that the median value provides a better description of the *typical* FUV luminosity produced by a cluster of size N. However, the distribution of possibilities is wide, and caution must be taken in characterizing the probability distribution by only one number.

Figure 2.7 shows the probability distributions for FUV luminosity for three choices of stellar size, namely, $N = 100, 300$, and 1000. The plot shows the cumulative probability distributions for the normalized FUV luminosity of the clusters, i.e., the total FUV luminosity divided by the number of cluster members N. In this representation, the distribution with $N = 100$ (*dashed curve*) is the widest, and the distributions grow narrower with increasing N. In the limiting case $N \to \infty$, the distribution becomes a step function at the mean value $\langle L_{FUV} \rangle_*$ (where $\log_{10} \langle L_{FUV} \rangle_* \approx 35.9$). For the three cluster sizes shown here, the normalized probability distributions converge near $P \approx 0.85$ and

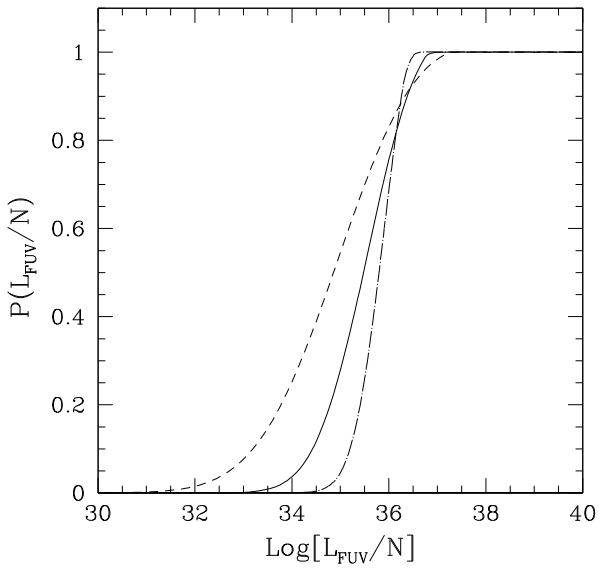

Figure 2.7: Cumulative probability distribution for the number of clusters that produce a given normalized FUV luminosity, where the normalized FUV luminosity is the total FUV luminosity of the cluster divided by the number N of cluster members. The three curves shown correspond to clusters of size $N = 100$ (*dashed curve*), $N = 300$ (*solid curve*), and $N = 1000$ (*dot-dashed curve*).

$\log[L_{FUV}/N] \approx 36.2$. This convergence defines a benchmark for the high end of the distribution; namely, 15% of the clusters are expected to have FUV luminosity greater than the limit $L_{FUV} \geq N(1.6 \times 10^{36})$ erg s^{-1} $\approx 2N\langle L_{FUV}\rangle_*$.

The distributions described above apply to clusters of a given size N and show how the results depend on N. However, since stars are born in groups/clusters with a distribution of sizes N (Figure 2.1; Lada & Lada 2003; Porras et al. 2003), we also need to determine the overall distribution of FUV luminosities that affects the entire ensemble of forming solar systems. Toward that end, we assume that the distribution of stellar groups/clusters is the same as that of the Lada & Lada (2003) sample (which is equivalent to that of Porras et al. 2003). We then sample the distribution of cluster systems to find a system size N, and for each such system we sample the IMF N times to find the FUV luminosity. Using $10,000$ realizations of the cluster sample (corresponding to a total of 127 million

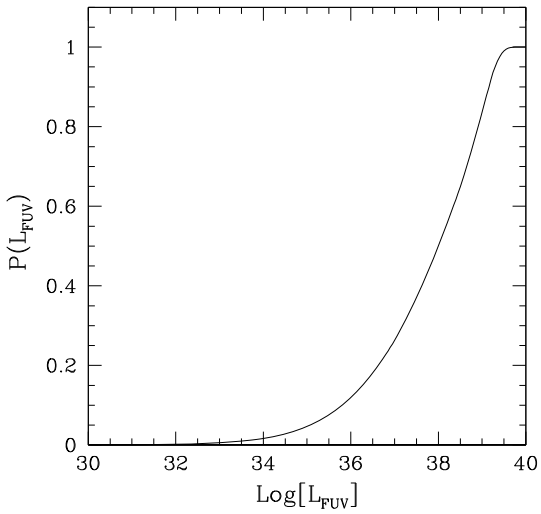

Figure 2.8: Cumulative probability distribution for the number of stars that live in a cluster with total FUV luminosity L_{FUV} as a function of L_{FUV}. This distribution is calculated under the assumption that the cluster size distribution (the number of stars N) follows the data set of Lada & Lada (2003). The size distribution of the data set is sampled 10,000 times to produce the probability distribution shown here. The median FUV luminosity occurs at $L_{FUV} = 10^{38}$ erg s^{-1}. Note that the distribution has a long tail at low FUV luminosities.

stars), we find the cumulative probability distribution for the expected FUV luminosity. The result is shown in Figure 2.8. This calculation shows that the median FUV luminosity experienced by a forming solar system is 10^{38} ergs^{-1}. This benchmark cluster luminosity is 122 times the mean FUV luminosity per star given by equation [2.13]. If every star had the mean FUV luminosity, this result would imply a typical cluster size $N \approx 122$; since the typical (median) star has FUV luminosity less than the mean, the implied typical cluster size is somewhat larger (consistent with the distribution of Figure 2.1). Note also that individual stellar orbits within the cluster also lead to different radiation exposure - this issue is discussed below.

2.3.2 Effects of FUV Radiation

The physical quantity that affects forming solar systems is the FUV flux, which depends on both the FUV luminosity (Section 2.3.1) and the radial position of the solar system

within its birth aggregate (Section 2.2). For relatively "small" clusters of interest in this study, we can assume that the FUV luminosity originates from the few largest stars, which are generally observed to live near the cluster center (e.g., Testi et al. 1999). Here we make the approximation that the FUV luminosity can be modeled as a point source at the origin. Any given solar system in orbit within a given cluster will thus experience a time-dependent flux $\mathcal{F}_{FUV} = L_{FUV}/4\pi r^2$, where the radial position r is specified by the orbit.

Each cluster provides a distribution of FUV fluxes to its cluster members, and each ensemble of clusters with a given size N provides a wider distribution of FUV fluxes to the ensemble of members. Since clusters come in a distribution of sizes N, the collection of all forming solar systems is thus exposed to a wide distribution of FUV fluxes. Figure 2.9 shows an estimate for the probability distribution of FUV flux experienced by the entire ensemble of cluster stars as a function of flux. In this context, we express FUV flux in units of G_0, where $G_0 = 1$ corresponds to a benchmark value of 1.6×10^{-3} erg s^{-1} cm^{-2} at FUV wavelengths (close to the value of the interstellar radiation field). This ensemble distribution for the FUV flux was calculated assuming that the number of stars living in groups/clusters of size N follows the distribution shown in Figure 2.1 (Lada & Lada 2003; Porras et al. 2003), the radial size R_c of clusters follows the scaling relation shown in Figure 2.2, the distribution of FUV luminosity follows that calculated in Section 2.3.1, and the density distribution within the cluster has the form $\rho_* \propto r^{-1}$ for $0 \leq r \leq R_c$. The dashed curve in Figure 2.9 shows a Gaussian distribution with the same peak location and the same FWHM; the true distribution has a substantial tail at low values and a much smaller tail at high flux values.

In Figure 2.9, the vertical lines at $G_0 = 300, 3000$, and $30,000$ are values for which the photoevaporation of circumstellar disks due to FUV radiation has been calculated in detail

(Adams et al. 2004). In that study, the value $G_0 = 3000$ was chosen as a benchmark flux value (which corresponds to a cumulative probability of ~ 0.74 for the flux distribution found here). This FUV flux will drive the evaporation of a circumstellar disk around a 1.0 $M_\odot$ star down to a radius of $r_d \approx 36$ AU in a time of 10 Myr. As a result, the region of the disk where giant planets form ($5 - 30$ AU) is relatively safe for solar type stars. For smaller stars, however, flux levels of $G_0 = 3000$ can be significant. A disk orbiting a 0.5 $M_\odot$ (0.25 $M_\odot$) star can be evaporated down to $r_d \approx 18$ AU (9 AU) within 10 Myr. As a result, giant planet formation may be compromised around smaller stars (see also Laughlin et al. 2004). The results of the detailed photoevaporation models (Adams et al. 2004) can be summarized by a rough scaling law: an FUV flux of $G_0 = 3000$ truncates a circumstellar disk down to a radius $r_d \approx 36$ AU $(M_*/M_\odot)$, over a time of 10 Myr.

The flux experienced by a typical star within a cluster can be characterized in a variety of ways. As shown by Figure 2.9, however, the distribution of flux values is extremely wide and cannot be fully described by a single number. If we consider the composite distribution of Figure 2.9 as representative, then the median FUV flux experienced by a forming solar system is $G_0 \approx 900$, the peak of the distribution is at $G_0 \approx 1800$, and the mean is at $G_0 \approx 16,500$ (note how the mean is much larger than the median).

We can also estimate the typical flux provided by a cluster of a given size N. This determination requires an integration over both the distribution of radial positions and the distribution of possible FUV luminosities. We can use either the mean or medians of these distributions as the typical values, but they lead to markedly different results, as shown in Table 2.5. For a given FUV luminosity, the mean radiation flux exposure is given by

$$\langle \mathcal{F}_{FUV} \rangle = \frac{L_{FUV}}{4\pi} \left\langle \frac{1}{r^2} \right\rangle, \tag{2.18}$$

where the average is taken over all stars and over all times. To evaluate $\langle r^{-2} \rangle$, we use the radial distributions $N(r)$ calculated from our numerical simulations (analogous to the

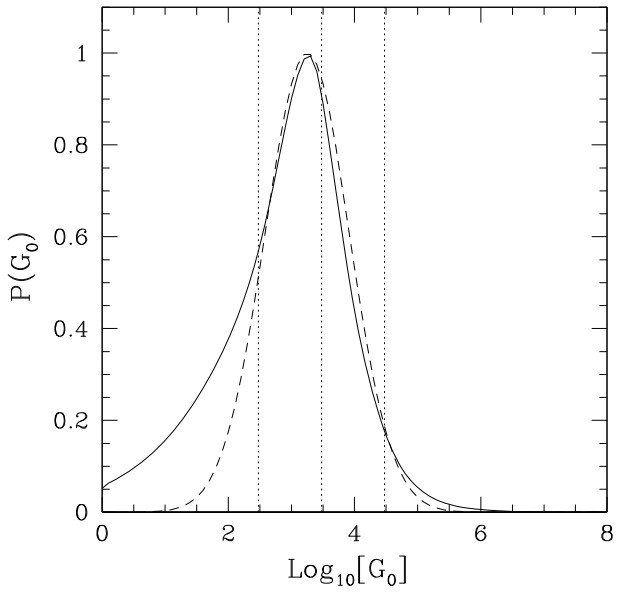

Figure 2.9: Probability distribution for FUV flux experienced by the ensemble of cluster stars as a function of the FUV flux, expressed here in units of G_0 (where $G_0 = 1$ corresponds to a flux of 1.6×10^{-3} erg s^{-1} cm^{-2}, which is close to the value of the interstellar radiation field). The ensemble distribution was calculated assuming that the number of stars living in groups/clusters of size N follows the distribution of Figure 2.1, the radial size R_c of clusters follows the distribution shown in Figure 2.2, the distribution of FUV luminosity follows that calculated in Section 2.3.1, and the density distribution within the cluster has the simple form $\rho_* \propto r^{-1}$ for $0 \leq r \leq R_c$. The dashed curve shows a Gaussian distribution with the same peak location (at $\log_{10} G_0 = 3.25$) and the FWHM (1.575). The calculated distribution has a significant tail at low flux values. The vertical lines at $G_0 = 300, 3000$, and $30,000$ are benchmark values for which the effects of photoevaporation on circumstellar disks have been calculated in detail (Adams et al. 2004).

mass profiles $M(r)$ given by equation [2.4] and Table 2.2). We can write this expectation value in terms of an effective radius r_{eff} defined by

$$r_{eff} \equiv \left\langle \frac{1}{r^2} \right\rangle^{-1/2}. \tag{2.19}$$

The effective radii for our six sets of simulations are given in Table 2.5. Using the mean values of the FUV luminosity in conjunction with the quantity $\langle r^{-2} \rangle$, we find a "mean" flux value, as listed in the table. Although this value provides one characterization of the FUV flux, the distributions are extremely wide, more than an order of magnitude wider than the mean value. As a result, most of the exposure occurs for those (relatively few) stars that wander close to the cluster center. The median thus provides a better measure of the typical FUV flux. The median values for the radial position, coupled with the median value of the FUV luminosity, provide an estimate for the "median" flux. The resulting values are also listed in Table 2.5. Note that the flux levels calculated from the median values of radial position and FUV luminosity are much smaller than those calculated from the means (by factors of $17 - 190$). The mean and median values of the FUV flux, calculated from the composite distribution of Figure 2.9, are included as the final line in Table 2.5. Note that the median flux of the composite ($G_0 = 900$) is smaller than the median values for $N = 1000$, larger than the values for $N = 100$, and roughly comparable to the values for $N = 300$. This ordering is consistent with finding that the median (weighted) value of cluster sizes occurs at $N \approx 300$ (from Figure 2.1), i.e., half of the stars in the sample are found in groups/clusters with $N < 300$, and half are found in systems with $N > 300$.

The distributions considered thus far describe the FUV flux experienced by forming solar systems in a statistical sense. A related question is to find the radiation experienced by a given solar system over the course of its orbit. Here we would like an analytic description of the orbits in order to see how the results depend on the relevant physical quantities.

Table 2.5: Expected FUV Flux Values

System	r_{eff} [pc]	G_0 -mean-	r_{med} [pc]	G_0 -median-
100 Subvirial	0.080	66500	0.323	359
100 Virial	0.112	34300	0.387	250
300 Subvirial	0.126	81000	0.549	1550
300 Virial	0.181	39000	0.687	992
1000 Subvirial	0.197	109600	0.944	3600
1000 Virial	0.348	35200	1.25	2060
Composite	–	16500	–	900

Toward this end, the mean flux intercepted by a solar system can be written in the form

$$\langle \mathcal{F}_{FUV} \rangle = \frac{1}{\tau_{1/2}} \int \frac{L_{FUV}}{4\pi r^2} \, dt \,, \tag{2.20}$$

where $\tau_{1/2}$ is the time of a half-orbit (e.g., from the inner turning point to the outer turning point) and the integral is taken over that same time interval. Here we can model the orbits by assuming that the total cluster potential has the form of the Hernquist profile; orbits in this general class of extended mass distributions have a similar form (for further details, see Adams & Bloch 2005, hereafter AB05). The mean flux can then be written in the form

$$\langle \mathcal{F}_{FUV} \rangle = \frac{\tau_0}{\tau_{1/2}} \frac{L_{FUV}}{4\pi r_s^2} \int_{\xi_1}^{\xi_2} \frac{dt}{\xi^2} = \frac{\tau_0}{\tau_{1/2}} \frac{L_{FUV}}{4\pi r_s^2} (\Delta\theta) \,, \tag{2.21}$$

where $\tau_0 \equiv r_s (2\Psi_0)^{-1/2}$, $\xi = r/r_s$, r_s is the scale length of the Hernquist profile, ξ_j are the turning points, and $\Delta\theta \leq \pi$ is the angle subtended by the half-orbit. The total depth of the gravitational potential well Ψ_0 is given by $\Psi_0 \equiv GM_T/r_s$, where the mass scale $M_T = 4M_1$, where M_1 is the mass of the cluster (including both stars and gas) contained within the boundary R_c. The orbit time and turning angle are known functions of the dimensionless energy $\epsilon \equiv |E|/\Psi_0$ and angular momentum variable $q \equiv j^2/2\Psi_0 r_s^2$ (AB05). To within an accuracy of a few percent, one can express the dimensionless orbit time and the turning angle by the functions

$$\frac{\tau_{1/2}}{\tau_0} = \epsilon^{-3/2} \big(\cos^{-1} \sqrt{\epsilon} + \sqrt{\epsilon} \sqrt{1-\epsilon} \big), \tag{2.22}$$

$$\frac{\Delta\theta}{\pi} = \frac{1}{2} + \Big[(1+8\epsilon)^{-1/4} - \frac{1}{2}\Big]\Big[1 + \frac{\ln(q/q_{max})}{\ln 10}\Big]^{3.6}, \tag{2.23}$$

where q_{max} represents the maximum angular momentum for a given energy (that of a circular orbit) and the fitting function is restricted to the range $10^{-6} \leq q/q_{max} \leq 1$. The maximum value of the angular momentum variable is also a known function of dimensionless energy,

$$q_{max} = \frac{1}{8\epsilon}\frac{(1+\sqrt{1+8\epsilon}-4\epsilon)^3}{(1+\sqrt{1+8\epsilon})^2}\,. \tag{2.24}$$

Equations [2.21] – [2.24] thus specify the radiation exposure for a solar system on any orbit with given dimensionless energy ϵ and angular momentum q. The angular momentum dependence is relatively weak, much weaker than the dependence on energy. Since $\epsilon > 3/8$ for orbits confined to the inner part of the Hernquist profile ($\xi < 1$), the turning angle is confined to the narrow range $(\Delta\theta)/\pi = 1/2 - \sqrt{2}/2$. We can simplify the flux expression to take the form

$$\langle \mathcal{F}_{FUV} \rangle = \frac{L_{FUV}}{8r_s^2}\,\frac{A\epsilon^{3/2}}{\cos^{-1}\sqrt{\epsilon} + \sqrt{\epsilon}\sqrt{1-\epsilon}}\,, \tag{2.25}$$

where the parameter A is slowly varying and encapsulates the angular momentum dependence (with $1 \leq A \leq \sqrt{2}$). The leading coefficient sets the magnitude of the flux. The numerator can be written as $L_{FUV} = f_N N \langle L_{FUV} \rangle_*$, where f_N is the fraction of the mean FUV luminosity that the cluster produces. For example, the median flux corresponds to $f_N = 0.088$ for $N = 100$ and $f_N = 0.75$ for $N = 1000$ (see Figure 2.6), whereas the mean flux corresponds to $f_N = 1$ by definition. In the denominator, the scale length $r_s \sim R_c$, so that $r_s^2 \sim (1\text{ pc})^2(N/300)$. The leading coefficient can thus be evaluated and written in terms of the interstellar FUV radiation field, i.e., $G \approx 2000 f_N$. The remaining dimensionless function in equation [2.21] is of order unity and accounts for the orbital shape. Deep orbits (close to the central part of the potential well) with $\epsilon \gtrsim 0.93$ have values of the dimensionless function greater than unity, whereas lower energy orbits have values less

than unity. In any case, we find $G \sim 1000$, in agreement with the median values calculated above (Table 2.5).

The dynamics of the cluster determine the distributions of energy and angular momentum parameters (ϵ, q), and these distributions can be used in conjunction with equation [2.25] to calculate the distribution of fluxes experienced by young solar systems. For example, for an isotropic velocity distribution and a density profile $\rho \sim r^{-1}$, the differential energy distribution (see BT87) has the form $h(\epsilon) = dm/d\epsilon \propto (1 - \epsilon)$. Note, however, that the flux distribution calculated from the distribution of energy ϵ (and q) is narrower than that calculated from the distribution of positions (that shown in Figure 2.9). The fluxes in the former case are already averaged over the orbits, whereas those in the latter case are not and therefore explore a greater range of values.

2.4 Scattering Interactions and the Disruption of Planetary Systems

The ultimate goal of this section is to calculate the probability that a solar system will be disrupted as a result of being born within a group/cluster. In this case, disruption occurs through scattering interactions with other cluster members and should thus depend on the size N of the birth aggregate. In general, the rate of disruption for a solar system can be written in the form

$$\Gamma = n\sigma v \,, \tag{2.26}$$

where σ is the disruption cross section, n is the mean density of other systems, and v is the relative velocity (typically, $v \sim 1$ km s^{-1}). In this case, however, the results of N-body simulations provide the rate at which solar system experience close encounters within a closest approach distance b as a function of b. As a result, we only need to determine how close such scattering encounters must be in order for disruption to take place. Here we make the approximation that the cluster dynamics (which determines the rate f close encounters) is independent of the scattering dynamics between a solar system and a passing

star (which determines the cross sections).

Using our planet scattering code developed previously (Laughlin & Adams 2000; Adams & Laughlin 2001), we can calculate the cross sections for the disruption of solar systems with varying stellar masses (see also Heller 1993; 1995; de La Fuente Marcos & de La Fuente Marcos 1997; 1999). Since most stars passing nearby with the potential for disrupting a solar system are binaries, we want to find the effective cross section $\langle\sigma\rangle$ for a specified change in orbital parameters resulting from scattering encounters with binaries. We define this effective cross section $\langle\sigma\rangle$ through the relation

$$\langle\sigma\rangle \equiv \int_0^\infty f_D(a)(4\pi a^2)p(a)\,da\,, \tag{2.27}$$

where a is the semimajor axis of the binary orbit and $p(a)$ specifies the probability of encountering a binary system with a given value of a. Note that for a given value of a, this integral only includes those scattering interactions that fall within the predetermined area $4\pi a^2$, where the numerical coefficient 4 is chosen to be large enough to include all relevant interactions and small enough to allow for finite computing resources (in principle, one should include all interactions, no matter how distant). In practice, we find that the area $4\pi a^2$ provides a good compromise between accuracy and computational expediency. The function $f_D(a)$ specifies the fraction of the encounters that result in a particular outcome (e.g., a given change in the orbital parameters of the solar system), and the determination of f_D is the main computational task. The distribution $p(a)$ is determined by the observed distribution of binary periods and by the normalization condition

$$\int_0^\infty p(a)da = 1\,, \tag{2.28}$$

where we use observational results to specify the period distribution (Kroupa 1995b). The observed distribution is extremely broad, with roughly equal numbers of systems in each logarithmic interval in semimajor axis a and with a broad overall peak falling near $P = 10^5$

days. Although the distribution includes binaries with periods longer than 10^7 days, this set of scattering experiments only includes binaries with $a < 1000$ AU because wider binaries do not contribute appreciably to the cross sections.

The set of possible encounters that can occur between a given solar system and a field binary is described by 10 basic input parameters. These variables include the binary semimajor axis a, the stellar masses, m_{*1} and m_{*2}, of the binary pair, the eccentricity $e_{\rm bin}$ and the initial phase angle $\ell_{\rm bin}$ of the binary orbit, the asymptotic incoming velocity $v_{\rm inf}$ of the solar system with respect to the center of mass of the binary, the angles θ, ψ, and ϕ - which describe the impact direction and orientation - and finally the impact parameter h of the collision. Additional (intrinsic) parameters are required to specify the angular momentum vector and initial orbital phases of the planets within the solar system. In this study, we consider a class of solar systems in which the central stellar mass varies, but the planetary orbits are always taken to be those of our solar system. In other words, each solar system has an analog of Jupiter, a planet with one Jupiter mass m_J in an initial orbit of semimajor axis $a_J = 5$ AU; similarly, each solar system has an analog of Saturn, Uranus, and Neptune. The planetary orbits are assumed to be circular (initially) so that we can determine the change in orbital parameters from a known baseline. All of the planetary properties are kept fixed so we can isolate the effects of changing the mass of the central star.

In order to compute the fraction of disruptive encounters $f_D(a)$ and the corresponding cross sections, we perform a large number of scattering experiments using a Monte Carlo scheme to select the input parameters. This section reports on the results from more than 10^5 such scattering experiments. Individual encounters are treated as N-body problems in which the equations of motion are integrated using a Bulirsch-Stoer scheme (Press et al. 1986). During each encounter, we require that overall energy conservation be maintained

to an accuracy of at least one part in 10^8. For most experiments, energy and angular momentum are conserved to one part in 10^{10}. This high level of accuracy is needed because we are interested in the resulting planetary orbits, which carry only a small fraction of the total angular momentum and orbital energy of the system.

For each scattering experiment, the initial conditions are drawn from the appropriate parameter distributions. More specifically, the binary eccentricities are sampled from the observed distribution (Duquennoy & Mayor 1991). The masses of the two binary components are drawn separately from a log normal IMF that is consistent with the observed distribution of stellar masses (for completeness, we note that the IMF has a power-law tail at high masses, although this departure will not affect the cross sections calculated here). For both the primary and the secondary, we enforce a lower mass limit of 0.075 $M_\odot$ and hence our computed scattering results do not include brown dwarfs. This cutoff has a relatively small effect because our assumed IMF peaks in the stellar regime. The impact velocities at infinite separation, $v_{\rm inf}$, are sampled from a Maxwellian distribution with dispersion $\sigma_v = 1$ km s^{-1}, which is a typical value for stellar clusters with the range of parameters considered here (BT87). The initial impact parameters h are chosen randomly within a circle of radius $2a$ centered on the binary center of mass (a circular target area of $4\pi a^2$ as in equation [2.27]).

Using the Monte Carlo technique outlined above, we have performed $N_{\rm exp} \approx 20{,}000$ scattering experiments for collisions between binary star systems and solar systems of each stellar mass (i.e., a total of $\sim 10^5$ simulations). We use logarithmically spaced mass values: $M_*/M_\odot = 2, 1, \frac{1}{2}, \frac{1}{4}$, and $\frac{1}{8}$. As described above, all solar systems are taken to have the architecture of our outer solar system. From the results of these seven-body scattering experiments, we compute the cross sections for orbital disruption of each outer planet (according to equation [2.27]). Note that the procedure described thus far implicitly

assumes that all passing stars are binary. Although the majority of solar-type stars have binary companions, smaller stars (e.g., M stars) have a lower binary fraction. The true cross sections should thus be written as $\langle\sigma\rangle_T = F_b\langle\sigma\rangle_{\rm bin} + (1 - F_b)\langle\sigma\rangle_{\rm ss}$, where F_b is the binary fraction and $\langle\sigma\rangle_{\rm ss}$ is the cross section of interactions between single stars and solar systems (and is not calculated here). However, $\langle\sigma\rangle_{\rm ss} \ll \langle\sigma\rangle_{\rm bin}$ (Adams & Laughlin 2001) so that to a good working approximation one can use $\langle\sigma\rangle_T \approx F_b\langle\sigma\rangle_{\rm bin}$.

The cross sections for the planets to increase their orbital eccentricities are shown in Tables 2.6 – 2.10 for varying stellar mass (see also Figure 2.10). For each given value of eccentricity e, the table entries give the cross sections [in units of $(\mathrm{AU})^2$] for the eccentricity to increase to any value greater than the given e; these cross sections include events leading to either ejection of the planet or capture by another star. The listings for $e = 1$ thus give the total cross sections for planetary escape and capture (taken together). The last two lines of the tables present the cross sections for planetary escapes and captures separately. For each cross section listed, the tables also provide the 1 standard deviation error estimate [also in $(\mathrm{AU})^2$] for the Monte Carlo integral; this quantity provides a rough indication of the errors due to the statistical sampling process (Press et al. 1986). Figure 2.10 shows the cross sections plotted as a function of the eccentricity increase for each of the four planets and for the four largest stellar mass values.

Another way for solar systems to be disrupted is by changing the planes of the planetary orbits. One can use the results of the Monte Carlo scattering calculations to compute the cross sections for the inclination angles of the planetary orbits to increase by varying amounts. These results are shown as a function of angle in Table 2.11 for the five stellar mass values used here. More specifically, we define the inclination angle increase Δi to be the maximum angle between the orbital plane of the perturbed (post-encounter) planets and the original orbital plane. In Table 2.11, the Monte Carlo uncertainties are not listed,

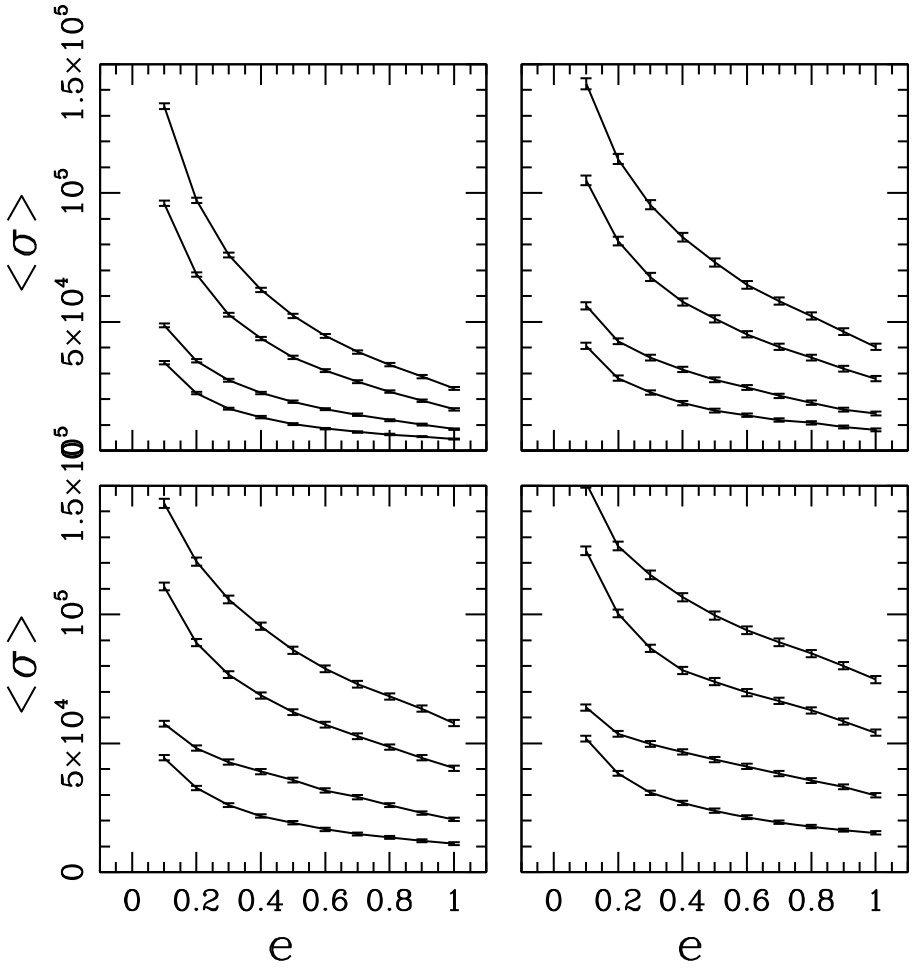

Figure 2.10: Scattering cross sections for solar systems to increase the eccentricity e of planetary orbits as a function of eccentricity. All cross sections are given in units of $(\mathrm{AU})^2$. The four panels shown here correspond to the four largest stellar mass values of our computational survey, i.e., $M_* = 2.0\ \mathrm{M}_\odot$ (*top left*) $1.0\ \mathrm{M}_\odot$ (*top right*), $0.5\ \mathrm{M}_\odot$ (*bottom left*), and $0.25\ \mathrm{M}_\odot$ (*bottom right*). In each panel, the four curves shown correspond to four giant planets orbiting the central star, where the planets have the same masses and starting semimajor axes as the giant planets in our solar system. The top curve in each panel corresponds to an analog of Neptune, and the bottom curve corresponds to an analog of Jupiter. The cross section for increasing the eccentricity beyond unity (*right end points of the curves*) corresponds to ejection of the planet. The error bars correspond to the uncertainties incurred due to the (incomplete) Monte Carlo sampling of the parameter space.

Table 2.6: Scattering Cross Sections for $M_* = 2.0$ $M_\odot$ Stars

e/Outcome	$\langle\sigma\rangle$ (Jupiter)	$\langle\sigma\rangle$ (Saturn)	$\langle\sigma\rangle$ (Uranus)	$\langle\sigma\rangle$ (Neptune)
0.10	34200 ± 632	48600 ± 738	96000 ± 1030	133700 ± 1180
0.20	22300 ± 513	34900 ± 631	68400 ± 881	97200 ± 1040
0.30	16300 ± 436	27300 ± 563	52800 ± 782	75900 ± 926
0.40	13000 ± 389	22400 ± 511	43500 ± 714	62400 ± 846
0.50	10300 ± 343	18900 ± 471	36100 ± 653	52300 ± 780
0.60	8560 ± 314	16100 ± 439	31100 ± 609	44600 ± 725
0.70	7300 ± 291	13900 ± 410	26800 ± 569	38300 ± 677
0.80	6240 ± 269	11900 ± 380	22900 ± 526	33300 ± 635
0.90	5470 ± 253	10100 ± 351	19400 ± 486	28700 ± 595
1.00	4550 ± 231	8350 ± 321	16000 ± 446	24200 ± 555
Escape	4010 ± 216	7590 ± 306	13900 ± 413	20600 ± 504
Capture	539 ± 83	764 ± 99	2100 ± 168	3640 ± 232

Table 2.7: Scattering Cross Sections for $M_* = 1.0$ $M_\odot$ Stars

e/Outcome	$\langle\sigma\rangle$ (Jupiter)	$\langle\sigma\rangle$ (Saturn)	$\langle\sigma\rangle$ (Uranus)	$\langle\sigma\rangle$ (Neptune)
0.10	40700 ± 1190	56300 ± 1380	104900 ± 1860	142400 ± 2110
0.20	28100 ± 996	42500 ± 1200	81300 ± 1650	113200 ± 1910
0.30	22600 ± 895	36100 ± 1110	67400 ± 1510	95400 ± 1780
0.40	18500 ± 801	31500 ± 1040	57700 ± 1400	82900 ± 1670
0.50	15500 ± 731	27500 ± 974	51200 ± 1330	73100 ± 1580
0.60	13700 ± 692	24500 ± 924	45200 ± 1250	64300 ± 1480
0.70	11900 ± 640	21300 ± 865	40300 ± 1190	58000 ± 1420
0.80	10800 ± 606	18600 ± 812	36100 ± 1130	52200 ± 1360
0.90	9270 ± 564	16000 ± 754	31800 ± 1060	46200 ± 1280
1.00	8040 ± 529	14400 ± 728	28000 ± 1010	40300 ± 1220
Escape	7060 ± 488	13100 ± 688	24900 ± 952	33900 ± 1100
Capture	973 ± 203	1350 ± 238	3010 ± 347	6390 ± 517

Table 2.8: Scattering Cross Sections for $M_* = 0.5$ $M_\odot$ Stars

e/Outcome	$\langle\sigma\rangle$ (Jupiter)	$\langle\sigma\rangle$ (Saturn)	$\langle\sigma\rangle$ (Uranus)	$\langle\sigma\rangle$ (Neptune)
0.10	44400 ± 1010	57700 ± 1140	110900 ± 1560	143200 ± 1730
0.20	32700 ± 870	48200 ± 1050	89100 ± 1400	120600 ± 1610
0.30	26000 ± 775	42800 ± 993	76600 ± 1310	105900 ± 1520
0.40	21800 ± 708	39100 ± 952	68600 ± 1250	95500 ± 1460
0.50	19200 ± 664	35800 ± 914	62200 ± 1190	86200 ± 1390
0.60	16600 ± 618	31700 ± 860	57300 ± 1150	78900 ± 1340
0.70	14800 ± 585	29200 ± 828	52900 ± 1110	72900 ± 1290
0.80	13500 ± 557	26000 ± 782	48600 ± 1070	68200 ± 1260
0.90	12200 ± 531	23000 ± 732	44400 ± 1020	63500 ± 1220
1.00	11100 ± 510	20500 ± 693	40400 ± 982	57900 ± 1190
Escape	10400 ± 496	18900 ± 665	36200 ± 922	50600 ± 1090
Capture	701 ± 119	1560 ± 194	4150 ± 338	7300 ± 458

Table 2.9: Scattering Cross Sections for $M_* = 0.25$ $M_\odot$ Stars

e/Outcome	$\langle\sigma\rangle$ (Jupiter)	$\langle\sigma\rangle$ (Saturn)	$\langle\sigma\rangle$ (Uranus)	$\langle\sigma\rangle$ (Neptune)
0.10	51900 ± 1140	63900 ± 1250	124800 ± 1720	151100 ± 1850
0.20	38400 ± 979	53800 ± 1150	100500 ± 1560	126700 ± 1710
0.30	30900 ± 875	49700 ± 1110	86900 ± 1460	115400 ± 1650
0.40	26900 ± 810	46700 ± 1080	78300 ± 1390	106800 ± 1600
0.50	23900 ± 761	43800 ± 1050	74000 ± 1350	99700 ± 1550
0.60	21300 ± 717	41100 ± 1020	69700 ± 1320	93900 ± 1510
0.70	19400 ± 683	38300 ± 988	66500 ± 1290	89300 ± 1480
0.80	17700 ± 655	35600 ± 959	62800 ± 1260	84900 ± 1450
0.90	16300 ± 630	33200 ± 929	58600 ± 1220	80200 ± 1410
1.00	15300 ± 614	29900 ± 880	54100 ± 1190	74800 ± 1400
Escape	14500 ± 597	27800 ± 842	49300 ± 1120	65300 ± 1290
Capture	741 ± 140	2040 ± 257	4880 ± 394	9440 ± 546

Table 2.10: Scattering Cross Sections for $M_* = 0.125$ $M_\odot$ Stars

e/Outcome	$\langle\sigma\rangle$ (Jupiter)	$\langle\sigma\rangle$ (Saturn)	$\langle\sigma\rangle$ (Uranus)	$\langle\sigma\rangle$ (Neptune)
0.10	65100 ± 1170	77700 ± 1260	147500 ± 1690	208200 ± 1940
0.20	50200 ± 1030	67800 ± 1190	111600 ± 1480	134700 ± 1590
0.30	37600 ± 888	63800 ± 1160	99400 ± 1410	121400 ± 1530
0.40	30800 ± 796	61500 ± 1140	92400 ± 1370	113600 ± 1490
0.50	26700 ± 734	58900 ± 1120	87200 ± 1340	107200 ± 1450
0.60	24000 ± 694	56000 ± 1100	83100 ± 1310	101800 ± 1420
0.70	21800 ± 664	52700 ± 1070	79100 ± 1280	97800 ± 1400
0.80	20000 ± 637	49300 ± 1040	75100 ± 1250	93800 ± 1380
0.90	18600 ± 612	45200 ± 1000	72100 ± 1230	90100 ± 1350
1.00	17200 ± 588	40100 ± 948	65900 ± 1190	84700 ± 1340
Escape	16100 ± 564	38000 ± 920	60100 ± 1130	74500 ± 1240
Capture	1060 ± 167	2160 ± 231	5750 ± 386	10200 ± 524

Table 2.11: Scattering Cross Sections for Angular Increase

Δi (deg)	$\langle\sigma\rangle$ 0.125 $M_\odot$	$\langle\sigma\rangle$ 0.25 $M_\odot$	$\langle\sigma\rangle$ 0.5 $M_\odot$	$\langle\sigma\rangle$ 1.0 $M_\odot$	$\langle\sigma\rangle$ 2.0 $M_\odot$
10.0	108800	104400	97400	89600	75500
20.0	91100	85600	78000	65800	50700
30.0	83200	77300	68000	55100	40400
40.0	77600	71900	61600	48800	34400
50.0	72800	67600	55900	43700	30200
60.0	68000	62500	51900	40100	26500
70.0	63000	57400	47900	36500	24000
80.0	58300	53000	43600	33700	21800
90.0	54100	48600	40300	30700	19400

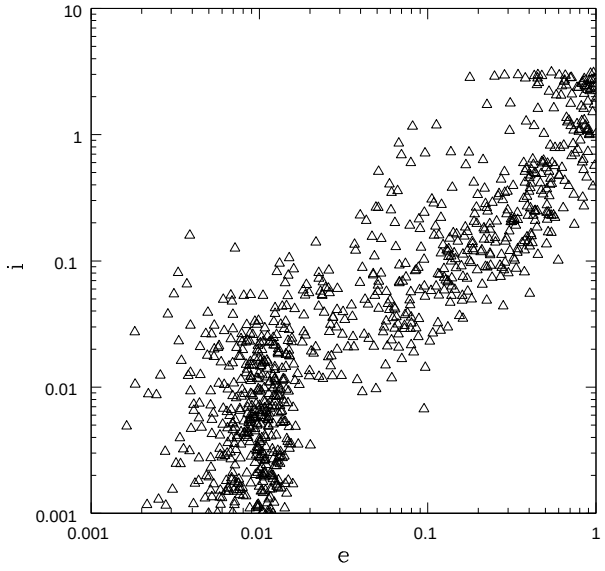

Figure 2.11: Scatter plot showing the correlation of changes in eccentricity with changes in the orbital inclination angle (in radians). Each symbol shows the result of one scattering simulation (not all cases are shown). The inclination angle is defined to be the maximum angle between the perturbed orbital planes of the planets and the original orbital plane. The eccentricity considered here is the (final) eccentricity of the Neptune analog. This plot shows results from the scattering experiments using stellar mass $M_* = 1.0$ $\mathrm{M}_\odot$; the results are similar for all five stellar masses considered herein.

but the sampling statistics are good, and the effective errors are approximately 2%. In addition, we find that the increases in inclination angle are well correlated with the predicted increases in eccentricity, as shown in Figure 2.11. For the five stellar masses considered here, the linear correlation coefficient between the inclination angle increase and the (final) eccentricity of the Neptune-analog planet lies in the range $\mathcal{R} = 0.70 - 0.75$.

The cross sections scale roughly with the inverse square root of the stellar mass. For example, the total ejection cross section is one of the more useful quantities considered here. We find that the mass dependence of the cross section for a given planet to be ejected can be written in the form

$$\langle \sigma \rangle_{\mathrm{ej}} \left(\frac{M_*}{\mathrm{M}_\odot} \right)^{1/2} \approx \mathcal{C}_P \approx constant, \tag{2.29}$$

where the constant $\mathcal{C}_P$ depends on which planet is being ejected. For Jupiter, Saturn, Uranus, and Neptune, respectively, we find $\mathcal{C}_J = 7200 \pm 800$, $\mathcal{C}_S = 14,000 \pm 1100$, $\mathcal{C}_U = 25,900 \pm 2440$, and $\mathcal{C}_N = 36,600 \pm 4070$ AU^2. When we scale the cross sections by the mass of the central star, the scaling law is not perfect, but rather retains some variation that is quantified by the quoted "error bars" given here. Next we note that these cross sections almost scale linearly with the semimajor axes of the planet. If we perform such a scaling, the ejection cross section can be written in the form

$$\langle \sigma \rangle_{\rm ej} \approx \mathcal{C}_0 \left(\frac{a_p}{\rm AU} \right) \left(\frac{M_*}{\rm M_\odot} \right)^{-1/2}, \tag{2.30}$$

where $\mathcal{C}_0 = 1350 \pm 160$ AU^2 and a_p is the semimajor axis of the planetary orbit.

Now we can put the pieces together and apply these results to clusters. The output measures from the numerical simulations show that the rates of close encounters have the form $\Gamma = \Gamma_0 (r/r_0)^\gamma$, where the parameters Γ_0 and γ depend on the starting conditions in the cluster. The length scale $r_0 = 1000$ AU defines the units. The rate of ejection of planets is thus given by

$$\Gamma_{ej} = \Gamma_0 \left[\frac{\mathcal{C}_0 (a_p/\rm AU)}{\pi r_0^2} \right]^{\gamma/2} \left(\frac{M_*}{\rm M_\odot} \right)^{-\gamma/4}. \tag{2.31}$$

This expression gives the ejection rate per star for a given M_*. To find the total ejection rate for the cluster, one must integrate over the IMF, normalized to the cluster size N, i.e., $\int dm (dN/dm) m^{-\gamma/4}$, where $\int (dN/dm) dm = N$. For example, the rate of ejection of planetary analogs of Jupiter in a cluster of $N = 300$ stars with a subvirial starting condition can be readily found: the numerical simulations provide $\Gamma_0 = 0.096$ (interactions per star per megayear) and $\gamma = 1.7$ (see Table 2.3). The ejection rate of Jupiters is thus $\Gamma_J \approx 0.15$ ejections per cluster per megayear. Over the 10 Myr lifetime spanned by the simulations, only one or two Jupiter ejections are expected per cluster (these results are consistent with those obtained by Smith & Bonnell 2001 and de La Fuente Marcos & de La Fuente Marcos

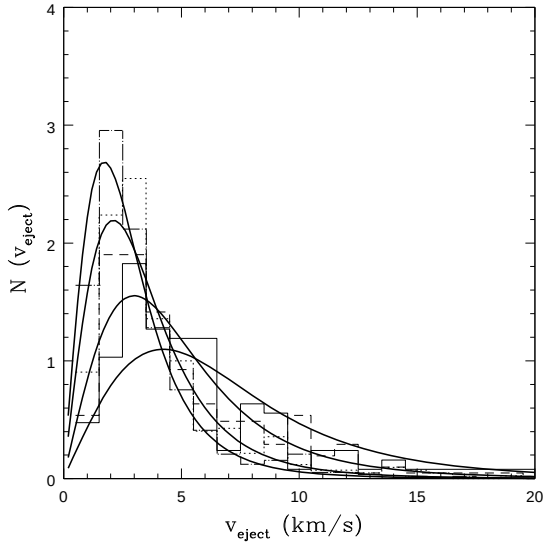

Figure 2.12: Distribution of ejection speeds for scattering interactions with central stellar mass $M_* = 0.50$ $M_\odot$. The histograms show the distributions of ejection speeds found in the numerical simulations for the analogs of Jupiter (*solid*), Saturn (*dashed*), Uranus (*dotted*), and Neptune (*dot-dashed*). The four smooth solid curves show the expected distribution from the simple theory outlined in the text.

1997). The number of ejected planets is not only small, but it is also much smaller than the number of ejections expected from internal (planet-planet) scattering events (Moorhead & Adams 2005). Even for the larger cross section for the ejection of Neptunes, the number of expected events is only about seven. For solar systems orbiting smaller stars, e.g., with mass $M_* = 0.25$ $M_\odot$, the ejection cross sections, and hence the expected number of ejected planets, are larger by a factor of ~ 2. Of course, smaller stars may have trouble forming planets due to increased efficacy of disk evaporation (Section 2.3; Adams et al. 2004) and other difficulties (Laughlin et al. 2004).

Another result from our ensemble of scattering experiments is the distribution of ejection speeds for planets that are removed from their solar systems during the interaction. The resulting distributions are shown for each of the four giant planets in Figure 2.12 (for stellar mass $M_* = 0.50$ $M_\odot$) and Figure 2.13 ($M_* = 0.25$ $M_\odot$). Also shown are the theoretically

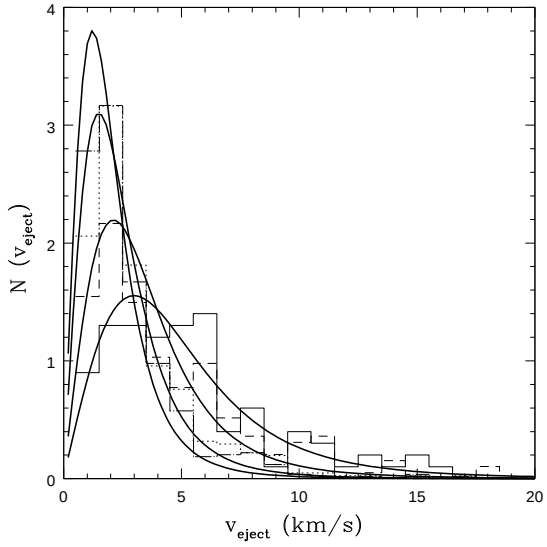

Figure 2.13: Distribution of ejection speeds for scattering interactions with central stellar mass $M_* = 0.25$ M$_\odot$. The histograms show the distributions of ejection speeds found in the numerical simulations for the analogs of Jupiter (*solid*), Saturn (*dashed*), Uranus (*dotted*), and Neptune (*dot-dashed*). The four smooth solid curves show the expected distribution from the simple theory outlined in the text.

expected distributions based on the idea that ejections involve sufficiently close encounters that the gravitational potential of the perturber (the passing star) dominates that of the central star. This type of interaction implies a distribution of ejection speeds of the basic form

$$\frac{dp}{du} = \frac{4u}{(1+u^2)^3}\,, \tag{2.32}$$

where $u = v/v_0$ and the velocity scale is given by $v_0^2 = GM_*/a$ (Moorhead & Adams 2005). Note that the impact speed of the binary $v_{\rm inf}$ does not enter into this formula because $v_0 \gg v_{\rm inf}$. As shown in Figures 2.12 and 2.13, this type of distribution provides a good fit to that found in the simulation data. Note that the numerical and analytic distributions are given the same normalization for all four planets. The overall number of ejections will vary with the planet's semimajor axes, as given by the cross sections in Tables 2.6 – 2.10.

2.5 NGC 1333 – A Case Study

The recent identification of 93 N_2H^+ $(1-0)$ clumps in the young cluster NGC 1333 by Walsh et al. (2004) provides an excellent opportunity to apply the theoretical program developed in this investigation toward the understanding of an observed cluster. More specifically, the data provide two-dimensional (2D) position measurements (in the plane of the sky) and one-dimensional (1D) velocity measurements (along the line-of-sight) for each of the 93 clumps. As a result, we need to reconstruct the remaining three phase-space variables in order to make full three-dimensional (3D) simulations of the cluster. Because the reconstruction process contains a random element (see below), we have to perform multiple realizations of the simulations in order to describe the dynamics. In addition, because the data do not completely specify the starting conditions (without reconstruction), this set of simulations represents a "theoretical model inspired by observations of NGC 1333" rather than a faithful model of the NGC 1333 cluster itself.

The starting conditions for the simulations are determined as follows. For a given 2D radius r_{2D} (as measured by Walsh et al. 2004), we use the fact that $r_{2D} = \sin\theta r_{3D}$ and assume that $\mu = \cos\theta$ is distributed randomly over the interval $[-1, 1]$. This procedure allows us to reconstruct the missing spatial coordinate. The resulting radial mass profiles of the cluster are illustrated in Figure 2.14. The resulting mass profile is intermediate between that of an isothermal sphere with $M(r) \propto r$ and a less centrally dense profile with $M(r) \propto r^2$ (which corresponds to $\rho_* \sim r^{-1}$ as used in Section 2.2). This particular cluster is thus somewhat more centrally concentrated than the theoretical models. In a similar manner, we assume that the (small) measured line-of-sight velocities are one component of an isotropic (small) 3D velocity vector and reconstruct the missing velocity components accordingly. Since the observed speeds are small compared to the virial speeds, the starting conditions are much like the subvirial starting states of Section 2.2.

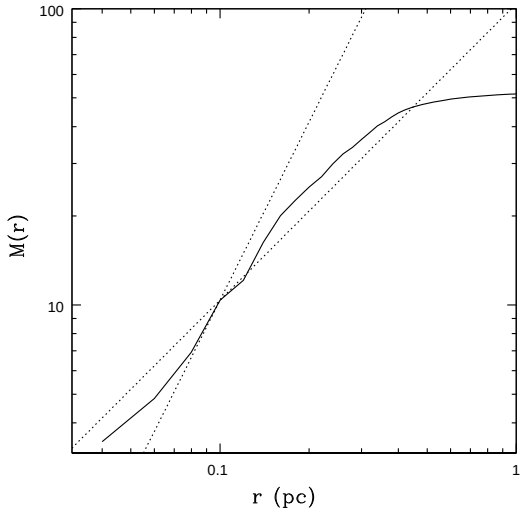

Figure 2.14: Reconstructed radial mass profile of the young embedded cluster NGC 1333, where $M(r)$ is given in $M_\odot$. To obtain this profile, the 2D observational map (Walsh et al. 2004) is converted into 10^5 different realizations of the 3D cluster structure (and averaged) according to the procedure outlined in the text. The two dotted lines, included for reference, have power-law slopes $p = 1$ and 2, i.e., $M(r) \propto r$ (which corresponds to $\rho_* \sim r^{-2}$), and $M(r) \propto r^2$ (which corresponds to $\rho_* \sim r^{-1}$).

The observations also provide mass estimates for the clumps. For the sake of definiteness, we assume that each clump forms a star and that the mass of the star is given by the mass of the clump. In actuality, the mass of the clump is not exactly given by the mass estimated from N_2H^+, as there is no hard boundary at the radius where the molecule becomes too faint to be seen; this effect makes the true clump masses larger than reported. On the other hand, we expect some inefficiency in the star formation process (e.g., Adams & Fatuzzo 1996), which would make the stellar masses smaller than the clump masses. We are thus implicitly assuming that these two effects cancel out. The observations indicate that the clump masses in NGC 1333 are somewhat segregated, with the more massive clumps found near the cluster center. This trend is illustrated in Figure 2.15: within the central 0.1 pc radius, 50% of the clumps have masses greater than 1 $M_\odot$, compared to 18% in the region as a whole. In this regard, the simulations of NGC 1333 differ from the

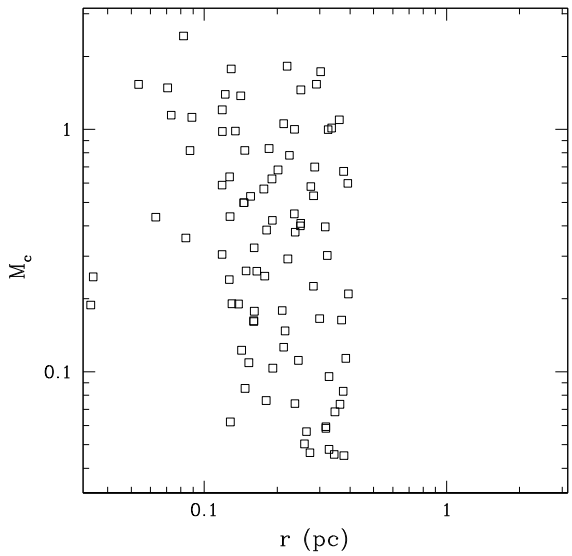

Figure 2.15: Mass M_c of observed clumps (in $M_\odot$) as a function of 2D radius for the young embedded cluster NGC 1333. The data are taken from Walsh et al. (2004). Note that the primordial mass segregation in this system is somewhat greater than the minimal segregation used in the purely theoretical models (Section 2.2).

purely theoretical models of Section 2.2, where only minimal primordial mass segregation was included (the most massive star was placed at the cluster center). In addition to the mass in clumps, we include a smooth background potential of gas analogous to the gas component used in Section 2.2.

The results of the simulations for NGC 1333 are listed as the final entries in Tables 2.1, 2.2, and 2.3. As expected, the output parameters for this cluster are most like the theoretical clusters with $N = 100$ and subvirial starting conditions. However, the NGC 1333 simulations produce clusters that are somewhat more concentrated and interactive. All of the indicators point in the same direction: compared to $N = 100$ simulations with subvirial starting states, the NGC 1333 simulations have half-mass radii that are smaller by a factor of ~ 1.8, a somewhat larger fraction of stars that remain bound (69% vs. 54%), and a smaller isotropy parameter β (see Table 2.1). The mass profiles have roughly the

same scale length $r_0 \approx 0.3 - 0.4$ pc (Table 2.2) and a somewhat smaller index ($p = 0.55$ compared to 0.69), indicating a more centrally concentrated cluster.

The largest difference between the NGC 1333 simulations and the others is reflected in the interaction rates, where the fiducial rate Γ_0 for NGC 1333 is larger by a factor of $5 - 6$ (Table 2.3). This higher interaction rate is a direct result of the smaller half-mass radius (a simple analytic approximation suggests that $\Gamma_0 \sim R_{1/2}^{-7/2}$). The characteristic interaction distance $b_C \approx 238$ AU, which implies that the NGC 1333 cluster facilitates disk truncation down to radii $r_d \sim 80$ AU (still well outside the realm of the giant planets in our solar system). Planetary analogs of Neptune can be stripped from the smaller stars with $M_* = 0.25$ $M_\odot$ and can experience large eccentricity enhancements ($e \sim 0.7$) when orbiting solar-type stars (see Tables 2.6 – 2.11). Planetary analogs of Jupiter remain largely unperturbed around all stars. This level of disruption is somewhat higher than found earlier for the purely theoretical clusters but still remains modest.

One important lesson resulting from this case study of NGC 1333 is the extent to which initial conditions can affect forming planetary systems. Compared to the starting conditions used for the simulations in Section 2.2 (where these starting conditions were motivated by observational surveys of cluster conditions, e.g., Figures 2.1 and 2.2), the NGC 1333 starts with a higher degree of central concentration and a greater amount of primordial mass segregation. The result is a more compact cluster (smaller $R_{1/2}$) and hence a higher interaction rate. In addition, the subvirial starting condition allows stars to fall inside much of the original gas and this geometry enhances cluster survival after gas removal (cf. Adams 2000 with Geyer & Burkert 2001). In order to fully determine the effects of the cluster environment on forming solar systems, we need to determine the range of starting density profiles and mass segregation.

2.6 Conclusion

This chapter has explored the early dynamical evolution of embedded stellar groups and clusters with stellar membership in the range $N = 100 - 1000$. This work includes N-body simulations of the dynamics, compilations of the distributions of FUV luminosities and fluxes, the calculation of scattering cross sections for young planetary systems, and an application to the observed embedded cluster NGC 1333. Our main conclusion is that clusters (with the range of properties considered here) have relatively modest effects on star and planet formation. The interaction rates and radiation levels are low, so that forming stars and their accompanying planetary systems are largely unperturbed by their environment. This finding, in turn, implies that cluster structure is due primarily to the initial conditions, rather than interactions. These results can be summarized in greater detail as follows.

- In order to obtain good statistics for our output measures, we have performed 100 realizations of each set of initial conditions for groups/clusters with $N = 100, 300$, and 1000. In addition to considering different cluster sizes N, we consider both virial and subvirial initial conditions. These simulations show a significant difference between the two types of starting conditions. Compared with virial initial conditions, subvirial clusters are more centrally concentrated, retain more of their stars for longer times, and exhibit more radial velocity distributions (Tables 2.1 and 2.4). As expected, all clusters lose stars and gradually spread out with time. This behavior is quantified by finding the average time evolution of each group/cluster type using 100 realizations of each set of initial conditions (Figure 2.3 and Table 2.1). We also provide quantitative descriptions of these systems by finding the mass profiles of the clusters (Figure 2.4, equation [2.4], and Table 2.2) and the distributions of close encounters (Figure 2.5, equation [2.6], and Table 2.3). All of these quantities can be used in a variety of other

contexts to test further the effects of the cluster environment on the processes of star and planet formation.

- We have calculated the FUV radiation expected from this class of groups and clusters. This issue involves (at least) three separate distributions: clusters of a given size N display a wide distribution of FUV luminosities due to incomplete sampling of the stellar IMF; we have determined this distribution $P(L_{FUV})$ as a function of N (Figures 2.6 and 2.7). Clusters themselves come in a distribution of sizes $P(N)$ (Figure 2.1) and we have found the distribution of FUV luminosities sampled over all clusters (Figure 2.8) using the observed range of cluster radii R_c (Figure 2.2). Finally, the stars within a cluster explore a range of radial positions, which in turn specify the distribution of radial positions $P(r)$ in the cluster. These three probability distributions [$P(N)$, $P(L_{FUV})$, and $P(r)$] jointly determine the composite distribution of FUV fluxes that impinge on the composite ensemble of forming solar systems (shown in Figure 2.9). The median FUV flux for the composite distribution is only $G_0 \approx 900$, which is not intense enough to evaporate disks orbiting solar-type stars (over 10 Myr) for the range of radii of interest for planet formation ($r \leq 30$ AU). We have also found the fluxes averaged over individual orbits within the clusters as a function of orbital energy and angular momentum (equations [2.21] - [2.25]). The results of this section imply that FUV radiation in clusters does not generally inhibit planet formation. In addition, the distributions found here can be used to determine the radiation exposure for forming solar systems in a variety of other contexts.

- We have calculated the cross sections for the interaction of newly formed solar systems with passing binaries (Tables 2.6 – 2.11) using an ensemble of $\sim 10^5$ Monte Carlo scattering experiments. These cross sections, in conjunction with the interaction rates determined via the N-body simulations, show that the typical solar system

is not greatly affected by scattering interactions within its birth aggregate. The typical star within a cluster of size $N = 100 - 1000$ will experience approximately one close encounter within a distance b_C over a 10 Myr window of time. We find that $b_C = 700 - 4000$ AU for the systems considered here. This passage is not close enough to appreciably enhance the eccentricity of Neptune in our solar system. The mildest disruption event considered here is the increase in eccentricity of a Neptune-analog planet orbiting a 0.125 $M_\odot$ star; the cross section for this event is $\langle\sigma\rangle \sim 2 \times 10^5$ AU^2 (Table 2.10), requiring a closest approach distance of ~ 250 AU. Similarly, disks are truncated by passing stars down to radii of $\sim \frac{1}{3}$ of the closest approach distance (Kobayashi & Ida 2001), so the disks in these clusters are expected to be limited to $230 - 1300$ AU, much larger than the regimes of interest for planet formation. Our main conclusion is that planet-forming disks and newly formed solar systems generally survive their birth aggregates with little disruption. In addition, the cross sections calculated herein can be used to study solar system disruption in a wider range of contexts and environments. For example, planet formation can potentially be induced by weak scattering encounters which can generate gravitational instabilities in the protoplanetary disks (Thies et al. 2005). As another application, we note that some star-forming regions are reported to have higher binary fractions than the field. As a result, one issue is whether or not the cluster environment can disrupt binaries (e.g., Kroupa et al. 2003, and references therein). Our results imply that the clusters considered here do not facilitate the disruption of binaries, except for those that begin with separations greater than ~ 1000 AU. If the primordial period distribution is similar to that measured in the field, only $\sim \frac{1}{7}$ of binaries would be affected by scattering interactions (of course, more binary disruption would occur if these clusters did not suffer an early demise due to gas expulsion at $t = 5$ Myr).

- We have performed an ensemble of 100 simulations of the observed young embedded cluster NGC 1333, where we start with observed positions in the plane of the sky and line-of-sight velocity components, and then reconstruct the remaining phase-space coordinates. This set of simulations is used to construct the output measures for clusters of this type, and we use the results to assess the impact of the background environment on star and planetary systems forming within this type of group/cluster. This cluster is most like the $N = 100$ subvirial simulations performed in Section 2.2. Compared to the purely theoretical simulations, NGC 133 has more primordial mass segregation and a smaller half-mass radius $R_{1/2}$. This property leads to a somewhat larger bound fraction f_b and a higher interaction rate Γ compared to the $N = 100$ simulations with subvirial starts. Nonetheless, the overall amount of disruption is small (e.g., circumstellar disks are truncated down to $\sim$ 80 AU, well outside the region where giant planets form) so that the cluster environment has only a modest effect on star and planet formation.

This chapter represents an assessment of dynamical effects in six classes of young embedded clusters. The treatment is extensive in that we run 100 N-body simulations for each type of cluster in order to obtain robust statistical descriptions, and we assess the effects of FUV radiation and solar system scattering on forming solar systems. On the other hand, the parameter space available to such clusters is enormous and a great deal of additional work remains to be done. For example, the simulations in this study were started with cluster sizes R_c near the low end of the observed range (Figure 2.2, *lower dashed curve*) and gas removal times (5 Myr) near the high end of the observed range (Lada & Lada 2003). These choices tend to make the clusters denser and long-lived, which makes the effects of interactions and radiation more important. Since we find that interactions and radiation have only modest effects on planet-forming disks, we can consider this conclu-

sion as conservative. However, a more detailed treatment of gas removal, including shorter lifetimes and more realistic time dependence (not a step function in time), is warranted.

A number of additional processes may also affect cluster evolution and should be studied; these include the role played by additional primordial mass segregation (beyond the minimal treatment used here), nonspherical starting conditions for both the stars and gas, and the effects of primordial binaries. Mass segregation – both primordial and evolutionary – may be particularly interesting, as suggested by our simulations motivated by NGC 1333. Our work to date indicates that the disruption of planetary systems is a sensitive function of the mass M_* of the central star (e.g., scattering cross sections scale approximately as $\langle\sigma\rangle \sim M_*^{-1/2}$, and FUV radiation truncates disks approximately at $r_d \sim M_*$) and a sensitive function of location within the cluster (both the FUV flux and interaction rates are much greater near the cluster center). If substantial mass segregation is present during the ~ 10 Myr while the clusters remain intact, the larger stars will be closer to the center where they are exposed to greater probability of disruption, and the smaller stars will be farther out and relatively safer. The degree to which this effect occurs should be quantified in future studies.

Finally, this work emphasizes the fact that cluster environments display a distribution of properties, and the full distributions must be considered in order to assess their effects on forming stars and planets. Some previous studies (e.g., Bonnell & Bate 2002) have focused on the densest regions of large clusters where the interaction rates are high and the background environment has an important effect on star formation. Although most clusters have a central zone of high interaction, for the clusters considered here most stars do not live in the highly interactive zone. It is thus crucial to determine the full distribution of environmental properties that forming stars are exposed to, including how often the various environments arise. Clusters are sampled from a distribution of sizes $P(N)$. For a given

size N, clusters have a range of radial sizes $P(R_c)$, a range of starting speeds and hence a distribution of virial parameters $P(Q_i)$, and display a distribution of FUV luminosities $P(L_{FUV})$. For given sizes R_c and N, and a given starting condition Q_i, stellar members explore a distribution of radial positions $P(r)$ within the cluster. The methods developed in this chapter show that we can find the distributions of luminosities (Figure 2.8), radial positions (analogous to Figure 2.4), closest approaches (Figure 2.5), and other quantities of interest from a given set of starting conditions. Perhaps the most important goal of future studies is thus to make a better observational determination of the distributions $P(N)$, $P(Q_i)$, and $P(R_c)$, which would allow for more complete predictions of the effects of the cluster environment on star and planet formation.

CHAPTER III

Early Evolution of Stellar Groups and Clusters: Parameter Space Study

In this chapter we continue the exploration from Chapter II and complete a parameter space study of the dynamics of young embedded clusters over a wide range of initial conditions. As outlined previously, this study is motivated by recent observations of a large number of young embedded clusters that have provided a broad survey of the star formation conditions found in the solar neighborhood (see Lada & Lada 2003; Megeath et al. 2004; Allen et al. 2007, and references therein).

3.1 Simulation Overview

A modified version of the NBODY2 code developed by Aarseth (2001) is employed to numerically calculate the dynamics in young stellar clusters from the embedded stage out to ages of 10 Myr. The modifications made to this code allow for the cluster's initial conditions to be more like those observed in young stellar clusters. These modifications allow us to specify the form and time evolution of the embedding gas, provide differing amounts of initial mass segregation, and define the geometry and velocity structure of the stellar distribution. Additional modifications are designed to produce the output parameters of interest in this study, i.e. closest approach distributions, velocity distributions, mass profiles, etc.

In addition to focusing on clusters with initial conditions similar to those found in nearby young clusters, this work is distinguished by its statistical character. The N-body problem is by nature chaotic and thus even clusters with the similar initial configurations may have dissimilar results. Therefore, in order to produce robust statistical descriptions of cluster evolution, for each initial condition configuration considered within this study a total of 100 cluster simulation realizations are completed. Specifically, for a given set of initial cluster conditions (i.e., cluster membership, radius, velocity distribution, etc.), 100 simulations are completed using a different random number seed to sample the relevant distributions. The resulting output parameters are then averaged over the set of realizations to provide a statistical understanding of how a similar cluster is likely to evolve.

In this section we outline the standard initial conditions assumed in the simulated clusters. Specifically, we discuss the qualities most commonly observed in nearby young embedded clusters and identify these qualities as the center of our parameter space survey. These initial conditions define the typical cluster, and the parameter space survey is conducted by varying one or more of the initial conditions at a time. . In Section 3.2 we motivate the particular range of parameter space investigated in this survey. Finally, we present the results of the cluster simulations in Section 3.3 and discuss implications for planet formation within these clusters.

Cluster Membership, N. In this study we consider intermediate-sized clusters with stellar memberships ranging from $N = 100$ to 3000. The shape of the initial mass function (IMF) observed in young stellar clusters is fairly universal for clusters with more than ~ 100 members (Lada & Lada 2003). Therefore in our simulations, stellar masses are sampled from the log-normal analytic fit to the standard IMF of Miller & Scalo (1979) presented by Adams & Fatuzzo (1996). The average stellar mass in a cluster is 0.5 $M_\odot$ (the average stellar mass is somewhat higher than the median stellar mass which is roughly ~ 0.3 $M_\odot$),

consistent with observations of young stellar clusters (Muench et al. 2002; Luhman et al. 2003).

Cluster Radius, R_c. Stars are distributed within the cluster radius R_c according to the density profiles described below. We define cluster radius R_c as a function of the cluster membership N, the scaling radius R_{sc}, and the power law index α.

$$R_c = R_{sc}\left(\frac{N}{300}\right)^{\alpha}. \tag{3.1}$$

This membership-radius relationship is observed in young clusters in the solar neighborhood (Lada & Lada 2003; Porras et al. 2003, see also Figure 2.2), and typical values of the parameters R_{sc} and α are 1 pc and $\frac{1}{2}$, respectively. Therefore a cluster with $N = 300$ stars has a radius of 1 pc.

Initial Stellar Profile. Many young embedded clusters display degrees of central concentration (Lada & Lada 2003, and references therein). The simulated clusters are correspondingly centrally condensed and have stellar density distributions of the form $\rho_* \sim r^{-1}$. Density profiles of this form are consistent with the observed density profiles embedding gas in cluster-forming cores (see below).

Mass Segregation. Young stellar clusters exhibit various amounts of mass segregation even though the clusters themselves are not old enough to have undergone dynamical mass segregation (i.e. they are less than a relaxation time old). The simulated clusters contain minimal mass segregation implemented by a straightforward algorithm. At initialization, the most massive star in the cluster is relocated to the center of the cluster.

Initial Stellar Velocities. Kinematic observations of youngest stellar objects and of starless dense cores indicate that in many young clusters, these objects are moving at speeds that are a fraction of the virial speed (Walsh et al. 2004; André 2002; Peretto et al. 2006; Kirk et al. 2006). In the cluster simulations, initial stellar velocities are sampled from a spatially isotropic distribution and then scaled by the initial virial ratio of the cluster

Q_i. The virial ratio is defined as $Q \equiv |K/W|$, where K is the total kinetic energy and W is the total potential energy of the cluster. A cluster that is in virial equilibrium has a virial ratio $Q = 0.5$. Most simulations considered in this study are initialized with a virial ratio $Q_i = 0.04$ which results in stellar velocities that are approximately one-third of the virial velocity of the cluster and is consistent with the kinematic observations of young embedded clusters.

Star Formation History. The stars in the simulated clusters have a spread in formation times of $\Delta t = 1$ Myr. The formation time of each star is sampled from a uniform distribution over the range from 0 to 1 Myr, independent of position within the cluster or stellar mass. We then assume that the forming stars are tied to their formation site until the collapse phase is complete, i.e., until the star is formed. The stars are included in the simulations as static point masses until their formation time after which they are allowed to move through the gravitational potential of the cluster with an initial velocity sampled from the distribution described above.

Embedding Gas Profile. Extremely young ($\lesssim 3$ Myr) stellar clusters are almost always associated with a molecular cloud core (Leisawitz et al. 1989). These cores are often centrally concentrated (Larson 1985; Myers & Fuller 1993; Jijina et al. 1999). In the simulated clusters the embedding gas is represented as a static gravitational potential with a Hernquist profile with potential, density, and mass profiles of the form

$$\Psi = \frac{2\pi G \rho_0 r_s^2}{1+\xi}, \qquad \rho = \frac{\rho_0}{\xi(1+\xi)^3}, \qquad \text{and} \qquad M = \frac{M_\infty \xi^2}{(1+\xi)^2}, \tag{3.2}$$

where $\xi \equiv r/r_s$ and r_s is a scale length, which is chosen to be equal to the cluster radius, i.e., $r_s = R_c$ (Hernquist 1990). In the inner limit this profile has the form of $\rho \sim r^{-1}$ and outside of the cluster the density profile matches onto the force-free background. We are thus neglecting external forces on the cluster.

Star Formation Efficiency. Estimates of the star formation efficiency ε_{SF}in young star-

forming regions vary from $\sim 10\%$ to 50% (Lada & Lada 2003). In our simulated clusters, a standard star formation efficiency of $\varepsilon_{SF} = 33\%$ is assumed. This corresponds to a total stellar mass M_{T*} in the cluster that is one half of the mass of the embedding gas M_{gas} (from equation [3.2], $M_{gas} = M_{\infty}/4$ is the effective gas mass within the cluster radius R_c).

Gas Removal History. Although very young stellar clusters are associated with embedding molecular gas, the gas is quickly dispersed from the cluster by stellar winds from young stars, ionizing radiation from massive stars, or nearby supernova explosions. Clusters with ages greater than $\sim$ 3 Myr are rarely associated with molecular gas. In the cluster simulations the depth of the potential well associated with the embedding gas is reset to zero instantaneously at time t_{gas}, and thus the gas removal mechanism is assumed to rapidly disperse gas from the vicinity of the cluster.

3.2 Parameter Space Overview

As evidenced by the list in Section 3.1, the number of initial parameters which must be specified in a cluster simulation is quite high. As a result, the parameter space available in which to study of the evolution of stellar clusters is extremely large. In our current work, we target our parameter space survey on embedded cluster environments similar to those observed in our solar neighborhood (Lada & Lada 2003; Allen et al. 2007; Megeath et al. 2004, Gutermuth et al. 2009, in preparation), with an extrapolation to somewhat larger clusters. In this section we identify the range of parameter space in which our survey is conducted. It is important to note that this range, while motivated by observations of nearby clusters, does not necessarily encompass all of the initial conditions observed in these clusters. The range of parameter space surveyed and the initial conditions assumed in the clusters are summarized in Table 3.1

3.2.1 Cluster Membership, N

We perform a series of simulations to study the effect that stellar membership has on the dynamics of young embedded clusters. We consider spherical clusters embedded in centrally concentrated gas potentials with a star formation efficiency $\varepsilon_{SF} = 0.33$. The stellar membership in the simulated clusters ranges from $N = 100$ to 3000. Clusters of this size roughly span the range of young clusters observed in the solar neighborhood (Lada & Lada 2003; Porras et al. 2003). Motivated by observations of young stellar objects with subvirial velocities, this study considers embedded clusters with both subvirial and virial initial velocity distributions. The subvirial and virial clusters have $Q_i = 0.04$ and 0.5 respectively. Therefore, the subvirial clusters have initial stellar velocities that are approximately $\frac{1}{3}$ of the virial velocity.

It is possible that the index α appearing in the membership-radius relation (equation [3.1]) varies over different clusters of different sizes N. For example, the value $\alpha = \frac{1}{2}$ is a reasonable fit to the observed data within approximately 2 kpc of the sun (Lada & Lada 2003; Porras et al. 2003, see also Figure 2.2), which contains clusters with memberships $N \lesssim 2000$. In environments with star formation rates much higher than that of the solar neighborhood, a significant amount of star formation occurs in clusters much more massive than those found in our solar neighborhood. These extremely massive young clusters, some which are thought to be progenitors of globular clusters, contain as many as $N \sim 10^6$ stars, have sizes on the order of $R_c \sim 10$ pc (Mengel et al. 2008). If we extend the cluster membership-radius relation out to stellar memberships as high as $N \sim 10^6$, the choice of $\alpha = \frac{1}{2}$ overestimates the cluster radius by a factor of ~ 5. A power law index of $\alpha = \frac{1}{4}$ more closely approaches the observed data points (over the full range of N). In this study, we investigate the evolution of intermediate-sized clusters for both $\alpha = \frac{1}{2}$ and $\alpha = \frac{1}{4}$ power law indices in the cluster membership-radius relation. In both cases, we chose $R_{sc} = 1.0$ pc

so that the power law passes through the point $N = 300$, $R_c = 1.0$ pc. The different choices of cluster membership-radius functions are depicted in Figure 1.1.

These two choices of α result in clusters whose average number density varies differently as a function of cluster membership. Specifically, substituting the membership-radius relation into the equation for average number density n_0 gives:

$$n_0 \sim \frac{N}{{R_c}^3} \sim \frac{N}{N^{3\alpha}} = N^{1-3\alpha}. \tag{3.3}$$

Therefore, for the choice $\alpha = \frac{1}{2}$ the average stellar density decreases as a function of N, whereas for $\alpha = \frac{1}{4}$ the stellar density is an increasing function of N. In the results summarized in Section 3.3, many of the trends observed as a function of cluster membership, N are in actuality traced to the trends in average stellar density as a function of N.

Note that an intermediate value of the index, $\alpha = \frac{1}{3}$, implies a constant stellar density. This benchmark value is $n_0 \sim 100$ stars pc^{-3}. Figure 3.1 displays the average number densities found in clusters in the solar neighborhood. The data are taken from the cluster catalogs of Lada & Lada (2003) (diamonds) and Carpenter (2000) (triangles). Number densities are calculated assuming spherical symmetry in the stellar clusters. Nearby young clusters may have higher densities in the cluster cores (Hillenbrand & Hartmann 1998; Gutermuth et al. 2005; Teixeira et al. 2006), but their average stellar densities are relatively constant.

3.2.2 Initial Virial Parameter, Q_i

As discussed in Section 3.1 (and in Chapters I and II), recent observations of young embedded clusters indicate that stars may be formed with velocities lower than the virial velocity of the cluster. During the early evolution of a subvirial cluster, the average stellar velocities increase as individual stars fall through the global potential well of the cluster. Stars with initially subvirial velocities thus trade potential energy for kinetic energy as

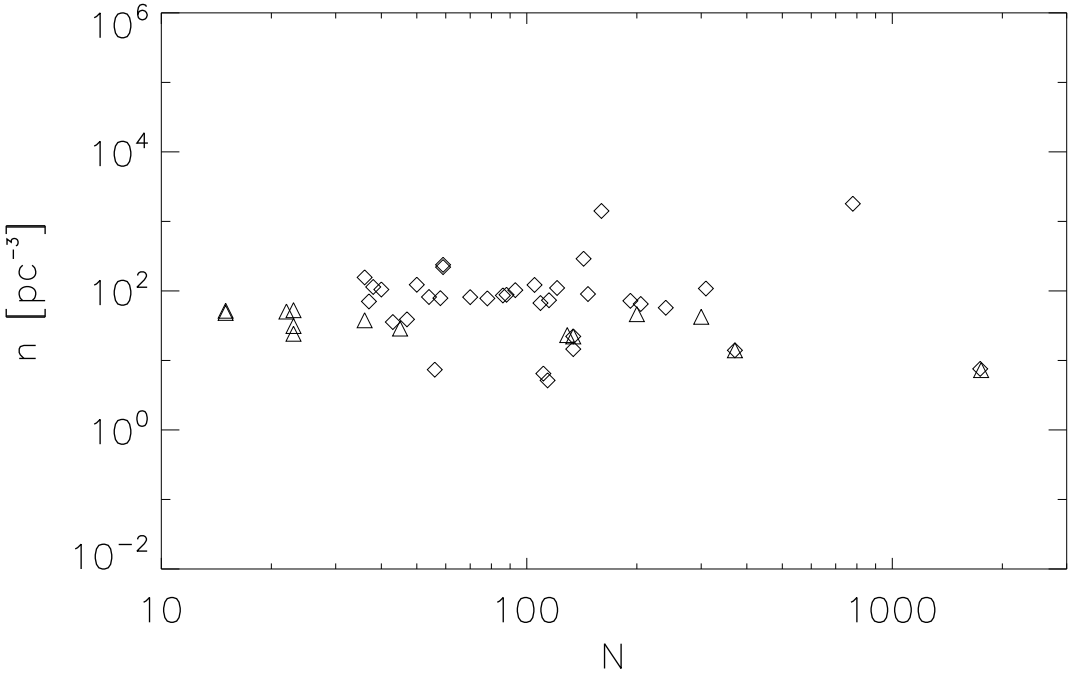

Figure 3.1: Average number density (in stars per cubic parsec) of clusters in the solar neighborhood plotted as a function of cluster membership N. Diamonds indicate data from the catalogs presented by Lada & Lada (2003) and triangles indicate data from the catalog of Carpenter (2000).

the cluster approaches virial equilibrium. We complete a series of experiments designed to investigate the effect that the initial virial ratio Q_i has on the evolution of clusters. While the simulations completed as a part of the cluster membership parameter study make a gross comparison between subvirial and virial clusters, this set of simulations samples a wide range of virial ratios $0.025 \leq Q_i \leq 0.5$ with much higher resolution. Simulations are completed for clusters with initial membership $N = 300, 1000$, and 2000 that have a membership-radius relation characterized by $\alpha = \frac{1}{2}$, similar to that observed in the solar neighborhood.

One question that this study attempts to address is: how subvirial must stellar velocities be for the cluster evolution to differ significantly from that of a cluster in virial equilibrium? Our results indicate that even moderately subvirial clusters display characteristics significantly different from virial clusters (Section 3.3). For instance, the bound fraction in a cluster with initial virial parameter $Q_i = 0.35$ is almost 50% larger than in a virial

cluster $Q_i = 0.5$. A value of $Q_i = 0.35$ corresponds to an average stellar velocity which is approximately 84% of the virial velocity of the cluster. Therefore, stars need not have *very* subvirial velocities for the effects to be significant.

3.2.3 Cluster Scaling Radius, R_{sc}

The cluster membership-radius relation presented in equation [3.1] depends on both the power law index α and the fiducial scaling radius R_{sc} which sets the radius of a cluster with $N = 300$ members. From Figure 2.2 it is evident that although this scaling relationship is reasonable, there is considerable scatter in the radius of observed clusters. Some of this scatter is due to the observational difficulty in determining the outer radius of a cluster as the surface density approaches that of the background sky. In addition, it is difficult to determine cluster radii for nonspherical clusters and clusters with small memberships (Gutermuth et al. 2005; Allen et al. 2007).

A series of simulations are completed to investigate how cluster evolution varies under different assumptions regarding the scaling radii. Specifically cluster simulations are completed for scaling radii in the range $\frac{1}{3}$ pc $\leq R_{sc} \leq 3$ pc with power law index $\alpha = \frac{1}{2}$ in the membership-radius relation. The clusters are assumed to have stellar memberships $N = 300, 1000$, and 2000 members and subvirial initial velocities, i.e., $Q_i = 0.04$. Changing the scaling radius R_{sc} effectively changes the average stellar density in a cluster, and many of the trends observed in the cluster evolution as a function of scaling radius R_{sc} are linked to this change in density.

3.2.4 Star Formation Efficiency, ε_{SF}

The star formation efficiency (SFE) of a region is defined as $\varepsilon_{SF} = M_{T*}/(M_{T*} + M_{gas})$ where M_{T*} and M_{gas} are the total stellar and gaseous mass contained in the region, respectively. Estimates of the young embedded cluster SFE within the solar neighborhood range between 0.1 and 0.3 (Lada & Lada 2003; Allen et al. 2007). These efficiencies are

significantly higher than the SFEs of entire giant molecular clouds which are typically less than $\sim 5\%$ (Duerr et al. 1982; Evans & Lada 1991). As a part of this parameter space study we complete a suite of cluster simulations in which the SFE is varied from $0.1 \leq \varepsilon_{SF} \leq 0.5$. The clusters are assumed to be in an initially subvirial state, and have memberships of $N = 300$ and 1000. A particular value of the efficiency parameter ε_{SF} is attained by varying the mass of the gas in the simulated cluster. The SFE of a cluster is a major factor in determining the probability that a cluster will remain bound after the embedding gas is dispersed due to outflows from young stars or ionizing radiation from the most massive star (see Section 3.3).

3.2.5 Gas Removal Timescale, t_{gas}

While the youngest star-forming clusters are deeply embedded in their natal molecular clouds, clusters with ages greater than a few Myr are rarely associated with molecular interstellar material (Leisawitz et al. 1989). In this series of simulations, we consider the evolution of young clusters with rapid gas removal at time t_{gas} ranging from 1 Myr to 7 Myr. The study considers subvirial clusters with memberships of $N = 300, 1000$, and 2000. A significant fraction of the stars in a given cluster become gravitationally unbound at the time of gas dispersal and the cluster begins to expand radially outward. As the cluster expands, the average density decreases and close interactions between stellar members become less frequent. Therefore, in addition to affecting how much of the cluster remains gravitationally bound, the gas removal time t_{gas} places limits on the close encounter rates in young clusters.

3.2.6 Mass Segregation, F_{seg}

Observations indicate that massive stars are preferentially found near the center of evolved open clusters. Mass segregation in these evolved clusters can be well explained by kinetic theory: high mass stars lose energy to low mass stars through two-body interactions

and subsequently sink toward the cluster's center. This process takes place on timescales comparable to a cluster's relaxation time:

$$t_{relax} \approx \frac{N}{8 \ln N} t_{cross} \approx \frac{N R_c}{8 \ln N \langle v \rangle}, \tag{3.4}$$

where t_{cross} is the cluster crossing time and $\langle v \rangle$ is the average stellar velocity (Binney & Tremaine 1987). Open clusters have ages of a few tens to hundreds of Myr and thus are old enough for dynamical mass segregation to have occurred. However, observations of mass segregation in young embedded clusters are more difficult to explain (Bonnell & Davies 1998). A (logarithmically) average embedded cluster in the solar neighborhood has $N \sim 300$, $R_c \sim 1$ pc, $\langle v \rangle \sim 1$ km s^{-1}, and a corresponding relaxation time of roughly 6.5 Myr. Therefore, dynamical evolution is unlikely to be responsible for the mass segregation observed in young clusters such as the Trapezium, NGC 2071, or NGC 2074 (Hillenbrand & Hartmann 1998; Lada et al. 1991; Bonnell & Davies 1998), which suggests that the mass segregation is due to a primordial tendency to form massive stars near the center of clusters. In addition, primordial mass segregation is naturally produced in embedded clusters through some proposed massive star formation scenarios. For instance, competitive accretion preferentially forms massive stars in the deepest part of the cluster potential well, near the center of the cluster (Bonnell et al. 2001; Beuther et al. 2007).

One experiment in the parameter space survey explores the evolution of clusters with various amounts of primordial mass segregation. We define the primordial mass segregation parameter F_{seg} as the fraction of the cluster membership which has been ordered by mass at the center of the cluster, $F_{seg} = N_{seg}/N$. Specifically, at simulation initialization the stellar masses are sampled from a standard IMF and stellar positions are sampled from a $\rho_* \sim r^{-1}$ density profile (regardless of mass). Then the most massive star in the cluster is moved from its initial randomly assigned position to the center of the cluster. This state represents a cluster with minimal mass segregation. For values of $F_{seg} > 1/N$,

Table 3.1: Parameter Space Survey Initial Conditions

Experiment	Parameter Varied	Parameter Range	Variations	# Sims
Cluster Membership	N	$100 - 3000$	$Q = 0.04, 0.5$ $R_c = (N/300)^{1/2}$ pc	6,200
Cluster Membership	N	$100 - 3000$	$Q = 0.04, 0.5$ $R_c = (N/300)^{1/4}$ pc	6,200
Virial Ratio	Q_i	$0.025 - 0.5$	$N = 300, 1000, 2000$ $R_c = (N/300)^{1/2}$ pc	6,000
Radius Scaling Factor	R_{sc}	$0.33 - 3.0$ pc	$N = 300, 1000, 2000$ $Q = 0.04$	2,700
Star Formation Efficiency	ε_{SF}	$0.1 - 0.5$	$N = 300, 1000$ $Q = 0.04$	1,600
Mass Segregation	F_{seg}	$\frac{1}{N} - 0.99$	$N = 300, 1000, 2000$ $Q = 0.04$	2,100

additional mass segregation is implemented by rearranging the stellar positions so that the N_{seg} most massive stars are located at the inner N_{seg} radial positions. The mass segregation parameter is varied over the range $1/N \leq F_{seg} \leq 0.99$ in subvirial clusters with $N = 300, 1000$, and 2000 members.

3.3 Summary of Results

3.3.1 Bound Fraction, f_b

Observational studies which compared the formation rates of embedded clusters and open clusters found that the embedded cluster formation rate was significantly higher than that of open clusters (Elmegreen & Clemens 1985; Battinelli & Capuzzo-Dolcetta 1991; Piskunov et al. 2006). This discrepancy in the formation rates leads to the interesting conclusion that although most star formation occurs in clusters, only a fraction (about 10%) of main sequence stars remain bound in open clusters for ~ 100 Myr, which suggests that very few embedded clusters remain gravitationally bound after the interstellar molecular gas has been removed from them. The process by which the removal of molecular gas leads to the unbinding of a cluster has been dubbed embedded cluster "infant mortality" and has been addressed via both analytical (Hills 1980; Elmegreen 1983; Verschueren & David

1989; Adams 2000) and numerical methods (Lada et al. 1984; Geyer & Burkert 2001; Boily & Kroupa 2003a;b), and evidence that this process is occurring in extragalactic young massive clusters has been presented by Bastian & Goodwin (2006).

An important output parameter explored in our simulations is the fraction f_b of stars that remain gravitationally bound as a function of time. The bound fraction is defined as $f_b \equiv N_{bound}/N$ where N is the initial stellar membership, and N_{bound} is the number of stars which have total energy (kinetic plus potential) less than zero. Throughout the embedded phase of cluster evolution, the bound fraction remains equal to 1. The embedding gas potential is removed from the simulated clusters instantaneously at t_{gas} which significantly reduces the depth of the potential well in which the cluster members reside. Rapid gas removal is an appropriate approximation to gas expulsion due to high mass star formation (Whitworth 1979), which removes the embedding gas over timescales as short as $\sim 10^4$ years.

As the gravitational potential of the gas is removed, the high-velocity stars become gravitationally unbound while the low-velocity stars remain bound to the cluster's gravitational potential. Therefore, the bound fraction f_b decreases significantly over a very short period of time (by as much as 50%) and, then levels off approaching its determined value at $t = 10$ Myr. (Note that 10 Myr is our chosen temporal cutoff, but the clusters will continue to evolve and f_b will continue to decrease, albeit on longer timescales.) Figure 3.2 displays f_b as a function of time for the range of initial condition parameter space surveyed in this study. Each panel illustrates the temporal evolution of f_b for a specific cluster parameter where the individual curves correspond to different values of the cluster parameter. For instance, in Figure 3.2 panel (a) the evolution of f_b is plotted for clusters with different star formation efficiencies ε_{SF}. The top curve corresponds to a cluster with $\varepsilon_{SF} = 0.75$ and the bottom curve corresponds to a cluster which has $\varepsilon_{SF} = 0.05$. For each of the curves

in Figure 3.2 the other initial conditions (i.e., cluster membership N, initial cluster radius R_c, amount of mass segregation F_{seg}, etc.) are held constant. The rapid decrease in f_b at $t = 5$ Myr in each panel (except for panel (e), which presents data from the gas removal timescale t_{gas} parameter study) corresponds to the time at which the gas is removed from the cluster.

The value of the bound fraction at $t = 10$ Myr provides some measure of how tightly bound a cluster remains after the embedding gas is removed. Figure 3.3 displays the value of the bound fraction at $t = 10$ Myr as a function of the initial cluster parameter values for the range of parameters considered in this survey. Previous theoretical and numerical work has identified a cluster's star formation efficiency ε_{SF} as the most important parameter in determining whether or not a cluster will remain gravitationally bound (Hills 1980; Elmegreen 1983; Lada et al. 1984). In clusters with high SFEs, a large proportion of the total cluster mass remains behind (in the form of stars) after the embedding gas is removed. Therefore, clusters with high SFEs remain more tightly bound after gas dispersal than clusters with low SFEs. In our cluster parameter survey we too find that the bound fraction f_b at $t = 10$ Myr depends most sensitively on the star formation efficiency ε_{SF} of the cluster. Figure 3.3 panel (a) displays the cluster bound fraction f_b as a function of star formation efficiency, ε_{SF}. The data is well fit by a power law in ε_{SF}:

$$f_b = 2.22\,(\varepsilon_{SF})^{1.2}\,, \qquad \text{for } \varepsilon_{SF} \leq 0.5. \tag{3.5}$$

In the suite of simulations completed to investigate the effects of star formation efficiency, the clusters are initially subvirial. After gas removal, subvirial clusters are more tightly bound than virial clusters (Adams et al. 2006). Therefore, for even relatively high star formation efficiencies, $\varepsilon_{SF} = 0.3$ and small velocities, which produce the most tightly bound clusters, the clusters are significantly disrupted by gas removal, losing $\sim 40\%$ of their stars. Star formation efficiencies larger than $\sim 30\%$ are rarely observed (Lada &

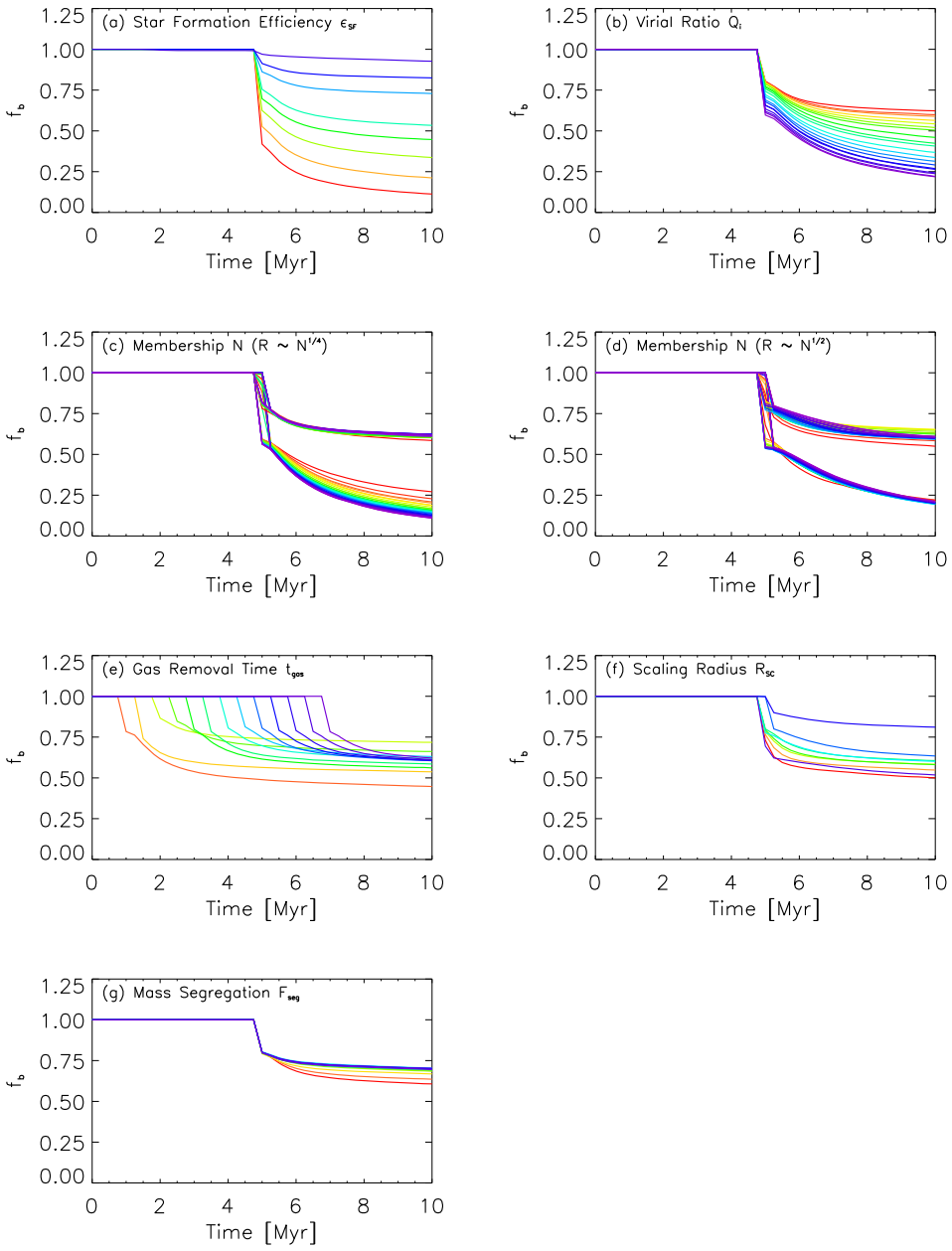

Figure 3.2: Fraction of stars that are bound to the cluster's gravitational potential f_b as a function of time, for all clusters included in the parameter space survey. Each panel corresponds to a different cluster parameter that is varied: (a) Star formation efficiency ε_{SF}, (b) Initial virial ratio Q_i, (c) Stellar Membership N for scaling relationship $R_c \sim N^{1/2}$, (d) Stellar Membership N for scaling relationship $R_c \sim N^{1/4}$, (e) Gas removal time t_{gas}, (f) Cluster scaling radius $R_{sc}$and (g) Amount of primordial mass segregation F_{seg}. The individual curves correspond to clusters with different initial values of the cluster parameter of interest. In all simulations (except those in panel (e)), the gas expulsion takes place at $t_{gas} = 5$ Myr. Immediately after gas removal, a significant fraction of stars become unbound from the cluster. As the cluster's evolution continues, the mass loss rate drops significantly and f_b approaches a constant value.

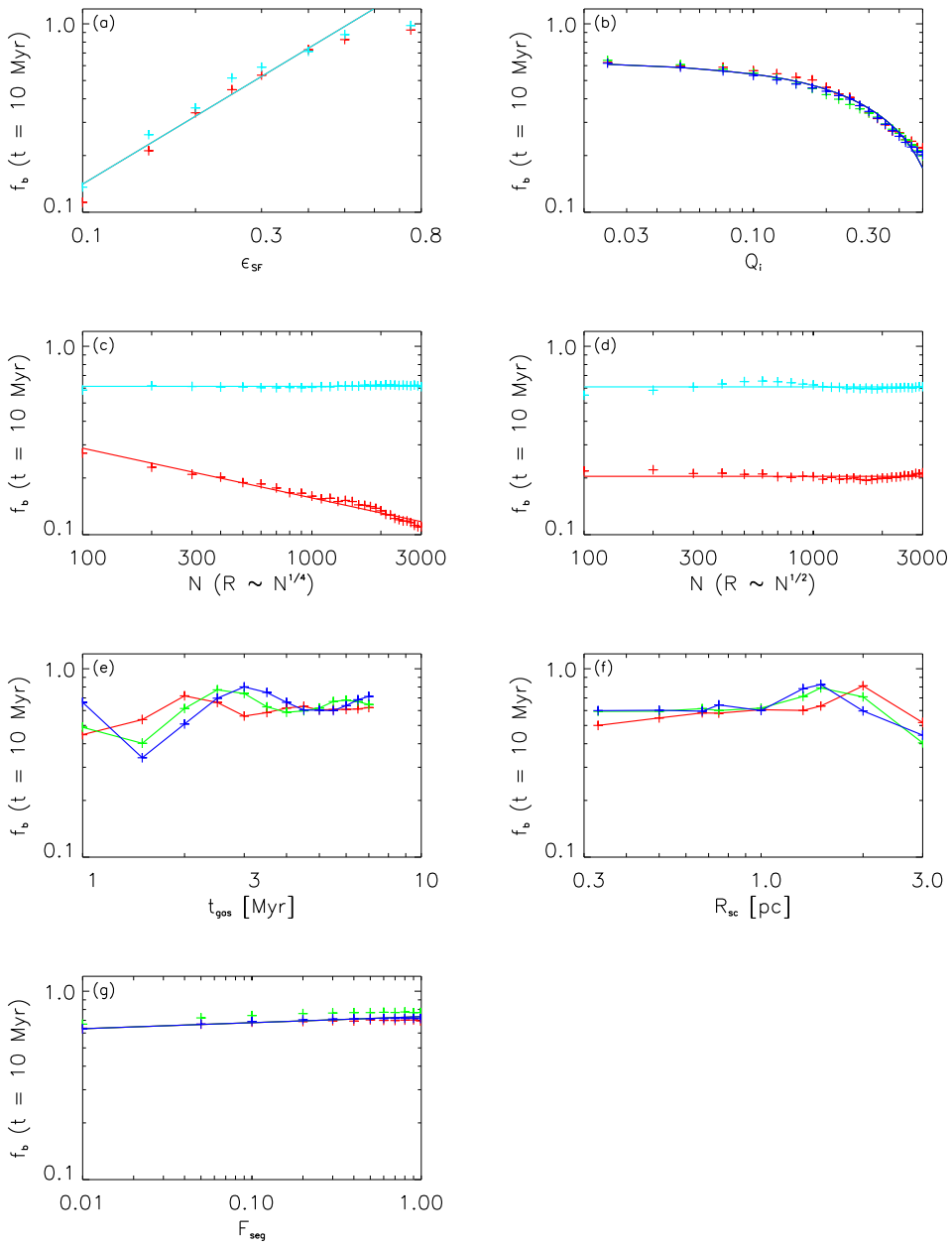

Figure 3.3: Cluster bound fraction f_b at $t = 10$ Myr plotted as a function of cluster initial conditions, for all clusters included in the parameter space survey. The best fit functions described in the text are also displayed when applicable. The cluster parameter varied in each panel is as follows: (a) Star formation efficiency ε_{SF}, (b) Initial virial ratio Q_i, (c) Stellar Membership N for scaling relationship $R_c \sim N^{1/2}$, (d) Stellar Membership N for scaling relationship $R_c \sim N^{1/4}$, (e) Gas removal time t_{gas}, (f) Cluster scaling radius R_{sc}, and (g) Amount of primordial mass segregation F_{seg}. Different colored curves indicate different initial conditions within each series of simulations. In panels (a), (b), and (g), $N = 300, 1000$, and 2000 are indicated by the red, green, and blue symbols, respectively, though there are no major differences between the clusters as a function of size. In panels (c) and (d), subvirial clusters are indicated by the blue (*upper*) curve while virial clusters are indicated by the red (*lower*) curve. In panels (e) and (f), $N = 300, 1000$, and 2000 are indicated by the red, green, and blue curves, respectively (*lower, middle, and upper curves* as measured on the left hand side of the panel).

Lada 2003, and references therein), and are difficult to attain theoretically (Matzner & McKee 2000). Our results thus corroborate previous studies indicating that a significant fraction of the stellar population is lost from a cluster during the gas removal phase.

As mentioned above, clusters with subvirial initial velocities are more tightly bound than clusters with virial initial conditions. Figure 3.3 panel (b) demonstrates this trend in initial virial ratio. The bound fraction is plotted as a function of the initial virial ratio. The bound fraction decreases almost linearly with the initial virial ratio, Q_i over the range considered, $0.01 \leq Q_i \leq 0.5$, and is reasonably fit by a line with slope ~ -1 (this fit is indicated by the curve in Figure 3.3 panel (b)). Gas removal has a weaker effect on spherical clusters with subvirial initial conditions because as a subvirial cluster collapses, the stars remain interior to the embedding gas (which is assumed to be static, i.e., not in a state of global collapse). Thus, when the embedding gas is removed from the cluster, many of the cluster members are interior to the gas and thus are affected by the change in the potential. The results from this suite of simulations again indicate that a significant fraction of cluster members are lost due to the change in the gravitational potential that occurs during the dispersal of the natal gas; In the most tightly bound subvirial clusters $Q_i = 0.025$ approximately 40% of stars become unbound due to dispersal of the embedding gas.

In clusters with subvirial initial conditions, the bound fraction remains constant as a function of cluster membership, N for both the $R_c \sim N^{1/2}$ and the $R_c \sim N^{1/4}$ cluster membership-radius scaling relations. This finding also holds true for virial clusters that have cluster membership-size relations similar to those observed in the solar neighborhood ($R_c \sim N^{1/2}$). The bound fraction at $t = 10$ Myr is plotted as a function of cluster size N in panels (c) and (d) of Figure 3.3. The upper lines in these panels indicate the bound fraction at 10 Myr in the more tightly bound subvirial clusters, whereas the lower lines

correspond to the virial clusters.

In virial clusters with a lower cluster membership-size power index ($R_c \sim N^{1/4}$), the bound fraction decreases as a function of the cluster membership N. The bound fraction decreases roughly as $f_b \sim N^{-1/4}$ (see Figure 3.3 panel (c), lower curve). This decrease in $f_b(N)$ is due to a combination of effects arising from the relationship between cluster radius and cluster membership defined by equation [3.1]. In clusters with $R_c \sim N^{1/4}$, mean velocity and velocity dispersion roughly scale as $\langle v \rangle \sim \sigma_v \sim \sqrt{GmN/R_c} \sim N^{3/8}$. The velocity distributions in the clusters are roughly Gaussian during the embedded phase (rather than perfectly Maxwellian as would be expected in a collisionless isothermal sphere of stars). Therefore, the increased velocity dispersion in clusters with larger N results in more stars with velocities high enough to escape from the cluster $v_{esc} \sim \sqrt{2GmN/R_c}$. In addition, the interaction rate between cluster members increases with the stellar density which increases as $n \sim N^{1/4}$ in these clusters. In virial clusters with $R_c \sim N^{1/2}$ (Figure 3.3 panel (d), lower curve), the bound fraction is roughly constant. This trend occurs because although the average velocity and velocity dispersions increase as a function of cluster membership, the dependence on N is not as strong: $\langle v \rangle \sim \sigma_v \sim N^{1/4}$. In addition, the stellar density actually decreases with N, $n \sim N^{-1/2}$, and the competing effects of increased velocities and lower interactions rates are comparable and act to cancel each other out.

The bound fraction does not appear to be simply related to either the gas removal timescale, t_{gas}, or the scaling radius, R_{sc}, (see Figure 3.3 panels (e) and (f)). This is because in subvirial clusters, such as the ones considered in these parameter space surveys, changing either the scaling radius or the gas removal time affects the relationship between the gas removal time and the initial collapse and relaxation time. The resulting f_b is sensitive to the particular dynamical state at the time of gas removal, e.g., if the cluster is

re-expanding after initial collapse when the gas is removed, most stars have trajectories that are directed radially outward and are thus more likely to become gravitationally unbound.

Next, we consider the effects of primordial mass segregation. In general, the effects of mass segregation saturate when more than approximately 20% of the stars are segregated by mass. Mass segregation only slightly affects the bound fraction, and clusters with minimal mass segregation (where the largest star is located at the cluster's center) have slightly lower bound fractions than clusters with $F_{seg} = 0.2$, as shown in panel (g) of Figure 3.3.

In summary, the results of this study indicate that while the star formation efficiency ε_{SF} is the parameter that most significantly affects the probability that a cluster will emerge from its natal cloud as a bound entity, the initial virial state of the cluster, as well as the specific dynamical state at the time of gas dispersal, are also important parameters which determine how tightly bound a cluster may remain. We find that in sufficiently subvirial clusters, $Q_i \lesssim 0.2$, the bound fraction is not a sensitive function of the initial stellar density (as indicated by the suite of simulations varying N and the cluster membership-radius relations), but rather is dominated by the fact that the initial global collapse produces a cluster whose members reside interior to the bulk of the embedding gas and thus are not strongly affected by the gas removal.

Two caveats should be included in this discussion. First, observations of young emerging clusters cannot determine whether a cluster member is gravitationally bound or unbound its host cluster. Over the first $\sim 10-20$ Myr, bound and unbound clusters are visibly similar and thus the results of simulations such as those presented here are not easily compared directly to observations. Secondly, this parameter space study focuses on the early evolution of embedded clusters. Additional dynamical evolution of the clusters (on timescales greater than $\sim$ 10 Myr will lead to lower bound fractions at later times. Therefore the bound

fractions presented in this work should be considered as upper limits on the total bound fraction in clusters with older ages.

3.3.2 Stellar Interaction Rates

A significant consequence of living in the higher density environments, such as those found in nearby young embedded clusters, is that close encounters with other cluster members may be relatively frequent. If these interactions are sufficiently close, they can have important ramifications for planet formation and solar system survival in circumstellar disk systems. During early stages of solar system formation, encounters may disrupt the protoplanetary disk and limit planet formation (Ostriker 1994; Heller 1993; 1995; Kobayashi & Ida 2001). At later times, close encounters may disrupt planetary systems, significantly altering the eccentricities of planets and, in sufficiently close encounters, ejecting planets from the solar system entirely (Adams & Laughlin 2001; Adams et al. 2006).

Throughout the cluster simulations, close encounters with impact parameters less than $b = 10,000$ AU are recorded. A cumulative distribution of close encounters is constructed, and an interaction rate Γ is calculated by averaging the encounter distributions over the time span of interest (the embedded phase $t = 0 - t_{gas}$, the exposed phase $t = t_{gas} - 10$ Myr, or the entire 10 Myr evolution). Specifically, the interaction rate is defined as the number of close encounters with impact parameter $r \leq b$ per star per million years. We find that the interaction rates have the form of power laws for encounters with closest approach distances less than ~ 3000 AU. These power laws may be presented as a function of closest approach distance, b

$$\Gamma = \Gamma_0 \left(\frac{b}{1000\mathrm{AU}} \right)^{\gamma}, \tag{3.6}$$

where the fiducial interaction rate Γ_0 and the power law index γ are fit to the cumulative closest approach distribution for each set of cluster simulations. The fiducial interaction rate Γ_0 corresponds to the number of encounters with impact parameter b less than 1000

AU per star per million years. The fiducial interaction rate Γ_0 is displayed as a function of cluster initial conditions in Figure 3.4.

For all of the parameter space considered in this study, the interaction rate Γ depends most sensitively on a single parameter, the stellar number density n. Specifically, the trends observed as a function of stellar membership N and cluster scaling radius R_{sc} (Figure 3.4 panels (a)-(c)) are actually trends in Γ_0 as a function of the average stellar density n.

We can understand this trend in simple terms as follows: Consider a cluster with N stars and radius R_c. For simplicity, we ignore the different between impact parameters and distance of closest approach b. A star passing through a cluster will experience on average

$$\delta n = \frac{2N}{{R_c}^2} b \delta b \tag{3.7}$$

close encounters with impact parameters within the range b to $b + db$ (Binney & Tremaine 1987). The crossing time in a cluster is given by $\tau_c \approx R_c/v$ where v is the average stellar velocity. Therefore the a star will experience on close encounters at the rate

$$\delta\Gamma \approx \frac{2N}{{R_c}^2} \left(\frac{v}{R_c}\right) b \ \delta b = 2nvb \ \delta b. \tag{3.8}$$

In Figure 3.4 panel (d) the Γ_0 values are plotted as a function of initial stellar density $n_0 = N/{R_c}^3$ for all of the simulations varying cluster membership N and scaling radius R_c (data from Figure 3.4 panels (a)-(c)). The plus symbols indicate the interaction rate Γ_0 for clusters with initially subvirial velocities and the interaction rates for clusters with initially virial velocities are indicated by x's. Lines indicating a power law index of 1 are included in the panel; and the numerically determined data is consistent with $\Gamma_0 \sim n_0$.

Using the simple argument constructed above, the total rate Γ_b of close encounters with impact parameter less than b in a cluster of membership size N is given by

$$\Gamma_b \approx \left(1.22 \times 10^{-1}\right) N^{-1/2} \left(\frac{b}{1000 \text{ AU}}\right)^2 \text{Myr}^{-1}, \qquad \text{for R}_\text{c} = 1.0 \text{ pc} \left(\frac{\text{N}}{300}\right)^{1/2}, \tag{3.9}$$

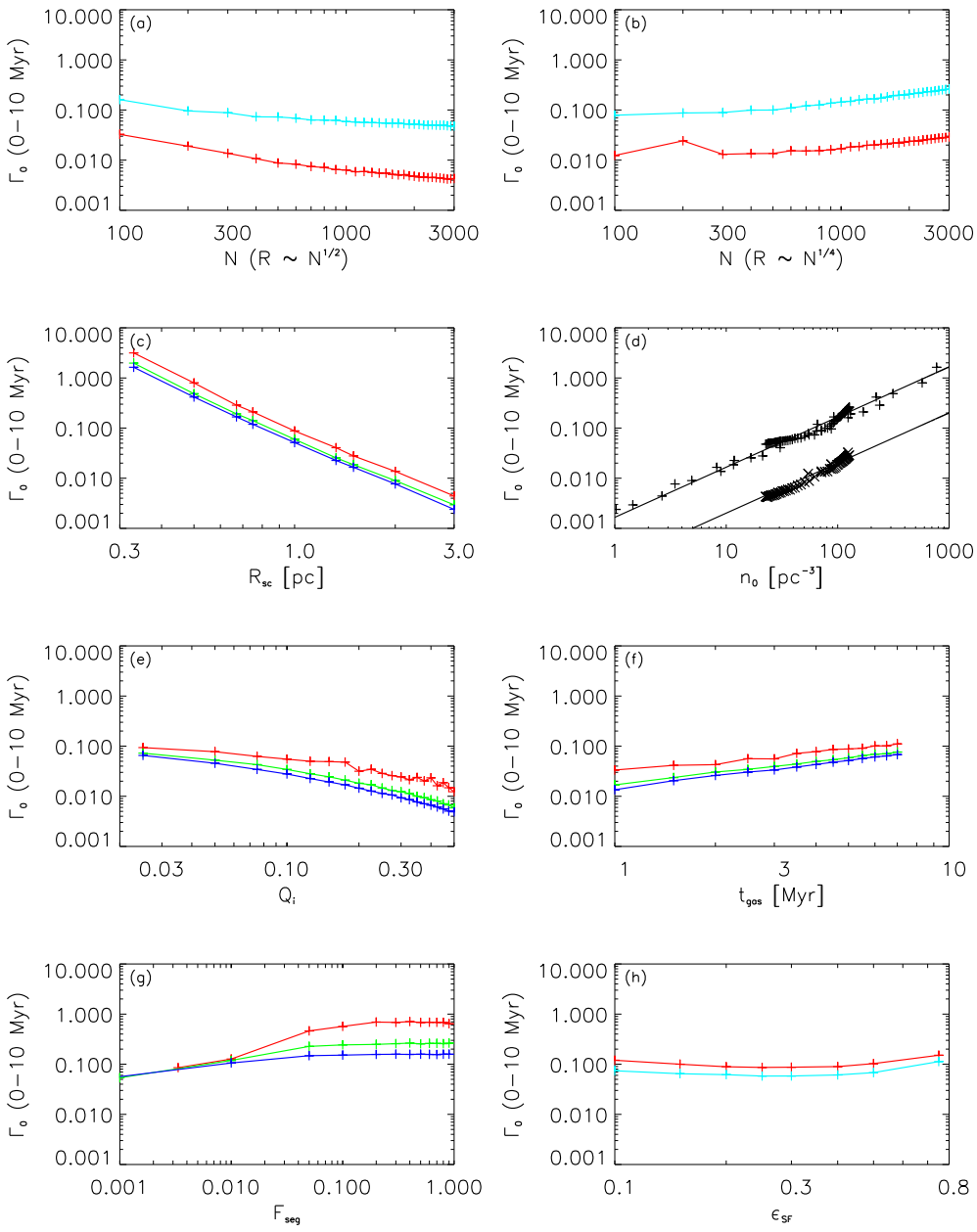

Figure 3.4: Fiducial interaction rate Γ_0 (in units of the number of interactions per star per Myr) is plotted as a function of initial cluster parameter, for all clusters included in the parameter space survey. The cluster parameter varied in each panel is as follows: (a) Stellar Membership N for scaling relationship $R_c \sim N^{1/2}$, (b) Stellar Membership N for scaling relationship $R_c \sim N^{1/4}$, (c) Cluster scaling radius R_{sc}, (d) Initial number density n_0 (for varying stellar memberships and cluster scaling radii), (e) Initial virial parameter Q_i, (f) Gas removal time t_{gas}, (g) Amount of primordial mass segregation F_{seg}, and (h) Star formation efficiency ε_{SF}. Panel (d) displays the combined data from panels (a) - (c) as a function of initial stellar number density n_0 and displays the trend $\Gamma_0 \sim n_0$ discussed in the text. In panels (a) and (b), subvirial clusters are indicated by the blue (*upper*) curve while virial clusters are indicated by the red (*lower*) curve. In panels (c), (e), (f), (g), and (h), $N = 300, 1000$, and 2000 are indicated by the red, green, and blue curves (*upper, middle, and lower curves*), respectively.

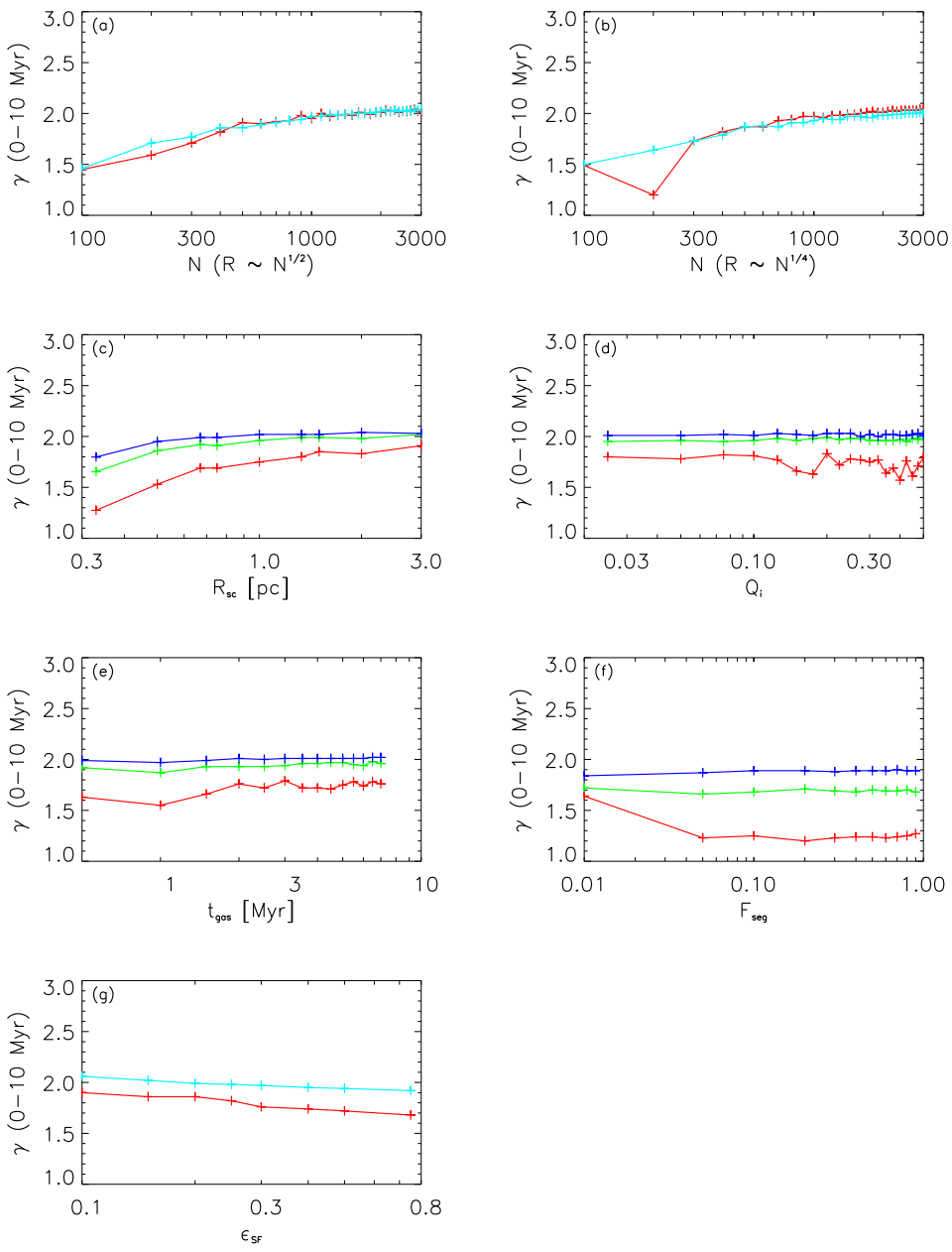

Figure 3.5: The power law index γ for the interaction rates is plotted as a function of initial cluster parameter, for all clusters included in the parameter space survey. The cluster parameter varied in each panel is as follows: (a) Stellar Membership N for scaling relationship $R_c \sim N^{1/2}$, (b) Stellar Membership N for scaling relationship $R_c \sim N^{1/4}$, (c) Cluster scaling radius R_{sc}, (d) Initial virial ratio Q_i, (e) Gas removal time t_{gas}, (f) Amount of primordial mass segregation F_{seg}, and (g) Star formation efficiency ε_{SF}. In panels (a) and (b), subvirial clusters are indicated by the blue (*upper*) curve while virial clusters are indicated by the red (*lower*) curve. In panels (c), (e), (f), (g), and (h), $N = 300, 1000$, and 2000 are indicated by the red, green, and blue curves (*lower, middle, and upper curves*), respectively.

$$\Gamma_b \approx \left(9.5 \times 10^{-3}\right) N^{1/4} \left(\frac{b}{1000 \text{ AU}}\right)^2 \text{Myr}^{-1}, \qquad \text{for R}_\text{c} = 1.0 \text{ pc} \left(\frac{\text{N}}{300}\right)^{1/4}. \tag{3.10}$$

These estimates are roughly similar to the interaction rates found in the virial clusters, however the fitted value of the index γ is slightly lower than 2 (due to gravitational focusing) in the numerically determined distributions (see Figure 3.5), and the fiducial interaction rate is somewhat higher.

The subvirial clusters have interaction rates that are roughly 8 times larger than the rates for virial clusters of the same density (as defined by $n_0 = N/{R_c}^3$). This is due to a combination of the smaller effective cluster radius that a subvirial cluster attains after initially collapsing and a higher bound fraction after gas dispersal. During the embedded phase, subvirial clusters ($Q_i = 0.04$) behave as if they have nearly zero temperature starting states and thus collapse to roughly $\sqrt{2}$ of their initial size. This decrease in radius corresponds to a $2\sqrt{2}$ increase in density. In addition, subvirial clusters retain more of their members after the gas is removed from the cluster ($f_{b,sub}/f_{b,vir} \sim 0.6/0.2 = 3$). Since the encounter profiles are averaged over the initial number of stars in the cluster the interaction rates in subvirial clusters will be roughly 3 times higher than in virial clusters over the exposed phase of cluster evolution (due to retention effects). Note that combining these two factors increases the interaction rates by $\sim 6\sqrt{2} \sim 8$. The results of the virial parameter survey also indicate that subvirial clusters have higher interaction rates. In Figure 3.4 panel (e) the interaction rate clearly decreases as a function of initial virial parameter Q_i.

In addition, interaction rates are higher in clusters that have more massive stars residing near the cluster's center (see Figure 3.4 panel (g)). This finding is consistent with the modeling results of NGC 1333 presented in Chapter II. The fiducial interaction rate Γ_0 in the simulated NGC 1333 cluster was approximately 5 times higher than the Γ_0 calculated in the subvirial clusters with minimal mass segregation. We suggested that the increased

interaction rate was due to the primordial mass segregation observed in NGC 1333 (see Figure 2.15). For comparison, subvirial clusters with $N = 300$ stars and $F_{seg} = 0.05$ have fiducial interaction rates that are roughly 5 times larger than those found in subvirial clusters with $N = 300$ members and minimal mass segregation (see Figure 3.4 panel (g), top curve).

The average interaction rate also increases as a function of gas removal time t_{gas} as shown in Figure 3.4 panel (f) (*solid curves*). This interaction rate is averaged over the 10 Myr simulation time. However the majority of close encounters occur during the embedded phase, and hence the average interaction rate increases as the length of the embedded phase increases. For clusters with embedded phases lasting more than ~ 2 Myr, the rate of close encounters during the embedded phase is roughly constant. Embedded phases lasting less than ~ 2 Myr have lower encounter rates due to lower densities during the first ~ 1 Myr while the subvirial cluster is still contracting.

For completeness we note that the interaction rate does not display strong trends with varying star-formation efficiency, ε_{SF} (see Figure 3.4 panel (h)).

3.3.3 Interaction Velocities

In addition to constructing the distribution of impact parameters associated with the close encounters in the simulated clusters, we also determine the distribution of encounter velocities. The distribution of encounter velocities provides additional information regarding the effect that close encounters may have on the constituent solar systems. For example, the interaction cross sections depend on the encounter speeds.

We define the encounter velocity v_{enc} as the magnitude of the relative velocities of the stars at the moment of closest approach, and create distributions of the frequency of encounter velocities throughout the simulation. Figure 3.6 presents the encounter velocity distribution in a cluster with radius $R_c = 1$ pc, $N = 300$ stars, and subvirial initial speeds

($Q_i = 0.04$). A binning size of 0.25 km s^{-1} has been used to construct the histogram, and error bars are included on the distribution to indicate the dispersion within each velocity bin.

We find that the encounter velocity distribution can be approximated reasonably well by a Gaussian curve where the mean μ and the width (as measured by the variance, σ^2) of the Gaussian are varied to fit the encounter velocity distribution for each particular set of initial conditions. The Gaussian fit to the velocity distribution in Figure 3.6 is indicated by the dashed line. We note that the Gaussian fit slightly overestimates the number of very low velocity encounters $v_{enc} < 1$ km s^{-1} (and predicts a few encounters with negative velocities). However, the general shape and width of the distribution is well represented by these fits.

In Figure 3.7, the mean encounter velocity $\langle v_{enc} \rangle$ is plotted as a function of initial cluster parameter. The encounter velocity has been normalized by the mean velocity within the cluster's half-mass radius (where most of the interactions occur within the cluster). The error bars indicate the normalized width (FWHM) of the Gaussian that best fits the velocity distribution. This figure demonstrates that the normalized encounter velocity distributions do not vary strongly as a function of the initial conditions, but are rather a robust function of mean cluster velocity.

The encounter velocities are roughly 2 times the average velocity in the interactive region of the cluster, a result which is roughly consistent with an analytical estimate of the relative velocities of cluster members whose velocities are sampled from a Maxwellian distribution, $\sqrt{v_{rel}^2} \sim \sqrt{2 \langle v^2 \rangle}$ (Binney & Tremaine 1987). The encounter velocities are somewhat larger than predicted by this estimate (~ 2 times the mean velocity) due in part to gravitational focusing. The numerically calculated distribution of interaction velocities includes only a subsample of the relative velocities, because only encounters with impact

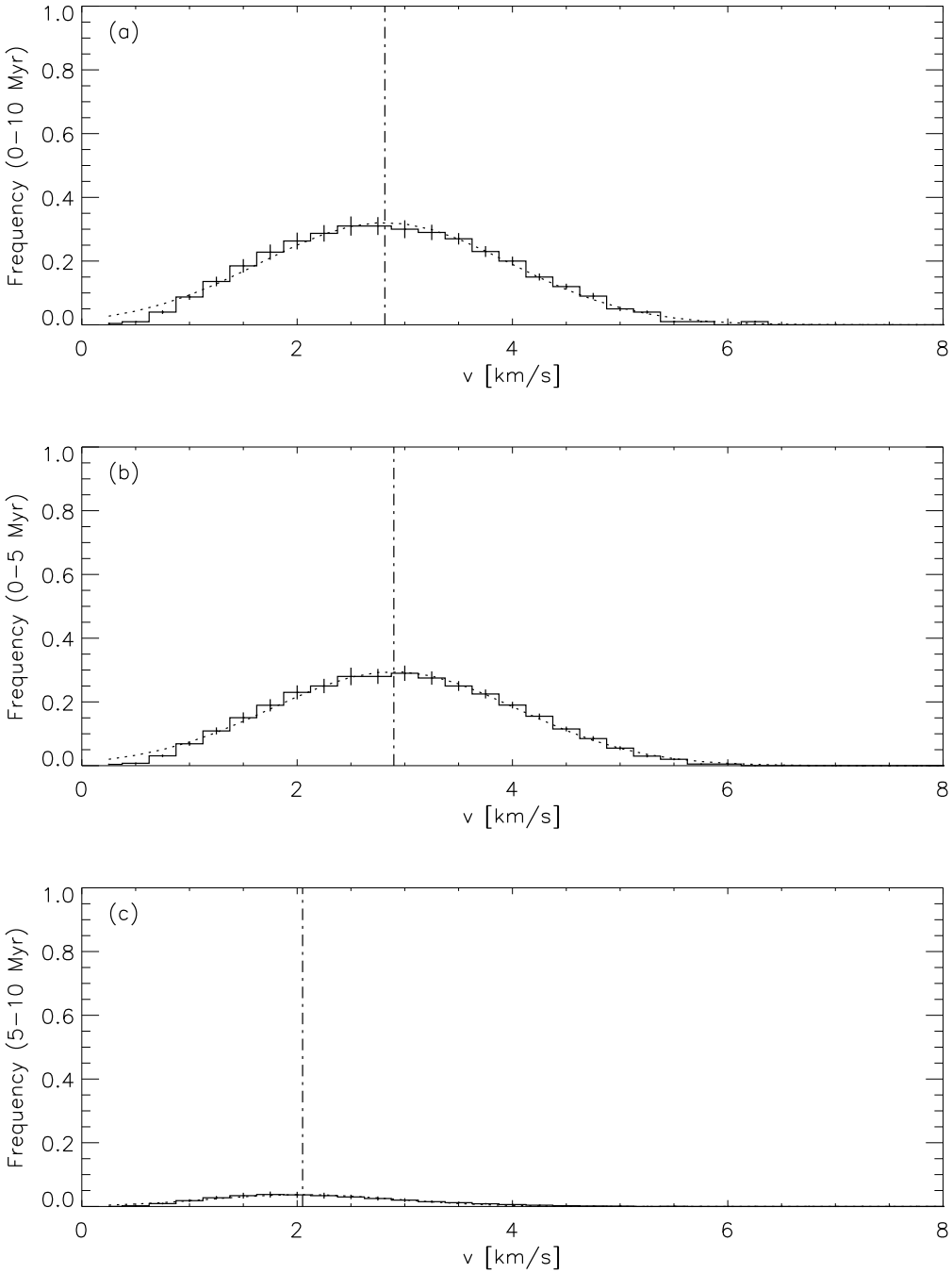

Figure 3.6: The distribution of interaction velocities in a subvirial cluster with $N = 300$, $R_c \sim N^{1/2}$ and $Q_i = 0.04$. The distribution averaged over $t = 0 - 10$ Myr is presented in panel (a). Panel (b) displays the time averaged distribution of interaction velocities during the embedded phase ($t = 0 - 5$ Myr) and panel (c) presents the distribution averaged over the remainder of the cluster evolution ($t = 5 - 10$ Myr). The histogram binning size is 0.25 km s^{-1}. Error bars correspond to the dispersion (variance) within each velocity bin. The best fit Gaussian curve is indicated by the dashed curve, and the mean of the Gaussian is indicated by the vertical dash-dot line.

parameter $b \lesssim 10,000$ AU are included in the interaction velocity distribution, and this subsample is likely to have larger relative velocities.

3.3.4 Radial and Mass Distributions

As a cluster evolves, interactions between stars and between the stars and the background gas potential produce a distribution of stellar positions and velocities. The distribution of stars within a cluster at a given time t can be characterized by the cumulative mass distribution $M(r,t)/M_{T*}$ or the cumulative number distributions $N(r,t)/N$ where the subscript M_{T*} and N are the total masses and numbers of the stars that are gravitationally bound to the cluster at time t, respectively. In the simulated clusters, each of these distributions is calculated at intervals of 0.25 Myr. The profiles are then averaged over the cluster lifetime and over 100 realizations of the cluster used to produce a statistical description of the mass and number profiles. We find that both of these distributions may be fit by simple functions of the form

$$\frac{M(r)}{M_{T*}} = \left(\frac{\xi^a}{1+\xi^a} \right)^p , \tag{3.11}$$

$$\frac{N(r)}{N} = \left(\frac{\xi^a}{1+\xi^a} \right)^p , \tag{3.12}$$

where $\xi = r/r_0$ and the scale radius r_0 and index p are free parameters that are fit to the distributions observed in the simulated clusters. The parameter a may also be varied to fit the data. We find that the choice $a = 2$ gives the best fit for the subvirial clusters and $a = 3$ gives the best fit for the initially virial clusters (this finding is consistent with the choice of index a in Chapter II). In the series of simulations in which the initial virial parameter Q_i is varied, $a = 2$ best fits simulations for which $Q_i < 0.25$, and $a = 3$ best fits those for which $Q_i \geq 0.25$. The parameters r_0 and p which provide the best fit for the radial distributions (equation [3.12]) and the mass profiles (equation [3.11]) are similar, though not identical due to the IMF assumed in the simulations.

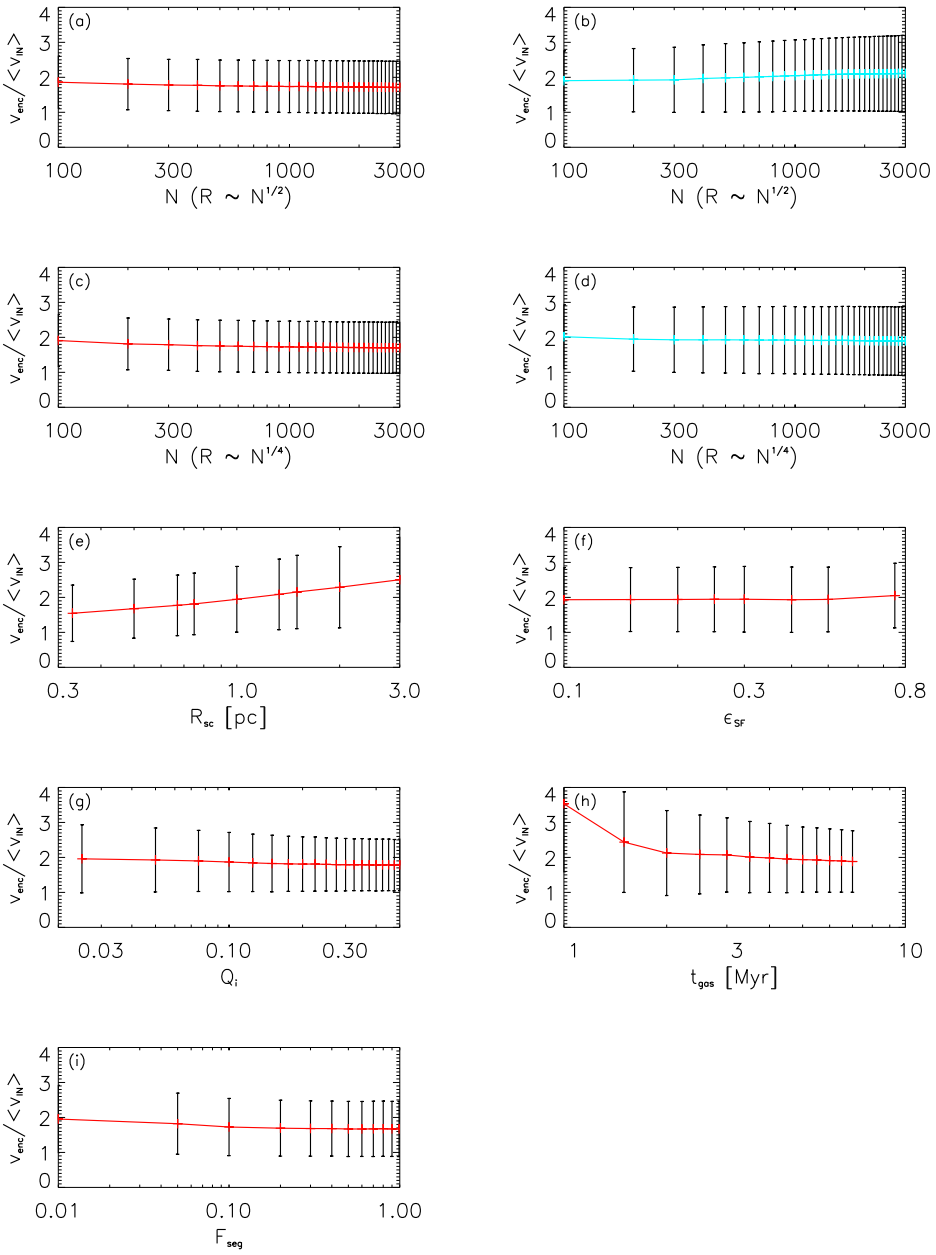

Figure 3.7: The parameters specifying the distribution of interaction velocities, specifically the mean μ and the FWHM of the distribution as a function of initial cluster parameter, for all clusters included in the parameter space survey. The mean interaction velocity, μ in km s^{-1} is indicated by the data points and the FWHM is noted by the size of the error bars. Velocities are scaled by the cluster mean velocity. The distribution parameters μ and FWHM are presented as a function of (a) Stellar membership N for virial clusters $Q_i = 0.5$ and $R_c \sim N^{1/2}$, (b) Stellar membership N for subvirial clusters $Q_i = 0.04$ and $R_c \sim N^{1/2}$, (b) Stellar membership N for virial clusters $Q_i = 0.5$ and $R_c \sim N^{1/4}$, (d) Stellar membership N for subvirial clusters $Q_i = 0.04$ and $R_c \sim N^{1/4}$, (e) Initial cluster scaling radius R_{sc}, (f) Star formation efficiency ε_{SF}, (g) Initial virial parameter Q_i, (h) Time of gas removal t_{gas}, and (i) Amount of primordial mass segregation F_{seg}.

The radial profiles of clusters provide insight into the general evolution of a cluster, and perhaps more importantly into the expected radiation fields that young solar systems in the cluster will experience. Circumstellar disks and forming solar systems residing in a cluster will be subjected to the FUV and EUV radiation fields produced by the cluster population, and these fields are dominated by the large stars in the cluster. If these radiation fields are strong enough, they are capable of photoevaporating circumstellar disks and preventing (or at least limiting) giant planet formation. The massive young stars producing the majority of the UV radiation are often located near the center of the cluster (see Chapter I Section 1.2, and references therein). Thus, an understanding of the EUV and FUV fields associated with young clusters combined with the average radial distributions of stars in young clusters provides the framework with which to predict how effectively cluster radiation can restrict planet formation. (Johnstone et al. 1998; Fatuzzo & Adams 2008; Adams et al. 2006).

Figure 3.8 presents the median cluster radius r_{med} calculated from the fit to the cumulative radial distributions for the entire set of parameter space. The scale r_{med} is defined as the radius at which $N(r)/N = 0.5$ and thus represents the radius which, on average, contains half of the cluster members. As is evident from Figure 3.8, the median cluster radius r_{med} scales with the initial virial parameter Q_i, the gas removal timescale t_{gas}, the cluster membership N, and the cluster scaling radius R_{sc}. On the other hand, r_{med} does not vary strongly with the either star formation efficiency ε_{SF} or the amount of primordial mass segregation F_{seg}.

Scaling the median radius r_{med} by the initial cluster radius R_c removes the dependency on this initial cluster parameter and more readily identifies trends that are distinct from the initial assumptions concerning cluster size. Figure 3.9 displays r_{med} normalized by the initial cluster radius R_c. It is clear in panel (a) of this figure that the median radius depends almost linearly on the initial virial parameter Q_i for $Q_i \leq 0.5$. This result is

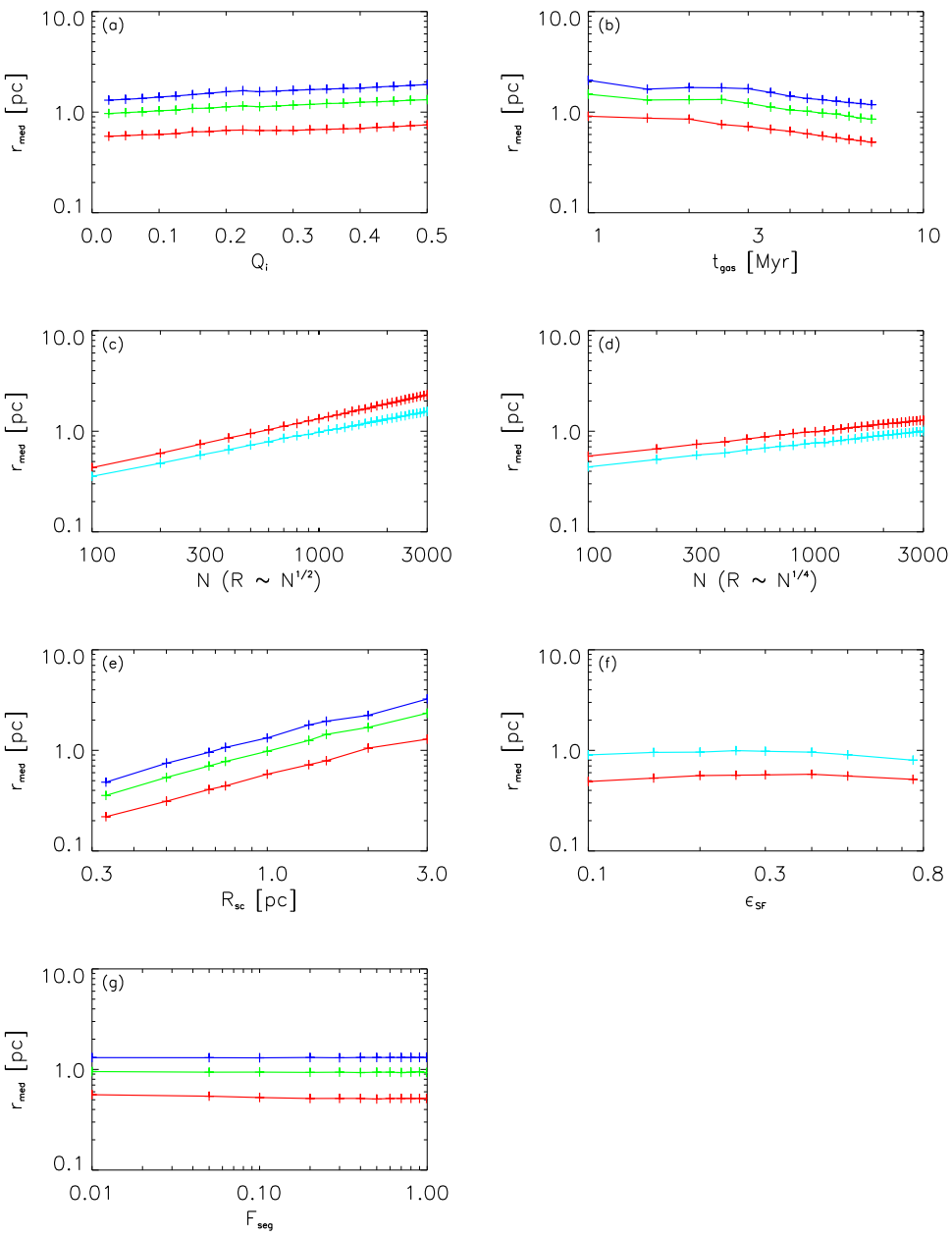

Figure 3.8: The median radius calculated from the radial profiles $N(r)/N$ as a function of initial cluster parameter, for all clusters included in the parameter space survey. The cluster parameter varied in each panel is as follows: (a) Initial virial ratio Q_i, (b) Gas removal time t_{gas}, (c) Stellar Membership N for scaling relationship $R_c \sim N^{1/2}$, (d) Stellar Membership N for scaling relationship $R_c \sim N^{1/4}$, (e) Cluster scaling radius R_{sc}, (f) Amount of primordial mass segregation F_{seg}, and (g) Star formation efficiency ε_{SF}. In panels (a), (b), (e), (f), and (g), $N = 300, 1000$, and 2000 are indicated by the red, green, and blue curves (*lower, middle, and upper curves*), respectively. In panels (c) and (d), subvirial clusters are indicated by the blue (*lower*) curve while virial clusters are indicated by the red (*upper*) curve.

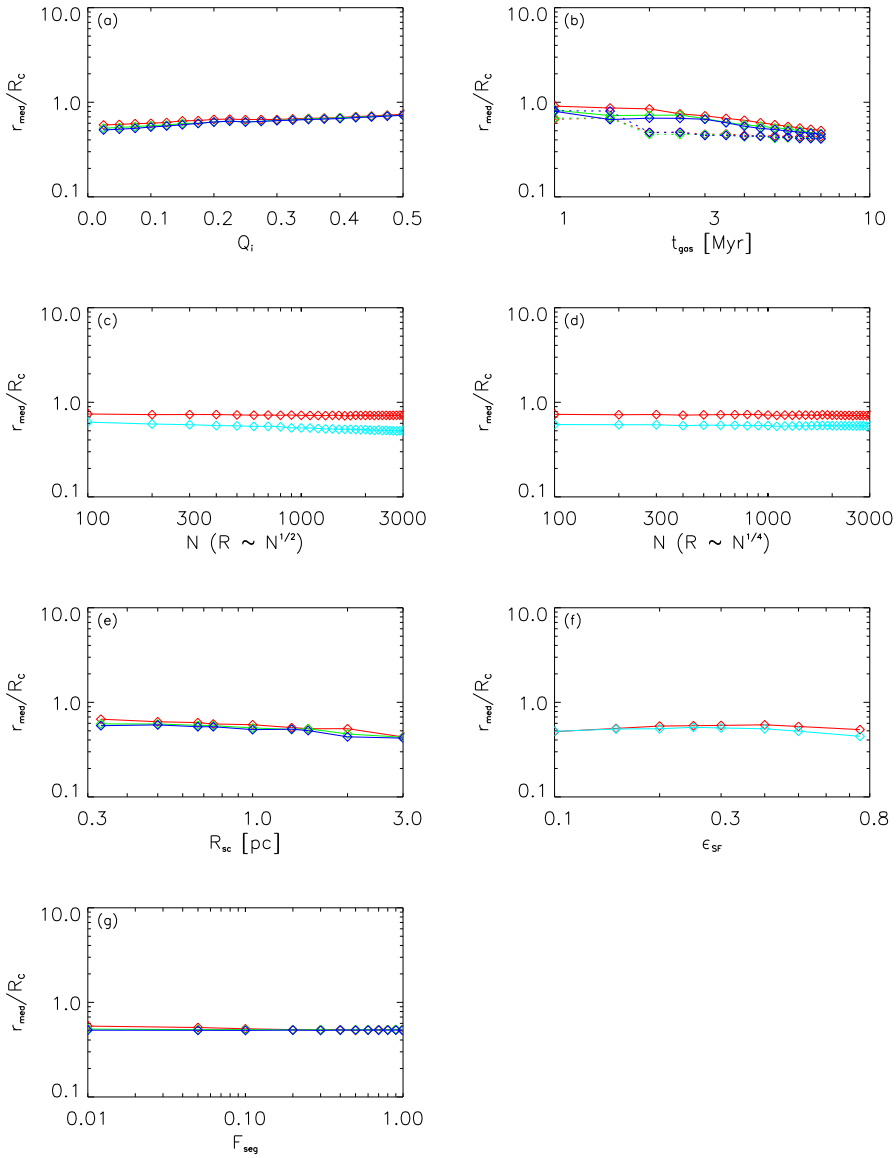

Figure 3.9: The median radius calculated from the radial profiles $N(r)/N$ normalized by the initial cluster radius R_c as a function of initial cluster parameter, for all clusters included in the parameter space survey. The cluster parameter varied in each panel is as follows: (a) Initial virial ratio Q_i, (b) Gas removal time t_{gas}, (c) Stellar Membership N for scaling relationship $R_c \sim N^{1/2}$, (d) Stellar Membership N for scaling relationship $R_c \sim N^{1/4}$, (e) Cluster scaling radius R_{sc}, (f) Amount of primordial mass segregation F_{seg}, and (g) Star formation efficiency ε_{SF}. In panels (a), (b), (e), (f), and (g), $N = 300, 1000$, and 2000 are indicated by the red, green, and blue curves (*lower, middle, and upper curves*), respectively, though there are no major differences between the clusters as a function of size. In panels (c) and (d), subvirial clusters are indicated by the blue (*lower*) curve while virial clusters are indicated by the red (*upper*) curve.

consistent with the initial collapse associated with the evolution of a cluster with subvirial velocities: the equilibrium radius scales linearly with the initial virial parameter. Clusters with completely subvirial starting states have median radii that are approximately $\sqrt{2}$ of the median radii of virial clusters.

The median radius also decreases as a function of the gas removal time t_{gas}. The data points connected by a solid line in Figure 3.9 panel (b) correspond to the time averaged $(0-10$ Myr) normalized median radius r_{med} of clusters with differing values of t_{gas}. During the embedded phase, these (initially subvirial) clusters remain bound and do not expand. As a result, clusters that become unbound early in their history have larger median radii simply due to time averaging (over the 10 Myr simulation). The data points connected by the dotted curve correspond to the normalized median radius averaged over the embedded stage of the cluster evolution $(0 - t_{gas}$ Myr). Removing the apparent dependence on t_{gas} that is actually due to the time averaging, we find that in clusters with dispersal times greater than ~ 2 Myr, the cluster median radius does not depend on t_{gas}.

However, clusters with early gas dispersal times ($t_{gas} \lesssim 2$ Myr) have much larger median radii than clusters with later gas dispersal times. The average crossing time in a subvirial cluster is roughly 1 Myr, and thus gas removal within the first couple of crossing times prevents the cluster from approaching a state of virial equilibrium. This behavior is also why the bound fractions in clusters with $t_{gas} \lesssim 2$ Myr are very low (see Figure 3.3 panel (e) and the discussion in Section 3.3.1). In other words, the process of gas dispersal in a cluster that is not in virial equilibrium is much more destructive to the cluster than if it were to occur after a cluster has approached a state of equilibrium (Goodwin & Bastian 2006).

Panel (c) in Figure 3.9 displays the normalized median cluster radius as a function of the initial scaling radius R_{sc} used in equation [3.1]. The normalization of the median

cluster radius includes the intrinsic dependence on R_{sc}, and so the trend observed in the normalized median radius r_{med}/R_c must be accounted for by another mechanism. The larger normalized median radius observed in clusters with smaller initial values of R_{sc} can be understood in light of the higher interaction rates observed in these clusters which keep the cluster cores slightly inflated. This trend should be observed to some extent in any clusters with high interaction rates, but is easiest to observe in the R_{sc} series of simulations because the interaction rates have the widest dynamical range, varying by three orders of magnitude (see Figure 3.4).

3.4 Conclusion

In this chapter we have presented the results of a parameter space survey of dynamics in young cluster environments. Our choice of parameter space was motivated by recent catalogs and surveys of young star-forming regions in the solar neighborhood. We consider clusters with a range of memberships N, a variety parameters values R_{sc} and α defining the cluster membership-radius relation (equation [3.1]), a range of gas removal timescales t_{gas}, initial virial states Q_i, star formation efficiencies ε_{SF}, and amounts of primordial mass segregation F_{seg}. The range of parameter space surveyed is summarized in Table 3.1.

We have identified how evolutionary parameters of interest vary as a function of the initial cluster environment. Specifically, in Section 3.3.1 we considered the cluster's bound fraction at $t = 10$ Myr, f_b. The bound fraction varies most sensitively as a function of the star formation efficiency, ε_{SF}, but also depends quite strongly on the initial virial state of the cluster. Stars that are formed with subvirial velocities have a higher probability of remaining bound to a cluster than those that have initially virialized velocities.

In Sections 3.3.2 and 3.3.3 we considered the distributions of close encounters between cluster members over the course of the cluster's evolution. We find that the encounter rates scale as the average stellar density, $\Gamma \sim n$, and that the interaction rates increase as the

initial virial parameter decreases. Subvirial clusters have interaction rates that are roughly 8 times higher than those found in clusters that star in a virialized state. We also show that the interaction rates are higher in clusters which have larger amounts of primordial mass segregation. In addition, the distributions of interaction velocities are nearly Gaussian (see Figure 3.7). The interaction velocities do not themselves vary as a function the initial conditions in the cluster. Rather the interaction velocities are approximately 2 times the average stellar velocity within the cluster.

Finally, in Section 3.3.4 we present the results of the empirical fits to the cluster radial profiles. We find that in general, the median cluster radius r_{med} scales as the initial cluster radius R_c. However, in some clusters, the interactions between stellar members break the $r_{med} \sim R_c$ relationship. Specifically, clusters which are initially subvirial have smaller median radii than those which are initially in virial equilibrium. In addition, if the embedding gas is removed from a subvirial cluster early in the cluster's evolution ($t_{gas} \lesssim 2$ Myr), the median cluster radius are much larger than it would be if the gas removal occurred at a later time. This difference occurs because the cluster is not in virial equilibrium at the time of gas removal. As a result, gas dispersal is more destructive in a cluster that has not yet approached virial equilibrium.

We note that these general trends in the output parameters (i.e., that the interaction rate $\Gamma \propto n$) are not unexpected. However, this work puts these (perhaps expected) results on a firm, statistically significant footing. In addition, we find quantitative results, well beyond the expected qualitative scaling behavior.

This chapter presents a database of cluster evolution parameters as a function of cluster initial conditions. Our future work will include combining this database with calculations of the radiation fields in young clusters and cross sections for planetary system disruption, as was done in Chapter II. We plan to produce disk truncation radii (due to FUV and EUV

radiation, and close encounters between cluster members) and planetary ejection rates as a function of cluster environmental conditions. These combined results will provide a more complete statistical description of cluster evolution and the impact of clustered environment on planet formation.

CHAPTER IV

Kinematic Signatures of Subvirial Initial Conditions in Young Clusters

4.1 Introduction

Most stars are thought to form within clusters of some type (e.g., Lada & Lada 2003; Porras et al. 2003), although a great deal of controversy remains concerning the distribution of cluster properties. Nonetheless, given that stars form in clusters, two overarching questions immediately arise. The first considers the clusters as astrophysical objects: [1] how can molecular clouds produce aggregates of $N > 100$ stars with centrally concentrated surface density, with the massive stars near the center, and with a stellar mass distribution that follows the IMF, all within a few pc and within a few Myr? A second vital question then becomes: [2] if stars form in clusters, how does the cluster environment affect star formation and the accompanying process of planet formation? A complete understanding of star and planet formation requires detailed answers to both questions. However, this chapter will focus on one specific issue within this larger context. Observed young embedded stellar clusters display departures from both spherical symmetry and initial virial equilibrium, and this chapter will explore the effects of these complications on the kinematics of cluster members through N-body simulations. These results, in turn, will help provide a contribution to the overarching questions posed above.

Departures from spherical symmetry in star-forming regions have long been known, but

have been little studied. On the scale of cluster themselves (with radii of a few pc, and masses of $100 - 3000$ $M_\odot$), for example, some systems are categorized as irregular (Lada & Lada 2003), or filamentary (Walsh et al. 2004), or otherwise described as nonspherical (Allen et al. 2007). Furthermore, the star formation efficiencies are low, so that the gravitational potential in these systems is dominated by the mass of the gas (at least in the early phases of evolution, before gas expulsion). As a result, the gas potential must be generalized to include the observed departures from spherical symmetry (see Adams et al. 2007 and Section 4.2). For completeness, we also note that on the smaller scale of cores (or clumps or kernels) that represent individual star formation events, the precollapse gas is observed to be nonspherical, with typical aspect ratios of $2 : 1$ (e.g., Myers et al. 1991; Ryden 1996).

Observations are starting to show that clusters begin their evolution with subvirial initial conditions, and hence this complication must be included in our simulated clusters. In many regions, prestellar clumps are observed to move subsonically before the clumps form stars (Peretto et al. 2006; Walsh et al. 2004; André 2002; Kirk et al. 2007), implying that newly formed stars begin their dynamical evolution with subvirial speeds. Motivated by such observations, our work considers clusters that are seeded with subvirial stellar velocities. As such, our N-body simulations (see Section 4.2) differ from those of many preceding studies (though not all, see Bonnell & Davies 1998; Adams et al. 2006) that assume the initial phase-space variables of the stars are close to virial equilibrium. Subvirial initial conditions can have a significant impact on the early cluster evolution (Adams et al. 2006), and are thus considered herein.

The theoretical work presented here provides a determination of the kinematic signature of young embedded clusters with both subvirial starting conditions and nonspherical gas potentials. Fortunately, astronomical observations are now becoming available to compare

with these theoretical calculations. In this chapter, we focus on clusters of moderately large size, with stellar membership $N \sim 10^3$, appropriate for the Orion Nebula Cluster (ONC). Clusters of this size are large enough for interesting kinematic signatures to arise in observations, and small enough that many such clusters are expected within the galactic cluster population. In addition, the ONC is an example of a nonspherical cluster as the stellar population is elongated north to south along the filament of dense molecular gas in the region (Hillenbrand & Hartmann 1998). Recent observations in the ONC (Fűrész et al. 2008; Tobin et al. 2009, TO9 hereafter) display a gradient in the radial velocity structure along the length of the cluster, much like that expected for the elongated subvirial clusters considered herein.

This chapter is organized as follows. In Section 4.2, we outline the theoretical approach used in this chapter. Specifically, we describe the N-body codes, the required number of realizations of the numerical experiments, the implementation of subvirial starting speeds, the inclusion of axisymmetric and triaxial gas distributions, as well as the specification of simulation parameters. We then present the theoretical results of our simulations in Section 4.3, with a focus on the velocity signatures produced by the departures from equilibrium and spherical symmetry. In Section 4.4, we compare our results to observations, primarily the kinematic velocity measurements recently carried out in the ONC. We find good qualitative agreement, and reasonable quantitative agreement, and suggest that the observed kinematic signature requires subvirial starting conditions, nonspherical potentials, and viewing angles that do not coincide with the principal axes of the systems. These conclusions and other results are summarized in Section 4.5, along with a discussion of their implications.

4.2 Methods

N-body simulation techniques are used to calculate the dynamics of young stellar clusters during the embedded star-forming epoch. We consider clusters with nonspherical geometries and subvirial initial velocities and study the observed kinematics of these clusters. In this section, we discuss the N-body code used, the simulation parameters chosen, and the experiments performed to identify and characterize kinematic signature in nonspherical clusters with subvirial initial conditions.

4.2.1 N-Body Simulation Techniques

The dynamical evolution of a young embedded cluster depends on its initial stellar distribution, the distribution and removal mechanism of the embedding gas, the star formation history, and is especially sensitive to the initial velocity distribution (e.g., Adams et al. 2006). In this chapter, we complete a suite of N-body simulations of young embedded clusters to understand how the cluster's initial spatial and velocity distribution imprints itself on the evolved cluster's kinematic structure. The NBODY2 direct integration code developed by Aarseth (2001) is used as a starting point to calculate the cluster's dynamics from the star-forming epoch out to ages of 10 Myr. As outlined below, we modify the code to include specific stellar and gas distributions and star formation epochs that are similar to those observed in young embedded clusters.

Distributions of stellar positions and velocities are required to characterize kinematic signatures in these young clusters. We find that ~ 50 equivalent realizations of each set of cluster initial conditions are required to provide statistically robust distributions of stellar positions and radial velocities. This study focuses on the kinematic signatures produced by two different contributions to the initial conditions commonly present in young embedded clusters: asphericity (combined with effects due to projection of a three-dimensional cluster onto the two-dimensional sky), and subvirial initial velocities. In addition, we consider the

effect of extinction on the observed kinematic structure of young clusters.

Cluster evolution is numerically integrated from the star formation epoch ($0 - 1$ Myr) through the gas removal phase (at $t = 5$ Myr) out to ages of 10 Myr (see Section 4.2.2 for further detail). After 50 realizations of each set of initial conditions are completed, the results are combined to produce distributions of stellar positions and velocities. The simulations provide three-dimensional position and velocity information for each stellar member at intervals of 0.1 Myr. These six phase-space coordinates are reduced to two position coordinates in the plane of the sky and two velocity components, one along the line-of-sight (radial velocity) and one in the plane of the sky (transverse velocity). For the sake of definiteness, the $\hat{z}'$-projected axis is defined by the projection of the three-dimensional $\hat{z}$-axis (the major axis in elongated clusters) onto the plane perpendicular to the line-of-sight. The terms "north" and "south" with reference to projections of simulated clusters correspond to positive and negative $\hat{z}'$ values, respectively. This nomenclature is arbitrary and has been chosen to coincide with that of the ONC, which is elongated north to south and displays north-south asymmetry in the radial velocity structure (see Section 4.4).

4.2.2 Simulation Parameters

Cluster Membership, N. We consider moderately large young clusters comparable in size to the Orion star-forming region. Specifically, our simulated clusters contain $N = 2000$ or 2700 stars. Estimates of the stellar population of the ONC vary depending on the cluster radius adopted, and our choices of N roughly reflect the range of this variation (e.g., Hillenbrand & Hartmann (1998) advocate $N = 2300$, near the center of this range). We found that there were no significant differences in the kinematic signature observed in clusters of 2000 and 2700 stars. Another motivation for our choice of cluster size is that clusters of this size have large enough memberships that kinematic signatures may be

identified in the data from observed clusters and compared to the results presented in this study.

The stellar masses are sampled from the log-normal analytic fit presented by Adams & Fatuzzo (1996) to the standard IMF of Miller & Scalo (1979). The masses range from 0.07 to 10 $M_{\odot}$. A limited number of simulations with equal stellar masses were completed and we found that the kinematic signature discussed herein was present in both the single stellar mass clusters and those with a more realistic stellar mass distribution.

Stellar Distribution. One goal of this study is to compare kinematical signatures of clusters with spherical geometries to those of elongated clusters. Spherical clusters have centrally concentrated stellar distributions described by an $\rho_* \sim r^{-1}$ density profile. Two elongated stellar distributions are considered: uniform density prolate spheroids and centrally concentrated clusters with $\rho_* \sim m^{-1}$, where $m^2 = x^2/a^2 + y^2/b^2 + z^2/c^2$ is the triaxial coordinate. We compare elongated clusters with different aspect ratios to characterize the effect of cluster elongation on the observed kinematic signature. Table 4.1 summarizes the initial stellar density distributions used in the cluster simulations.

Initial Speeds. Initial stellar velocities are sampled from a uniform distribution within a unit sphere, producing an isotropic and position-independent velocity distribution. The velocities are then scaled to produce a cluster in a particular virial state, defined by the virial ratio $Q \equiv |K/W|$, where K is the total kinetic energy of the cluster and W is the total virial potential energy of the cluster. A cluster in virial equilibrium is defined to have $Q = 0.5$. Simulations of clusters with virialized initial velocities are compared to clusters with subvirial initial velocities. The subvirial clusters are chosen to have $Q_i = 0.04$ or 0.15, which corresponds to initial velocities that are approximately one-third or one-half of the virial velocity, respectively.

Star Formation History. The simulated clusters have a star formation epoch that lasts

for the first $\Delta t = 1$ Myr of the cluster's evolution. During simulation initialization each star, regardless of mass or initial position within the cluster, is assigned a random formation time between 0 and 1 Myr (with a uniform distribution, independent of stellar mass, over this interval). A star is then tied to its formation site (chosen as described above) until its collapse phase of star formation is complete. That is, the stars are initially included in the simulation as point masses, but are held at a fixed position until their formation time. After that time, the star becomes free to move through the total gravitational potential of the cluster with an initial velocity sampled from the distribution described above. As a result, the stars do not execute ballistic orbits until after they have formed. For completeness, we note that stellar evolution is not included in these simulations.

We vary the star formation efficiency (SFE) from 17% to 50%, which spans the range of mass estimates of the gas in the region of the ONC. It is important to note that although the evolution of a cluster subsequent to gas removal depends strongly on the SFE, its evolution prior to gas removal is more sensitive to the initial virial ratio than it is to the SFE alone. In other words, provided that the stars are moving with sufficient velocities to account for the additional potential due to excess gas (i.e., their virial ratios are comparable), the evolution of a cluster with an SFE of 33% or 50% will be qualitatively similar during the embedded stage. Increasing the SFE will, however, decrease the average virial velocity. After gas is removed from the cluster, the subsequent dynamical evolution does depend on the SFE. Of course, increasing the SFE will increase the rate of close encounters, but this effect on global cluster evoltuion is modest on the (short) timescales of interest here (Adams et al. 2006).

Embedding Gas Distributions. We assume that the distributions of stars in a cluster roughly traces the geometry and density of the embedding gas. Thus, a spherical centrally concentrated Hernquist profile (Hernquist 1990) is chosen to represent the embedding gas

in a spherical cluster (see Adams et al. 2006).

Likewise, the elongated stellar distributions are embedded in elongated gas potentials. Specifically, the uniform density stellar distributions are embedded in a uniform density gas distribution that is twice the extent of the stellar distribution. The homoeoid theorem states that the net force on a particle within a uniform density homoeoid shell is zero. Thus the larger gas distribution allows for a simpler computation of the force and potential terms due to the embedding gas without changing the dynamics of the system (Binney & Tremaine 1987).

The centrally concentrated prolate clusters are embedded in a static gas potential of the form $\rho \sim m^{-1}$, where m is the generalized coordinate. Calculation of the force terms, analytic expressions for the potential, and a discussion of orbits and orbit instabilities within this triaxial potential were presented in Adams et al. (2007). The gas distributions and associated parameters are summarized in Table 4.2.

Observations indicate that embedding gas does not remain in young clusters for a long time. After a few million years, winds from hot young stars begin to carve out the embedding gas and very few embedded clusters are found with ages greater than ~ 5 Myr. Our simulations account for gas removal as a temporal step function in the evolution of the static gas potential: at $t = 5$ Myr, the gas potential is completely removed from the cluster which then continues to evolve due to interactions between the stars. After gas removal, the cluster expands and a significant fraction of the members become gravitationally unbound.

4.2.3 Numerical Experiments

In this section we discuss the specific parameters that were varied to study the effects of particular initial conditions on the kinematic structure observed in the clusters. A more detailed discussion of each experiment's initial set-up and result is reserved until Section 4.3.

Table 4.1: Stellar Distributions

Description	Density Profile			Parameters
Spherical	$\rho(\xi)$	$= \begin{cases} \rho_0/\xi, & 0 < \xi \leq 1 \\ 0, & \xi > 1 \end{cases}$		$\xi = r/r_0$
Uniform Spheroid	$\rho(m)$	$= \begin{cases} \rho_0, & 0 \leq m \leq 1 \\ 0, & m > 1 \end{cases}$		$m^2 = (x/a)^2 + (y/b)^2 + (z/c)^2$ $a = b < c$
$1/m$ Spheroid	$\rho(m)$	$= \begin{cases} \rho_0/m, & 0 < m \leq 1 \\ 0, & m > 1 \end{cases}$		$m^2 = (x/a)^2 + (y/b)^2 + (z/c)^2$ $a = b < c$

Table 4.2: Embedding Gas Distributions

Description	Density Profile			Parameters
Spherical	$\rho(\xi)$	$= \rho_0/\xi(1+\xi)^3,$	$0 < \xi$	$\xi = r/r_0$
Uniform Spheroid	$\rho(m)$	$= \begin{cases} \rho_0, & 0 \leq m \leq 2 \\ 0, & m > 2 \end{cases}$		$m^2 = (x/a)^2 + (y/b)^2 + (z/c)^2$ $a = b < c$
$1/m$ Spheroid	$\rho(m)$	$= \rho_0/m,$	$0 < m$	$m^2 = (x/a)^2 + (y/b)^2 + (z/c)^2$ $a = b < c$

Cluster Geometry and Virial Ratio. We compare the evolution of clusters under various assumptions of initial geometry and virial balance. Specifically, we compare centrally concentrated ($\rho_* \sim r^{-1}$) spherical clusters with subvirial ($Q_i = 0.04$) and virial ($Q_i = 0.5$) initial velocities to uniform density elongated clusters with similarly subvirial and virial velocities. The spherical clusters are 2 pc in radius, and the elongated clusters have axis parameters $a = b = 2$ pc and $c = 4$ pc. Each of these clusters had stellar membership $N = 2000$ and an SFE of 50%. We find that only clusters with subvirial initial velocities *and* elongated geometries produce significant gradients in the radial velocity along the length of the cluster. The observed radial velocity gradients are thus a combined effect of global collapse and the projection of a nonspherical cluster. Hereafter, the term 'kinematic signature' refers to this radial velocity gradient. This kinematic signature is discussed in detail in Section 4.3.1.

With the requirements of subvirial velocities and elongated stellar/gas distributions identified as prerequisites for the kinematic signature, we proceed to complete a series of

numerical experiments to determine how changing cluster parameters in subvirial elongated clusters changes the observed structure of the signature.

Initial Virial Ratio. To characterize the effect of subvirial velocities on the kinematic signature, the evolution of centrally concentrated elongated clusters with initial virial ratio Q_i ranging from 0.04 to 0.15 is compared. These virial ratios correspond to average initial velocities that are roughly one-third to one-half of the virial velocity and are comparable to pre-stellar clump velocities observed many star-forming regions including NGC 2264 (Peretto et al. 2006) and Perseus (Kirk et al. 2007).

Cluster Elongation. The effect of cluster elongation on the evolved velocity structure of the cluster is studied by comparing subvirial clusters that range from spherical to elongated with aspect ratios ranging from 1 to 4. Recent results from the *Spitzer* Young Cluster Survey indicate this range of aspect ratios is appropriate, as the clusters in the survey had aspect ratios between 0.53 and 3.88 (Gutermuth et al. 2009, in preparation).

Initial Density Distribution. Another experiment compares subvirial elongated clusters with uniform density distributions to those with $\rho_* \sim m^{-1}$ to study the effect of the density distribution on the strength of and evolution of the kinematic signature.

Star Formation Efficiency. To determine the effect of SFE on the kinematic signatures observed in the cluster, we compare subvirial elongated clusters with efficiencies ranging from 17% to 50%.

4.3 Simulation Results

4.3.1 Radial Velocity Structure Due to Global Collapse and Elongation

We find that radial velocity gradients along the length of the clusters are produced by a combination of two effects: [1] projection of an elongated or nonspherical cluster, and [2] subvirial initial velocities. The separation of these two effects is nontrivial, as discussed below.

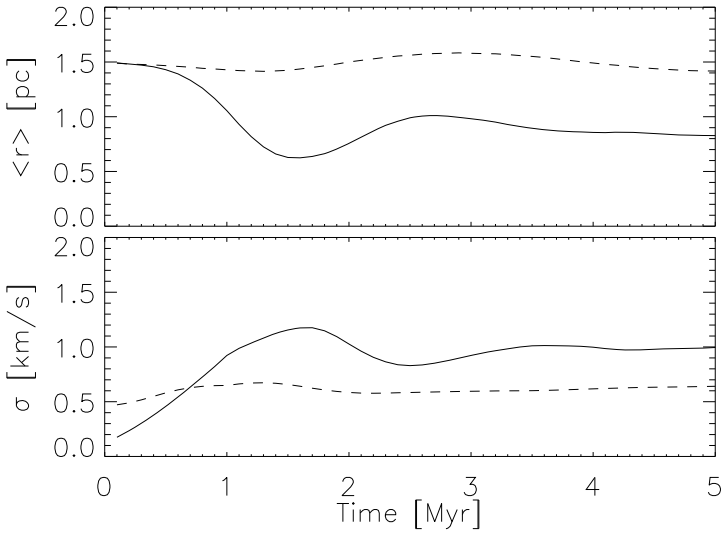

Figure 4.1: Evolution of the mean radius and velocity dispersion in spherical clusters with virial and subvirial initial velocities. The top panel displays the evolution of the mean radius of a spherical cluster with virial (*dashed curve*) and subvirial (*solid curve*) initial velocities. The bottom panel displays the evolution of the velocity dispersion of a spherical cluster with virial (*dashed curve*) and subvirial (*solid curve*) initial velocities.

A cluster that is initially subvirial will collapse as stars in the outer parts of the cluster fall toward the cluster's center of mass. This collapse takes place because cluster members that are seeded with subvirial velocities are not moving fast enough to remain in orbit (at their starting radial positions) around the cluster's center. Instead they fall through the gravitational potential, gain kinetic and potential energy, and eventually reach an equilibrium state in which the virial theorem is satisfied. Thus, during the first crossing time, a subvirial cluster will collapse significantly as the stellar velocities increase. Figure 4.1 compares the mean cluster radius and velocity dispersion as a function of time for spherical clusters with both virial and subvirial initial conditions. The overall cluster collapse and velocity enhancement in subvirial clusters are clearly demonstrated by these plots.

During the initial collapse phase, the velocity vectors of the cluster members are preferentially directed toward the center of mass until the stars pass close to the cluster's center and continue on (mostly) radial trajectories outward. During this first crossing time, some

close encounters may cause the individual stellar motions to deviate from this general pattern. As shown in Adams et al. (2006), however, close encounters are relatively rare on these short timescales (a few Myr or less) and the aggregate dynamics are thus dominated by this initial collapse and re-expansion.

Elongated subvirial clusters display a gradient in the radial velocity along the direction of elongation due to this initial collapse. For example, consider a cluster with its major axis in the $\hat{z}$-axis direction and let the system be observed along a line-of-sight that is less than 90° from the major axis. For clarity, we define north and south to be the projected positive and negative $\hat{z}$-axes, respectively. During the first half of a crossing time, the northern part of the cluster appears to be redshifted away from the observer while the southern hemisphere is blueshifted toward the observer. The collapse of an elongated subvirial cluster naturally results in a north-south gradient in the radial velocities along the length of the cluster (see Figure 4.2). The magnitude and direction of the radial velocity gradient depend on the line-of-sight chosen to "observe" the simulated cluster (see Section 4.3.3).

This kinematic signature in the radial velocities is present only if an elongated cluster is viewed along a line-of-sight that is *not* coincident with a principal axis *and* if the cluster has subvirial velocities. When viewed along a minor axis, a subvirial elongated cluster displays no north-south gradient in the radial velocities, as the stars are preferentially moving perpendicular to the line-of-sight. Viewed along the major axis, the portion of the cluster moving away from the observer is projected directly onto the region of the cluster moving toward the observer, and hence a gradient is not observed.

Likewise, a virial cluster does not display a strong radial velocity gradient, as it is not globally collapsing and the stellar velocities have no spatial correlation. A very slight gradient is observed in the virial clusters at early times; however, it is approximately 10

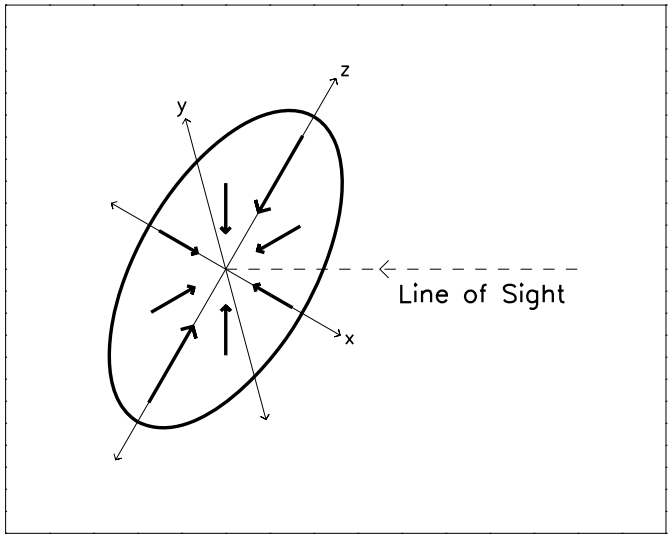

Figure 4.2: Diagram represents an elongated collapsing cluster which is viewed along a line-of-sight not coincident with a primary axis. During the initial (collapse-like) phase of a cluster with subvirial initial conditions, the upper portion of the cluster will appear redshifted while the lower portion of the cluster appears more blueshifted. This asymmetry results in a radial velocity gradient along the extent of the cluster.

times weaker than that observed in the subvirial clusters and is associated with the slight contraction of the simulated virial clusters as the stellar velocities are redistributed from the random isotropic distribution to a true virial distribution (see Figure 4.1).

A cluster that is undergoing global expansion can also produce a gradient in the radial velocities similar to that observed in the collapsing elongated cluster (Figure 4.3, panel(d)). However, the signature will differ in shape because the stars that populate outermost spatial bins will not have bound orbits. The stars will not be at the furthest point in their orbits and therefore will not have reduced velocities as they change direction and return to the cluster's center. Therefore, instead of having an S-shaped kinematic signature, an expanding cluster will have a relatively flat gradient, with no turnover at the end-points. We also note that rotation of a virial cluster may produce a kinematic signature that is similar to the one observed in subvirial clusters, but only if the rotation takes place around an axis perpendicular to the line-of-sight.

Figure 4.3 illustrates the radial velocity signature for various projections of spherical and elongated subvirial and virial clusters. In each panel, the data points correspond to the mean radial velocity of the stars in 0.2 pc bins and the lengths of the error bars correspond to the standard deviation of the velocities within each bin. For completeness, we note that this radial velocity gradient calculated from the simulated clusters is not sensitive to the choice of bin size for bin sizes ranging from 0.05 to 1.0 pc. In individual clusters (such as the ONC), the lower limit of the bin size is determined by small number statistics.

It is clear from this figure that the radial velocity signature is created by a combination of two effects: projection of an elongated cluster and subvirial initial velocities (the latter implies global collapse). The bottom right panel shows the only cluster that demonstrates this kinematic signature. This cluster is elongated, is not viewed along a primary axis, and is seeded with subvirial initial velocities.

One way to characterize the strength of a radial velocity gradient is by using the amplitude of the cumulative velocity distribution, $\mathcal{A}_{CRV}$. The cumulative radial velocity distribution is created by sorting the individual radial velocity measurements by the $\hat{z}'$-coordinate and then producing the cumulative distribution from this sorted data set. We normalize this measure by both the number of stars in the cluster, N, and the velocity dispersion of the cluster, $\sigma_{\rm RV}$. This procedure results in a (dimensionless) normalized cumulative radial velocity distribution that can be more meaningfully compared across clusters of different sizes and velocity dispersions. An additional advantage of the cumulative velocity distribution is that it is created from individual stellar radial velocities and thus is insensitive to the choice of bin size.

A cluster with no radial velocity gradient will have (on average) the same number of stars with positive and negative radial velocities with respect to the cluster's center of mass or mean radial velocity. Therefore, the cumulative velocity distribution in such a cluster

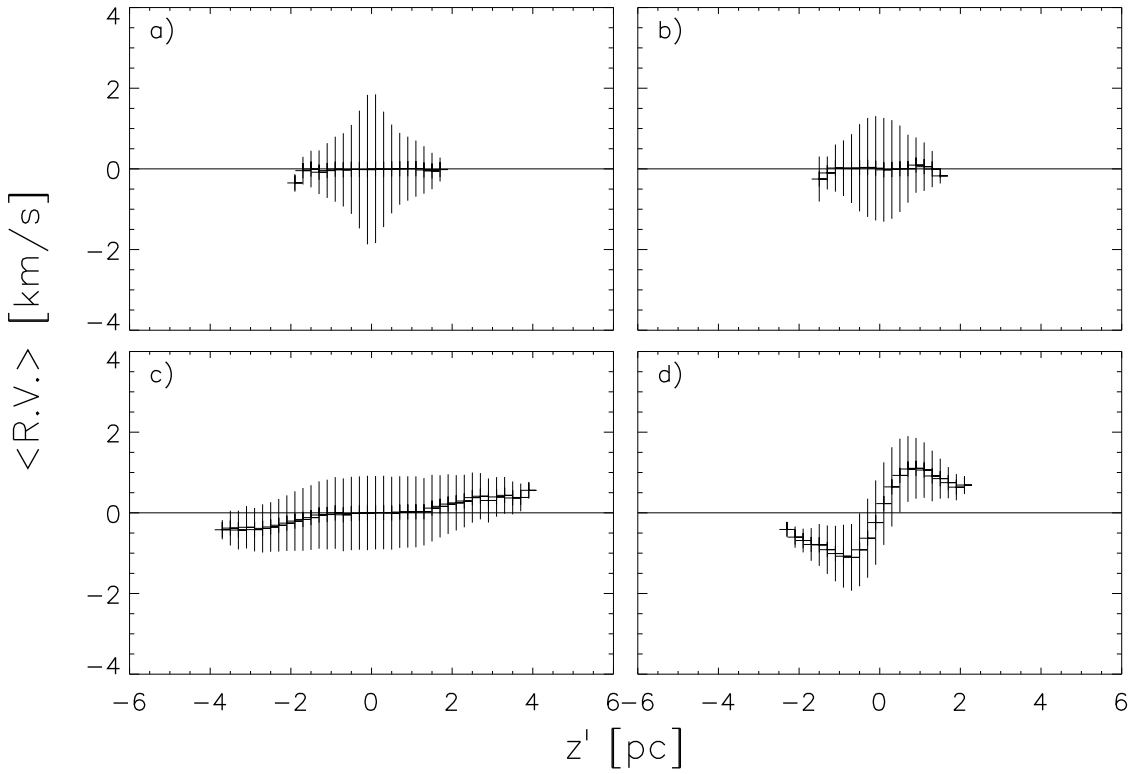

Figure 4.3: Radial velocity as a function of $\hat{z}'$ position for a differing geometries, initial velocity distributions, and projections for simulated embedded clusters. The mean radial velocity (averaged over 0.2 pc bins) is indicated by the data points. The error bars correspond to the standard deviation of the radial velocity distribution within the bins. The panels correspond to differing initial geometries, initial velocity distribution, and projections of simulated embedded clusters: (a) spherical cluster, with subvirial initial conditions, (b) elongated cluster, with subvirial initial conditions, and viewing angle of 0° from major axis, (c) elongated cluster, with virial initial conditions, and viewing angle of 30° from major axis, and (d) elongated cluster, with subvirial initial conditions, and viewing angle of 30° from major axis. The first distribution is shown at time $t = 1.5$ Myr after the start, whereas the other three cases are shown at $t = 2.1$ Myr.

will fluctuate around zero and be relatively flat as a function of z'.

On the other hand, a cluster with a strong gradient along $\hat{z}'$ will have preferentially more blueshifted stars at the negative $\hat{z}'$ end of the cluster center and more redshifted stars at the positive $\hat{z}'$ end of the cluster. Therefore, the cumulative radial velocity distribution will be a decreasing function for $z' < 0$ and an increasing function for $z' > 0$, resulting in a dip in the cumulative radial velocity distribution.

The normalized cumulative radial velocity distributions for the clusters depicted in Figure 4.3 are displayed in Figure 4.4. The ranges on the $\hat{y}$-axes are held constant to emphasize how this distribution varies for subvirial and virial initial conditions. Although the virial elongated cluster in panel (c) of Figure 4.3 appears to have a slight gradient in the radial velocity, the cumulative distribution indicates that the strength of this signature is more than seven times weaker than in the subvirial elongated cluster. The cumulative distribution for the virial cluster peaks at $\mathcal{A}_{CRV} \sim 0.04$, whereas that of the subvirial cluster peaks at $\mathcal{A}_{CRV} \sim 0.29$. Note that the minimum is not observed in the subvirial spherical cluster, panel (a), which indicates that subvirial velocities alone are insufficient to produce this kinematic signature. As a result, in general, both subvirial and nonspherical initial conditions are required to observe the kinematic signature.

The key feature in the cumulative radial velocity distribution signature is neither the growth nor the decay of the function, but rather the peak produced by both a region of growth and then a region of decay. While either the growth, or the decay, of the distribution can be mimicked by constructing the distribution in a velocity frame that is significantly different from the average velocity of the cluster, both cannot be created in the same frame. For instance, if the cumulative radial velocity distribution for a virial cluster is constructed by shifting into a velocity frame that is significantly higher than the cluster's average velocity, then almost all stars contribute negative values to the distribution, and thus the

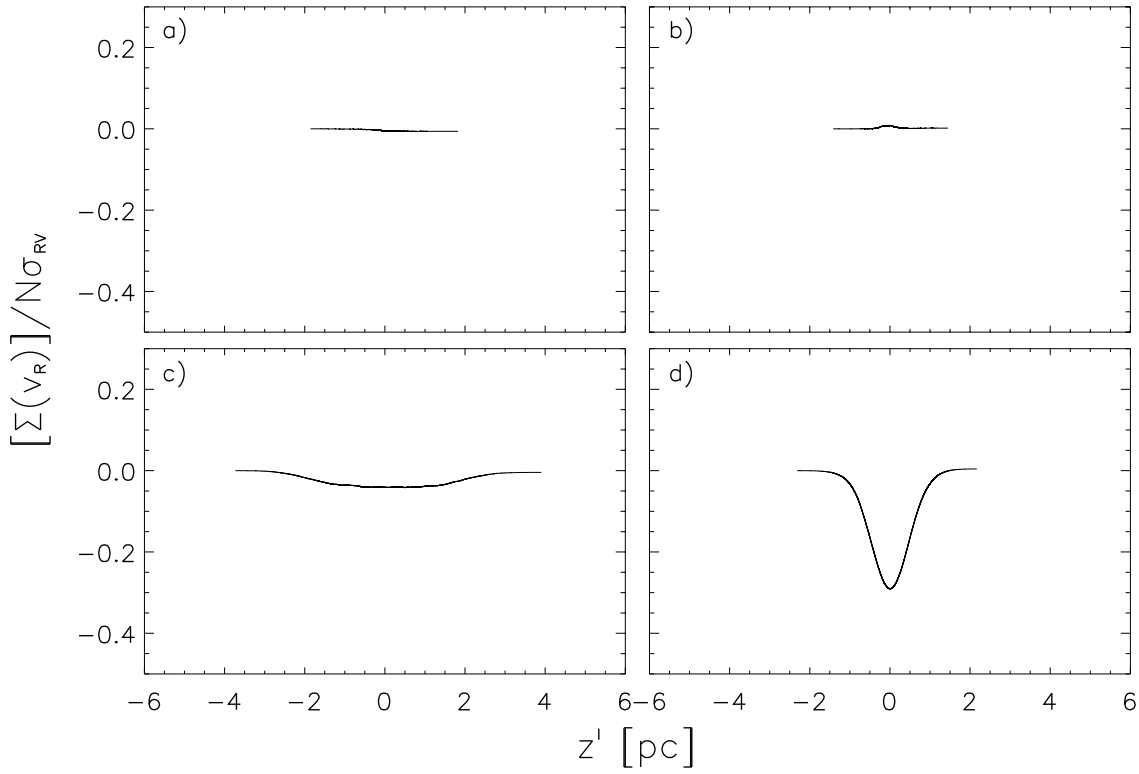

Figure 4.4: Cumulative radial velocity distribution (normalized by cluster size and velocity dispersion) summed along the $\hat{z}'$-axis of the projected cluster. The panels correspond to differing initial geometries, initial velocity distribution, and projections of simulated embedded clusters: (a) spherical cluster, with subvirial initial conditions, (b) elongated cluster, with subvirial initial conditions, and viewing angle of 0° from major axis, (c) elongated cluster, with virial initial conditions, and viewing angle of 30° from major axis, and (d) elongated cluster, with subvirial initial conditions, and viewing angle of 30° from major axis. The first distribution is shown at time $t = 1.5$ Myr after the start, whereas the other three cases are shown at $t = 2.1$ Myr.

distribution decreases as a function of z'. For the purpose of this study, we construct all cumulative radial velocity distributions by shifting each stellar velocity by the median radial velocity.

We also note that a flat radial velocity gradient, such as that produced by a rotating virial cluster, or an expanding elongated cluster, can produce a peak in the cumulative radial velocity distribution similar to the one observed in the collapsing elongated cluster. Therefore, both the kinematic signatures presented in Figure 4.3 and the integrated distributions presented in Figure 4.4 should be considered when looking for signs of collapse in an observed cluster's radial velocity structure.

4.3.2 Velocity Dispersions

Observations of kinematic signatures in young clusters can be compared to these simulated signatures only if the observed clusters are large enough that the binned radial velocity data do not suffer significantly from small number statistics. We investigate trends in the total, radial, and tangential velocity dispersions in order to allow for comparison to smaller and less studied clusters for which only estimates for the total velocity dispersions are available.

In both spherical and elongated subvirial clusters, the velocity dispersions increase as a function of time during the initial collapse phase and then decrease as the cluster evolves toward virial equilibrium. Clusters that experience multiple collapse and re-expansion cycles before gas removal also display corresponding cycles in their velocity dispersions. The dispersions peak before the re-expansion phase and bottom out before the collapse phase, with the peak values becoming smaller with each successive cycle. Virial clusters have velocity dispersions that increase only slightly during the first 1 Myr, the star formation epoch, and then remain relatively flat through the rest of the embedded stage. These trends are similar to the ones depicted in Figure 4.1. While an elongated cluster's total

velocity dispersion does not depend on the projection, its radial and tangential velocity dispersions do. This dependence on projection angle, θ is discussed in Section 4.3.3.2.

4.3.3 Kinematic Signatures

As discussed in Section 4.3.1, only clusters with subvirial initial velocities *and* elongated geometries produce radial velocity gradients. The kinematic signature evolves over time. During the first 1 Myr, the radial velocity gradient arises as stars become free to move through the gravitational potential of the cluster. The gradient becomes larger during the first "free-fall time" while the stars fall toward the cluster center. As a majority of the stars pass through the cluster center, the radial velocity gradient decreases and eventually changes sign as the cluster re-expands. Clusters with sufficiently small crossing times will undergo several gradient sign changes before gas removal at $t = 5$ Myr as the cluster size oscillates around its equilibrium size. In addition, as the cluster evolves toward equilibrium, the strength of the kinematic signature decays.

At $t = 5$ Myr, the embedding gas potential is removed from the cluster which then continues to evolve due to gravitational interactions between the stars. Depending on the specific kinematic status of the cluster at the time of gas removal, the signature considered here may or may not remain in the cluster. If the gas is removed while a significant portion of the stars are in the re-expanding phase, the kinematic signature is amplified and remains in the cluster even after 5 Myr of evolution. It is important to note that the details of the gas removal process may significantly affect the characteristics of the signature, and hence we refrain from making any strong conclusions about the kinematic signature's presence after gas removal.

4.3.3.1 Effect of Initial Virial Ratio

We compare centrally concentrated elongated clusters ($\rho \sim m^{-1}$) clusters with virial parameters $Q_i = 0.04$ and 0.15 to determine how the departure from virial equilibrium

affects the strength of the kinematic signature. The clusters have $N = 2000$ members, an SFE of 50%, and axis parameters $a = b = 2$ pc and $c = 4$ pc. We find that as the initial virial ratio (and the average starting stellar velocity) decreases, the strength of the kinematic signature increases. Therefore, the larger the departure from virial equilibrium corresponds to a larger kinematic signature. We measure the strength of the signature by the amplitude of the normalized cumulative radial velocity distribution $\mathcal{A}_{CRV}$, and find that the $Q_i = 0.04$ cluster had a maximum at $\mathcal{A}_{CRV} \sim 0.33$ whereas the $Q_i = 0.15$ cluster had a maximum at $\mathcal{A}_{CRV} \sim 0.20$.

In addition, even though the $Q_i = 0.15$ cluster had larger initial velocities, the $Q_i = 0.04$ cluster has a larger average velocity dispersion over the embedded stage. Specifically, the average velocity dispersions were 0.51 km s^{-1} and 0.47 km s^{-1} for the $Q_i = 0.04$ and 0.15 clusters respectively.

4.3.3.2 Effect of Projection Angle

For a subvirial elongated cluster, the strength of the radial velocity signature varies most strongly with projection angle. This trend is due to two competing effects. First, the most significant collapse occurs along the major axis of the cluster, the $\hat{z}$-axis. The component of the velocity that is observed along the line-of-sight varies as the cosine of the projection angle θ between the $\hat{z}$-axis and the line-of-sight. Therefore, the smaller the projection angle, the stronger the signature. Second, the radial velocity signature is only observed when there are significantly more redshifted stars in a declination bin than blueshifted stars (or vice versa). Therefore, a larger projection angle θ will cause the red- and blueshifted populations to be more spatially separated, whereas a small projection angle will result in a projected cluster whose redshifted and blueshifted populations appear to overlap.

Figure 4.5 displays the amplitude of the normalized cumulative radial velocity distribution $\mathcal{A}_{CRV}$, as a function of projection angle θ, for the uniform density elongated cluster

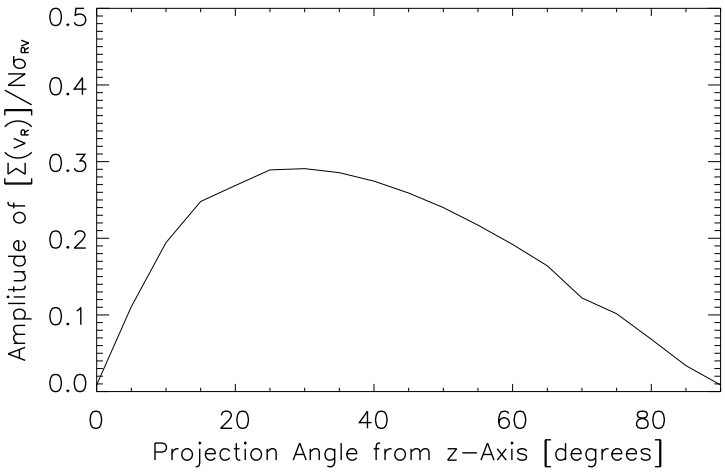

Figure 4.5: Amplitude of the normalized cumulative radial velocity distribution $\mathcal{A}_{CRV}$, as a function of projection angle θ. The data are shown for an elongated cluster with axis ratios $(1:1:2)$, uniform stellar and gas densities, and subvirial initial velocities at the time $t = 2.1$ Myr.

with $a = b = 2$ pc and $c = 4$ pc at $t = 2.1$ Myr. A projection angle between 25° and 35° from the $\hat{z}$-axis produces the strongest radial velocity signature. The peak of the distribution is relatively broad, however, with a full width at half-maximum of approximately 60°, which suggests that a radial velocity gradient will usually be observable in elonagated subvirial clusters.

During collapse, the dispersion in the radial velocities $\sigma_{\rm RV}$ is a decreasing function of the projection angle θ from the $\hat{z}$-axis, whereas the velocity dispersion along the $\hat{z}'$-axis $\sigma_{\parallel,\, z'}$ is an increasing function of θ. This result occurs because the dispersions are geometrically related to each other by $\sigma_{\rm RV}(\theta) = \sigma_{\parallel,\, z'}(90 - \theta)$. These trends are representative of the fact that during the collapse phase, the velocity dispersions are largest along the principal axis.

In contrast, the plane-of-sky velocity dispersion perpendicular to the $\hat{z}'$-axis does not depend on the projection angle. This result is due to the $x,\ y$ symmetry of the prolate spheroid. Figure 4.6 displays $\sigma_{\rm RV}$ (top panel), $\sigma_{\parallel,\, z'}$ (middle panel), and $\sigma_{\perp,\, z'}$ (bottom panel) for the same cluster shown in Figure 4.5. Each curve corresponds to a different choice of projection angle, $\theta = 0,\ 15,\ 30,\ 45,\ 60,\ 75$, and 90°. The relationship between

$\sigma_{\rm RV}$ and $\sigma_{\parallel,\ z'}$ described above is apparent in Figure 4.6.

4.3.3.3 Effect of Cluster Elongation

To observe differences caused by the amount of elongation, we compare two subvirial clusters with differing axis ratios. Specifically, we compare a cluster with an aspect ratio of 0.5 ($a = b = 2$ pc, $c = 4$ pc) to one with an aspect ratio of 0.25 ($a = b = 1$ pc, $c = 4$ pc). Each of the clusters has 2700 members, a density profile $\rho \sim m^{-1}$, an SFE of 33%, and a virial parameter $Q_i = 0.04$.

We find that the more elongated cluster evolves on a slightly shorter timescale and that the mean radial velocities in a given declination bin are larger. As a result, the kinematic signature discussed in Section 4.3.1 is stronger. For comparison, the maximum mean radial velocity in a declination bin is approximately 1 km s^{-1} for the less elongated cluster and 2 km s^{-1} for the more strongly elongated cluster. Therefore the overall change in radial velocity is approximately 4 km s^{-1} over the length of the cluster in the strongly elongated geometry. The average velocity dispersion is also larger in the more elongated cluster, $\sigma = 1.60$ km s^{-1}, compared to the less elongated cluster where $\sigma = 1.18$ km s^{-1}.

4.3.3.4 Effect of Initial Density Distribution

The kinematic signatures also vary as a function of initial density distribution. We investigate this variation by comparing subvirial ($Q_i = 0.04$) elongated cluster with uniform density distributions to those with centrally concentrated $\rho_* \sim m^{-1}$ density profiles. Each cluster contains $N = 2000$ members, has an SFE of 50%, and has axis parameters $a = b = 2$ pc and $c = 4$ pc.

Elongated clusters that are more centrally concentrated have central regions which evolve on shorter timescales than the outer regions. This trend can be seen by considering the gravitational contraction of an centrally concentrated sphere with radius r_0 and density profile $\rho \sim r^{-1}$. The collapse is inside out because free-fall time for a particle initially at a

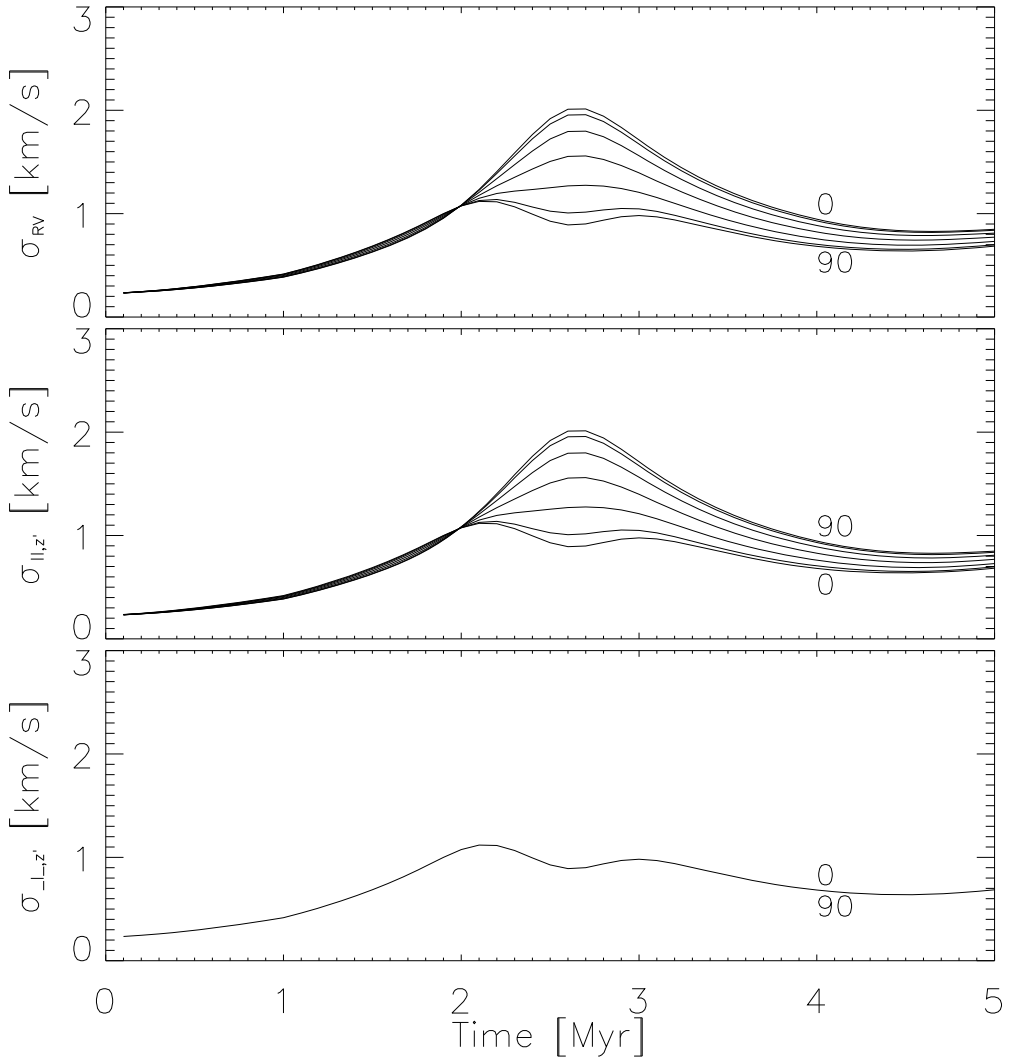

Figure 4.6: Evolution of the velocity dispersions in an elongated subvirial cluster during the embedded stage for various projection angles. The top panel displays the radial velocity dispersion $\sigma_{\rm RV}$ as a function of time for $\theta = 0,\ 15,\ 30,\ 45,\ 60,\ 75,$ and $90°$. The middle panel displays the velocity dispersion parallel to the $\hat{z}'$-axis, $\sigma_{\parallel,\,z'}$ for the same projection angles. Note that $\sigma_{\rm RV}(\theta) = \sigma_{\parallel,\,z'}(90-\theta)$ by definition. The bottom panel shows the velocity dispersion in the plane of the sky perpendicular to the $\hat{z}'$-axis, $\sigma_{\perp,\,z'}$. On account of the $x,\ y$ symmetry of a prolate spheroid, $\sigma_{\perp,\,z'}$ does not vary as a function of θ. The data presented here are from a uniform spheroid cluster with subvirial initial velocities and axis parameters $a = b = 2$ pc and $c = 4$ pc.

position r is given by $t_{\rm ff} \sim \rho^{-1/2} \sim \sqrt{r}$, and so the central regions of the system evolve on shorter timescales. Goodman & Binney (1983) showed that this general argument holds true for spheroidal clusters as well.

On account of this inside-out collapse, the center of a subvirial cluster will collapse and begin to re-expand while the outskirts of the cluster are still collapsing. As a result, the red- and blueshifted populations will not be as spatially separated as in the uniform density cluster shown in Figure 4.3, panel (d). Instead, the generally redshifted $z' > 0$ portion of the cluster will contain many blueshifted stars near the center, and this addition acts to blueshift the average radial velocity in the central z' bins. On the other side of the cluster's center, redshifting may occur for the same reason, resulting in a kinematic signature that is flat or even oppositely sloped (with respect to the general trend) near $z' = 0$.

In addition, the inside-out collapse causes the average velocity dispersion during the embedded stage to be higher in centrally concentrated clusters than in uniform density clusters. This effect occurs because the peak in the velocity dispersion, which occurs during the cluster's collapse and re-expansion, is broader (in time) in the $\rho_* \sim m^{-1}$ clusters than in the $\rho_* \sim \rho_0$ clusters. In a centrally concentrated spheroid, the stellar members reach their highest speeds at a time that depends on their initial position within the cluster. In contrast, in a uniform spheroid, the stellar members reach their highest speeds at roughly the same time. Therefore, the velocity dispersion in a centrally concentrated cluster remains higher for a longer period of time. This finding has observational consequences: initially centrally concentrated clusters are more likely to be seen with high velocity dispersions.

4.3.3.5 Effect of Star Formation Efficiency

To investigate the effect of SFE on the kinematic signatures observed, we compare elongated clusters with SFE of $17\%, 33\%$, and 50%. Each cluster has a $\rho_* \sim m^{-1}$ stellar density profile, axis parameters $a = b = 2$ pc and $c = 4$ pc, and subvirial $Q_i = 0.04$ initial

velocities. The clusters with SFEs of 17% and 13% have $N = 2700$ stars, whereas the cluster with a 50% SFE has $N = 2000$ stars.

Clusters with lower star formation efficiencies evolve on shorter timescales due to the higher velocities associated with the deeper potential wells of the gas component. In addition, both the amplitude $\mathcal{A}_{CRV}$ and the total velocity dispersion increase as SFE decreases.

4.3.3.6 Effect of Extinction due to High Column Density

Most very young clusters are still embedded in the molecular cloud from which they formed. In cases where optical spectra are used to determine stellar kinematics, extinction from the embedding clouds can potentially change the observed kinematic signatures in these clusters. For example, consider a cluster that is roughly shaped like a prolate spheroid with its north end tipped toward the observer. The southern region is farther away, and is collapsing toward the center of mass, and thus appears blueshifted with respect to the stars in the northern region. If even a modest fraction of the cluster members that are farthest from the observer are not included in the observed data set due to extinction by the embedding cloud, this blueshifted population would appear less blueshifted than if it were not obscured. These observed selection effects may be mitigated by using H- or K-band spectra to select targets.

As an example, consider an embedding cloud that has a dust opacity of $\kappa_V = 200$ cm g^{-1} at optical wavelengths and a mean molecular mass $\mu = 2.4 m_H$. In order to have an optical depth with the value of unity, the minimum column density is required to be $N_{col} \approx 1.28 \times 10^{21}$ cm^{-2}. A typical molecular cloud has number densities ranging from $n = 10^2 - 10^3$ cm^{-3}. Therefore, if the sources are being observed through more than $0.4 - 4$ pc of molecular cloud, they would be undetected and hence removed from the sample.

To test this hypothesis, we re-analyzed the simulated cluster data by omitting stars

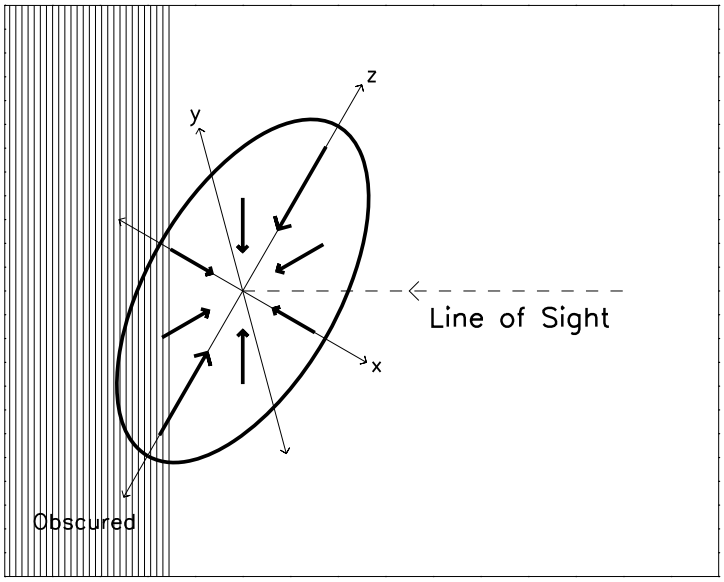

Figure 4.7: Same as Figure 4.2, but indicates portion of cluster that is assumed to be obscured due to extinction.

that are behind an "obscuring plane" (see Figure 4.7) which includes a column density threshold. In this model, the obscuring plane is introduced with an orientation normal to the line-of-sight and at a distance $0 \leq d_{obs} \leq 5$ pc beyond the center of the cluster from the observer. We found that if only a modest number of stars in the southern region of the cluster are removed from the sample (due to the fact that they are beyond the obscuration plane) and their velocities are not included in the velocity versus position plot, the southern portion of the cluster will have a significantly less steep velocity gradient compared to the northern region. Specifically, if $10\% - 15\%$ of the stellar population is unobservable, the kinematic signature in the southern half of the simulated cluster is completely washed out. Figure 4.8 displays the radial velocity signatures for a cluster with various amounts of the stars extincted. In the top panel, $d_{obs} = 0.6$ pc and 32% of the cluster members are removed from the sample. The radial velocity signature in the middle panel is observed when $d_{obs} = 1.4$ pc and 12% of the cluster members are thus obscured. For comparison, the bottom panel is the radial velocity signature produced when all stars are included in the sample.

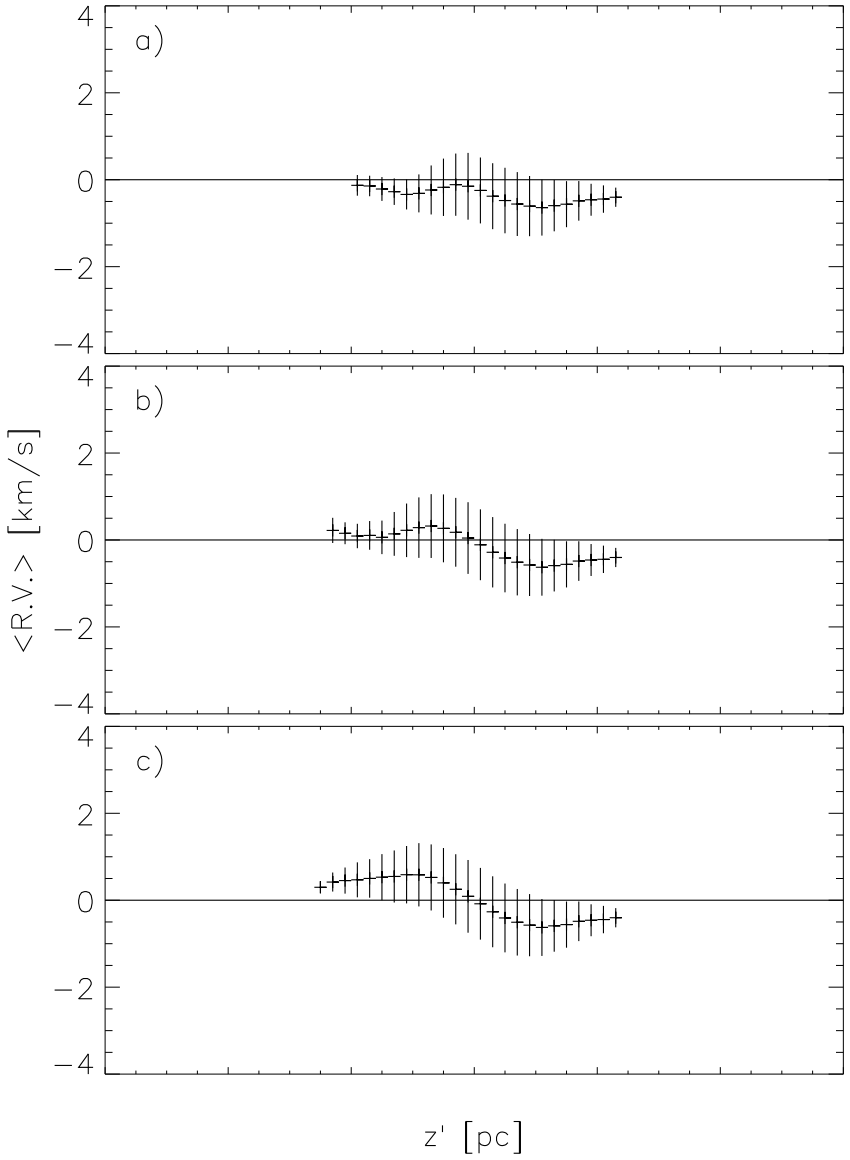

Figure 4.8: Each panel displays the radial velocity as a function of $\hat{z}'$ position in a uniform density subvirial elongated cluster for different locations of the obscuring plane. The mean radial velocity (averaged over 0.2 pc bins) is indicated by the data points. The error bars correspond to the standard deviation of the radial velocity distribution within the bins. In the top panel, $d_{obs} = 0.6$ pc and 32% of the cluster members are removed from the sample. The radial velocity signature in the middle panel is observed when $d_{obs} = 1.4$ pc and 12% of the cluster members are thus obscured. The bottom panel is the radial velocity signature produced when all stars are included in the sample. Even modest amounts of extinction can wash out the structure of the kinematic signature.

4.4 Comparison to Observations - The Orion Nebula Cluster

Recent kinematic studies of the Orion star-forming region have determined radial velocities for a large sample ($\sim$ 1200) of visible sources within the region. In this section we discuss the kinematic results of these studies in light of the numerical simulations presented above.

The ONC region is a good environment in which to look for kinematic signatures such as the ones observed in our simulated clusters for many reasons. First, the ONC has a large population and is close enough to be well studied so that many of the cluster members have measured radial velocities. The large sample size of the cluster allows the data to be binned in declination while maintaining a reasonable number of data points in each bin, so that the results suffer only mildly from small number statistics. Furthermore, the ONC is visibly elongated in projection (Hillenbrand & Hartmann 1998), which is one of the requirements for the kinematic signature to be observed.

Finally, although opinions vary, there are significant arguments supporting the assertion that the ONC region as a whole is young and is estimated to be less than one crossing time old. Observations of the ONC by Fűrész et al. (2008) and more recently by T09 identify spatially coherent kinematic structure in the stellar distribution that closely matches the observed kinematic structure of the gas in the region as measured in ^{13}CO by Bally et al. (1987). The authors argue that this correlation indicates that the cluster is not dynamically relaxed and that in fact, the region is less than a crossing time old. The results of the previous section indicate that the strength of the kinematic signature peaks before the cluster is a crossing time old. Therefore, the strongest observed signature will occur in clusters that are less than a crossing time old, as the ONC may be.

4.4.1 Observations

The radial velocities cited in this study were determined from multiple observations using Hectochelle on MMT and MIKE fibers at Magellan. The Hectochelle observations from Fűrész et al. (2008) have been combined with additional Hectochelle and MIKE observations (T09) to produce a list of ~ 1200 sources with radial velocity measurements in the region surrounding the ONC. A detailed discussion of the observations, data reduction, spectral fitting, and radial velocity measurements is provided in the observational papers. In addition, much care has been taken to identify binaries and non-cluster members from the ONC data, and this procedure is detailed in T09.

4.4.2 Kinematic Signatures

As discussed in these observational papers (Fűrész et al. 2008, and T09), the stars and gas in the region surrounding the ONC show similar north-south velocity gradients. We consider the ONC members that are near the molecular cloud filament by selecting the R.A. range $84.0 - 83.5$, and remove identified binaries from the sample. The distribution of sources is shown in the left panel of Figure 4.9. In the right panel of Figure 4.9, the binned median velocities are plotted as a function declination. To calculate the median velocity in each declination bin, a histogram of the radial velocities is created. The median is calculated ignoring all bins that have less than half of the maximum value in the distribution. The medians calculated without localizing on the filament differ from those shown here by a few 0.5 km s^{-1} shifts to the red or blue.

Figure 4.9 is analogous to Figure 4.3 for the simulated cluster data. The north-south velocity gradient is clear, though the gradient is steeper in the northern part of the ONC (north of declination ~ -5.5) than it is in the southern region. The observed kinematic structure in the ONC region is qualitatively similar to the kinematic structure of elongated subvirial clusters viewed off axis (bottom right panel of Figure 4.3).

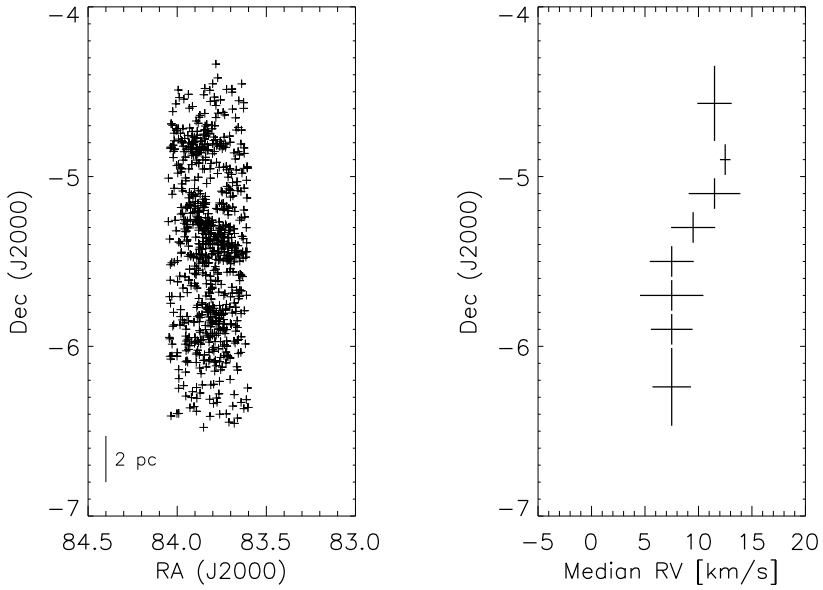

Figure 4.9: Left panel displays the positions of stars in the ONC with radial velocities measured by (Fűrész et al. 2008, and T09) that are spatially associated with the filament of dense gas. In the right panel, the median radial velocity of the stellar population is plotted for each declination bin. Bin width is indicated by the vertical extent of the bars. The horizontal error bars indicate the velocity dispersion in each bin, where the dispersion is defined by the distribution's full width at half-maximum divided by $2\sqrt{2\ln 2}$. There is a noticeable radial velocity gradient in the northern ONC, which is qualitatively similar to the one observed in the simulated subvirial clusters.

Figure 4.10 presents the cumulative radial velocity distribution observed in the ONC (analogous to Figure 4.4) for the entire sample (solid curve) as well as the distribution for only those stars north of declination −6 and −5.5 (dashed curves). This distribution is composed of the radial velocities of the ONC members that have velocities within 3 σ of the median radial velocity of the distribution of the median velocity, where σ = 3.1 km s^{-1} (Fűrész et al. 2008). The constrained data set (without the declination cuts) includes approximately 89% of the sources shown in the left panel of Figure 4.9. To produce these plots, the radial velocities were shifted by the median observed velocity and normalized by the velocity dispersion of and number of stars in the data set. This shift and normalization allows the observed data to be directly compared to the cumulative radial velocity distribution in the simulated clusters, where the velocities are measured in the center of mass reference frame. The kinematic signature peak observed in our simulated

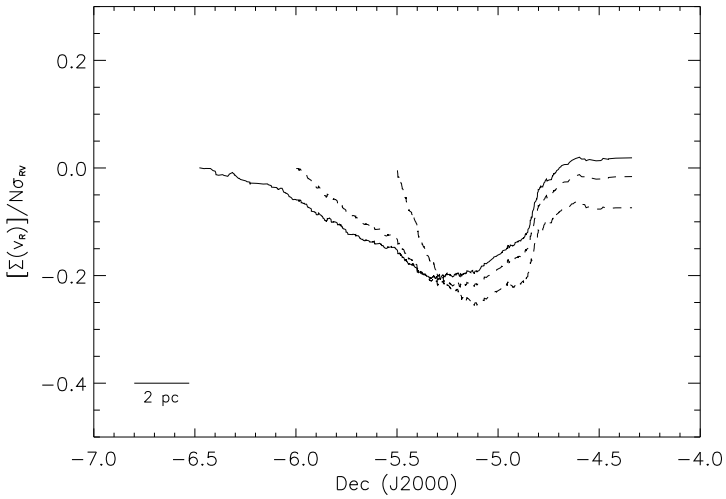

Figure 4.10: Normalized cumulative radial velocity distribution summed along declination in the Orion star-forming region. This cumulative distribution is created from the ONC members with radial velocities within 3 σ of the median radial velocity of the distribution. From Fűrész et al. (2008), the radial velocity dispersion in this region of the ONC is $\sigma = 3.1$ km s^{-1}. The cumulative radial velocity distributions for the stars north of declination -6 and -5.5 are indicated by the dashed lines.

clusters is also observed in the ONC, over the extent of the cluster, as well as over just the northern portion. The ONC data are significantly less smooth than the theoretical results. This difference is mostly due to the summing of 50 simulations used to produce the theoretical results shown in Figure 4.4.

4.4.3 Comparison to Simulation Results

The kinematic structure observed in the ONC may be understood in light of the simulated cluster kinematics. The correlation between the motion of the stars and the gas in the ONC indicates that the region is fairly young and that the stars and gas are still collapsing. The observed radial velocity gradient also supports the theory that the ONC is dynamically young and that the region is less than a crossing time old. Also, the signature suggests the stars in the region are formed with subvirial velocities, an initial condition required by the simulations to produce the structure observed. The ONC region is elongated and the combination of elongation, subvirial initial velocities, and extremely young dynamical age can account for the kinematic structure observed as demonstrated by the

simulations presented in this study. This interpretation requires that the northern region of the ONC be closer to the observer than the southern region. However, at this time, the distance to the ONC as a whole is still poorly constrained (Jeffries 2007, and references therein) and determining distance differences on the order of 10 pc between the northern and southern regions of the ONC is not yet possible.

The kinematic signatures observed in the ONC are qualitatively similar to those observed in the elongated subvirial clusters. The simulated cluster that is physically most similar to the ONC region is the centrally concentrated elongated cluster with axis ratio: $2:2:8$ pc and a low SFE of $\sim 17\%$. This cluster displays a kinematic signature similar in magnitude to the observed signature in the ONC. Specifically, at $t = 0.7$ Myr, the simulated cluster has a radial velocity gradient of ~ 2 km s^{-1} pc^{-1}, and $\mathcal{A}_{CRV} \sim 0.15$. In addition, the simulated cluster has a radial velocity dispersion of ~ 3 km s^{-1}. In comparison, the Orion data have a radial velocity gradient of ~ 5 km s^{-1} over 0.6° in declination; at a distance of 420 pc, the parameters are approximately a gradient of 1.1 km s^{-1} pc^{-1}, $\mathcal{A}_{CRV} \sim 0.2$, and a radial velocity dispersion of 3.1 km s^{-1}.

Proper-motion studies in Orion (such as the one conducted by Jones & Walker 1988) found plane-of-sky velocity dispersions along the cluster's major axis that are somewhat larger than the dispersions perpendicular to the major axis. In the notation adopted in this chapter, $\sigma_{\parallel,\, z'} = 2.63 \pm 0.9$ km s^{-1} and $\sigma_{\perp,\, z'} = 2.03 \pm 0.11$ km s^{-1}. Fűrész et al. (2008) determined a radial velocity dispersion of $\sigma_{\rm RV} = 3.1$ km s^{-1}. This relatively large difference between $\sigma_{\rm RV}$ and $\sigma_{\perp,\, z'}$ is indicative of some type of global collapse because virial elongated clusters have at most modest differences between $\sigma_{\rm RV}$ and $\sigma_{\perp,\, z'}$. In our simulated virial clusters $1 < \sigma_{\rm RV}/\sigma_{\perp,\, z'} \leq 1.3$, whereas in the subvirial clusters $1 < \sigma_{\rm RV}/\sigma_{\perp,\, z'} \leq 2.3$.

The ONC region displays significant mass segregation among the most massive stars ($m \gtrsim 2$ M$_\odot$) which reside in the Trapezium at the center of the ONC. Previous numerical

studies of the ONC cluster indicate that the mass segregation must be primordial as the cluster is not old enough for dynamical mass segregation to account for the presence of the Trapezium (Bonnell & Davies 1998). Our simulated clusters begin with somewhat different initial conditions, by focusing on subvirial initial velocities and cluster elongation, but arrive at the same conclusion: the region is not old enough for dynamical mass segregation to have taken place. In the simulated clusters, we compared the radii that enclosed 25%, 50%, and 75% of the stellar mass in different mass bins. The results of these simulations showed no difference in the radii of different mass bins during the first $1-3$ Myr of evolution, indicating that dynamical mass segregation had not yet occurred. Subvirial initial velocities will result in a higher central density at earlier times on account of global collapse, but even with an increased density and thus higher interaction rate, the ONC is still too young for significant mass segregation to have occurred.

In addition to the lack of mass segregation in the spatial distribution of stars within the cluster, no significant differences in the kinematic distributions are observed as a function of stellar mass in the simulations. The masses of stars in the Orion region are not well enough constrained to compare this result of the simulations to the observations at this time. However, future studies of young stars in this region may yield mass information that, combined with kinematic data, will be able to test this prediction.

As seen in Figure 4.9, the radial velocity gradient apparent in the northern region is not as evident in the region south of the ONC. The asymmetry may indicate that the center of the gravitational collapse is not the Trapezium, but rather is located slightly north of the Trapezium. The collection of cumulative radial velocity distributions displayed in Figure 4.10, however, indicates that the signature is present even if the center of the gravitational collapse is assumed to be somewhat north of the Trapezium. The asymmetry could also be due to a north-south asymmetry in the initial conditions that is not well represented

by the idealized simulations of Section 4.3. The star-forming region north of the ONC is located at the edge of the integral-shaped molecular cloud, whereas the region south of the ONC extends into a larger complex of molecular clouds. Therefore, the dynamics in the northern region is better suited to our approximate of an isolated elongated centrally concentrated cluster than those of the south.

4.5 Conclusion

This study presents N-body simulations that explore the kinematic signatures produced by asphericity and subvirial initial velocities in young embedded clusters. We have identified a robust kinematic signature, in particular a gradient in the radial velocities, which is naturally produced by elongated subvirial clusters. We characterize the properties of this kinematic signature as a function of initial conditions. Specifically, we compare the kinematics of evolving spherical and aspherical clusters and with both virial and subvirial initial conditions. We consider changes in the kinematic signature due to differing amounts of cluster elongation, SFE and departure from virial equilibrium, and discuss possible sample bias due to extinction in observed clusters. Finally, we compare the signature displayed in our simulated clusters to kinematic data from the ONC. The main results of our work are summarized as follows:

- Elongated clusters with subvirial initial velocities display a gradient in the radial velocities as a function of projected position along the cluster. Both aspherical initial geometries and subvirial initial velocities are required to produce this kinematic signature (see Figure 4.3).

- The strength of the kinematic signature increases during the first free-fall time as the cluster collapses, and then decreases as the stars pass through the center of the cluster. The gradient changes sign as the cluster re-expands, and the amplitude of

the cumulative radial velocity distribution decreases (see Figure 4.4) as the cluster evolves (see also Figure 4.1).

- The strength of the kinematic signature varies most sensitively as a function of the projection angle, as measured from the major axis of the cluster. The signature is weakest at projection angles of 0° or 90° and strongest at projection angles of $\sim 25° - 35°$ (see Figure 4.5). The peak is broad, however, with a full-width at half-maximum of $\sim 60°$, indicating that the kinematic signature is strong at most viewing angles.

- Making the cluster more elongated increases the gradient of the radial velocity across the cluster while leaving the velocity dispersions roughly similar.

- The initial stellar (and gas) density distribution affects the rate at which the cluster evolves and thus the timescale on which the kinematic signature evolves. In addition, centrally concentrated clusters have higher velocity dispersions than uniform density clusters.

- The kinematic signature is sensitive to observational selection effects. Extinction in an embedded cluster can preferentially deselect stars further from the observer and will thus affect the kinematic signature. A modest amount of extinction that removes 10% of the cluster members will wash out the kinematic signature in the region of extinction (see Figure 4.7).

- The asymmetric kinematic signature is qualitatively similar to the observed kinematics of the Orion star-forming region, suggesting that in addition to being elongated (as observed) a significant fraction of the cluster members started with subvirial initial velocities (see Section 4.4). The large gradient observed ($\sim$ 1 km s^{-1} pc^{-1}) indicates that the cluster is dynamically young. This result is consistent with previous

independent claims (e.g., Bonnell & Davies 1998).

Previous studies have shown that the SFE of clusters and the initial velocity distribution have significant effects on the long-term evolution of a cluster (Adams 2000; Boily & Kroupa 2003b; Adams et al. 2006), i.e., the cluster bound fraction and stellar interaction rates. This work emphasizes the fact that these conditions affect the short-term evolution of the cluster as well. In addition, this work is significantly different from previous studies in that it considers nonspherical initial conditions in both the stellar and gaseous components in young embedded clusters. Although many examples of clusters with nonspherical geometries exist and a considerable amount of work has considered orbits of individual stars within axisymmetric and triaxial potentials, little work has been done theoretically to understand how these clusters, taken as a whole, differ from spherical clusters. We have shown that elongated clusters naturally produce observable kinematic signatures that depend on the initial starting velocities of the cluster members and the projection of the cluster onto the plane of the sky. These signatures may allow us to identify, or at least constrain, the initial conditions in star-forming clusters that still retain most of their embedding gas.

The kinematic signatures found in the elongated subvirial cluster simulations may shed some light on kinematics within nearby young clusters. As one example, this work shows that the gradient produced in simulated clusters is qualitatively similar to that observed in the radial velocities of the ONC members. Although the ONC kinematic data display some additional asymmetry not observed in the simulated clusters, this asymmetry is likely to be due to the more complicated environment and feedback processes which are not well represented by the simulation. Nevertheless, the general structure and magnitude of the observed kinematic signature in the ONC may be explained theoretically, provided that the stars are formed with subvirial initial velocities.

Current instruments such as the Hectochelle and MIKE have helped make large spectroscopic studies of many objects more efficient and have produced many radial velocity studies of stellar clusters as well as larger globular clusters and dwarf galaxies. These instruments have provided insight into the kinematics of astronomical objects ranging from the rotation of individual stars to the large-scale dynamics of galaxies. In the next decade, the *GAIA* mission will provide the opportunity to study the three-dimensional kinematics of clusters with exquisite detail. For example, proper motions and radial velocities will be measured for stars in ONC brighter than 20th magnitude. This study will result in accurate transverse velocities to combine with the radial velocities supplemented by ground-based observations. As more detailed kinematic data become available for the ONC and other young clusters, they should be used in conjunction with cluster simulations such as those presented here to understand the initial conditions necessary to produce the observed kinematics. A more detailed understanding of the initial conditions can then inform cluster formation and evolution models, with the overarching goal of better understanding star and planet formation within young stellar clusters.

CHAPTER V

Tidal Disruption of Protoclusters in Giant Molecular Clouds

5.1 Introduction

Over the last three decades it has become evident that molecular clouds serve as the site of all star formation within galaxies with the result that a clear understanding of molecular cloud structure and evolution is necessary to fully describe the initial conditions for star formation. Typical giant molecular clouds (GMCs) are $\sim 10 - 50$ pc across and have masses between 10^6 and 10^7 $M_\odot$ (Liszt et al. 1981; Solomon et al. 1987). They are nonuniform, composed of high density clumps with sizes of $\sim 1 - 10$ pc and masses of $\sim 10^2 - 10^5$ $M_\odot$ embedded in a lower density background (Kramer et al. 1998; Heyer & Terebey 1998). These high density clumps are the sites of star formation within GMCs.

Although GMCs do not globally collapse, many of the small-scale high density clumps undergo local collapse and fragmentation. The most massive of these clumps produce clusters of young stars (Ballesteros-Paredes et al. 2007). Throughout this chapter, the term "protocluster" will refer to these massive, high density regions within molecular clouds which have the potential to produce clusters of stars. The process by which protoclusters fragment into collapsing substructures and eventually protostars is complex and not completely understood. It may be due to a combination of Jeans instabilities, the decay of turbulence (Klessen & Burkert 2000; 2001), and the decoupling of fluid and MHD waves (Myers 1998). Observations of star-forming regions reveal that newly formed clusters of

stars are not isolated within molecular clouds. Rather, star-forming regions of molecular clouds tend to contain multiple clusters and smaller groups of young stellar objects near each other (Allen et al. 2007).

Since GMCs are highly nonuniform in structure and there is evidence of clusters forming near other clusters, a relevant question in cluster formation is: under what conditions can the collapse of a protocluster be treated in isolation, i.e. ignoring the influence of the surrounding GMC environment?

This question is analogous to the question of how star and planet formation in cluster environments differs from formation in isolation. Studies that have considered star and planet formation within clustered environments have shown that environment may have modest to significant effects on the formation processes depending on the properties of cluster considered. Specifically, in very dense massive clusters frequent close encounters between stars may disrupt disks and young solar systems and UV radiation from massive stars may cause photoevaporation of protostellar disks (Bonnell & Kroupa 1998; Störzer & Hollenbach 1999). However, in more intermediate-sized clusters, with parameters typical of those observed within $\sim$ 1 kpc of the sun, interactions between stars are much less common, and the cluster's effects on planet-forming disks are relatively modest (Adams et al. 2006). In this study, we consider a similar question, but on a larger scale and at an earlier time in cluster development.

The above question can be addressed in a gross way with simple tidal force estimates, i.e. calculating the Roche limit. However the analytic Roche limit does not provide the details of how tidal distortion affects the evolution of the internal protocluster structure, how this evolution varies with the initial cloud structure, nor how it depends on the relative motion of the protocluster with respect to its environment. To address these questions, one must complete numerical simulations of the collapsing protocluster within its GMC

environment.

To this end, we perform an ensemble of N-body simulations to calculate the collapse of a protocluster in the presence of a nearby massive object in the same GMC. The point mass is intended to represent another protocluster or high density region that is sufficiently massive and compact enough to be roughly modeled as a point mass. These calculations treat only the gravitational interactions and ignore the effects of gas pressure, stellar winds, and radiation. Molecular cloud maps of star-forming regions contain numerous dense gas structures with varying geometries, so a full numerical investigation of this question should consider protoclusters with spherical, flattened, and filamentary initial geometries. In this study, we focus on flattened disk-shaped protoclusters.

Our choice of protocluster geometry is partially motivated by observations of star-forming regions revealing flattened, layered, and/or filamentary cloud structures. For example shells of molecular gas surrounding OB stars have been identified by Deharveng et al. (2005) and Churchwell et al. (2006). Within many of these shells triggered star formation appears to be occurring (Churchwell et al. 2006; Zavagno et al. 2006). Furthermore, the distribution of young stars within embedded clusters is often aligned with the elongation or filament structure of the embedding gas (Allen et al. 2007; Kumar et al. 2007; Teixeira et al. 2006). Observations such as these suggest that "reduced dimensionality" may be a characteristic of star-forming clouds.

Flattened cloud structures may be formed by OB winds (Weaver et al. 1977; Whitworth et al. 1994) or expanding H II regions (Elmegreen & Lada 1977) sweeping up and condensing nearby cold molecular gas. Cluster-forming clouds that are believed to have been compressed by these mechanisms include Orion B near the OB1 association (Wilson et al. 2005) and the DR 21 ridge near the Cyg OB2 association (Schneider et al. 2006; Kumar et al. 2007). Elmegreen (1998) and Whitworth (2005) provide more detailed dis-

cussions of proposed flattening mechanisms capable of producing the structure observed in many star-forming regions. Simulations by Burkert & Hartmann (2004) demonstrated that even in isolation, finite self-gravitating sheets collapse into dense structures with interesting geometries.

In addition to the observational evidence for flattened initial states, we choose to simulate flattened protoclusters because they are harder to disrupt than spherical protoclusters of the same mass and radius. This is because the disks are more centrally concentrated and thus more tightly bound. Therefore they are more likely to succeed in forming stellar clusters than their 3D counterparts, all else being equal.

We simulate the collapse of a disk-shaped protocluster in the presence of another dense object in the GMC to determine the survivability of collapsing protoclusters in GMCs. In Section 5.2 the N-body collapse calculations are described. The results from these simulations are summarized in Section 5.3, and a discussion of these results in the context of observed star-forming regions is presented in Section 5.4. Appendix B contains a discussion of the simulations of collapsing systems with analytic solutions used to estimate the uncertainties in N-body calculations of the dynamics of gaseous systems.

5.2 Numerical Calculation of Disk Collapse

In this study, we complete an ensemble of N-body simulations to study the collapse of flattened protoclusters in the presence of a nearby dense object represented by a massive point particle. This dense object may be another dense protocluster, a region that is currently forming stars, a stellar cluster, or another significant density enhancement in the GMC, provided that it is more massive than the protocluster and small enough that its gravitational influence on the protocluster can be well approximated as a point mass. A modified version of the NBODY2 direct N-body integration code (Aarseth 2001; 2003) is used to complete the simulations. The NBODY2 code was modified to implement a sink

cell algorithm associated with the particle initially located at the center of the protocluster disk. This algorithm allows particles that collapse to the center of the disk to accrete onto it. A more detailed discussion of the sink cell algorithm in included in the Appendix.

A fluid dynamics code will always model a fluid system with more precision than will an N-body code because on small scales close encounters between point masses deviate from fluid behavior. For this reason N-body techniques are not widely used to study fluid problems. Two significant concerns arise when modeling a fluid system with an N-body code. First, N-body simulations do not take into account the pressure forces between point particles. Secondly, close gravitational scattering encounters between point particles are not physically realistic in fluid systems. If these two concerns are appropriately addressed, an N-body code may be competitive with a full fluid simulation when studying the large-scale gravitational evolution of a fluid.

Specifically, if the fluid can be approximated as cold and pressure free, the dominant force between fluid elements is gravity and thus the fluid elements may be modeled as individual particles moving under the influence of their mutual gravitational potential. Protoclusters are cold with typical temperatures of $\lesssim 20$ K (Liszt et al. 1981; Solomon et al. 1987) and can be approximated as pressure free fluids until the late stages of collapse. Our choice of radially symmetric ring structure was chosen specifically to minimize the number of close scattering interactions that particles undergo during disk evolution (For a more detailed discussion, see Appendix.) Thus we can carefully use an N-body code to address the large-scale question of when the collapse of a protocluster may be treated as if it occurs in isolation, neglecting the effects of the surrounding GMC environment.

In addition, for modest values of N (in this study, $N \lesssim 1000$) N-body simulations are computationally more efficient than fluid codes. Therefore, judicious use of an N-body code with a relatively modest investment of computational time can return a broad

understanding of a system over a wide range of parameter space.

To better understand the regime in which the N-body simulation reliably models gaseous disk collapse behavior and thus can be used effectively in this study, the code must be systematically tested. Therefore, this particular N-body code was used to complete simulations of collapsing systems for which analytic solutions exist. Specifically, the collapse of an isolated Maclaurin disk and Mestel disk were simulated and the results of the simulations compared to the analytic collapse solutions. We find that the N-body simulations predict free-fall times for the Maclaurin and Mestel disks with errors less than 3.4% and 2.4% and cumulative mass profiles with errors less than 6.1% and 7.4%, respectively. A complete discussion of these test calculations and comparison to the pressure-free analytic collapse solutions is provided in the Appendix and summarized in Table B.1.

It is important to stress that this approach investigates only the gravitational interactions within the disk and between the disk and the point mass. Other physical processes in gas such as pressure and turbulence are not included in our simulations of protocluster collapse. The detailed structure of the final cluster-forming cloud and the amount of star formation which will subsequently occur depends on these processes. A more in depth discussion of how these physical processes may affect the results of our simulations is reserved for Section 5.4.2.

We assume that the flattened protoclusters are formed when a three dimensional dense cloud is compressed into a two dimensional disk. This assumption is motivated by evidence that flattened structures in star-forming regions may be created by stellar winds or shocks sweeping material into a layer. Thus the surface density of the protocluster disk depends on the assumed density of the pre-flattened three dimensional cloud from which it is formed. Consider a uniform density sphere which is compressed along one dimension. The resulting

density distribution, a Maclaurin disk, has the surface density profile

$$\Sigma(r) = \begin{cases} \Sigma(0)\left[1 - \left(\frac{r}{r_d}\right)^2\right]^{1/2}, & 0 \leq r \leq r_d \\ 0, & r > r_d, \end{cases} \tag{5.1}$$

where r_d is the disk radius (Binney & Tremaine 1987).

The majority of our simulations considered disks that are initially described by Maclaurin surface density profiles. These disks are weakly centrally condensed and consistent with the disk formation scenario described above. It is difficult to form a less centrally condensed disk distribution by flattening a realistic three dimensional clump of gas. However, flattening of a somewhat centrally condensed three dimensional clump of gas will produce an even more strongly centrally concentrated disk. To investigate the evolutionary differences central concentration may create, a limited number of strongly centrally concentrated disks were also completed. Specifically we considered the pre-flattened three dimensional dense cloud with the density distribution of a singular isothermal sphere. When flattened it produces a Mestel disk described by the surface density distribution

$$\Sigma(r) = \frac{\Sigma(A)A}{r}, 0 < r < \infty, \tag{5.2}$$

where $\Sigma(A)$ is the surface density at the fiducial radius A (Mestel 1963). A comparison of the Maclaurin and Mestel disk evolution is included in Section 5.4.1.

The free-fall time for a particle initially at rest at radius $r \leq r_d$ in a Maclaurin disk of mass M_d is

$$t_{\rm ff}(r) = \sqrt{\frac{\pi}{6}}\sqrt{\frac{r_d^3}{GM_d}}. \tag{5.3}$$

Therefore, a Maclaurin disk collapses all at once. The free-fall time for a particle initially at rest at radius r in a Mestel disk is

$$t_{\rm ff}(r) = \frac{\sqrt{\pi}}{4}\frac{r}{\sqrt{G\Sigma(A)A}} \tag{5.4}$$

resulting in an inside-out collapse.

Each simulated disk is composed of a central point mass and 25 rings of 32 equal mass particles. The mass of the central particle and of each ring is varied to produce the desired surface density distribution. Each disk has a total mass of $M_d = 10^3$ $M_\odot$ and a radius of $r_d = 1$ pc. (The simulated Mestel disk is truncated at r_d.) For star formation efficiencies of ~ 0.3 these parameters are consistent with observations of young clusters with a stellar masses of a few hundred solar masses and radii on the order of a parsec (Lada & Lada 2003; Porras et al. 2003). For Maclaurin and Mestel disks with these parameters the free-fall time of a particle initially at rest at r_d is 0.342 Myr and 0.525 Myr respectively.

In this study we investigate the disruption of a protocluster disk due a massive point particle M_c which represents a neighboring high density region in the GMC a distance d from the center of the disk and in the plane defined by the disk. We choose this initial geometry because the most efficient way to tidally disrupt an axisymmetric disk is by placing the massive perturber in the plane of the disk. A point mass coincident with the symmetry axis will encourage disk collapse or, if the separation distance is small enough, accretion onto the massive particle. A point mass that is neither coincident with the symmetry axis nor in the disk plane will tidally distort the disk, but not as strongly as a point mass at the same distance but located in the plane of the disk.

We consider disks that have both zero and nonzero initial velocities with respect to the nearby point mass, point masses within the range $M_c = 1 - 10^3 M_d$ ($10^3 - 10^6$ $M_\odot$), and separation distances of $d = 2 - 10 r_d$ ($2 - 10$ pc). The majority of the simulations consider disks with Maclaurin density profiles. A limited number of simulations were also completed using the more centrally condensed Mestel density distribution. The results for the Maclaurin and Mestel disks are compared in Section 5.3. Disk collapse begins at time $t = 0$ and continues until the disk is accreted onto the neighboring point mass or reaches a maximum mean surface density. This maximum value occurs at approximately the disk's

free-fall time and is explained in more detail in Section 5.3.3.

By modeling the nearby high density region as a point mass, we overestimate its effect on the collapsing disk. The point mass representation is only exact for density enhancements that have spherically symmetric mass distributions (and a handful of special nonspherical mass distributions). The high density clump in the GMC will likely be a distributed mass which does not fall into one of these special cases, and will exert a force on the disk that is less than the force of a point particle with a mass equal to the mass of the clump and located at the clump's center. Therefore, our estimates of tidal disruption may not be applicable in regions containing larger amounts of distributed dense gas, for example the Orion (L1641) region (see Section 5.4 for further discussion).

A large body of work exists concerning the destructive effects galaxy and GMC environment can have on stellar clusters. Terlevich (1987) and Theuns (1991) completed N-body simulations to investigate the effect the galactic tidal field and interstellar clouds have on the long-term evolution of initially bound stellar clusters. More recent studies have considered the disruption of a stellar cluster due to interactions with passing spiral arms and GMCs (Gieles et al. 2006; 2007). In addition, there have been many numerical studies of the disruption of stellar clusters when the original embedding gas is violently removed by winds from massive stars or nearby supernovae (Lada et al. 1984; Geyer & Burkert 2001; Adams 2000). These works consider the interaction of stellar clusters and stellar cluster members with their environments while our calculations consider an earlier stage in the life of a stellar cluster. Specifically we determine the effects of GMC environment on the clouds that are possible progenitors of stellar clusters.

5.3 Simulation Results

The initial simulations consider the behavior of a collapsing Maclaurin disk in the presence of a massive point particle for various mass ratios and separation distances. For

comparison, a limited number of simulations of collapsing Mestel disks were also completed. The results of these calculations are summarized below.

5.3.1 Interaction Outcomes

In each simulation, the disk evolves according to one of three distinct behavior patterns: *collapse*, *elongation*, or *accretion*. The disk evolution depends most sensitively on the mass of the neighboring point mass and the initial distance of separation (see Section 5.3.2 for further discussion.) Figure 5.1 provides a face on view of disks evolving via different scenarios. For clarity, all of the disks depicted in Figure 5.1 are initially 3.0 pc from a massive particle, and only the mass of the particle is varied.

Figure 5.1 (a) depicts the evolution of a disk that follows the *collapse* evolution scenario. This disk collapses to a point-like object with little to no distortion in the disk's shape. A small amount of elongation along the x-axis does occur. This is to be expected as it is the axis which intersects the center of the disk and the massive point particle. However, the ratio of the short axis of the disk to the long axis of the disk ($(\Delta y/\Delta x)_{min}$, see Section 5.3.4) remains greater than 0.5 for all disks that evolve via the collapse scenario.

Elongation refers to disks that collapse while being tidally squeezed. These disks result in filament-like dense structures. The elongation scenario is further subdivided into two categories: weak and strong elongation. *Weak elongation* occurs when the disk collapses into a filament that is shorter than the initial diameter of the disk. On the other hand, *strong elongation* occurs when the disk is stretched into a filament that is longer than the initial disk diameter. The latter behavior indicates that the force of tidal disruption is stronger than the force of collapse.

Figure 5.1 (b) displays the evolution of a Maclaurin disk that undergoes weak elongation. The disk collapses as in the collapse scenario, but at earlier times shows significant distortion. The differences between strong and weak elongation become apparent when

Figure 5.1 (b) is compared to Figure 5.1 (c). A disk that is strongly elongated becomes significantly tidally stretched. Tidal interaction, rather than gravitational collapse dominates the disks evolution. In addition, a strongly elongated disk accelerates toward the system's center of mass more than a weakly elongated disk, which is another indication of the strength of the force between the disk and the neighboring point mass.

The evolution of a disk *accreting* onto the neighboring point mass is shown in Figure 5.1 (d). The disk is significantly stretched out by the tidal force of the massive neighbor. Moreover, it travels the initial separation distance quickly enough that the disk does not have time to collapse under its own self-gravity (as in the collapse or weak elongation scenarios), or reach a maximum density as a filament (as in the strong elongation scenario).

5.3.2 Dependence of Outcome on Neighbor Mass and Distance

Figure 5.2 displays the behavior of the Maclaurin and Mestel disks as a function of the influencing particle mass, M_c, and the initial separation distance, d. The portions of M-d space in which the systems behave differently are separated by lines in the figure. Systems that reside in the lower right portion of the plot will have disks that collapse without disruption or distortion from the nearby clump. This is the region of M-d space in which protocluster disk collapse occurs as if in isolation. The band of M-d space stretching from low mass and low separation distance to high mass and high separation distance is the region in which the disk undergoes elongation into a filament as it collapses. Systems residing within this regime should form filaments stretched out toward the massive nearby high density regions. Finally, systems with properties in the upper left portion of the M-d plot are those in which the protocluster disks will accrete onto the nearby massive object. We should not expect to find individually collapsing protoclusters near massive dense objects with these properties.

A constant value of initial force between the center of the disk and the massive particle

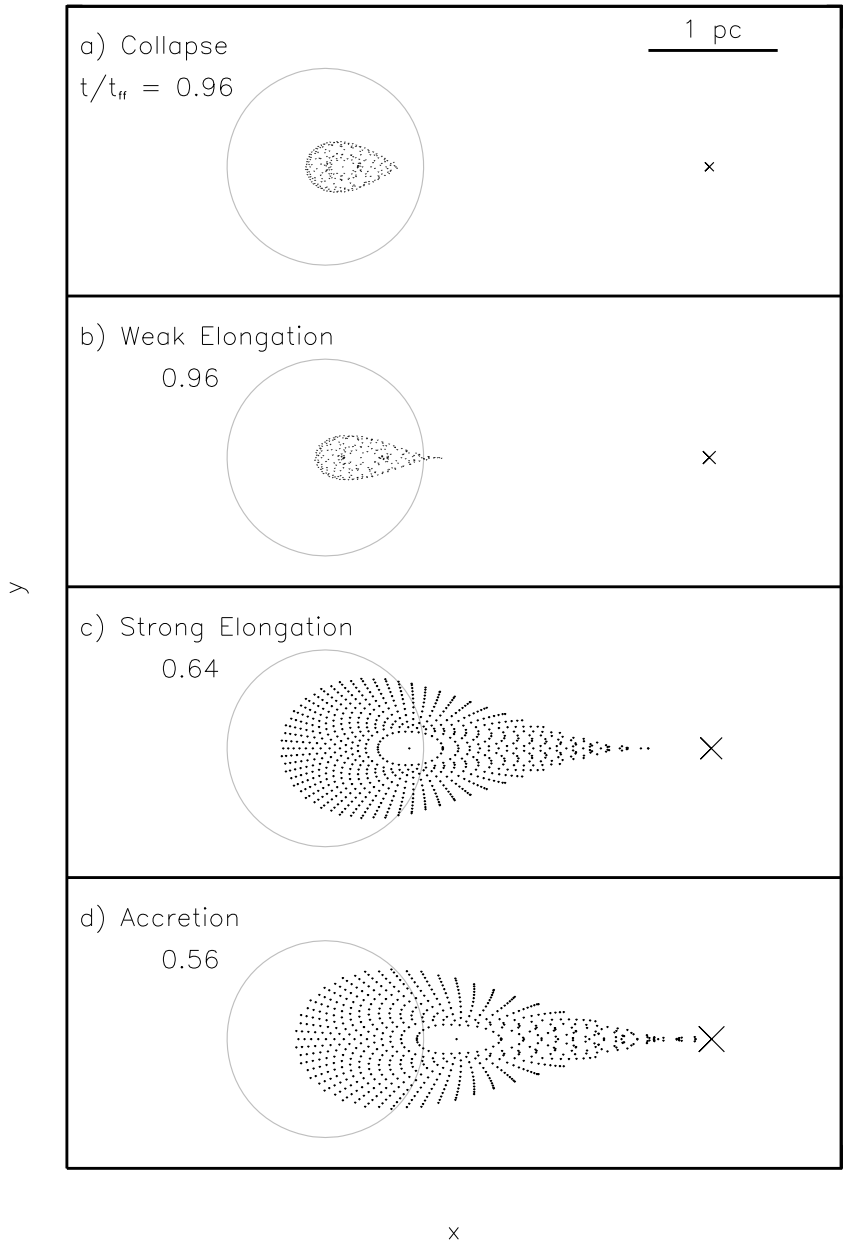

Figure 5.1: Face-on view of the collapse of a Maclaurin disk 3.0 pc away from a high mass particle. Each point denotes the position of a particle within the disk. Panel a): *Collapse:* undistorted collapse of disk to a point, point mass $M_c = 5M_d$. Panel b): *Weak Elongation:* collapse of a disk to short filament, point mass $M_c = 10M_d$. Panel c): *Strong Elongation:* stretching of disk into a long filament, point mass $M_c = 50M_d$. Panel d): *Accretion:* accretion of disk onto a nearby massive particle, point mass $M_c = 100M_d$. The location of the point mass is marked by an X where the size of the X indicates the mass. For each simulation, the display time which most clearly represents the evolution scenario was chosen. The times are noted in units of the analytic free-fall time of the disk in isolation ($t_{\rm ff} = 0.342$ Myr). The size and position of the disk at time $t = 0$ is indicated by the circle.

corresponds to a slope of 2 in Figure 5.2 due to the inverse-square nature of the gravitational force. The dividing lines between regions of different system behavior have slopes slightly steeper than 2 due to the geometry of the interacting system. For smaller values of d, the disk has less distance to travel before it will accrete onto the nearby point mass. Furthermore, for smaller values of d the point mass will more effectively squeeze the disk along the y-axis and stretch the disk along the x-axis (where the axes are defined as in Figure 5.1). These processes combined cause two systems with equal values of M_c/d^2 but different initial separations to behave differently. Specifically, the system with smaller d will be more easily distorted by the nearby point mass, which is consistent with the results of our simulations.

Calculation of the Roche limit also provides insight into the behavior of a collapsing disk under the influence of a nearby massive object. In our nomenclature, the Roche limit is the distance d at which an object with radius r_d and mass M_d will be torn apart by a point mass M_c (Shu 1982). Specifically, it is the distance at which the tidal force from the nearby point mass is equal to the force that causes the disk to collapse under its own self-gravity. The calculation of the Roche limit depends on the density distribution of the disk and is given by $d_R = \kappa(M_d/M_c)^{1/3} r_d$ where $\kappa = (8/3\pi)^{1/3}$ for the Maclaurin disk and $\kappa = 2^{1/3}$ for the Mestel disk. In Figure 5.2 the Roche limit is denoted by a dashed line with slope 3 in each panel. Note that the Roche limit approximately corresponds to the separation between the weak and strong elongation. This further supports the distinction between the regime in which the tidal disruption dominates the system behavior and the regime in which self-gravitational collapse dominates the disk behavior.

The evolution of a Mestel and Maclaurin disks are very similar for a given disk-to-point mass ratio and initial separation. However, the Mestel disks are slightly more easily disrupted. Specifically, accretion and significant elongation occur at more modest mass

ratios for a given initial separation, d. Comparison of the inside-out collapse of a Mestel disk to the uniform collapse of the Maclaurin disk provides insight into why this is so. The free-fall time for the outer portion of a Mestel disk is about 50% longer than that of a corresponding Maclaurin disk. Therefore the exterior of the Mestel disk is exposed to the tidal forces due to the nearby point mass for a longer period of time. In addition, the Mestel disk has a longer amount of time to travel toward the massive particle before it collapses, more easily coming near enough for edge accretion to occur. This difference is also borne out by the Roche limit calculation: the power law coefficient κ is larger for the Mestel disk which indicates that tidal disruption occurs at larger distances for the Mestel disk than for the Maclaurin disk. It is important to note that although the outer regions of the Mestel disk are more vulnerable to distortion and accretion, the interior of a Mestel disk is extremely robust against tidal distortion. Even a Mestel disk that is stretched into a filament (strong elongation) contains a massive core which is a remnant of the rapid collapse of the inner portion of the disk.

5.3.3 Disk Density Enhancement

Figure 5.3 presents the maximum surface density enhancement factor for each simulated Maclaurin disk over the course of the disk's evolution or distortion. The density enhancement factor $\Sigma(t)/\Sigma_0$ is defined as the ratio of the mean surface density at time t to the initial mean surface density. To calculate the mean surface density one of the outer rings in the disk is identified as the boundary of the disk. The average surface density is then the ratio of the mass contained interior to that ring (including the mass of the ring itself) to the area of the convex hull that encircles all particles interior to the chosen ring. The convex hull of a set of points is the smallest convex set that contains all of the points in the set, and can be informally thought of as the polygon created by stretching a rubber band around the outside of a set of points (Ripley & Rasson 1977). For the data presented in

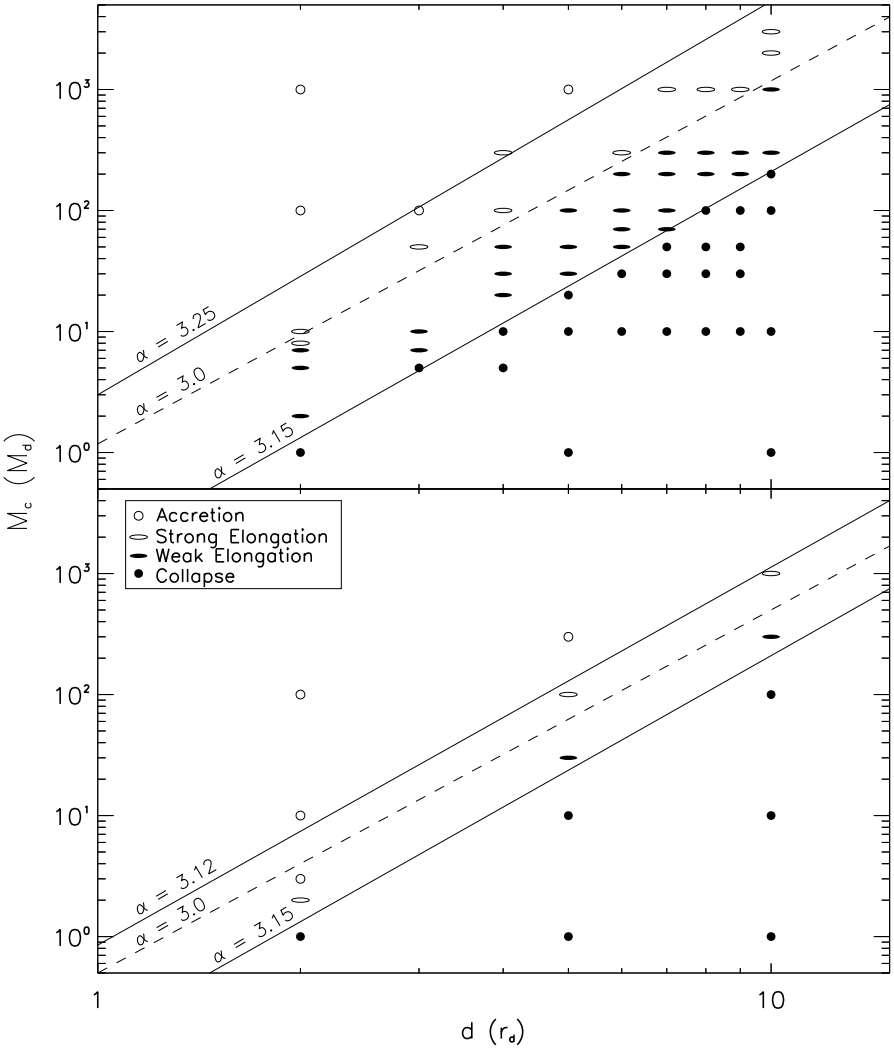

Figure 5.2: Maclaurin (*upper panel*) and Mestel (*lower panel*) disk collapse behavior as a function of the mass of the point mass M_c in units of disk mass and the initial separation d in units of disk radius. Filled circles correspond to disks that collapse to point-like objects with little or no distortion due to the nearby massive point mass, *Collapse*. Filled ellipses correspond to disks that collapse to filament-like structures under the influence of a nearby massive point mass, *Weak Elongation*. Open ellipses correspond to disks that are tidally stretched to long filament-like structures under the influence of a nearby point mass, *Strong Elongation*. Open circles correspond to disks that accrete onto the nearby point mass before significant collapse occurs, *Accretion*. Solid lines separate the portions of the M-d space in which systems exhibit significantly different collapse behaviors. The dashed line in each panel indicates the Roche limit. The slopes α of the solid and dashed lines are indicated in each panel.

Figure 5.3 the boundary chosen to calculate the surface density enhancement factor is the smallest ring containing at least 90% of the mass (We do not choose the ring that encloses 100% of the mass in order to reduce "edge effects" discussed in the Appendix).

As disk collapse proceeds the value of $\Sigma(t)/\Sigma_0$ increases as the particles in the disk approach the disk's center. An artifact of the simulation technique is that some disk particles pass close to the sink cell without entering it and continue outward on a radial path away from the disk's center. Thus the mean density reaches a maximum (at approximately the analytic free-fall time for the disk collapse in isolation) and then begins to decrease. This is not commensurate with the behavior of a fluid which continues to collapse until pressure forces slow and eventually halt the collapse. Therefore, when a collapsing disk reaches a maximum density we consider this to be the end of the collapse phase.

While the evolution scenarios give general information about the fate and morphology of disrupted protoclusters, the surface density enhancement factor gives more detailed information about the amount of collapse that occurs within the protocluster. The disks that collapse to a point with little to no distortion attain the highest values of Σ_{max}/Σ_0. The Mestel disks attain values of Σ_{max}/Σ_0 which are significantly higher than the Maclaurin disks. This again is due to the fact that the Mestel disk collapses from the inside-out. The collapse produces a massive central core which is not even slightly distorted due to the tidal stretching/squeezing of the nearby massive object. For larger values of M_c/d^2 the maximum density enhancement factor drops due to the more significant interactions between the collapsing disk and the point mass. The filamentary structures created during these interactions have much lower surface densities than the point-like structures. Disks that do not collapse onto themselves but instead accrete directly onto the nearby point mass have disk surface densities that decrease as a function of time, and thus attain values of $\Sigma_{max}/\Sigma_0 \sim 1$ near the beginning of the disk's evolution.

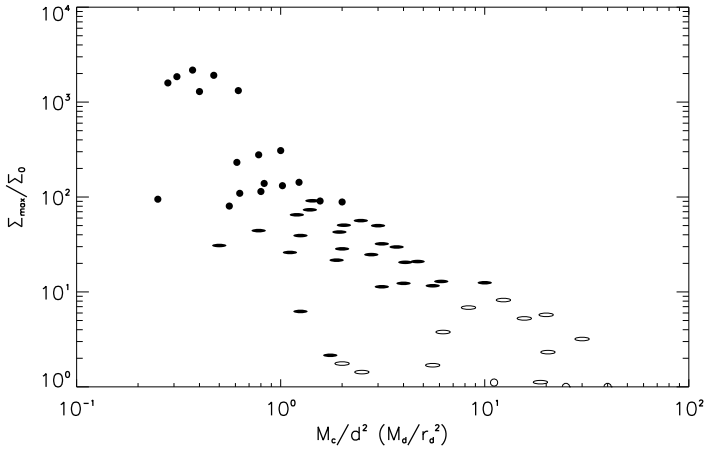

Figure 5.3: Maximum density enhancement factor as a function of initial disk-point mass configuration in terms of M_c/d^2 (in units of M_d/r_d^2) for the Maclaurin disk simulations. Plotting symbols correspond to behavior of disk-point mass system as in Figure 5.2.

5.3.4 Disk Elongation

A final way of representing the difference between the evolution of disks in the presence of a nearby massive particle is to compare the amount of disk distortion which occurs as the disk collapses. Because the point mass is located on the x-axis, tidal forces cause the disks to collapse along the y direction faster than along the x direction. Therefore, as the disk evolves the ratio of the disks' extent along the y-axis to its extent along the x-axis decreases from the initial value of 1. Figure 5.4 displays the minimum axis ratio $(\Delta y/\Delta x)_{min}$ that each simulated Maclaurin disk acquires during collapse. As is evident in the plot, the larger the initial force value, the more effectively tidal forces squeeze and stretch the disk as it collapses. The scatter in this plot is due to the geometric considerations discussed in Section 5.3.2 which cause systems with small separation distances to be more severely distorted due to tidal squeezing. Because the outer portions of a Mestel disk are bound less tightly to the center of mass of the disk, Mestel disks develop significantly smaller values of $(\Delta y/\Delta x)_{min}$ than do the Maclaurin disks with the same values of M_c/d^2.

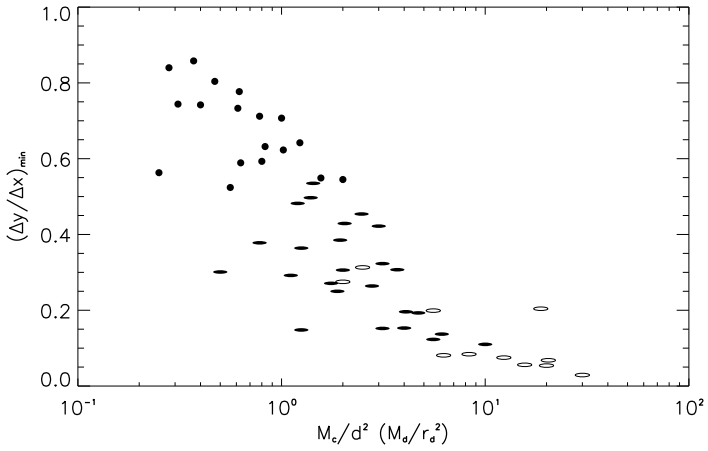

Figure 5.4: Minimum axis ratio ($\Delta y/\Delta x$) as a function of initial disk-point mass configuration in terms of M_c/d^2 (in units of M_d/r_d^2) for the Maclaurin disk simulations. Plotting symbols correspond to behavior of disk-point mass system as in Figure 5.2.

5.3.5 Disk Dispersal

It is important to note that even a disk which is substantially distorted due to the interaction ultimately forms a dense structure. For the mass ratios and initial separations considered in this study, the tidal forces are not violent enough to disperse the disk mass into the background GMC. Instead the tidal forces determine the resulting geometry of the dense structure. Even the most violent interactions between a disk and a point mass result in the disk accreting onto the massive particle. We assume this point mass represents a high density region. It is likely that this region is gravitationally unstable, or becomes so with the additional accreted mass, and therefore will collapse into a dense structure as well. Thus, for the considered range of initial conditions, gravitational interaction alone is incapable of making dense structures (i.e., the disks) significantly less dense. The most destructive an interaction can be is to collect nearby gas onto another dense structure. This effectively moves the dense structures around but does not destroy them. Consequently, under the influence of gravity alone, dense structures are destined to remain dense structures.

Our simulations assume that a protocluster starts in an initially cold state, that is there

are no internal motions. Therefore, the initial conditions force our protoclusters to be gravitationally bound objects. Thus, the final states of the tidally distorted protoclusters are also gravitationally bound. In order to disperse the mass contained within these dense objects a mechanism other than gravity must be invoked, for example winds from young massive stars formed within or very near to the protocluster.

5.3.6 Moving Interactions

Observations indicate that GMCs are not quiescent static objects but rather they exhibit moderate amounts of internal motion. For GMCs with sizes of $10-50$ pc, the corresponding clump to clump velocities are on the order of a few kilometers per second. Therefore, in addition to the simulations described above, we complete simulations of the collapse of Maclaurin disks that are initially moving with respect to the nearby massive particle.

This ensemble of simulations considers systems with particle-to-disk mass ratios of $10-1000$, initial separation distances of $5-10$ pc, and initial relative velocities of $1-10$ km s^{-1}. The angle between the x-axis and disk's velocity vector varies from 15 to 45 degrees. We found that for these initial conditions, the disk-point mass systems behaved in much the same way as the corresponding zero velocity systems. The collapse times for the disks are short (0.342 Myr) so that the disks do not travel a significant distance before collapse, and therefore the non-zero velocities do not significantly change the behavior of the disk-point mass system.

For the 60 simulations completed, over 80% of the systems with initial non-zero relative velocities exhibited behavior patterns in the same category (as defined in Section 5.3.1) as the corresponding system with an initial relative velocity of zero. Systems that did not exhibit the same behavior as their zero velocity counterparts were slightly more interactive. Specifically, the system with $M_c = 1000M_d$, $d = 7r_d$, and $v_0 > 0$ km s^{-1} accreted onto the nearby point mass. The disk had a positive initial velocity component in the direction of

the point mass. This effectively reduced the separation distance d and shifted the position of the system in the behavior diagram (Figure 5.2) to the left.

5.4 Discussion

5.4.1 Initial Central Concentration and Tidal Disruption

The results of our simulations imply that central concentration has a modest effect on the evolution of disks in the presence of a massive perturber. Specifically the Mestel disks, which are strongly centrally concentrated, have outer regions which are more easily disrupted by the point mass than the Maclaurin disks. For a given disk to point mass ratio, Mestel disks exhibit accretion onto the point mass and stronger elongation at larger distances than the Maclaurin disks, due in large part to the longer free-fall time of the outer portions of the Mestel disk.

While Mestel disks have exteriors that are more easily disrupted, their interiors collapse rapidly producing a dense core (Section 5.3.3). In Mestel disks that are tidally stretched into filaments, the result is a very dense inner core with little elongation that is surrounded by an elongated lower density halo of material. On the other hand, Maclaurin disks which are tidally stretched produce structures that are less centrally peaked and less strongly elongated. Assuming stellar cluster structure reflects the initial protocluster structure, the ONC is a good example of a dense centrally concentrated cluster with a relatively lower density star-forming region surrounding it (O'dell 2001). NGC 1333 is a good example of a cluster which shows moderate elongation (axis ratio $\sim 2:1$) but a roughly constant density in the central regions. (Gutermuth et al. 2008b). If NGC 1333 formed from a flattened protocluster disk, it is likely that the disk was less centrally condensed and more closely resembled a Maclaurin disk than a Mestel disk.

An important point to note is that the tidal zone outside of which disks can be considered to collapse as if in isolation is the same for both Maclaurin and Mestel disks. The bottom

line separating the collapse and weak evolution scenarios in the M-d plot (Figure 5.2 is the same for both the Maclaurin disks (top panel) and the Mestel disks (bottom panel). Thus, on the largest scales, disruption of the protocluster disk is not sensitive to the specific surface density distribution. However, once a protocluster is within the tidal zone, the amount of distortion the disk will experience does depend on the amount of central concentration. The more centrally condensed disks have exteriors that are more easily disrupted and interiors that are more robust against tidal distortion.

5.4.2 Effects of Other Physical Processes

The effects of pressure have not been included in the N-body simulations and will produce some modifications to the results presented here. As disk collapse proceeds, pressure will increase and at the latest states of collapse may prevent the entire disk from collapsing to a concentrated point. Therefore, actual protocluster disks will probably not have mean surface densities that are as high as those reached by our simulated disks. In addition, tidal stretching of the protocluster gas will produce pressure enhancements along the x-axis which may results in less compression in the y direction, producing clusters with elongations less extreme than those quoted in Section 5.3.4.

Small deviations from a perfectly smooth initial density distribution will be magnified during collapse and will likely cause fragmentation and lead to star formation (Klessen & Burkert 2000; 2001; Heitsch et al. 2008). If O and B stars are formed within the protocluster, strong winds produced by these stars may act to disrupt the protocluster from the inside out, possibly halting star formation near the O and B stars and altering the shape of the embeddeding gas. However, these effects take place at a later time in cluster evolution than is considered in this investigation.

Our simulations considered protocluster disks composed of particles with zero initial velocity. However, observations of protocluster sized cloud cores reveal unstructured internal

velocities of ~ 1 km s^{-1}. These velocities are less than the escape speed from the edge of a 10^3 M$_\odot$ disk with a 1 pc radius which is ~ 3 km s^{-1}, and below the average speed required for the protocluster disk to be in virial equilibrium ~ 2 km s^{-1}. Both the escape speed and the virial speed increase as $R_d^{-1/2}$ as the disk collapses (and R_d decreases). Collapse proceeds rapidly ($\lesssim 0.5$ Myr) once a protocluster disk becomes gravitationally unstable and thus it is unlikely that a significant fraction of the protocluster gas parcels will 'evaporate' due to internal motions.

These internal motions however, will contribute to the internal structuring of the collapsing cloud. The angular momentum associated with the internal motions will act to rearrange the density enhancements within the collapsing protocluster and thus perhaps give structure to the forming stellar cluster. These disordered motions may also work to enhance or inhibit star formation within regions of the collapsing disk. However, unless the internal motions are well ordered so that the total angular momentum of the disk is much greater than zero the angular momentum from the internal motions will not be capable of supporting the protocluster against gravitational collapse, or changing the gross geometry of the cluster.

5.4.3 Applications in Cluster-Forming Regions

With recent advances in infrared telescopes, and most recently, with the Spitzer Space Telescope there has been a shift in our understanding of the distribution of young stars within molecular clouds. These higher sensitivity observations reveal that clusters of young stars are not usually isolated within molecular clouds but often have neighboring smaller clusters which were previously unidentified. Examples of regions where clusters appear to be forming near other clusters include the Perseus molecular cloud, Orion A, and the region surrounding Mon R2 (Kirk et al. 2006; Allen 1995; Gutermuth et al., in prep.)

Our simulations allow us to estimate the regions around massive clusters where we

should not expect smaller clusters to successfully form from flattened protocluster clouds. If we consider the system from the perspective of the more massive disrupting point mass, our calculations allow us to define a "tidal zone" around the dense region or massive protocluster that the point mass represents. Within this tidal zone smaller clusters cannot form without significant disruption or distortion. The tidal zone's size depends on the mass and radius of the collapsing protocluster. Specifically, the size of the tidal zone around a given massive object increases as the mass of the collapsing protocluster decreases. In addition, the size of the tidal zone increases as the initial radius of the protocluster increases. This is consistent with the Roche calculation where $d \sim M_d^{-1/3} r_d$.

Recall that the high density disrupting object is treated as point mass in our simulations. This overestimates the strength and focusing of the force the disrupting object has on the collapsing protocluster (assuming that the disrupting object is not exactly spherically symmetric). Therefore, the estimates of the outer region of the tidal zones presented here are upper limits. That is, the tidal zones may in fact be smaller and the tidal distortion less apparent.

Consider a point mass of 10^4 $M_\odot$ a distance d parsecs away from the center of a 10^3 $M_\odot$ Mestel disk truncated at a radius of 1 pc. Figure 5.2 indicates that if the disk center lies within ~ 2 pc of the point mass, it will accrete onto the point mass. However, if the disk center is between ~ 2 and 4 pc from the point mass, the disk will collapse while being elongated into a filament-like structure. If the disk center is more than ~ 4 pc from the point mass, the disk will collapse axisymmetrically, as if in isolation. Therefore our calculations indicate that a 10^4 $M_\odot$ cluster should not have surviving neighbor clusters of 10^3 $M_\odot$ within ~ 2 pc.

The Roche limit for a 10^3 $M_\odot$ Mestel disk with a radius of 1 pc in the presence of a 10^4 $M_\odot$ point mass is $d_R = 2.71$ pc. Therefore the Roche limit falls neatly inside the region

where disk disruption is significant. However, our simulated disks exhibit some distortion at slightly larger distances (~ 4 pc) than the analytic calculation. This is because the Roche calculation ignores the effect of the disk accelerating toward the massive particle as it collapses, and thus underestimates the effect of the gravitational force on the protocluster.

The Maclaurin disk is even more robust against accretion onto the nearby point mass due to its shorter free-fall time. A 10^3 $M_\odot$ Maclaurin disk with radius 1 pc will accrete onto a nearby 10^4 $M_\odot$ point mass only if the separation distance is less than ~ 1.5 pc. If the separation distance is between ~ 1.5 pc and ~ 4 pc the Maclaurin disk will collapse into a filament-like structure, whereas if the separation distance is greater than ~ 4 pc, the disk will collapse as if in isolation. Thus, for both the Maclaurin and Mestel disks, the "tidal zone" in which collapsing protoclusters of 10^3 $M_\odot$ are compromised is ~ 4 pc from a 10^4 $M_\odot$ high density region.

Estimates of this kind are applicable when we consider the distribution of clusters within molecular clouds. For instance, these estimates are consistent with observations of the Perseus molecular cloud which reveal the cluster B5 forming in close proximity to the IC 348 region. Kirk et al. (2006) presented an extinction map of the Perseus star-forming region derived from the Two Micron All Sky Survey images created as a part of the COMPLETE survey (Ridge et al. 2006). They identified 11 "super cores" within this map, including the B5 and IC 348 star-forming regions. These large, high density cores are similar to the types of protoclusters our simulations considered.

In this region a 10^3 $M_\odot$ cluster (B5) appears to be forming near the 2×10^3 $M_\odot$ IC 348 cluster. According to Figure 5.2, we should expect to find a 10^3 $M_\odot$ cluster surviving near a 2×10^3 $M_\odot$ only if it is at least $2.5 - 3$ pc away. Assuming a distance to Perseus of 250 ± 50 pc, the separation of IC 348 and B5 is approximately 4.5 ± 0.9 pc away (in projection) and therefore B5 is safely outside of the tidal zone surrounding IC 348.

Another region where our estimates are applicable is in the region containing Mon R2. Observations of this region indicate smaller clusters surrounding the main Mon R2 cluster. The main Mon R2 cluster contains a total mass (in stars and gas) of ~ 1700 $M_\odot$ and has an effective rations of 3 pc (assuming an average stellar mass of 0.5 $M_\odot$ and an extinction to mass conversion of 1 A_V $pc^{-2} = 15$ $M_\odot$). Therefore, from Figure 5.2 clusters with masses greater than 10^3 $M_\odot$ should not form within about $1-2$ pc of the main Mon R2 cluster. No clusters are found within $1-2$ pc of the main Mon R2 cluster. In fact, the nearest region forming groups of stars is ~ 3.7 pc (in projection) to the east of the center of Mon R2 and has a mass of ~ 135 $M_\odot$ and a radius of 1 pc (Gutermuth et al., in prep). Using the Roche limit calculation, we find that the tidal zone in which a 135 $M_\odot$ cluster with radius may be disrupted in the presence of a 1700 $M_\odot$ point mass is $2-3$ pc depending on the disk density distribution chosen. Assuming the results of our simulations scale down in mass as the Roche calculation does, the estimated tidal zone is somewhat larger, ~ 4 pc. Thus we predict that a protocluster at a distance of 3.7 pc should collapse as if in isolation and not be significantly disrupted by the neighboring 1700 $M_\odot$ cluster.

In regions containing significant amounts of distributed gas, such as the region in L1641 south of the Orion Nebula Cluster (ONC), collapse disruption due to nearby massive objects (in this case the ONC) may be less effective than estimated by these simulations. In this region there is a string of stellar clusters that have developed near one another and near the ONC (Allen 1995; Allen et al. 2007). Dense gas distributed around the protocluster is likely to wash out the gravitational force felt by a collapsing protocluster due to a nearby massive object. This may allow clusters to form nearer each other than one would estimate solely based on the mass and proximity of the nearest massive neighbor. Therefore, care should be taken when applying the estimates presented here to significantly gas-rich regions.

A rough estimate of the average background density required to change the results of

our simulations can be made by assuming the background gas has a uniform density n_0. The force on a protocluster from a 10^4 $M_\odot$ point mass a distance 4 pc from the protocluster center equals the force on the protocluster due to sphere of gas with radius 4 pc centered 4 pc from the protocluster if $n_0 \approx 750$ cm^{-3} (assuming the gas is composed of molecular hydrogen). 4 pc is the edge of the tidal zone for a 10^3 $M_\odot$ protocluster near a 10^4 $M_\odot$ point mass. Thus background gas densities higher than this may begin to wash out the effects of nearby massive perturbers. However, the densities required for the forces to be equal scale as $n_0 \sim d^{-3}$. So for the background gas to have as much influence on the disk as a 10^4 $M_\odot$ point mass 2 pc from the protocluster, a much higher average gas density of $n_0 \approx 6000$ cm^{-3} is required. Typical densities in GMCs range from 10^2 to 10^3 cm^{-3} (Liszt et al. 1981). In the higher density regions, which often exhibit clustered star formation, densities may reach $5 - 15 \times 10^3$ cm^{-3} (Kirk et al. 2006), and so it is in these denser regions of GMCs that our simulations may overestimate the effects of nearby perturbers on protocluster evolution.

Tidal zone estimates of the kind presented here may be applied to other rich star-forming regions such as the Cyguns X region which contains many clusters as well as many sites of current star formation (Schneider et al. 2006, and references therein).

5.5 Summary

Our calculations of the collapse of protoclusters in GMCs provide the framework in which to identify regions where protocluster collapse can be assumed to proceed as if in isolation. The following conclusions can be drawn from the results of our simulations:

- Depending on the geometry and strength of the interaction, protocluster disks either collapse as if in isolation, are weakly or strongly elongated, or are accreted by the neighboring point mass. The outcomes of our simulations are presented in Figure 5.2 and are consistent with the Roche limit estimates of disruption.

- The amount of disk disruption due to a nearby massive particle depends most sensitively on the mass of and distance to the particle and less sensitively on the distribution of material within the protocluster disk.

- The tidal zone defined by the separation between *collapse* and *elongation* evolution scenarios does not sensitively depend on how centrally concentrated the disk is. Maclaurin (weakly centrally concentrated) and Mestel (strongly centrally concentrated) disks have tidal zones that are roughly the same for a given disk to point mass ratio.

- The interior of disks that are initially more centrally condensed are more robust against tidal distortion than those that are less centrally condensed. Therefore, for flattened protoclusters that formed from density distributions that were centrally peaked, it is likely that once the it becomes unstable against gravitational collapse, the inner portion of the disk will continue to collapse, even in the presence of another massive object.

- On account of both the short collapse times of protoclusters and the modest clump to clump velocities observed in GMCs, the interaction outcomes do not depend significantly on the relative velocity between the protocluster and the point mass.

- In systems with conditions consistent with those observed in GMCs, gravitational interactions alone only produce density enhancements within the protoclusters. Thus, tidal stripping does not significantly disperse mass from the condensing disk.

CHAPTER VI

Conclusions

Over the past three decades, a working theory of star and planet formation has been constructed, with the major successes of the theory applying specifically to the formation of single, isolated stars (e.g., Shu et al. 1987). Recent advances in infrared astronomy have unveiled star-forming regions in dramatic detail, revealing that most stellar nurseries contain clusters of young stars embedded in dark dusty clouds of molecular gas (Lada & Lada 2003; Porras et al. 2003; Allen et al. 2007). These observations raise a fundamental question in star and planet formation: if stars form in clusters, how does that clustered environment affect star formation and subsequent planet formation in the disks surrounding young stars? My thesis research addresses this question by characterizing young cluster evolution and determining how effective the cluster environment is at disrupting circumstellar disks and young solar systems.

Since the first discovery of a planet orbiting another main sequence star in 1995, the list of extrasolar planets has grown to over 340, including solar systems very different from our own. Understanding the interaction between planetary formation and the cluster environment is a crucial step in our quest to understand these systems. In young clusters, the planet-forming disks may be quickly evaporated by UV light from nearby massive stars (Johnstone et al. 1998; Shu et al. 1993; Störzer & Hollenbach 1999; Adams et al. 2004). Alternatively, portions of the disk may be disrupted or stripped away during close

encounters with other cluster members (Heller 1993; Ostriker 1994; Kobayashi & Ida 2001). Each of these processes inhibits planet formation within the disk. Furthermore, assuming that a solar system is able to form, a later encounter with another cluster member may jostle the planets out of stable orbits around their host star, or otherwise change the architecture of the planetary system.

This research has focused on the dynamics of young stellar clusters like those found in our solar neighborhood, that is, clusters with intermediate sizes, $N \sim 100 - 3000$, that are embedded in molecular gas during their earliest evolutionary states, and contain stars that initially have subvirial velocities. In Chapter II, we undertook an initial survey of the dynamical evolution of young stellar clusters, specifically comparing subvirial and virial clusters. In addition, we presented calculations of scattering cross sections for disrupting planetary systems and distributions of the FUV luminosities expected in these young clusters. Our work indicates that, when compared to virial clusters, clusters with subvirial initial velocities are more interactive and have members that are exposed to stronger radiation fields. This finding indicates that planet formation in subvirial clusters is more easily compromised by the cluster environment. However, even in subvirial clusters, the interaction rates and radiation levels are relatively low, so that planet formation is only modestly affected by the cluster environment. In Chapter III, we presented the results of a larger parameter space survey in which we systematically studied cluster evolution as a function of initial conditions commonly found in nearby stellar clusters. Armed with our statistical descriptions of the dynamics of the embedded clusters (e.g., the close encounter distributions and the radial profiles), we discussed the implications of specific cluster environments on planetary formation.

Motivated by observations of elongation in many young embedded clusters and by recent kinematic observations of the Orion Nebula Cluster (ONC), we completed a series of

simulations to explore the kinematic signatures produced by the combination of subvirial initial velocities and nonspherical cluster geometries. In Chapter IV, we present a robust kinematic signature that is naturally produced in elongated subvirial clusters: elongated clusters with subvirial initial conditions display a gradient in the radial velocities as a function of projected position along the cluster's major axis. We characterize this signature as a function of cluster elongation, star-formation efficiency, and initial virial state. In addition, we discuss how the strength and shape of the kinematic signature varies due to observational conditions including extinction and projection. Finally, we compared radial velocity measurements of stars in the ONC to the kinematic signature identified in our simulated clusters and found good qualitative agreement, which is an indication that the stars in the ONC were likely formed with subvirial initial velocities and that the ONC is still in a dynamically young state. This study underscores the need to include both subvirial initial conditions and nonspherical (e.g., triaxial) gravitational potentials in cluster studies.

In Chapter V we considered a larger physical system, and focused on the interaction of protocluster clouds. This work still addresses the overarching theme concerning the effects of environment on the formation of astrophysical objects. We studied the collapse of protocluster clouds under the influence of other nearby massive protocluster clouds (or clusters) embedded within the same giant molecular cloud (GMC). Our work concentrated on flattened cloud geometries and discussed the effectiveness of the GMC environment at disrupting and/or preventing protocluster collapse. These highly flattened cluster mass objects are called "disks", although they represented a much larger scale than circumstellar disks that form planets. We found that centrally concentrated disks were quite robust against tidal distortions and that, due to a combination of the short collapse times of protocluster disks and the modest densities of dense massvie objects in GMCs, the assumption

that protocluster collapse occurs as if in isolation is valid in most GMC environments.

This thesis has resulted in two important contributions to the study of young stellar cluster evolution. First, we have demonstrated the importance of including subvirial initial velocities in simulations of young cluster dynamics, as well as the need to break spherical symmetry. Subvirial starting states result in clusters that are more interactive than those which are initially assumed to be in virial equilibrium. These subvirial clusters provide environments in which planet formation may be more easily compromised. In addition, elongated clusters with subvirial initial velocities produce observable kinematic signatures that linger in the clusters throughout the embedded stage. These kinematic signatures may be used to constrain the initial virial state of observed clusters which can, in turn, inform theories of cluster and star formation.

Second, our work has underscored the need for multiple realizations of cluster simulations in order to accurately describe cluster evolution. Intermediate-sized young stellar clusters are intrinsically chaotic and each simulation results in a slightly different set of the output measures that characterize the cluster's evolution. These variations are naturally due to under-sampling of the distributions which describe young clusters, e.g., the initial mass function, the radial distribution of stellar positions, the velocity distribution, etc. By performing a large ensemble of realizations of the same cluster configurations, we are able to identify the average evolution of a cluster with a specific initial configuration and the distribution of possible output parameters that may result from that configuration. Most importantly, this approach allows us to discuss the general effects that cluster environment may have on planet formation without relying on the specific dynamics of individual cluster realizations.

Although we have completed a large parameter space survey, the range of initial conditions observed in young clusters is quite vast. In light of the results of Chapter IV,

which indicate that elongated subvirial clusters produce interesting observable kinematic signatures, and recent observations of the geometries in young clusters (e.g., Teixeira et al. 2006; Allen et al. 2007), perhaps the most interesting future direction in which to take this research is to study cluster dynamics under different assumptions of initial geometries. Specifically, the stellar distributions and embedding gas profiles should be generalized to include flattened and filamentary structures like those observed in nearby star-forming regions. Some progress toward this goal has already been made, including the development of a triaxial version of uniform and centrally concentrated gas potentials that can be included in the cluster simulations (Adams et al. 2007; Proszkow et al. 2009). However, a systematic study of the effect of initial geometry, such as the one presented for other initial cluster parameters in Chapter III, should be undertaken and is left for future studies.

With each new astronomical observation of young stellar clusters, our understanding of star-forming environments is honed, revealing cluster-to-cluster diversity while reinforcing underlying common elements such as elongated structure, subvirial stellar velocities, moderate levels of mass segregation, and rapid molecular gas removal. This work has come at an opportune time when observations can motivate simulations, and simulations can in return clarify observations and contribute to our understanding of the early stages of cluster evolution and planetary formation within young stellar clusters.

APPENDICES

APPENDIX A

Summary of N-Body Simulations

Table A.1 provides a summary of all of the N-body simulations included in this thesis. The simulations were completed with a modified version of the NBODY2 code developed by Aarseth (2001). Column (1) contains a name for the simulation or set of simulation described in each row. Column (2) indicates the cluster membership, N. Column (3) indicates the cluster geometry, "Sph" corresponds to a spherical geometry and "PSph" corresponds to a prolate spheroidal geometry. For clusters which are shaped like prolate spheroids, the aspect ratio is indicated in the simulation name. Column (4) contains the cluster radius, R_c in parsec. Column (5) contains the density profile of the stellar distribution in the cluster, ρ_*, centrally concentrated or uniform density. Column (6) indicates the amount of primordial mass segregation in the cluster, $F_{seg} \equiv N_{bound}/N$. Minimal mass segregation is indicated by "Min" and corresponds to the initial configuration in which the largest star is located at the center of the cluster. Column (7) indicates the average stellar mass in the cluster, $M_{T*} = N\langle m \rangle_*$. Column (8) contains the initial virial parameter $Q_i \equiv |K/W|$. Column (9) contains the density profile of the stellar distribution in the cluster, ρ_{gas}. "UniS", "SphH", and "TriH" correspond to a uniform density spheroid, spherical Hernquist profile, and triaxial Hernquist potential respectively. Column (10) indicates the time of instantaneous gas removal, t_{gas}. Column (11) contains the total star formation efficiency ε_{SF} of the cluster. Column (12) indicates which parameter (if any) is

varied over the set of simulations (for Chapters III and IV). Finally, column (13) references the chapter in which the simulations and their results are discussed.

Table A.1: Summary of All N-Body Simulations

Simulation	N	Geometry *[a]*	R_c [pc]	ρ_*	F_{seg} *[b]*	$\langle m \rangle_*$ [$M_\odot$]	Q_i	ρ_{gas} *[c]*	t_{gas} [Myr]	ε_{SF}	Parameter Varied	Chapter
Spherical Subvirial, $N = 100$	100	Sph	0.58	r^{-1}	Min	0.5	0.04	SphH	5	0.33		II
Spherical Virial, $N = 100$	100	Sph	0.58	r^{-1}	Min	0.5	0.5	SphH	5	0.33		II
Spherical Subvirial, $N = 300$	300	Sph	1.0	r^{-1}	Min	0.5	0.04	SphH	5	0.33		II
Spherical Virial, $N = 300$	300	Sph	1.0	r^{-1}	Min	0.5	0.5	SphH	5	0.33		II
Spherical Subvirial, $N = 1000$	1000	Sph	1.83	r^{-1}	Min	0.5	0.04	SphH	5	0.33		II
Spherical Virial, $N = 1000$	1000	Sph	1.83	r^{-1}	Min	0.5	0.5	SphH	5	0.33		II
NGC 1333	93	Sph	†				0.04	SphH	5	0.33		II
Cluster Membership, N	100 - 3000	Sph	$\left(\frac{N}{300}\right)^{1/2}$	r^{-1}	Min	0.5	0.04, 0.5	SphH	5	0.33	N, Q_i	III
Cluster Membership, N	100 - 3000	Sph	$\left(\frac{N}{300}\right)^{1/4}$	r^{-1}	Min	0.5	0.04, 0.5	SphH	5	0.33	N, Q_i	III
Initial Virial Parameter, Q_i	300, 1000, 2000	Sph	1.0, 1.83, 2.58	r^{-1}	Min	0.5	0.1 - 0.5	SphH	5	0.33	Q_i	III
Cluster Scaling Radius, R_{sc}	300, 1000, 2000	Sph	$R_{sc}\left(\frac{N}{300}\right)^{1/2}$, $R_{sc} = 0.33$ - 3	r^{-1}	Min	0.5	0.04	SphH	5	0.33	R_{sc}	III
Star Formation Efficiency, ε_{SF}	300, 1000	Sph	1.0, 1.83	r^{-1}	Min	0.5	0.04	SphH	5	0.1 - 0.75	ε_{SF}	III
Gas Removal Timescale, t_{gas}	300, 1000, 2000	Sph	1.0, 1.83, 2.58	r^{-1}	Min	0.5	0.04	SphH	1 - 7	0.33	t_{gas}	III
Mass Segregation, F_{seg}	300, 1000, 2000	Sph	1.0, 1.83, 2.58	r^{-1}	Min - 99%	0.5	0.04	SphH	5	0.33	F_{seg}	III
Spherical, $N = 2000$	2000	Sph	2.0	r^{-1}	Min	0.5	0.04, 0.5	SphH	5	0.50	Q_i	IV
Uniform Spheriod, (2 : 1)	2000	PSph	2.0	const.	Min	0.5	0.04, 0.15, 0.5	UniS	5	0.50	Q_i	IV
$1/m$ Spheriod, (2 : 1)	2000	PSph	2.0	m^{-1}	Min	0.5	0.04, 0.5	TriH	5	0.50	Q_i	IV
$1/m$ Spheriod, Subvirial (4 : 1)	2700	PSph	1.0	m^{-1}	Min	0.55, 0.5	0.04	TriH	5	0.17, 0.33	ε_{SF}	IV
$1/m$ Spheriod, Subvirial (2 : 1)	2700	PSph	2.0	m^{-1}	Min	0.55, 0.75	0.04	TriH	5	0.17, 0.33	ε_{SF}	IV

†R_c is set using the data from NGC 1333

APPENDIX B

The Use of N-Body Simulations to Study Gaseous Disk Collapse

In this Appendix we discuss the use of N-body simulations to calculate the dynamics of a collapsing gaseous disk. We provide the results from the simulated collapse of isolated Maclaurin and Mestel disks using an N-body code. Analytic treatments of collapsing gaseous systems provide generalized descriptions of collapse behavior by employing idealized geometries, density distributions, simplifying approximations, etc. However, analyses of this kind are limited by the very approximations that make them possible. On the other hand, fluid dynamics codes are capable of simulating various initial geometries and may include more complex physical processes such as gas pressure, drag forces, or interactions with magnetic fields, etc. N-body simulations are computationally much more efficient than fluid dynamics codes and can be used with care to simulate the behavior of gaseous (or gas dominated) systems. Toomre & Toomre (1972) is a classic example of using an N-body simulation (specifically, a restricted three-body simulation) to study the dynamics of interacting galaxies. More recently, full N-body simulations have been employed to study galaxy interactions in the stellar-dynamical limit (Hernquist 1993).

Modeling the behavior of a gaseous disk with an N-body code requires that care be taken when configuring the initial conditions and interpreting the results of the simulation. The initial configuration should minimize the scattering interactions that occur. This is

accomplished by choosing an axisymmetric ring configuration where particles in each ring have equal mass. Specifically, the simulated disk contains a central point mass and 25 rings of 32 equal mass particles. The total mass of each ring is then varied to produce a a 10^3 $M_\odot$ disk with radius 1 pc a desired initial density distribution.

The number of particles N chosen to represent the protocluster was determined by two competing factors: N must be large enough that the particles represent the smoothness of the density distribution and small enough to minimize particle-particle scattering interactions. We found that a choice of $N \sim 800$ produces a disk distribution that was both smooth enough to model accurately the behavior of the isolated disks and sparse enough to minimize the number of scattering interactions which occurred during the collapse simulation. For example, a disk with $N \sim 500$ particles had initial mass and force profiles with errors larger than the $N \sim 800$ disk. We compared simulations of disks with $N \sim 2000$ and $N \sim 800$ particles. We found that the evolution of both disks were very similar during the first half of the collapse, but at later times the $N \sim 2000$ disk had larger errors in their mass profiles and collapse times (when compared to the analytic solution) due to more frequent scattering interactions in the higher number density regions of the disk.

Another consideration when calculating the dynamics of fluids with N-body simulations is that the simulated behavior and conclusions drawn from that behavior should be consistent with the behavior of fluid systems. A consequence of using the N-body simulation is that as the disk of particles collapses, particle-particle interactions will allow some particles to pass through the center of mass and continue on a radial path outward. This collapse and subsequent expansion is an artifact of the simulation method. In a fluid system, mass collapses directly toward the center of mass until the pressure gradient becomes too large and collapse is slowed. Therefore, to simulate accretion in the N-body code, we have implemented a sink cell algorithm.

This algorithm allows the central particle in the disk to inelastically "absorb" the mass of any particle that comes within the sphere of radius r_{sink} surrounding the central particle. Experimentation with values of this fiducial radius resulted in the choice of $r_{sink} = 0.049$ pc $\approx 10,000$ AU. We required that the sink cell radius be small enough that it encompasses only the central particle at $t = 0$, and large enough that it maximized the number of disk particles that entered the sink cell during the simulation. For the test calculations of isolated Maclaurin and Mestel disks, more than 90% of the disk particles collapse from their initial position within the disk directly into the sink cell.

We model the continuous disk as a set of discrete particles arranged in an axisymmetric ring structure. The ring spacing, ring mass, and central particle mass are chosen so that these disks have radially averaged mass and force profiles that are in close agreement with a Maclaurin and Mestel profiles. Specifically, the simulated Maclaurin and Mestel disks have errors of 2.4% and 3.2% in their initial mass profiles, respectively. The initial force profiles have errors of 6.0% and 10.0%, respectively. These percent errors in the mass and force profiles are calculated as the r.m.s. error in the profile divided by $M(r_{1/2})$ and $F(r_{1/2})$ where $r_{1/2}$ is the initial half-mass radius of the Maclaurin or Mestel disk.

One of the problems inherent in representing a fluid disks as set of discrete particles is that the inner and outermost portions of the particle disk suffer from "edge effects" caused by the discrete nature of the ring structure. That is, these portions of the disks have mass and force profiles that differ from the edge of the analytic solutions. These "edge effects" are visible in the initial mass profiles depicted in Figure B.2 and in the calculated free-fall times in Figure B.1. We found that these effects do not propagate throughout the system but remain confined to their respective regions of the disk. Therefore, we can overcome these "edge effects" by describing the evolution of the disk without considering the inner and outermost regions in the description.

Thus, throughout this paper the descriptions of disk behavior do not include the innermost or outermost ring of the Maclaurin disk. The region of interest for collapse behavior is $r_1 < r < r_{25}$ for a disk with 25 rings, where r_i is the radius of the ith ring. The Mestel disk has the property that the equation of motion for a particle in the disk depends only on the mass interior to the ring containing that particle (Mestel 1963). This is not generally true for disk systems, but the Mestel disk is a special case where Gauss's law in disk geometry does hold. This allows us to embed the Mestel disk we are interested in simulating within a larger Mestel disk without changing the behavior of the smaller interior disk. Therefore, instead of ignoring the outer rings in the determination of disk behavior, we initially embed the Mestel disk in a larger disk with $R_{large} = 1.5 r_{Mestel}$, which effectively moves the "edge effects" outside of the region of interest ($r \leq r_{Mestel}$), and then consider the entire small Mestel disk except for the innermost ring ($r_1 < r \leq r_{Mestel}$). It is worth noting that more than 90% of the mass within the Maclaurin and Mestel disks is contained within the regions of interest defined above and thus only a small fraction of the disk suffers from these "edge effects".

The test calculations of disk collapse considered isolated Mestel and Maclaurin disks with initial radii of $r_d = 1.0$ pc and total masses of $M_d = 1000$ $M_\odot$. Analytic solutions to the pressure-free collapse of these systems exist and we compare our simulated results to the analytic solutions. For these initial conditions, the free-fall time for a Maclaurin disk 0.342 Myr independent of initial position within the disk. The Mestel disk has a free-fall time for a test mass initially at r of $t_{\rm ff}(r) = 0.526r$ Myr. The resulting free-fall times for the simulated disks are plotted in Figure B.1 as a function of initial position of the particle within the disk. The free-fall time for a particle is defined as the time that the particle enters the sink cell. For particles that do not enter the sink cell, the free-fall time is the time at which the particle passes closest to the disk's center.

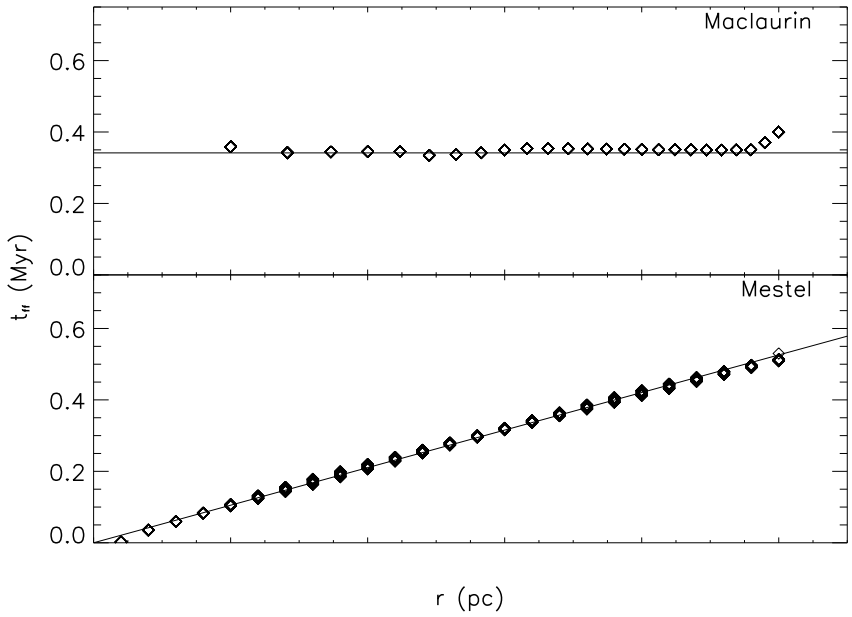

Figure B.1: The free-fall time for each particle in the simulated collapsing disk is plotted as a function of the initial radial position of the particle within the disk (*diamonds*). The upper (*lower*) panel displays the data from the Maclaurin (Mestel) disk simulation. Solid lines correspond to the analytic free-fall time calculated from the collapse solution for each initial surface density profile.

The "edge effects" are clearly seen in the free-fall times of the inner and outer rings in the Maclaurin disk. The error in the calculated free-fall times is 3.4% and 2.4% for the Maclaurin and Mestel disks respectively. This error is calculated by dividing the r.m.s. error by the free-fall time of a particle initially at the half-mass radius. By choosing to consider the regions of interest described above, the errors in the simulated behavior are reduced. For instance, if the entire disk was considered in the calculation of the free-fall times, the errors for the Maclaurin and Mestel disks would be 4.6% and 2.7%, respectively.

Figure B.2 depicts the evolution of the cumulative mass profiles for the collapsing Maclaurin (top panel) and the Mestel (bottom panel) disks. The solid curves correspond to the cumulative mass profiles of the simulated disk at $t = 0.0, 0.2, 0.4, 0.6$, and $0.8t_{\rm ff}$. The dashed curves correspond to the analytic solution for the cumulative mass profiles of the collapsing disk at the corresponding times. It is clear from this plot that discrepancies in the mass profile which are relics of the initial discrete particle configuration remain

throughout the simulation. However, the error is contained in the outermost rings, and does not significantly affect the evolution of the bulk of the disk. At each time step, the mass profile agrees well with the analytic solution out to a fraction of the disk radius, and this fraction does not change significantly over time. The errors in the mass profiles range from $2.4\% - 6.1\%$ and $3.2\% - 7.4\%$ for the Maclaurin and Mestel collapse simulations respectively for $t \leq 0.8\ t_{\rm ff}$, where the percent error in the mass profile is defined as the r.m.s. error in the profile divided by half of the total disk mass.

The error in particle positions was also calculated as a function of time. At a particular time and for a particular ring of particles in the disk, we calculate the r.m.s. error in the positions of the particles with respect to the analytic collapse solution. The r.m.s. error is scaled by the distance that the ring has collapsed, resulting in a percent error in the position of a ring at a particular time. For the Maclaurin disk, the errors in the simulated ring positions range from $0.13 - 39.19\%$ (with a mean of 7.04%) if we consider all rings, and all times. However, the largest percent errors occurred in the inner-most rings and at times close to the collapse time for the ring. If instead, we consider the region of the disk between rings 3 and 23 and times less than $0.75 t_{\rm ff}$ the errors in ring positions range from $0.13\% - 9.95\%$ (with a mean of 5.01%). This calculation was also completed for the simulated Mestel disk. Considering all rings and times, the errors in the simulated particle positions ranged from $0.14 - 16.88\%$ (with a mean of 5.53%). If only the portion of the disk between rings 3 and 24, and times less than $0.75 t_{\rm ff}$ are considered, the errors in ring positions range from $0.14 - 12.46\%$ (with a mean of 5.11%). Therefore, the bulk of the particles in the simulated Maclaurin and Mestel disks have small positional errors throughout most of the simulation. A summary of the errors in the simulated collapsing disks when compared to the pressure-free analytic collapse solutions is provided in Table B.1.

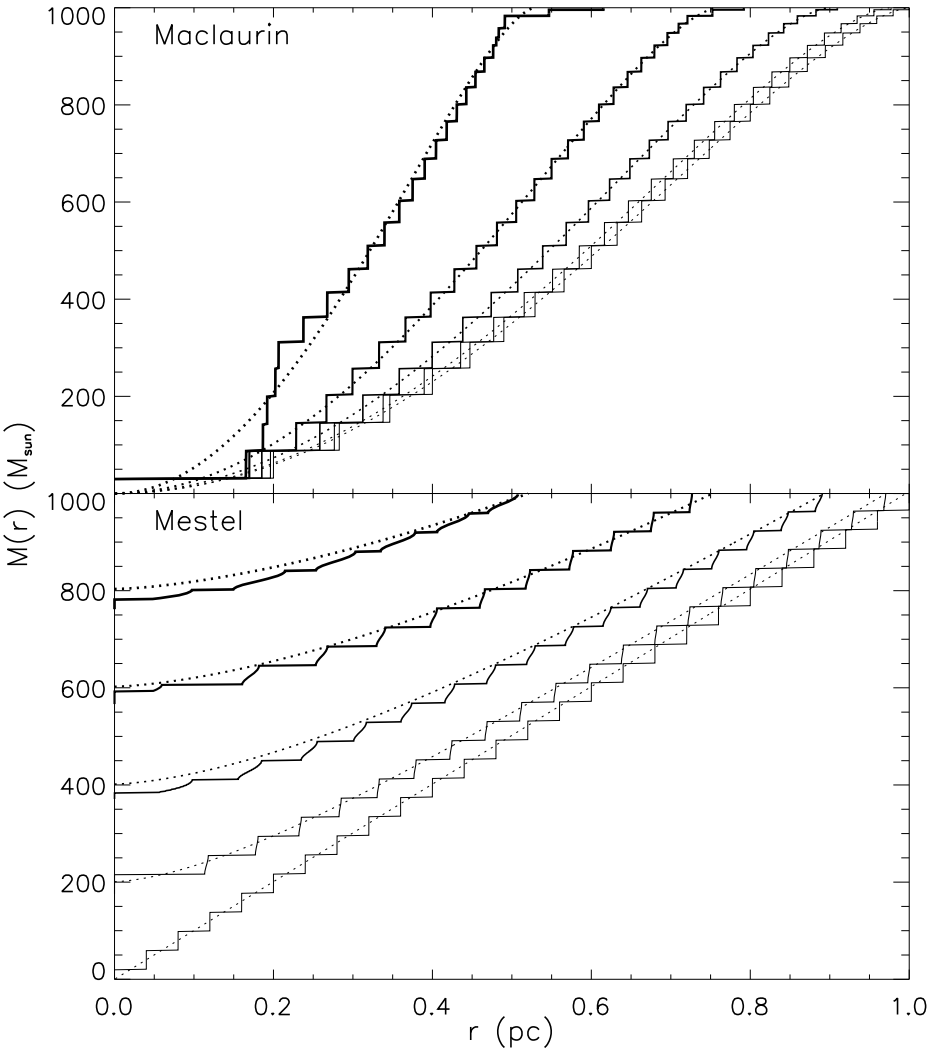

Figure B.2: Top panel displays cumulative mass distributions for the Maclaurin disk at times $t = 0, 0.2, 0.4, 0.6$, and $0.8\ t_{\rm ff}$ (in order from right to left). Thicker curves correspond to later times. The solid curve corresponds to the simulated data while the dashed curve corresponds to the analytic solution for the cumulative mass distribution at the corresponding times. Cumulative mass distributions for the Mestel disk at the same times are displayed in the bottom panel.

Table B.1: Simulation Errors

	Maclaurin Disk	Mestel Disk
Initial Force Profile, $F(r)/m$	6.0%	10.%
Free Fall Time, t_{ff}	3.4%	2.4%
Initial Mass Profile, $M(r, t = 0)$	2.4%	3.2%
Mass Profiles, $M(r, t \leq 0.8t_{ff})$	2.4 - 6.1%	3.2 - 7.4%

These test simulations provide evidence that our N-body code is indeed useful for studying systems of collapsing disks. We were able to reconstruct with our simulations disks of discrete particles that behaved as the corresponding gaseous disk with the smoothed surface density distribution behaves. These simulations brought to light the "edge effects" that our discrete systems displayed while at the same time revealing that those effects truly remained on the edge of the disks. Therefore, they can be consciously worked around by defining the region of interest as the inner portion of the disk. In addition, the particles in our simulation underwent very few particle encounters during the time leading up to the disk collapse indicating that the choice of the axisymmetric ring distribution succeeded in eliminating the scattering effect of random particle-particle interactions. And finally, our calculated initial force profiles, free-fall times, mass profiles, and particle positions agreed well with analytic solutions justifying use of this simulation method for calculation of Maclaurin and Mestel disk systems.

BIBLIOGRAPHY

BIBLIOGRAPHY

Aarseth, S. J. 1999, PASP, 111, 1333

—. 2001, New A, 6, 277

—. 2003, Gravitational N-Body Simulations (Gravitational N-Body Simulations, by Sverre J. Aarseth, pp. 430. ISBN 0521432723. Cambridge, UK: Cambridge University Press, November 2003.)

Adams, F. C. 2000, ApJ, 542, 964

Adams, F. C. & Bloch, A. M. 2005, ApJ, 629, 204

Adams, F. C., Bloch, A. M., Butler, S. C., Druce, J. M., & Ketchum, J. A. 2007, ApJ, 670, 1027

Adams, F. C. & Fatuzzo, M. 1996, ApJ, 464, 256

Adams, F. C., Hollenbach, D., Laughlin, G., & Gorti, U. 2004, ApJ, 611, 360

Adams, F. C. & Laughlin, G. 2001, Icarus, 150, 151

Adams, F. C. & Myers, P. C. 2001, ApJ, 553, 744

Adams, F. C., Proszkow, E. M., Fatuzzo, M., & Myers, P. C. 2006, ApJ, 641, 504

Allen, L., Megeath, S. T., Gutermuth, R., Myers, P. C., Wolk, S., Adams, F. C., Muzerolle, J., Young, E., & Pipher, J. L. 2007, in Protostars and Planets V, ed. B. Reipurth, D. Jewitt, & K. Keil, 361–376

Allen, L. E. 1995, PhD thesis, University of Massachusetts, Amherst

Alves, J., Lombardi, M., & Lada, C. J. 2007, A&A, 462, L17

André, P. 2002, Ap&SS, 281, 51

Armitage, P. J. 2000, A&A, 362, 968

Ballesteros-Paredes, J., Klessen, R. S., Mac Low, M.-M., & Vazquez-Semadeni, E. 2007, in Protostars and Planets V, ed. B. Reipurth, D. Jewitt, & K. Keil, 63–80

Bally, J., Stark, A. A., Wilson, R. W., & Langer, W. D. 1987, ApJ, 312, L45

Bastian, N. & Goodwin, S. P. 2006, MNRAS, 369, L9

Battinelli, P. & Capuzzo-Dolcetta, R. 1991, MNRAS, 249, 76

Baumgardt, H., Hut, P., & Heggie, D. C. 2002, MNRAS, 336, 1069

Beckwith, S., Evans, II, N. J., Becklin, E. E., & Neugebauer, G. 1976, ApJ, 208, 390

Beuther, H., Churchwell, E. B., McKee, C. F., & Tan, J. C. 2007, in Protostars and Planets V, ed. B. Reipurth, D. Jewitt, & K. Keil, 165–180

Binney, J. & Merrifield, M. 1998, Galactic astronomy (Princeton, NJ, Princeton University Press, 1998)

Binney, J. & Tremaine, S. 1987, Galactic dynamics (Princeton, NJ, Princeton University Press, 1987, 747 p.)

Boily, C. M. & Kroupa, P. 2003a, MNRAS, 338, 665

—. 2003b, MNRAS, 338, 673

Bonnell, I. & Kroupa, P. 1998, ArXiv Astrophysics e-prints

Bonnell, I. A. & Bate, M. R. 2002, MNRAS, 336, 659

Bonnell, I. A., Bate, M. R., Clarke, C. J., & Pringle, J. E. 2001, MNRAS, 323, 785

Bonnell, I. A. & Davies, M. B. 1998, MNRAS, 295, 691

Burkert, A. & Hartmann, L. 2004, ApJ, 616, 288

Carpenter, J. M. 2000, AJ, 120, 3139

Carpenter, J. M., Heyer, M. H., & Snell, R. L. 2000, ApJS, 130, 381

Carpenter, J. M., Meyer, M. R., Dougados, C., Strom, S. E., & Hillenbrand, L. A. 1997, AJ, 114, 198

Carpenter, J. M., Snell, R. L., Schloerb, F. P., & Skrutskie, M. F. 1993, ApJ, 407, 657

Chen, H., Tafalla, M., Greene, T. P., Myers, P. C., & Wilner, D. J. 1997, ApJ, 475, 163

Chini, R., Elsaesser, H., Hefele, H., & Weinberger, R. 1977, A&A, 56, 323

Churchwell, E., Povich, M. S., Allen, D., Taylor, M. G., Meade, M. R., Babler, B. L., Indebetouw, R., Watson, C., Whitney, B. A., Wolfire, M. G., Bania, T. M., Benjamin, R. A., Clemens, D. P., Cohen, M., Cyganowski, C. J., Jackson, J. M., Kobulnicky, H. A., Mathis, J. S., Mercer, E. P., Stolovy, S. R., Uzpen, B., Watson, D. F., & Wolff, M. J. 2006, ApJ, 649, 759

David, E.-M., Quintana, E. V., Fatuzzo, M., & Adams, F. C. 2003, PASP, 115, 825

de La Fuente Marcos, C. & de La Fuente Marcos, R. 1997, A&A, 326, L21

—. 1999, New Astronomy, 4, 21

Deharveng, L., Zavagno, A., & Caplan, J. 2005, A&A, 433, 565

Ducourant, C., Teixeira, R., Périé, J. P., Lecampion, J. F., Guibert, J., & Sartori, M. J. 2005, A&A, 438, 769

Duerr, R., Imhoff, C. L., & Lada, C. J. 1982, ApJ, 261, 135

Duquennoy, A. & Mayor, M. 1991, A&A, 248, 485

Elmegreen, B. G. 1983, MNRAS, 203, 1011

Elmegreen, B. G. 1991, in NATO ASIC Proc. 342: The Physics of Star Formation and Early Stellar Evolution, ed. C. J. Lada & N. D. Kylafis, 35

Elmegreen, B. G. 1998, in Astronomical Society of the Pacific Conference Series, Vol. 148, Origins, ed. C. E. Woodward, J. M. Shull, & H. A. Thronson, Jr., 150

Elmegreen, B. G. & Clemens, C. 1985, ApJ, 294, 523

Elmegreen, B. G., Efremov, Y., Pudritz, R. E., & Zinnecker, H. 2000, Protostars and Planets IV, 179

Elmegreen, B. G. & Lada, C. J. 1977, ApJ, 214, 725

Evans, II, N. J., Allen, L. E., Blake, G. A., Boogert, A. C. A., Bourke, T., Harvey, P. M., Kessler, J. E., Koerner, D. W., Lee, C. W., Mundy, L. G., Myers, P. C., Padgett, D. L., Pontoppidan, K., Sargent, A. I., Stapelfeldt, K. R., van Dishoeck, E. F., Young, C. H., & Young, K. E. 2003, PASP, 115, 965

Evans, II, N. J. & Lada, E. A. 1991, in IAU Symposium, Vol. 147, Fragmentation of Molecular Clouds and Star Formation, ed. E. Falgarone, F. Boulanger, & G. Duvert, 293–+

Fatuzzo, M. & Adams, F. C. 2008, ApJ, 675, 1361

Fatuzzo, M., Adams, F. C., & Myers, P. C. 2004, ApJ, 615, 813

Fűrész, G., Hartmann, L. W., Megeath, S. T., Szentgyorgyi, A. H., & Hamden, E. T. 2008, ApJ, 676, 1109

Fűrész, G., Hartmann, L. W., Szentgyorgyi, A. H., Ridge, N. A., Rebull, L., Stauffer, J., Latham, D. W., Conroy, M. A., Fabricant, D. G., & Roll, J. 2006, ApJ, 648, 1090

Fregeau, J. M., Chatterjee, S., & Rasio, F. A. 2006, ApJ, 640, 1086

Geyer, M. P. & Burkert, A. 2001, MNRAS, 323, 988

Gieles, M., Athanassoula, E., & Portegies Zwart, S. F. 2007, MNRAS, 376, 809

Gieles, M., Portegies Zwart, S. F., Baumgardt, H., Athanassoula, E., Lamers, H. J. G. L. M., Sipior, M., & Leenaarts, J. 2006, MNRAS, 371, 793

Giersz, M. & Heggie, D. C. 1994, MNRAS, 268, 257

Goodman, J. & Binney, J. 1983, MNRAS, 203, 265

Goodman, J., Heggie, D. C., & Hut, P. 1993, ApJ, 415, 715

Goodwin, S. P. & Bastian, N. 2006, MNRAS, 373, 752

Gutermuth, R. A., Bourke, T. L., Allen, L. E., Myers, P. C., Megeath, S. T., Matthews, B. C., Jørgensen, J. K., Di Francesco, J., Ward-Thompson, D., Huard, T. L., Brooke, T. Y., Dunham, M. M., Cieza, L. A., Harvey, P. M., & Chapman, N. L. 2008a, ApJ, 673, L151

Gutermuth, R. A., Megeath, S. T., Muzerolle, J., Allen, L. E., Pipher, J. L., Myers, P. C., & Fazio, G. G. 2004, ApJS, 154, 374

Gutermuth, R. A., Megeath, S. T., Pipher, J. L., Williams, J. P., Allen, L. E., Myers, P. C., & Raines, S. N. 2005, ApJ, 632, 397

Gutermuth, R. A., Myers, P. C., Megeath, S. T., Allen, L. E., Pipher, J. L., Muzerolle, J., Porras, A., Winston, E., & Fazio, G. 2008b, ApJ, 674, 336

Heggie, D. C., Hut, P., & McMillan, S. L. W. 1996, ApJ, 467, 359

Heitsch, F., Hartmann, L. W., Slyz, A. D., Devriendt, J. E. G., & Burkert, A. 2008, ApJ, 674, 316

Heitsch, F., Slyz, A. D., Devriendt, J. E. G., Hartmann, L. W., & Burkert, A. 2006, ApJ, 648, 1052

Heller, C. H. 1993, ApJ, 408, 337

—. 1995, ApJ, 455, 252

Herbig, G. H. & Dahm, S. E. 2002, AJ, 123, 304

Hernquist, L. 1990, ApJ, 356, 359

—. 1993, ApJ, 409, 548

Heyer, M. H. & Terebey, S. 1998, ApJ, 502, 265

Hillenbrand, L. A. 1995, PhD thesis, University of Massachusetts, Amherst

Hillenbrand, L. A. & Hartmann, L. W. 1998, ApJ, 492, 540

Hills, J. G. 1980, ApJ, 235, 986

Hodapp, K.-W. 1994, ApJS, 94, 615

Hurley, J. R. & Shara, M. M. 2002, ApJ, 565, 1251

Hut, P. & Bahcall, J. N. 1983, ApJ, 268, 319

Jeffries, R. D. 2007, MNRAS, 376, 1109

Jiang, Z., Yao, Y., Yang, J., Ando, M., Kato, D., Kawai, T., Kurita, M., Nagata, T., Nagayama, T., Nakajima, Y., Nagashima, C., Sato, S., Tamura, M., Nakaya, H., & Sugitani, K. 2002, ApJ, 577, 245

Jijina, J., Myers, P. C., & Adams, F. C. 1999, ApJS, 125, 161

Johnstone, D., Hollenbach, D., & Bally, J. 1998, ApJ, 499, 758

Johnstone, D., Wilson, C. D., Moriarty-Schieven, G., Joncas, G., Smith, G., Gregersen, E., & Fich, M. 2000, ApJ, 545, 327

Jones, B. F. & Walker, M. F. 1988, AJ, 95, 1755

Kirk, H., Johnstone, D., & Di Francesco, J. 2006, ApJ, 646, 1009

Kirk, H., Johnstone, D., & Tafalla, M. 2007, ApJ, 668, 1042

Klessen, R. S. & Burkert, A. 2000, ApJS, 128, 287

—. 2001, ApJ, 549, 386

Klessen, R. S., Heitsch, F., & Mac Low, M.-M. 2000, ApJ, 535, 887

Kobayashi, H. & Ida, S. 2001, Icarus, 153, 416

Kramer, C., Stutzki, J., Rohrig, R., & Corneliussen, U. 1998, A&A, 329, 249

Kroupa, P. 1995a, MNRAS, 277, 1522

—. 1995b, MNRAS, 277, 1507

Kroupa, P. & Bouvier, J. 2003, MNRAS, 346, 343

Kroupa, P., Bouvier, J., Duchêne, G., & Moraux, E. 2003, MNRAS, 346, 354

Kroupa, P., Petr, M. G., & McCaughrean, M. J. 1999, New Astronomy, 4, 495

Kumar, M. S. N., Davis, C. J., Grave, J. M. C., Ferreira, B., & Froebrich, D. 2007, MNRAS, 374, 54

Lada, C. J., Alves, J., & Lada, E. A. 1996, AJ, 111, 1964

Lada, C. J. & Lada, E. A. 2003, ARA&A, 41, 57

Lada, C. J., Margulis, M., & Dearborn, D. 1984, ApJ, 285, 141

Lada, C. J., Muench, A. A., Haisch, Jr., K. E., Lada, E. A., Alves, J. F., Tollestrup, E. V., & Willner, S. P. 2000, AJ, 120, 3162

Lada, C. J., Young, E. T., & Greene, T. P. 1993, ApJ, 408, 471

Lada, E. A., Depoy, D. L., Evans, II, N. J., & Gatley, I. 1991, ApJ, 371, 171

Larson, R. B. 1985, MNRAS, 214, 379

Laughlin, G. & Adams, F. C. 2000, Icarus, 145, 614

Laughlin, G., Bodenheimer, P., & Adams, F. C. 2004, ApJ, 612, L73

Leisawitz, D., Bash, F. N., & Thaddeus, P. 1989, ApJS, 70, 731

Liszt, H. S., Delin, X., & Burton, W. B. 1981, ApJ, 249, 532

Luhman, K. L., Stauffer, J. R., Muench, A. A., Rieke, G. H., Lada, E. A., Bouvier, J., & Lada, C. J. 2003, ApJ, 593, 1093

Maeder, A. & Meynet, G. 1987, A&A, 182, 243

Massey, P. 2003, ARA&A, 41, 15

Matzner, C. D. & McKee, C. F. 2000, ApJ, 545, 364

McKee, C. F. & Tan, J. C. 2003, ApJ, 585, 850

McMillan, S. L. W. & Hut, P. 1996, ApJ, 467, 348

Megeath, S. T., Allen, L. E., Gutermuth, R. A., Pipher, J. L., Myers, P. C., Calvet, N., Hartmann, L., Muzerolle, J., & Fazio, G. G. 2004, ApJS, 154, 367

Megeath, S. T., Flaherty, K. M., Hora, J., Allen, L. E., Fazio, G. G., Hartmann, L., Myers, P. C., Muzerolle, J., Pipher, J. L., Siegler, N., Stauffer, J. R., & Young, E. 2005, in IAU Symposium, Vol. 227, Massive Star Birth: A Crossroads of Astrophysics, ed. R. Cesaroni, M. Felli, E. Churchwell, & M. Walmsley, 383–388

Mengel, S., Lehnert, M. D., Thatte, N. A., Vacca, W. D., Whitmore, B., & Chandar, R. 2008, A&A, 489, 1091

Mestel, L. 1963, MNRAS, 126, 553

Miller, G. E. & Scalo, J. M. 1979, ApJS, 41, 513

Minier, V., Burton, M. G., Hill, T., Pestalozzi, M. R., Purcell, C. R., Garay, G., Walsh, A. J., & Longmore, S. 2005, A&A, 429, 945

Moorhead, A. V. & Adams, F. C. 2005, Icarus, 178, 517

Motte, F., Andre, P., & Neri, R. 1998, A&A, 336, 150

Muench, A. A., Lada, E. A., Lada, C. J., & Alves, J. 2002, ApJ, 573, 366

Muench, A. A., Lada, E. A., Lada, C. J., Elston, R. J., Alves, J. F., Horrobin, M., Huard, T. H., Levine, J. L., Raines, S. N., & Román-Zúñiga, C. 2003, AJ, 125, 2029

Muzerolle, J., Megeath, S. T., Gutermuth, R. A., Allen, L. E., Pipher, J. L., Hartmann, L., Gordon, K. D., Padgett, D. L., Noriega-Crespo, A., Myers, P. C., Fazio, G. G., Rieke, G. H., Young, E. T., Morrison, J. E., Hines, D. C., Su, K. Y. L., Engelbracht, C. W., & Misselt, K. A. 2004, ApJS, 154, 379

Myers, P. C. 1998, ApJ, 496, L109

Myers, P. C. & Fuller, G. A. 1993, ApJ, 402, 635

Myers, P. C., Fuller, G. A., Goodman, A. A., & Benson, P. J. 1991, ApJ, 376, 561

O'dell, C. R. 2001, ARA&A, 39, 99

Ostriker, E. C. 1994, ApJ, 424, 292

Padgett, D. L., Rebull, L. M., Stapelfeldt, K. R., Chapman, N. L., Lai, S.-P., Mundy, L. G., Evans, II, N. J., Brooke, T. Y., Cieza, L. A., Spiesman, W. J., Noriega-Crespo, A., McCabe, C.-E., Allen, L. E., Blake, G. A., Harvey, P. M., Huard, T. L., Jørgensen, J. K., Koerner, D. W., Myers, P. C., Sargent, A. I., Teuben, P., van Dishoeck, E. F., Wahhaj, Z., & Young, K. E. 2008, ApJ, 672, 1013

Peretto, N., André, P., & Belloche, A. 2006, A&A, 445, 979

Piskunov, A. E., Kharchenko, N. V., Röser, S., Schilbach, E., & Scholz, R.-D. 2006, A&A, 445, 545

Porras, A., Christopher, M., Allen, L., Di Francesco, J., Megeath, S. T., & Myers, P. C. 2003, AJ, 126, 1916

Portegies Zwart, S. F., Hut, P., Makino, J., & McMillan, S. L. W. 1998, A&A, 337, 363

Press, W. H., Flannery, B. P., & Teukolsky, S. A. 1986, Numerical recipes. The art of scientific computing (Cambridge: University Press, 1986)

Proszkow, E.-M., Adams, F. C., Hartmann, L. W., & Tobin, J. J. 2009, ApJ, 697, 1020

Proszkow, E.-M. & Myers, P. C. 2008, ApJ, 683, 226

Quillen, A. C., Thorndike, S. L., Cunningham, A., Frank, A., Gutermuth, R. A., Blackman, E. G., Pipher, J. L., & Ridge, N. 2005, ApJ, 632, 941

Rasio, F. A., McMillan, S., & Hut, P. 1995, ApJ, 438, L33

Richtmyer, R. D. 1978, Principles of Advanced Mathematical Physics (New York: Springer-Verlag, 1978)

Ridge, N. A., Di Francesco, J., Kirk, H., Li, D., Goodman, A. A., Alves, J. F., Arce, H. G., Borkin, M. A., Caselli, P., Foster, J. B., Heyer, M. H., Johnstone, D., Kosslyn, D. A., Lombardi, M., Pineda, J. E., Schnee, S. L., & Tafalla, M. 2006, AJ, 131, 2921

Ripley, B. D. & Rasson, J. P. 1977, J. Appl. Prob., 14, 483

Ryden, B. S. 1996, ApJ, 471, 822

Salpeter, E. E. 1955, ApJ, 121, 161

Scally, A. & Clarke, C. 2001, MNRAS, 325, 449

Schaller, G., Schaerer, D., Meynet, G., & Maeder, A. 1992, A&AS, 96, 269

Schmeja, S. & Klessen, R. S. 2006, A&A, 449, 151

Schneider, N., Bontemps, S., Simon, R., Jakob, H., Motte, F., Miller, M., Kramer, C., & Stutzki, J. 2006, A&A, 458, 855

Shu, F. H. 1977, ApJ, 214, 488

—. 1982, The physical universe. an introduction to astronomy (A Series of Books in Astronomy, Mill Valley, CA: University Science Books, 1982)

Shu, F. H., Adams, F. C., & Lizano, S. 1987, ARA&A, 25, 23

Shu, F. H., Johnstone, D., & Hollenbach, D. 1993, Icarus, 106, 92

Smith, K. W. & Bonnell, I. A. 2001, MNRAS, 322, L1

Solomon, P. M., Rivolo, A. R., Barrett, J., & Yahil, A. 1987, ApJ, 319, 730

Sterzik, M. F. & Durisen, R. H. 1998, A&A, 339, 95

Störzer, H. & Hollenbach, D. 1999, ApJ, 515, 669

Strom, K. M., Strom, S. E., & Vrba, F. J. 1976, AJ, 81, 308

Sugitani, K., Tamura, M., & Ogura, K. 1995, ApJ, 455, L39+

Szentgyorgyi, A. H., Cheimets, P., Eng, R., Fabricant, D. G., Geary, J. C., Hartmann, L., Pieri, M. R., & Roll, J. B. 1998, in Presented at the Society of Photo-Optical Instrumentation Engineers (SPIE) Conference, Vol. 3355, Society of Photo-Optical Instrumentation Engineers (SPIE) Conference Series, ed. S. D'Odorico, 242–252

Tafalla, M., Myers, P. C., Caselli, P., Walmsley, C. M., & Comito, C. 2002, ApJ, 569, 815

Teixeira, P. S., Lada, C. J., Young, E. T., Marengo, M., Muench, A., Muzerolle, J., Siegler, N., Rieke, G., Hartmann, L., Megeath, S. T., & Fazio, G. 2006, ApJ, 636, L45

Terlevich, E. 1987, MNRAS, 224, 193

Testi, L., Palla, F., & Natta, A. 1998, A&AS, 133, 81

—. 1999, A&A, 342, 515

Theuns, T. 1991, Memorie della Societa Astronomica Italiana, 62, 909

Thies, I., Kroupa, P., & Theis, C. 2005, MNRAS, 364, 961

Tobin, J. J., Hartmann, L., Furesz, G., Mateo, M., & Megeath, S. T. 2009, ArXiv e-prints

Toomre, A. & Toomre, J. 1972, ApJ, 178, 623

Verschueren, W. & David, M. 1989, A&A, 219, 105

Vrba, F. J., Strom, K. M., Strom, S. E., & Grasdalen, G. L. 1975, ApJ, 197, 77

Walker, M. G., Mateo, M., Olszewski, E. W., Bernstein, R., Sen, B., & Woodroofe, M. 2007, ApJS, 171, 389

Walsh, A. J., Myers, P. C., & Burton, M. G. 2004, ApJ, 614, 194

Walsh, A. J., Myers, P. C., Di Francesco, J., Mohanty, S., Bourke, T. L., Gutermuth, R., & Wilner, D. 2007, ApJ, 655, 958

Weaver, R., McCray, R., Castor, J., Shapiro, P., & Moore, R. 1977, ApJ, 218, 377

Whitney, B. A., Sewilo, M., Indebetouw, R., Robitaille, T. P., Meixner, M., Gordon, K., Meade, M. R., Babler, B. L., Harris, J., Hora, J. L., Bracker, S., Povich, M. S., Churchwell, E. B., Engelbracht, C. W., For, B.-Q., Block, M., Misselt, K., Vijh, U., Leitherer, C., Kawamura, A., Blum, R. D., Cohen, M., Fukui, Y., Mizuno, A., Mizuno, N., Srinivasan, S., Tielens, A. G. G. M., Volk, K., Bernard, J.-P., Boulanger, F., Frogel, J. A., Gallagher, J., Gorjian, V., Kelly, D., Latter, W. B., Madden, S., Kemper, F., Mould, J. R., Nota, A., Oey, M. S., Olsen, K. A., Onishi, T., Paladini, R., Panagia, N., Perez-Gonzalez, P., Reach, W., Shibai, H., Sato, S., Smith, L. J., Staveley-Smith, L., Ueta, T., Van Dyk, S., Werner, M., Wolff, M., & Zaritsky, D. 2008, AJ, 136, 18

Whitworth, A. 1979, MNRAS, 186, 59

Whitworth, A. P. 2005, in Cores to Clusters: Star Formation with Next Generation Telescopes, ed. M. S. N. Kumar, M. Tafalla, & P. Caselli, 15

Whitworth, A. P., Bhattal, A. S., Chapman, S. J., Disney, M. J., & Turner, J. A. 1994, A&A, 290, 421

Wilking, B. A. & Lada, C. J. 1983, ApJ, 274, 698

Wilson, B. A., Dame, T. M., Masheder, M. R. W., & Thaddeus, P. 2005, A&A, 430, 523

Winston, E., Megeath, S. T., Wolk, S. J., Muzerolle, J., Gutermuth, R., Hora, J. L., Allen, L. E., Spitzbart, B., Myers, P., & Fazio, G. G. 2007, ApJ, 669, 493

Zavagno, A., Deharveng, L., Comerón, F., Brand, J., Massi, F., Caplan, J., & Russeil, D. 2006, A&A, 446, 171

Zinnecker, H., McCaughrean, M. J., Rayner, J. T., Wilking, B. A., & Moneti, A. 1993, in Reviews in Modern Astronomy, Vol. 6, Reviews in Modern Astronomy, ed. G. Klare, 191–208